Aachener Verfahrenstechnik

RWTH AACHEN UNIVERSITY

Aachener Verfahrenstechnik Series
AVT.SVT – Process Systems Engineering
Volume 36 (2025)

Mohammad El Wajeh

Optimal Dynamic Operation of Electrified Biodiesel Production

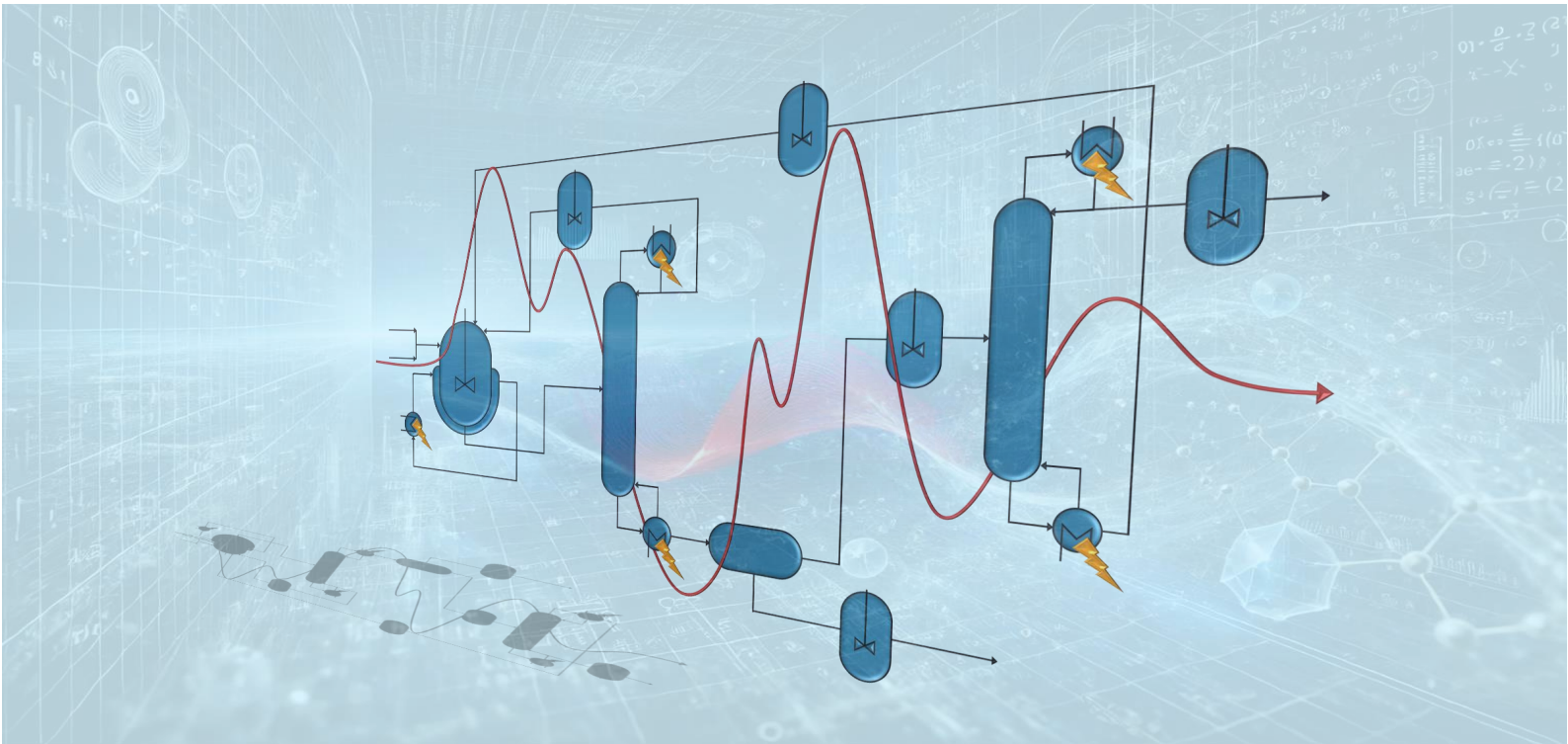

Optimal Dynamic Operation of Electrified Biodiesel Production

Optimale dynamische Betriebsführung der elektrifizierten Biodieselproduktion

Von der Fakultät für Maschinenwesen der Rheinisch-Westfälischen Technischen Hochschule Aachen zur Erlangung des akademischen Grades eines Doktors der Ingenieurwissenschaften genehmigte Dissertation

vorgelegt von

Mohammad El Wajeh

Berichter: Universitätsprofessor Alexander Mitsos, Ph.D.
Professor Christopher L. E. Swartz, Ph.D.

Tag der mündlichen Prüfung: 28. März 2025

Titel: Optimal Dynamic Operation of Electrified Biodiesel Production

Autor: Mohammad El Wajeh

Reihe: Aachener Verfahrenstechnik Series
AVT.SVT – Process Systems Engineering
Band 36 (2025)

Herausgeber: Aachener Verfahrenstechnik
Forckenbeckstraße 51
52074 Aachen
Tel.: +49 (0)241 80 97717
Fax.: +49 (0)241 80 92326
E-Mail: secretary.svt@avt.rwth-aachen.de
https://www.avt.rwth-aachen.de

Volltext verfügbar: 10.18154/RWTH-2025-03483

Preface

I am profoundly grateful for the opportunity to work, grow, and pursue my doctorate at the Chair of Process Systems Engineering (AVT.SVT) at RWTH Aachen University, ultimately leading to the completion of this dissertation.

First and foremost, I sincerely thank my advisor, Alexander Mitsos, for his academic guidance, exceptional mentorship, constant support, open-mindedness, and straightforward approach. My sincere thanks also go to Adel Mhamdi for his continuous support, our collaboration on my research project, his valuable feedback, and the many insightful discussions we shared. I am especially grateful for the memorable experiences we had together at international conferences. Additionally, I am equally grateful to Christopher Swartz for serving as the second examiner of this dissertation and for his academic inspiration.

I am indebted to all my colleagues at AVT.SVT for fostering a friendly and collaborative environment and for the enriching moments we shared both inside and outside the office. In particular, I would like to express my appreciation to Aron Zingler, Chrysanthi Papadimitriou, Georgianna Prokopou, Marc-Daniel Stumm, Laura Lang, Jan Schulze, and many others. Your support and teamwork created an inspiring, motivating, and enjoyable workplace, which was essential to the completion of my doctorate.

Furthermore, I would like to thank Wanda Frohn, Petra Eissa, Didem Uslu and her team, as well as Jutta Friedrich, Sascha Gerhards, and their team for their continuous support, which allowed me to focus on the core of my research.

I am also grateful to the students who contributed to my work, particularly Marcel Granderath, Vincent Klippel, and Jerome Jordan.

My main project partners in the Kopernikus SynErgie project were Siemens AG and Cargill. I would especially like to thank Volker Hirsch, Adrian Caspari, and Lena Lohner from Siemens, as well as Martin Kleber, Wolfgang Hoffmann, and Angela Kleber from Cargill, for their rewarding collaboration and many insightful discussions. I also gratefully acknowledge the financial support of the Kopernikus project SynErgie by the Federal Ministry of Education and Research (BMBF) and the project supervision by the project management organization Projektträger Jülich (PtJ).

Lastly, and most importantly, I am eternally grateful to my family—especially my mother—for being my greatest source of motivation, as well as for their unwavering support and encouragement not only throughout this journey but throughout my entire life.

Aachen, March 2025 *Mohammad El Wajeh*

Contents

Acronyms

AVT.SVT	Chair of Process Systems Engineering at RWTH Aachen University
CCs	complementarity constraints
CDOF	control degrees of freedom
COP	coefficient of performance
CS	carbon steel
CST	continuous stirred tank
CSTR	continuous stirred-tank reactor
CV	controlled variable
DA	differential-algebraic
DAE	differential-algebraic equation
DASSL	Differential Algebraic System Solver
DeNMPC	distributed economic nonlinear model predictive control
DIPPR	Design Institute for Physical Properties
DO	dynamic optimization
DSM	demand-side management
DyOS	Dynamic Optimization Software
eNMPC	economic nonlinear model predictive control
FAME	fatty acid methyl esters
FFA	free fatty acids
FMU	Functional Mockup Unit
HI	heat integration
IFSH	integrated framework of simulation and heuristics
LLE	liquid-liquid equilibrium
LP	low pressure
MESH	Material balance, phase Equilibrium, Summation, and Heat balance
MP	medium pressure
MPC	model predictive control
MV	manipulated variable
NCP	nonlinear complementary problem
NIXE	NIXE Is eXtrapolated Euler

NLP	nonlinear program
NMPC	nonlinear model predictive control
NRTL	non-random two-liquid
PWC	plantwide control
QSS	quasi-stationary scheduling
RSR	reaction-separation-recycle
SNOPT	Sparse Nonlinear OPTimizer
SQP	sequential quadratic programming
SS	steady-state
TPM	throughput manipulator
UFOP	Union for the Promotion of Oil and Protein Plants
VLE	vapor-liquid equilibrium
VLLE	vapor-liquid-liquid equilibrium
VRC	vapor recompression

Kurzfassung

Der flexible Betrieb elektrifizierter chemischer Prozesse, die mit erneuerbarem Strom betrieben werden, bietet sowohl wirtschaftliche als auch ökologische Vorteile. Die Umstellung vom herkömmlichen stationären Betrieb auf einen flexiblen Betrieb stellt jedoch eine große Herausforderung für die Prozessentwicklung und den Betrieb dar. Dieser Paradigmenwechsel bereitet zwar den Weg für einen optimalen flexiblen Betrieb, erfordert aber auch die Einbeziehung der Prozessdynamik in Planungsentscheidungen. Dies ist vor allem für chemische Anlagen, wie z. B. Biodieselproduktionsprozesse, relevant, bei denen die zeitlichen Charakteristika mit den Zeitpunkten der Strompreisschwankungen übereinstimmen. In dieser Dissertation entwickeln und implementieren wir modellierungs- und optimierungsbasierte Methoden, um Schlüsselaspekte des optimalen dynamischen Betriebs in elektrifizierten chemischen Prozessen zu adressieren.

Wir entwickeln und wenden einen Modellierungs- und Optimierungsrahmen an, um das Ziel eines optimalen flexiblen Betriebs für einen elektrifizierten Biodieselproduktionsprozess zu erreichen. Die Kapitel der Dissertation sind um diesen Rahmen aufgebaut, beginnend mit der Modellentwicklung, gefolgt von der Elektrifizierung und der Offline-Optimierung mit Berücksichtigung zur Prozessgestaltung, und abschließend mit der Online-Regelung. Wir beginnen mit dem Modellentwicklungsschritt, in der wir ein mechanistisches dynamisches Modell des Biodieselproduktionsprozesses zusammen mit zwei anlagenweiten Regelungsstrukturen einführen. Wir simulieren die Antworten der Anlage auf verschiedene Störungen, um die Notwendigkeit modellbasierter Kontrollstrategien zu verdeutlichen. Dieses Modell dient als Grundlage für die nachfolgenden Kapitel.

In dem Schritt der Offline-Optimierung formulieren wir dynamische Optimierungsprobleme, die flexibilitätsorientierte Prozessentwürfe einbeziehen. Wir demonstrieren den Nutzen von Puffertanks, die nicht nur die betriebliche Flexibilität erhöhen, sondern auch eine Systemzerlegung für eine verteilte Optimierung ermöglichen. Außerdem untersuchen wir die Auswirkungen der Wärmeintegration auf die betriebliche Flexibilität und zeigen, wie die Einbeziehung zusätzlicher Elektrifizierung die Freiheitsgrade der Optimierung erhöht.

Aufbauend auf den Ergebnissen der Offline-Studien und den flexibilitätsorientierten Prozesskonfigurationen implementieren wir in dem letzten Schritt Echtzeitregelungsanwendungen. Insbesondere nutzen wir die Prozesskonfiguration, die eine verteilte Optimierung unterstützt, um eine verteilte ökonomische nichtlineare modellprädiktive Regelung zu entwickeln und anzuwenden. Unsere verteilten Regelungsstrategien umfassen sowohl sequentielle und iterative Kommunikationsarchitekturen als auch Kompensationsverfahren für Rechenverzögerungen, die Verzögerungen über mehrere Abtastintervalle hinweg berücksichtigen.

Indem wir diese drei Schritte systematisch durchlaufen, erreichen wir das endgültige Ziel eines optimalen und realisierbaren flexiblen Betriebs. Diese Dissertation zeigt nicht nur die Zusammenhänge zwischen diesen Schritten während der Entwicklung und Implementierung auf, sondern präsentiert auch Methoden und Werkzeuge, die auf eine Vielzahl anderer chemischer Prozesse übertragbar sind.

Summary

The flexible operation of electrified chemical processes powered by renewable electricity offers both economic and ecological benefits, contributing to more sustainable chemical production. However, transitioning from conventional steady-state operations presents a significant challenge to process design and operation. While this change in operational paradigm paves the way for achieving optimal flexible operation and effective demand-side management, it also necessitates incorporating process dynamics into scheduling decisions to ensure both optimal and feasible outcomes. This is particularly relevant for chemical plants, such as biodiesel production processes, which operate on time scales comparable to fluctuations in electricity prices. In this dissertation, we develop and implement modeling- and optimization-based methods and tools to address key aspects of optimal dynamic operations in electrified chemical processes.

We develop and apply a modeling and optimization framework that guides process systems through essential stages to achieve the final goal of optimal flexible operation for an electrified biodiesel production process. The dissertation chapters are structured around these main stages, beginning with model development, followed by electrification and offline optimization with process design considerations, and concluding with online control. We begin with the model development phase, where we introduce a rigorous mechanistic dynamic model of the biodiesel production process, along with two plantwide base-layer control structures. We simulate plant responses under various disturbances to highlight the necessity of model-based control strategies in meeting operational goals. This model serves as the foundation for the subsequent chapters.

Moving to the offline optimization stage, we formulate dynamic optimization problems that incorporate flexibility-oriented process designs. We demonstrate the dual role of buffer tanks for storing intermediate and final products, which not only enhance operational flexibility but also enable system decomposition for distributed optimization by decoupling dynamics between different process sections. Additionally, we explore the impact of heat integration on operational flexibility and demonstrate how incorporating additional electrified heating units increases the degrees of freedom in optimization.

Building on the offline studies and flexibility-oriented process configurations, we then move to the final stage—online control—where we implement real-time control applications. In particular, we leverage the process configuration that supports distributed optimization to develop and apply distributed economic nonlinear model predictive control. Our distributed control strategies incorporate both sequential and iterative communication architectures, as well as compensation schemes for computational delays. These schemes account for subsystem couplings and delays across multiple sampling intervals.

By systematically progressing through these three stages, we achieve the final objective of optimal and feasible flexible operation for chemical processes. This dissertation not only demonstrates the interconnectivity between these stages during both development and implementation but also provides methods and tools with broad applicability to other chemical processes targeting optimal dynamic operations.

Publications and Copyrights

This dissertation stems from research conducted by the author during his time at the Chair of Process Systems Engineering at RWTH Aachen University (AVT.SVT). Parts of this work have been previously published, and the relevant material is incorporated into the chapters with permission, as outlined below. A detailed description of the contributions made by all authors is also provided.

- The introduction incorporates excerpts from the abstracts published in [1–5].
- Chapter 2 is partially based on [1]: M. El Wajeh, A. Mhamdi, and A. Mitsos. Dynamic Modeling and Plantwide Control of a Production Process for Biodiesel and Glycerol. *Industrial & Engineering Chemistry Research*, 62(27):10559–10576, 2023. doi: 10.1021/acs.iecr.3c00934. Copyright © 2023 American Chemical Society.
  Author contributions: *Mohammad El Wajeh*: Conceptualization, Methodology, Software, Investigation, Validation, Formal analysis, Writing - Original draft. *Adel Mhamdi*: Conceptualization, Project administration, Supervision, Funding acquisition, Writing - Review and editing. *Alexander Mitsos*: Conceptualization, Project administration, Supervision, Resources, Writing - Review and editing.
- Chapter 3 is partially based on [2]: M. El Wajeh, A. Mhamdi, and A. Mitsos. Optimal Design and Flexible Operation of a Fully Electrified Biodiesel Production Process. *Industrial & Engineering Chemistry Research*, 63(3):1487–1500, 2024. doi: 10.1021/acs.iecr.3c03074. Copyright © 2024 American Chemical Society.
  Author contributions: *Mohammad El Wajeh*: Conceptualization, Methodology, Software, Investigation, Validation, Formal analysis, Writing - Original draft. *Adel Mhamdi*: Conceptualization, Project administration, Supervision, Funding acquisition, Writing - Review and editing. *Alexander Mitsos*: Conceptualization, Project administration, Supervision, Resources, Writing - Review and editing.
- Chapter 4 is partially based on [3]: M. El Wajeh, A. Mhamdi, and A. Mitsos. Optimal Flexible Operation of Electrified and Heat-Integrated Biodiesel Production. *IFAC-PapersOnLine*, 58(14):513–518, 2024. doi: 10.1016/j.ifacol.2024.08.388. Copyright © 2024 The Authors. Peer review under responsibility of International Federation of Automatic Control (IFAC). Published by Elsevier Ltd.
  Author contributions: *Mohammad El Wajeh*: Conceptualization, Methodology, Software, Investigation, Validation, Formal analysis, Writing - Original draft. *Adel Mhamdi*: Conceptualization, Project administration, Supervision, Funding acquisition, Writing - Review and editing. *Alexander Mitsos*: Conceptualization, Project administration, Supervision, Resources, Writing - Review and editing.
- Chapter 5 is partially based on [4]: M. El Wajeh, M. Granderath, A. Mitsos, and A. Mhamdi. Distributed Economic Nonlinear Model Predictive Con-

trol for Flexible Electrified Biodiesel Production—Part I: Sequential Architectures. *Industrial & Engineering Chemistry Research*, 63(42):17997–18012, 2024. doi: 10.1021/acs.iecr.4c02453. Copyright © 2024 American Chemical Society.
Author contributions: *Mohammad El Wajeh*: Conceptualization, Methodology, Software, Investigation, Validation, Formal analysis, Writing - Original draft. *Marcel Granderath*: Methodology, Software, Investigation, Writing - Review and editing. *Alexander Mitsos*: Conceptualization, Project administration, Supervision, Resources, Writing - Review and editing. *Adel Mhamdi*: Conceptualization, Project administration, Supervision, Funding acquisition, Writing - Review and editing.

- Chapter 6 is partially based on [5]: M. El Wajeh, M. Granderath, A. Mitsos, and A. Mhamdi. Distributed Economic Nonlinear Model Predictive Control for Flexible Electrified Biodiesel Production—Part II: Sequential and Iterative Architectures with Computational Delay Compensation. *Industrial & Engineering Chemistry Research*, 63(42):18013-18026, 2024. doi: 10.1021/acs.iecr.4c02454. Copyright © 2024 American Chemical Society.
  Author contributions: *Mohammad El Wajeh*: Conceptualization, Methodology, Software, Investigation, Validation, Formal analysis, Writing - Original draft. *Marcel Granderath*: Methodology, Software, Investigation, Writing - Review and editing. *Alexander Mitsos*: Conceptualization, Project administration, Supervision, Resources, Writing - Review and editing. *Adel Mhamdi*: Conceptualization, Project administration, Supervision, Funding acquisition, Writing - Review and editing.

Additionally, during his time at AVT.SVT, the author published the following article [6], which is not included in this dissertation: M. El Wajeh, F. Jung, D. Bongartz, C. D. Kappatou, N. Ghaffari Laleh, A. Mitsos, and J. N. Kather. Can the Kuznetsov Model Replicate and Predict Cancer Growth in Humans? *Bulletin of Mathematical Biology*, 84(11):130, 2022. doi: 10.1007/s11538-022-01075-7.

While at AVT.SVT, the author supervised the Bachelor's theses of Mohamad Morobeid [7], Jérôme Jordan [8], and Andres Lachmund [9], as well as the Master's theses of Marcel Granderath [10], Niklas Groll [11], Vincent Klippel [12], and Aaron Weber [13]. The contributions of all students are acknowledged. The results from the Master's thesis of Marcel Granderath [10] were partially utilized in the publications [4, 5] (see author contributions), and are subsequently incorporated into Chapter 5 and Chapter 6.

1. Introduction

The electrification of chemical processes refers to the substitution of traditional fossil fuel-based energy sources with electricity, which can be derived from renewables such as wind, solar, or hydropower. This transition supports more sustainable chemical production, aligning with broader goals of defossilizing industrial processes [14–16]. As renewable energy sources are inherently variable—fluctuating due to weather conditions and time of day—the flexible operation of electrified and renewable-powered chemical processes offers economic and potentially ecological incentives [15, 17–19]. Notably, in response to fluctuating electricity prices, production rates can be increased during low-price periods and decreased otherwise. However, such an operational paradigm requires a departure from the traditional steady-state (SS) mode of operation, thereby realizing what is often referred to as demand-side management (DSM).

Zhang and Grossmann [17] describe DSM as a framework of coordinated activities between grid operators and electricity consumers aimed at adjusting the amount or timing of electricity use to improve grid performance and enhance consumer benefits. Grid operators assess the need for load adjustments and offer financial incentives, while consumers respond by making physical load adjustments. Mitsos et al. [15] highlight the importance of DSM in addressing the variability and unpredictability of renewable energy sources. In this context, an optimally flexible process operation enables effective DSM, allowing chemical processes to adapt to fluctuating energy and feedstock supplies—essentially managing dynamic operational conditions.

Dynamic operation of flexible chemical processes enables continuous adjustments in production rates, optimizing energy consumption while leveraging fluctuating energy prices [15]. Simultaneously, some industrial plants operate on time scales comparable to the frequency of these fluctuations. Consequently, the plant may remain in a transient state for extended periods during dynamic operation. Hence, achieving optimal and feasible flexible operations requires the consideration of process dynamics, operational limits, and product qualities. In other words, process dynamics must be incorporated into frequent scheduling decisions aimed at capitalizing on fluctuating energy prices. This, in turn, necessitates integrating decision-making across various time scales in process operations [20–22]. Such integration can be facilitated through trajectory optimization, which seeks to optimize process variables over a defined time horizon to maximize profit while ensuring operational feasibility and product quality requirements [23]. Conversely, the majority of conventional chemical plants are designed for continuous operation around SS operating points, requiring a constant energy and feedstock supply, thereby presenting significant challenges for flexible operation. Therefore, reassessing conventional process design to enhance flexibility in accommodating variable energy availability becomes imperative in this paradigm shift in process operation.

Recent research has explored methodologies for integrating decision-making in chemical process operations across various time scales, resulting in the emergence of two primary operational paradigms: top-down and bottom-up approaches [20, 22, 24–28]. Figure 1.1

illustrates the hierarchical separation of operational decisions by time scales for the conventional, top-down, and bottom-up paradigms. The conventional paradigm treats scheduling and process control as distinct layers, separated by time scales (cf. Figure 1.1a). In this paradigm, scheduling is typically performed under quasi-stationary assumptions, disregarding the detailed dynamics of the process and its control system [29, 30]. In contrast, the top-down approach involves incorporating detailed process information, including dynamics and control, into scheduling calculations (cf. Figure 1.1b). This is often achieved using dynamic real-time optimization [31], where dynamic models are utilized during scheduling, often based on data-driven models informed by closed-loop data from the process and control system [20–22]. Production schedules from top-down calculations are presented as setpoints for implementation by a multivariable tracking controller. This controller calculates manipulated variable profiles, passing them directly to the process or through subordinate base-layer controllers. On the other hand, the bottom-up paradigm embeds economic considerations directly within the process control layer itself, often via a supervisory controller such as economic nonlinear model predictive control (eNMPC) [32, 33], as shown in Figure 1.1c. eNMPC addresses an online dynamic optimization (DO) problem with an economic objective over a sufficiently long time horizon, using open-loop process models that are typically mechanistic or hybrid in nature. Unlike the top-down paradigm, a subordinated advanced tracking controller is unnecessary. Instead, eNMPC maximizes economic performance and directly controls the process.

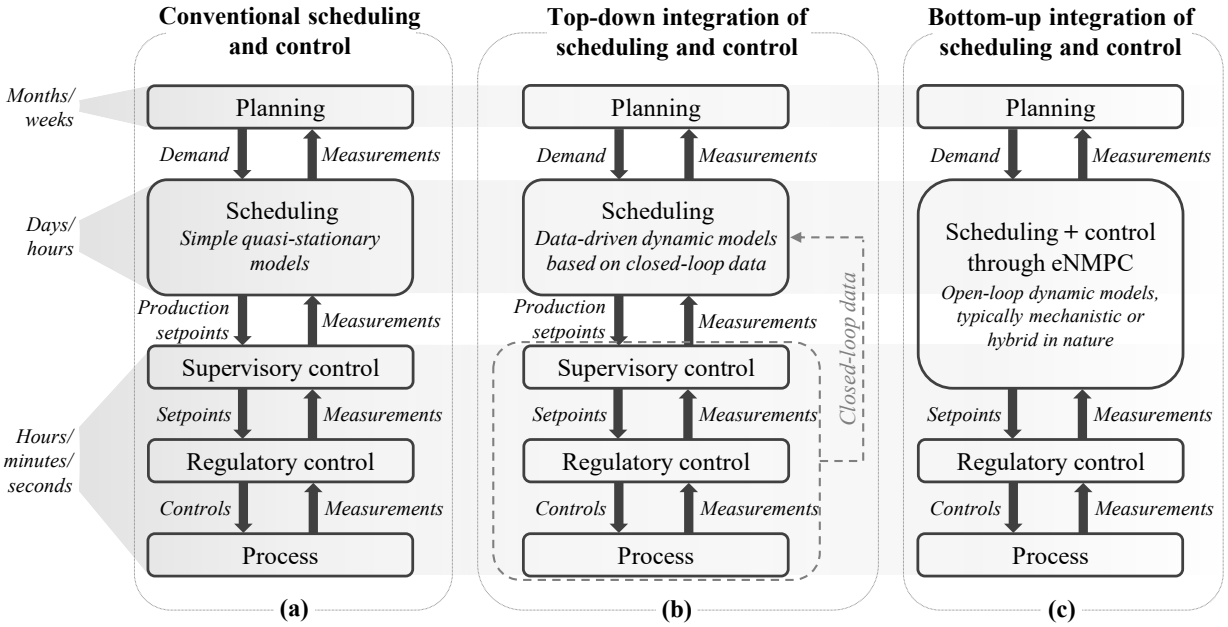

Figure 1.1.: Hierarchical separation of operational decisions in chemical processes by time scales, along with scheduling and control approaches for: (a) conventional, (b) top-down, and (c) bottom-up paradigms. Adapted from [21].

To achieve the aforementioned objectives in electrified chemical plants—specifically optimal flexible operations—modeling- and optimization-based strategies and tools are essential. Process systems engineering plays a key role in the development and implementation of these strategies within industrial processes, particularly chemical processes. Beginning with defining the final objectives for optimal flexible operation and systematically pro-

gressing through the necessary steps to achieve them, process development and operation strategies can be conceptualized within the modeling and optimization framework illustrated in Figure 1.2. This framework is specifically tailored to align with our final goals and application requirements. The target industrial process, an electrified chemical plant powered by renewable energy, aims to optimize flexible operations in response to fluctuating electricity prices. As discussed earlier, model-based scheduling and control are essential for meeting these goals. Consequently, the first step involves developing mathematical models to describe the plant and its control systems, specifically tailored to support the desired outcomes. In our case, these models are nonlinear and dynamic and can be mechanistic, data-driven, or hybrid in nature.

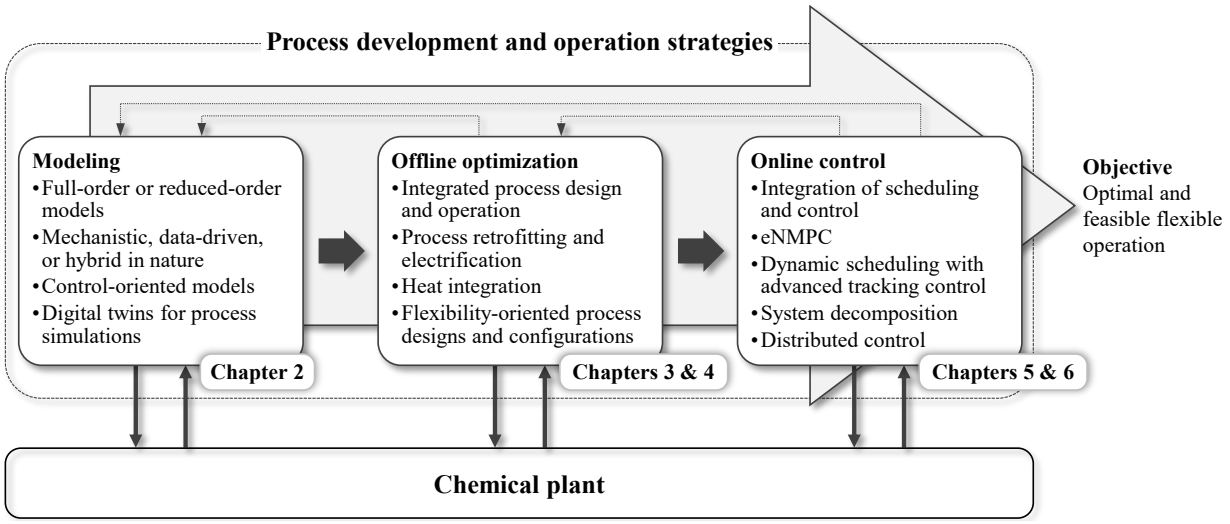

Figure 1.2.: Conceptual representation of process development and operation strategies within a modeling and optimization framework, highlighting the essential steps to achieve the desired process operation objectives.

Following model development, integrated process design and operational strategies must be established and evaluated, allowing for reassessment of process design considerations that facilitate optimal flexible operation. This stage may involve defining, formulating, and solving offline DO problems, including coupled design and operation problems. Retrofitting existing chemical plants to support flexibility-oriented designs is also essential. This could involve, e.g., reconfiguring or upgrading process units, integrating energy storage systems, and/or incorporating buffer (storage) tanks for intermediate and final products within the process to enable and enhance flexible operations. Offline optimization studies may further explore strategies for electrification, process intensification, and heat and material integration while considering flexible operation targets.

The third stage is online control, where the developed models, offline optimization strategies, retrofitting measures, and flexibility-oriented process designs are combined and applied in real-time plant operations. This phase primarily focuses on model-based control, particularly eNMPC in our case. Here, control-oriented models, reduced-order models, distributed control strategies, and system decomposition methods can be employed to enable online-tractable control. Additionally, flexibility-oriented process designs, such as decoupling process dynamics through the use of buffer tanks, can facilitate the practical application of distributed control strategies.

As illustrated in the flowchart in Figure 1.2, these three primary stages consist of various sub-steps and are inherently iterative. Each stage is interconnected and mutually influential. For instance, models developed in the initial stage may be refined or adapted to accommodate different optimization strategies and control approaches at later stages. This feedback mechanism illustrates the interplay between the second and third stages with the initial modeling phase. Similarly, real-time control strategies and distributed control implementations are significantly influenced by the optimization problem formulations, process configurations, and buffer tank allocations established earlier, exemplifying the feedback loop between the second and third stages. Consequently, these three main stages are not only iteratively refined with respect to the underlying process but also together and are continuously adapted in the development phase and later during the implementation of the online control phase.

In this dissertation, we address several topics related to the optimal flexible operation of chemical processes. Our focus is on developing and applying the necessary methods and tools, as illustrated in Figure 1.2, to optimize in silico the flexible operation of electrified transesterification processes under fluctuating electricity prices. Specifically, we examine the production of fatty acid methyl esters (FAME)—the primary chemical species in biodiesel—from vegetable oil [34, 35]. We consider the alkali-catalyzed homogeneous transesterification process, as it is the most widely used route in both academic literature and industry for biodiesel production [36–38]. This process consists of a main reaction unit, multiple separation processes, and two recycle streams. It typically operates on time constants of several hours and in SS modes [1, 36]. Consequently, achieving feasible flexible operation in such a process requires accounting for its transient behavior, as the relatively slow dynamics coincide with or even exceed the time scales of fluctuating electricity prices, which are treated here as known parametric process disturbances. We electrify the process using heat pumps and electric coils. Additionally, we incorporate buffer tanks to store intermediate and final products within the process, which not only enables flexible production but also enhances the overall operational flexibility [2].

Operational flexibility is central to this dissertation but is often interpreted in varied ways across the literature. Foundational work by Grossmann and Morari [39] introduced formal definitions of flexibility, resiliency, and operability for chemical processes. Although these definitions have not been consistently adopted in subsequent research, they provide valuable conceptual grounding. In this work, we adopt a practical definition of operational flexibility as the ability of a process to dynamically adjust production rates and operating conditions—through manipulation of control variables—in response to external disturbances, particularly electricity price fluctuations, while maintaining feasibility and performance.

The potential for optimal flexible operations has been explored in several load-shifting applications for electricity-intensive processes such as air separation units [21, 33], water desalination plants [40, 41], and chlor-alkali electrolyzers [42, 43]. However, the development and application of DSM methods to chemical processes, particularly those involving reaction, separation, and recycle components, have received limited attention in the literature. Additionally, the exploration of process design modifications in chemical plants—such as incorporating buffer tanks to enable flexible operation—remains largely unexamined. The biodiesel production process considered in this dissertation shares many characteristics with other chemical processes, particularly those involving reaction, separation, and recycle components—key elements of classical chemical plants. Therefore, the methods

developed and applied in this dissertation have broad applicability across a range of chemical processes, underscoring the generalizability of our approach. The selected electrified biodiesel production process, along with the interplay between its slow process dynamics (including regulatory control) and the integration of scheduling and control, underpins the theme of this dissertation: *Optimal Dynamic Operation of Electrified Biodiesel Production.*

Moreover, biodiesel has attracted significant attention from both industry and academia over the past few decades [44–47]. It is a promising alternative to fossil-based diesel due to its similar physico-chemical properties [44, 46], low aromatic and sulfur content [48], and the fact that it is a biomass-derived, biodegradable fuel [47]. Biodiesel production processes can utilize a variety of feedstocks [49], including various vegetable oils [50], algae oil, and waste cooking oil [51]. However, its production costs are higher than those of conventional diesel [52]. Therefore, reducing overall manufacturing costs and leveraging fluctuating energy prices through flexible operations are critical for ensuring its economic viability. Thus, examining the biodiesel production process not only advances the understanding and application of modeling- and optimization-based strategies for the flexible operation of electrified chemical processes but also integrates sustainability concepts from diverse research domains. This integration is crucial for the future of industrial biofuel and chemical synthesis powered by renewable energy sources.

The modeling- and optimization-based approaches outlined in Figure 1.2 require specialized methods and software capable of handling optimization problems with embedded dynamic models. Such tools are widely used in various engineering fields and typically involve differential-algebraic equation (DAE) systems with additional process constraints. Effective application and analysis of DO methods demands a framework that is both efficient, to handle large-scale problems, and modular, to support various algorithms and facilitate the integration of complex process models. In this dissertation, we utilize the Dynamic Optimization Software (DyOS) [53], an open-source DO framework developed at AVT.SVT. DyOS is based on direct adaptive shooting algorithms [54–57] and supports multi-stage problem formulations, including binary decision-making. Models can be imported as standardized Functional Mockup Unit (FMU), flat Modelica models, or C++ models. The modular design of DyOS allows for the use of a variety of open-source and commercial integrators and nonlinear program (NLP) solvers, which are based on different numerical methods. DyOS can be accessed through C++, MATLAB, or Python interfaces, and has been applied in several case studies involving optimal operation, model predictive control (MPC), and process design [53]. An open-source version of DyOS, including several components of its framework, is available at `permalink.avt.rwth-aachen.de/?id=295232`.

The following provides an overview of the chapters in this dissertation, detailing how each aligns with the steps outlined in the flowchart in Figure 1.2. We begin with the development of the biodiesel production process design and modeling, proceed to the implementation of offline DO strategies coupled with process intensification, and conclude with online control via eNMPC. Each chapter is self-contained, featuring an introduction, motivation, literature review, methodology, results, and conclusions specific to the topic addressed. Throughout, we emphasize the specific steps and sub-steps employed from the flowchart to ultimately achieve the goal of real-time tractable control for optimal flexible operation of the considered electrified biodiesel production process under fluctuating electricity prices.

Chapter 2 details the model development phase outlined in Figure 1.2, presenting a modular and rigorous mechanistic dynamic model for biodiesel and glycerol produc-

tion via homogeneous alkali-catalyzed oil transesterification. We implement the model in Modelica [58], an open and powerful equation-based modeling language that enables the creation of modular and hierarchical building blocks adaptable to other chemical processes and fluid systems. The Modelica model is available as open-source at `permalink.avt.rwth-aachen.de/?id=135903`. Moreover, to investigate the plant's dynamic behavior, assess its controllability, and establish a basic control level for subsequent studies, we design two plantwide decentralized control structures. A plantwide approach is essential due to the interconnected unit operations and recycle streams within the biodiesel production process. The first plantwide control (PWC) structure assumes information-rich measurement configurations, including species concentration data from process analytical technologies such as in-situ infrared or Raman spectroscopy [59, 60]. In contrast, the second PWC structure relies on conventional measurement setups using standard process variables like temperature, pressure, and flow rate, reflecting current industrial practices. We explore several disturbance scenarios to assess dynamic behavior, demonstrating the importance of a plantwide perspective. The information-rich PWC structure shows satisfactory control performance, while the conventional structure fails to always satisfy product quality requirements, underlining the need for dynamic models to enable model-based control and estimation techniques. This dynamic model forms the basis for subsequent models used in the offline optimization and online control phases. Since all studies in this dissertation are performed entirely in silico, it also represents the underlying operational process within the framework depicted in Figure 1.2.

Using the model developed in Chapter 2, Chapter 3 explores offline DO studies alongside flexibility-oriented process designs and configurations. This chapter addresses the second stage of the flowchart in Figure 1.2, incorporating process retrofitting with DO strategies tailored to achieve the final objectives of optimal flexible operations. Specifically, we investigate the role of buffer tanks for storing intermediate and final products within the biodiesel production process in enabling and enhancing flexible operation. We formulate several DO problems tailored to these configurations, targeting optimized and feasible flexible operations. We examine the operational flexibility of three process configurations and compare the outcomes of their DO strategies with those of a SS operation, considering a typical DSM scenario. The three process configurations differ based on the number and placement of the buffer tanks incorporated. For all strategies, we employ local gradient-based optimization and solve them using DyOS. We aim to demonstrate that, when chemical processes are electrified and powered by renewable energy, novel operational strategies rooted in flexibility through dynamic operation may emerge as the new paradigm for chemical plant operations. Achieving this transition requires leveraging advanced modeling and optimization techniques and reevaluating traditional process design considerations to fully harness the benefits of flexible operation. Our findings indicate that by incorporating intermediate tanks, we fully exploit the process flexibility potential, leading to energy cost savings of up to 29 %. Moreover, we show that these tanks not only decouple dynamics across different process sections—facilitating more flexible operations—but also enable the implementation of a distributed optimization strategy with smaller problem sizes, leading to enhanced computational performance. This proposed distributed optimization strategy yields similar energy cost savings to centralized optimization approaches while significantly reducing computational costs by over tenfold, thereby paving the way for real-time control applications.

The offline DO studies and the flexibility-oriented process designs explored in Chapter 3

do not consider heat integration (HI). However, HI is crucial for enhancing energy efficiency by reducing external energy requirements, making it a common practice in modern chemical plants. In Chapter 4, we investigate the impact of incorporating HI on operational flexibility, focusing on how it influences the degrees of freedom available for optimization. Continuing with the second stage of the flowchart in Figure 1.2, we further explore process intensification techniques and their implications for offline DO strategies. Integrating heat across multiple units introduces additional complexities and interdependencies within the process, which can complicate flexible operation and limit optimization options [61]. We present two configurations that implement full HI across all three distillation columns in the process. One configuration includes additional heating units for the reboilers, while the other operates without them. We aim to evaluate the effect of these external heat sources on process flexibility under dynamic operation. As anticipated, adding supplementary heating units enhances flexibility and results in greater energy cost savings. Additionally, we introduce a third configuration that enables the use of two distributed optimizers, each addressing a smaller DO problem, in contrast to the centralized optimization used in the other configurations. In this setup, vapor recompression (VRC) [62, 63] is applied to one column, while the remaining two columns are heat-integrated. The three configurations are subsequently benchmarked against their respective SS operations, as well as against a dynamic operation of a previous configuration from Chapter 3 without HI. Notably, the configuration employing distributed optimization significantly reduces computational costs while achieving comparable energy cost savings to its centralized counterparts, making it more suitable for online control.

Building on the offline DO strategies and flexibility-oriented process designs—particularly the strategy that enables decomposing the process into subsystems for distributed optimization—we progress to the third stage of the flowchart in Figure 1.2 to develop and implement methods for real-time control. Specifically, in Chapter 5, we present and apply distributed economic nonlinear model predictive control (DeNMPC) to optimize the flexible operation of the considered biodiesel production process under fluctuating electricity prices. Our approach utilizes sequential communication protocols for distributed control, employing non-cooperative cost functions. By leveraging the process configuration that incorporates buffer tanks for intermediate and final products, we decouple process dynamics, thereby segmenting the process into three distinct subprocesses. This decomposition significantly reduces the computational complexity of the eNMPC controller by breaking down the optimization problem into smaller subproblems managed by local controllers, i.e., DeNMPC. The DeNMPC strategy yields significant energy cost savings of 20 % compared to SS operation while being real-time tractable and ensuring operational feasibility. This stands in contrast to a benchmark strategy based on conventional scheduling with simple quasi-stationary models, which results in infeasible outcomes. Furthermore, the DeNMPC strategy handles unexpected disturbances in production demand and feed composition, mitigated by the buffer tanks. These tanks prove essential not only for enhancing operational flexibility but also for enabling realizable DeNMPC applications through system decomposition. Additionally, in this chapter, we extend the DeNMPC with two stability formulations from the literature, assessing their suitability and implications within the specific context of our biodiesel production application.

While the DeNMPC presented and applied in Chapter 5 enables an online-tractable control application, the computational times required to solve the optimization problems, even within subsystems, remain significant relative to the DeNMPC sampling periods. This is

particularly relevant in our case, as nonconvex problems involving nonlinear systems of equations must be solved at every sampling instant. Ignoring the computational delays involved in calculating control variables can result in discrepancies between predicted and actual system states, leading to degraded closed-loop performance or stability [64, 65]. In Chapter 5, we do not account for the computational delays incurred while solving the optimization problems, despite the considerable CPU times required. Additionally, alongside sequential communication architectures in DeNMPC, iterative architectures represent another primary protocol [66–68], which we do not consider in Chapter 5. Thus, to further advance the online control stage illustrated in Figure 1.2, Chapter 6 addresses an iterative DeNMPC approach additionally and incorporates computational delay compensation schemes. These compensation schemes leverage model-based predictive simulation algorithms [69–71] to mitigate the impact of delays. Notably, our control scheme incorporates delay compensation over multiple sampling time intervals, addressing subsystem couplings in distributed control. We provide the DeNMPC framework as open-source at `permalink.avt.rwth-aachen.de/?id=619269`. This framework, implemented in Python and integrated with DyOS, includes both sequential and iterative communication architectures, computational delay compensation schemes, and all associated model extensions. Through closed-loop simulations, we demonstrate that computational delays can significantly impact the stability and performance of DeNMPC strategies. Particularly, the sequential approach shows considerable discrepancies in control performance when comparing ideal computational conditions with those accounting for computational delay. Our results reveal that the iterative architecture, with bidirectional communication, outperforms the sequential approach, providing higher energy cost savings and greater adaptability to disturbances. Chapter 6 contributes to advancing DeNMPC applications with delay compensation techniques, underscoring their potential for sustainable biodiesel production and possible extensions to other chemical processes.

After developing and implementing the proposed methods across the stages outlined in Figure 1.2 to achieve the primary objectives of this dissertation—optimal and feasible flexible operation of electrified biodiesel production—we conclude in Chapter 7 by summarizing the key findings and highlighting potential directions for future research and applications.

2. Dynamic Modeling and Plantwide Control of a Production Process for Biodiesel and Glycerol

Figure 2.1 visually emphasizes the focus of this chapter within the broader framework outlined in Figure 1.2. As shown, this chapter concentrates on developing the mathematical model for the biodiesel production process and its base layer control structures.

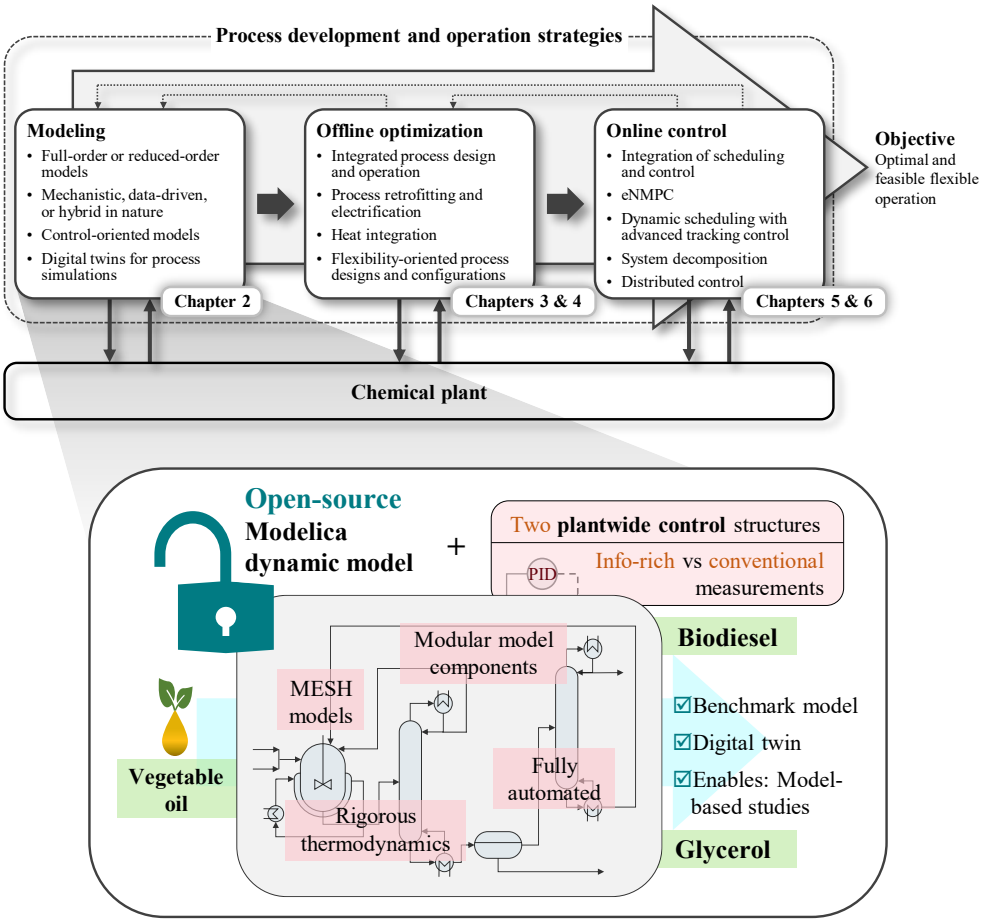

Figure 2.1.: Graphical illustration highlighting the focus of Chapter 2, specifically the model development phase within the modeling and optimization framework presented in Figure 1.2 in Chapter 1.

2.1. Introduction

Different catalytic and noncatalytic processes are employed for biodiesel production [49, 72]. Among the noncatalytic supercritical, acid/alkali catalytic heterogeneous, and acid/alkali catalytic homogeneous transesterification processes, the homogeneous alkali-catalyzed transesterification process is the most commonly utilized in practice and has been well considered in the literature [36–38, 46, 73]. It replaces glycerol from oil triglycerides with radicals from the alcohol used for the conversion process in presence of an alkali catalyst. The produced monoesters, known as FAME, are the biodiesel product [34, 35]. However, the industrial production of biodiesel still faces technical and economic challenges. The final product has to comply with stringent quality standards, while its purification relies on energy-intensive units (distillation), and the raw material may exhibit high variability [49]. This motivates the development of techniques to improve the economic and operational performance of its production processes while complying with the demanding quality standards.

Biodiesel production involves interconnected unit operations and recycle streams leading to complex process dynamics. Their modeling and simulation improve the understanding of the plant's dynamics and enable economic improvements in its design and operation. Biodiesel production processes have been considered extensively in the literature from different perspectives. For instance, Mandari and Devarai [74] reviewed biodiesel production processes using different catalysts, their prospects, and their challenges. Mohiddin et al. [75] presented a review of the recent advancement and classification of the feedstock and catalyst for biodiesel production. Salvi and Panwar [76], and Santori et al. [77] reviewed biodiesel production technologies and resources. Enweremadu and Mbarawa [78] studied the technical aspects of production and quality analysis of biodiesel from used cooking oil. Other studies focused on the techno-economic analysis of different transesterification methods [36, 46, 79–83]. Lee et al. [84] addressed the economic analysis of biodiesel production using fresh and waste vegetable oil and supercritical methanol. Zavarukhin et al. [85] focused on the plant design and economics of a biodiesel production and refining process using rapeseed oil. West et al. [80] studied four biodiesel production processes and their economic assessment with different levels of complexity. Other studies focused on the transesterification process only and its kinetic modeling. Noureddini and Zhu [86] modeled the kinetics of the soybean oil transesterification with methanol. Sharma et al. [87] studied the development of heterogeneous catalysts for transesterification reaction processes, and the development of their kinetics was investigated in refs. [73], [88], and [89]. Moreover, other process concepts for biodiesel production have been suggested. Wali et al. [90] developed a novel continuous microwave reactor for the conversion of waste oil and fats into biodiesel, and studied its temperature control. Also, biodiesel production with reactive absorption technology has been investigated [91].

The process dynamics and control of biodiesel production have also been addressed in the literature. Kariwala and Rangaiah [46] developed a PWC concept for a biodiesel production plant using control heuristics assisted with simulation. Shen et al. [92] studied the design and control of a biodiesel production process with phase separation and recycle. Da Silva et al. [93] proposed key performance indicators for the evaluation of different PWC structures for a biodiesel production process. The process control of biodiesel production by reactive absorption has been also studied [91, 94, 95]. Mjalli and Hussain [96] addressed the dynamics and control of a continuous reactor unit for biodiesel production. Brásio

et al. [97] applied nonlinear model predictive control (NMPC) for the reaction section of a continuous biodiesel plant. They determined optimal profiles of the process variables using a nonlinear mechanistic model of the whole transesterification section. Benavides and Diwekar [98] developed an optimal control problem for biodiesel production in a batch reactor to maximize the final concentration of FAME by determining the optimal temperature profile. They extended their work and studied the effect of uncertainty in the reactor feed [99], and developed a two-layer optimization strategy to minimize operation time and maximize conversion in the reactor [100].

The aforementioned studies rely on commercial process simulators, mainly Aspen Plus [101] and Aspen HYSYS [102], and thus the model equations cannot be accessed. This is discussed in the comprehensive review by Chang and Liu [103]. Besides, Martín and Grossmann [51] used a surface response methodology to model reactors and shortcut methods for distillation columns modeling in biodiesel production processes. Brásio et al. [104] developed first principle models for the reaction section and a simple decanter model based on fixed split ratios. Others developed mechanistic models for the reaction section of oil transesterification processes only [99, 105–107]. Farobie et al. [108] created an artificial neural network model by using experimental data, in order to predict biodiesel yield of a supercritical noncatalytic production reactor. However, we are unaware of any study in the literature that developed a detailed first-principle dynamic model of a complete biodiesel production plant with accessible and editable model equations that can be used as a digital twin and for model-based control applications like NMPC. Such a digital twin may be used to support the scaleup of biodiesel production processes and could improve cost-effectiveness in design and operation. Moreover, compared to models from commercial software, such modular models are needed for benchmark purposes and have a generic value for optimization and control applications, as they share features with many other chemical processes.

We present a rigorous mechanistic dynamic model of biodiesel production via homogeneous alkali-catalyzed transesterification of vegetable oils and provide the corresponding implementation open-source. We decouple unit operations and thermodynamic models. We model the reactors using material and energy balances and apply second-order elementary rate laws for kinetic modeling. We use the Material balance, phase Equilibrium, Summation, and Heat balance (MESH) equations for the separation units. Thermodynamic nonidealities are calculated based on the non-random two-liquid (NRTL) model [109] and the Design Institute for Physical Properties (DIPPR) relations [110]. We build the model framework in Modelica [58] as an open and powerful equation-based modeling language, which leads to modular and hierarchical building blocks that can be used for other chemical processes and fluids. Furthermore, we implement the same process in Aspen Plus v11 [101] in order to compare the SS results of both models.

Moreover, in order to investigate the dynamic behavior of the plant, assess its controllability and provide a basic control level for future investigations, we design two plantwide decentralized control structures. Plantwide considerations are necessary due to the interconnected unit operations and recycle streams. For one PWC structure, we assume the availability of information-rich measurement configurations, including species concentration measurements, e.g., through process analytical technologies such as in-sito infrared or Raman spectroscopic technologies [59, 60]. For the other PWC structure, we consider a structure that uses only conventional configuration with measurements for process quantities such as temperature, pressure, or flow rate, and thus matches current industrial prac-

tice. The design of the PWC structures and the tuning of their control loops must be based on the overall plant objectives [93, 111]. Only few PWC methodologies are available, e.g., Luyben's heuristic-based methodology [112], self-optimizing control [46, 113–115], and the integrated framework of simulation and heuristics (IFSH) [46, 116]. We choose the IFSH methodology because it employs process simulation for assistance in using the heuristic PWC design steps. In addition, Murthy Konda et al. [116] and Kariwala and Rangaiah [46] provide detailed applications of the IFSH methodology.

Our work primarily addresses the lack of open-source and rigorous dynamic models of chemical processes for model-based applications. Specifically, the model is versatile, making it suitable for optimization and control applications, and also significant on its own due to its application potential. It encompasses the reaction, separation, and recycle aspects of a chemical plant, making it relevant to a wide range of processes. Furthermore, by applying the two PWC structures, assuming different measurement availability, we aim to demonstrate the importance of having dynamic models developed for model-based control and estimation as well as the application potential of advanced process analytics for process control purposes. Overall, the novelty of the work lies in providing an open-source dynamic model that can serve as a benchmark for the application of model-based techniques in chemical processes.

The remainder of the chapter is structured as follows. We first introduce the considered biodiesel production process and discuss the operating conditions. Then, we explain the considered assumptions behind the mathematical process model. Afterward, we discuss the developed PWC structures following the steps of the IFSH methodology. Before discussing the results of the plant dynamic simulation and control, we show how we simulate the plant under several scenarios to assess the performance of the PWC structures in terms of setpoint tracking and disturbance rejection. Finally, we draw conclusions about our contribution. We provide the full mathematical model in Section A.1 in Appendix A and the Modelica model including the PWC structures at `permalink.avt.rwth-aachen.de/?id=135903`.

2.2. Process Description and Operating Conditions

We consider the homogeneous transesterification process of vegetable oil utilizing an alkali catalyst to produce biodiesel. This process is widely used in industrial production and is preferred over the acid-catalyzed and supercritical methods due to its faster reaction rates and lower methanol to oil ratios required under mild operating conditions [46, 73]. However, the alkali-catalyzed process is sensitive to the presence of water and free fatty acids (FFA) in the feed. The presence of water may cause ester saponification under alkaline conditions, while FFA can react with the alkali catalyst to produce soaps and water [36, 46]. Saponification consumes the alkali catalyst and may cause the formation of emulsions, which can complicate the downstream recovery and purification of biodiesel. Hence, if the feed contains water and FFA levels beyond the maximum tolerance level, a pretreatment step is necessary to eliminate them. For our study, we assume the use of pretreated and refined vegetable oil.

Rapeseed oil, palm oil, and soybean oil are typical oil feedstocks [49, 50]. The main constituents of these oils are the glycerides of the fatty acids. The glycerides of oleic fatty acid, mainly triglycerides, have been considered to represent the vegetable oil in

many case studies of biodiesel production in literature because it is the main constituent of rapeseed oil and soybean oil as well as the second main constituent in palm oil after the glycerides of palmitic acid [36, 46, 82, 117–120]. Chang and Liu [103] summarized the vegetable oil constituents used in several reported simulation models for biodiesel production plants. Triolein, the triglyceride of oleic acid, was mainly used to represent the oil feed in those models. Therefore, we use the glycerides of oleic acid to represent the vegetable oil. Based on Zhang et al. [36], Myint and El-Halwagi [82], and the summarized vegetable oil constituents in Chang and Liu [103], we use 95 wt% triolein and 5 wt% diolein as the nominal fed oil composition because it is a typical composition of oleic acid glycerides of vegetable oils. We use methanol for the transesterification of oil and sodium hydroxide solution ($NaOH \cdot H_2O$) as the alkali catalyst [36, 46], due to their low prices and availability.

A process flowsheet of the considered biodiesel and glycerol production plant is depicted in Figure 2.2. The design of all process units and operating conditions are based on Zhang et al. [36]. Methanol and $NaOH \cdot H_2O$ are mixed before they are fed into the transesterifier, i.e., a continuous stirred-tank reactor (CSTR). We feed the oil feed as well as the mixture of methanol and $NaOH \cdot H_2O$ into the CSTR without preheating. The outlets of the reactor are the biodiesel product, i.e., FAME, glycerol as a byproduct, the remaining reactants, and the catalyst solution. The products are then separated and purified in the separation section of the plant, and the reactants are recycled to the reactor. There are several configurations reported in the literature for the process separation section [36, 46, 82]. We apply the design of Zhang et al. [36] for the homogeneous alkali-catalyzed transesterification process. The main advantage of this design is that we can separate the unreacted oil from the biodiesel in a separate column, because methanol is separated in the methanol column before the decantation or water washing steps.

The optimal operating temperature of the CSTR for such a process is within the range of [55–75] °C [36, 38, 96]. Following Zhang et al. [36], we choose a nominal operating temperature of 60 °C. The homogeneous transesterification reaction could operate at atmospheric pressure. However, we operate the CSTR at 1.5 bar absolute pressure, by supplying nitrogen gas, to guarantee that methanol remains in the liquid phase at the nominal operating temperature as the bubble point of methanol at 1 bar is 65 °C [121]. We use the operating conditions that are optimal according to Zhang et al. [36] and Abbaszaadeh et al. [38] to achieve maximum conversion. We thus operate the CSTR at the optimal residence time of the reactor content of 1 h. The amount of the total methanol fed into the reactor is determined such that an optimal 6:1 methanol-to-oil mole ratio entering the reactor is achieved. The $NaOH \cdot H_2O$ is fed such that 2 wt% of NaOH in the mixture of methanol and $NaOH \cdot H_2O$ entering the reactor is preserved. We target 88% oil conversion with the 6:1 methanol-to-oil mole ratio and the preserved 2 wt% of NaOH ratio. We maintain the temperature of the reactor content by switching between hot and cold water as the input stream to the jacket of the CSTR.

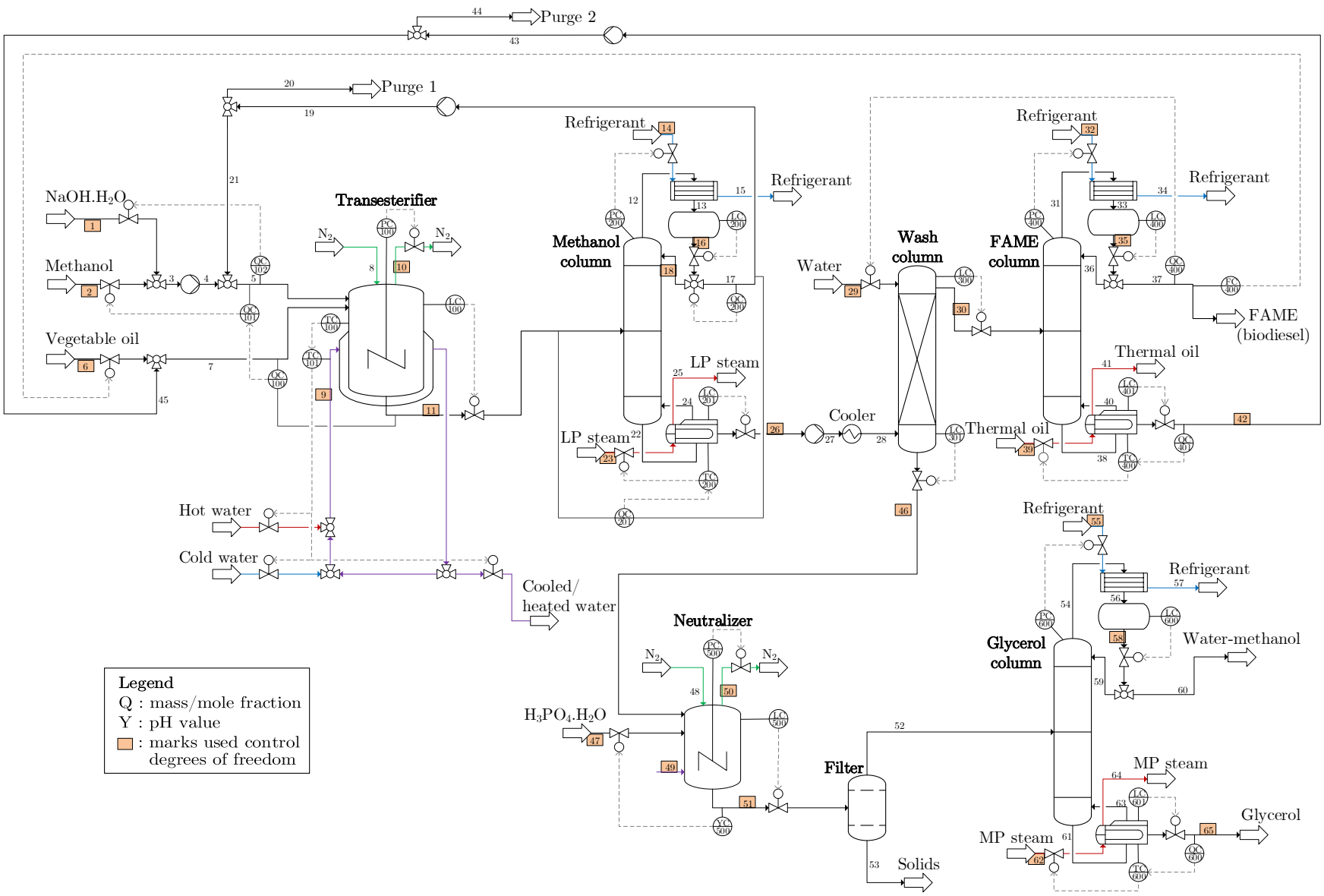

Figure 2.2.: Process flowsheet with controllers of a biodiesel production plant by oil alkali-catalyzed transesterification. The shown control structure is for the PWC structure having information-rich measurement configurations available (PWC-A).

The CSTR product stream is fed into the methanol column to recover methanol by a distillation process. The distillate, which has 99.5 wt% methanol as the nominal purity, is recycled to the transesterifier. The bottom product is cooled by a cooler that operates on water and fed to a wash column as the input raffinate. Water is fed as the input extract to the wash column to remove the polar species in the input raffinate. Glycerol, the dissolved NaOH, part of the methanol, and water are extracted from it to the fed water. The output raffinate is fed to the FAME column to separate the unreacted oil. The distillate is the biodiesel product which is mainly FAME and traces of water, monoglycerides, and methanol. The bottom product is recycled to the transesterifier after mixing it with the fresh-fed oil. The output extract of the wash column is sent to the glycerol purification section.

We adhere to the European specifications EN 14214 [122] (cf. Table 2.1) for biodiesel quality. The required low methanol concentration is achieved by adding the proper amount of water to the wash column. The oil glycerides concentration limits are guaranteed by achieving the required methanol-to-oil mole ratio entering the reactor.

Table 2.1.: Biodiesel specifications according to the European standard EN 14214 [122].

Ester content	$\geq$ 96.5 wt%
Triglycerides	$\leq$ 0.20 wt%
Diglycerides	$\leq$ 0.20 wt%
Monoglycerides	$\leq$ 0.80 wt%
Methanol	$\leq$ 0.20 wt%
Water	$\leq$ 0.05 wt%
Glycerol	$\leq$ 0.25 wt%

We consider a biodiesel production rate of 17,120 kg/h corresponding to the average capacity of an industrial biodiesel production plant in Germany (150,000 t/yr) according to the German Union for the Promotion of Oil and Protein Plants (UFOP) [123].

The byproduct glycerol is also valuable [124], but needs to be neutralized and purified (cf. Figure 2.2). The output extract is fed to a neutralization reactor (neutralizer) to remove the dissolved NaOH species by the addition of phosphoric acid solution ($H_3PO_4 \cdot H_2O$) [82]. The resulting salt from the neutralization reaction is valuable too as it can be used as a fertilizer. We determine the amount of acid added such that the neutralized solution reaches a pH value of 2.5 [125]. At this pH value, salt precipitation takes place and the formed solids can thus be filtered out in the filter unit. We assume that all of the dissolved NaOH is removed, and that the formed salt, which is monosodium phosphate (NaH_2PO_4), is completely precipitated. The liquid stream from the filter enters the glycerol column to purify glycerol from water and methanol. There are several grades of glycerol purity [126]. With the considered process design and operating conditions from Zhang et al. [36], we target to have the pharmaceutical purity grade, which is 99 wt% glycerol [46], in the bottom stream of the glycerol column.

The methanol, FAME, glycerol, and wash columns have nine, five, five, and six separation stages, respectively. Low pressure (LP) steam, synthesized thermal oil, and medium pressure (MP) steam are used to heat the reboiler of the methanol, FAME, and glycerol columns, respectively. These utilities are suitable for the respective reboiler duties of each column. For the condensers of the three columns, refrigerants are the utility streams.

The purge streams shown in the process flowsheet in Figure 2.2 are used to start up the plant. After starting the controller system (cf. Section 2.4), the plant is operated full automatically and the purge streams can thus be gradually decreased to zero.

2.3. Dynamic Process Model

We summarize in this section the chemical system involved in the process and the assumptions considered in the modeling. We provide further details in Section A.1 in Appendix A.

Ten species belong to the chemical system of the process model. Methanol, water, NaOH, triolein, diolein, and H_3PO_4 are the feeds. Monoolein is an intermediate educt and could be a constituent of the fed oil as well if its composition changes. The products are methyl oleate (FAME), glycerol, and NaH_2PO_4.

We model the transesterifier as a perfectly mixed CSTR by energy and material balances. We assume for the alkali-catalyzed transesterification of oil with methanol, the well-studied and known reversible three-step reaction system in the literature [73, 86, 117, 127]. We provide the reaction system and the rate law coefficients, and material and energy balances in Section A.1.1.1 in Appendix A. To account for the spatial distribution of the temperature of the reactor jacket, we model it as a series of equivalent continuous stirred tanks (CSTs), by which the spatial dynamics of the jacket temperature are accurately determined. We assume a quasi-steady-state approximation for each jacket CST because their temperature dynamics are much faster than that of the reactor temperature. This can be validated by simulating and comparing the accumulation terms of the reactor and jacket temperatures. Moreover, such an assumption is often considered when modeling energy balances for jacketed CSTRs [128, 129].

For the distillation and wash columns, we use equilibrium models for each stage of the columns to determine species distributions among phases, flow rates, temperature profiles, etc. We consider the following assumptions when developing the equilibrium models: perfect mixing in vapor and liquid phases; the tray holdup is only due to the liquid phase (heavy liquid in the wash column) since the quantity of vapor (light liquid in the wash column) holdup is typically much smaller than the total holdup [130]; two-phase system in thermal and mechanical equilibrium; no heat of mixing; no heat losses to the surroundings; and the temperature dynamics of the column structure are neglected. The wash column is a liquid-liquid extraction process, where the light phase is the raffinate stream. Since temperature dynamics on the column trays are faster than material dynamics, we utilize a quasi-steady-state approximation for their energy balances. This results in an index-1 differential-algebraic (DA) system as the outlet vapor (raffinate) flow from each tray can then be explicitly determined [130].

We model the heat exchangers by dividing them into segments. The thermal inertia from the metal wall between the two heat-exchanging streams is larger than that of the two streams. Therefore, we apply quasi-steady-state energy and SS material balances for the two heat-exchanging streams [131]. We neglect the axial heat of conductivity inside the metal wall.

We use the DIPPR temperature-dependent models for heat capacities to determine the molar heat capacities, enthalpies, entropies, and Gibbs free energies of the system's species in the solid, liquid, and vapor phases. Species' molar densities in the liquid and solid phases are also determined by the DIPPR correlations. All the coefficients of the DIPPR

correlations are retrieved from DIPPR's Project 801 database [110]. The values are unique for each species in each phase. The distillation columns operate at low pressure values. The transesterifier has the highest operating pressure value in the process, which is 1.5 bar. Therefore, we use the ideal gas equation of state to determine the molar densities in the vapor phase.

To account for the interactions among the polar species present in the system and describe the non-ideality in the liquid phase, we choose the NRTL [109] as an activity coefficient model and the Racket equation [132] for determining the liquid mixture molar densities. To avoid minimizing the Gibbs free energy globally, we assume that the thermodynamics are such that the number of the existing phases is known. We thus use the isofugacity conditions for describing the liquid-liquid equilibrium (LLE), vapor-liquid equilibrium (VLE), and vapor-liquid-liquid equilibrium (VLLE). We use the extended Antoine correlation [133] to allow the description of the entire vapor pressure curves of the species when determining vapor pressures. Since the process operates at low pressures, the Poynting correction is neglected when computing equilibrium relations.

Albuquerque et al. [119] created databases of VLE, LLE, and VLLE experimental data for the mixtures in the biodiesel production processes. They regressed the binary interaction parameters of the NRTL model for triolein, diolein, monoolein, methyl oleate, methanol, glycerol, and water. We use these values, which are provided in Table 6 and Table 7 in their publication [119]. We retrieve the parameter values of the remaining binary species from the database of Aspen Plus Physical Property [134].

2.4. Design of the Plantwide Control Structures

To design the PWC structures, we apply the IFSH methodology, which decomposes the control system design process into several tasks at different levels in a vertical hierarchy of priorities. Table 2.2 summarizes the main steps involved in applying the IFSH methodology. Murthy Konda et al. [116] and Kariwala and Rangaiah [46] provided detailed applications of the methodology. We consider two structures that assume the availability of different measurement configurations. We first discuss the PWC structure that is based on information-rich measurement configurations, where inline product quality measurements such as species concentrations are available. This structure is motivated by the recent advances in process analytical technology, e.g., infrared or Raman spectroscopy, for real-time process control applications. In the following, we refer to this PWC structure as PWC-A. We also provide a second PWC structure that is based on a more practical measurement configuration, in the sense of current industrial practice. Therein, only conventional measurements are available, i.e., real-time measurements for temperatures, pressures, flow rates, and pH (for the neutralizer output). We refer to this PWC structure as PWC-B. We illustrate the main steps of the conducted IFSH methodology for PWC-A, point out the differences for PWC-B, and summarize the two structures in Table 2.4. We tuned all control loops heuristically.

Table 2.2.: Main steps involved in the application of IFSH methodology, adapted from Murthy Konda et al. [116] and Kariwala and Rangaiah [46].

Step	Commonly conducted tasks
1	**Definition of control objectives** Achieve the required throughput and product quality Preserve stable operation and process constraints Involve safety and environmental constraints
2	**Analyze the control degrees of freedom** Identify the potential manipulated variables Involve material and energy streams Look-up tables exit for assistance in identification
3	**Identification of throughput manipulator** Identify the primary process path Selection of the throughput manipulator
4	**Definition of quality controllers** Identify primary quality manipulators Selection of the corresponding control loops
5	**Controlling the more severe controlled variables** Identify the manipulators of the more severe controlled variables Controlled variables involved in process, safety, and environmental constraints
6	**Controlling the less severe controlled variables** Controlled variables involved in material inventory Levels for liquids and pressures for gases
7	**Checking the material balances and remaining control degrees of freedom** Material balance checks for the whole process as well as for its units Check if the control system performance can still be further enhanced

2.4.1. IFSH Methodology for PWC-A

Step 1: Definition of PWC Objectives

The PWC overall objectives of the plant include achieving the required production rate while preserving product quality specifications, stable operation of the plant, process and equipment constraints, safety concerns, and environmental regulations. We target to achieve a production rate of 17,120 kg/h of biodiesel while preserving its quality according to the standard EN 14214 [122] as well as the pharmaceutical purity grade of the by-product glycerol, and operating below their thermal decomposition temperatures. The thermal decomposition temperature of glycerol is in the range of [150–180] °C [46, 135–137]. Therefore, we constrain the maximum allowable temperature in the reboiler of the glycerol column to 150 °C. The thermal decomposition temperature of FAME depends on the considered fatty acids in the oil. It is reported in the literature to be within a wide range of [250–350] °C [46, 138, 139]. For the FAME of oleic fatty acid, methyl oleate, the range starts from 325 °C [138]. We consider a maximum allowable temperature in the reboiler of the FAME column to be 300 °C since we represent the fed oil as the glycerides of oleic acid.

To achieve the required recovery in the distillation columns as well as product puri-

ties, while constraining the reboiler temperatures to the thermal decomposition limits, the FAME and the glycerol columns operate at low pressures. The absolute pressure values at the top of the FAME and glycerol columns are designed to be 3 kPa and 2 kPa, respectively. We also target to attain the required oil conversion in the transesterifier, which is 88 %. In addition, we target to have 94 wt% of methanol recovery in the methanol column and 2 wt% of FAME loss in the bottom product of the FAME column. We thus design the PWC structure and its tuning based on those overall objectives.

Step 2: Control Degrees of Freedom Analysis

We analyze the plant's control degrees of freedom (CDOF) to know what potential process streams we can manipulate to achieve the control objectives defined in Step 1. By following the flowsheet-oriented method of Murthy Konda et al. [140] and Kariwala and Rangaiah [46], CDOF is defined as:

$$\text{CDOF} = N_{\text{streams}} - N_{\text{restraining}} - N_{\text{redundant}} \,. \tag{2.1}$$

The total number of streams (including material and energy streams) N_{streams} is 65 (cf. numbered streams in Figure 2.2). The number of process streams that cannot be manipulated due to their dependency on other streams $N_{\text{restraining}}$ is 25. The total number of process streams that need not be manipulated $N_{\text{redundant}}$ is nine because each distillation column has three redundant streams [46, 140]. Table 2.3 provides the restraining and redundant number of streams of each process unit. It is easy to compute N_{streams}, given a process flowsheet. However, $N_{\text{restraining}}$ and $N_{\text{redundant}}$ depend on the nature of the unit and its operation. Consequently, they are determined based on the theoretical and operational knowledge of any given unit or combination of units (such as a distillation column with a condenser, reflux drum, and reboiler) in a process [46, 140]. Both terms are thus characteristic of a given unit and remain the same irrespective of whether the unit is a standalone or an integral part of a process. Therefore, once determined, they do not require recalculation and can be accessed from look-up tables such as the tables in Murthy Konda et al. [140] and Kariwala and Rangaiah [46]. Nevertheless, it should be noted that the value of $N_{\text{restraining}}$ is contingent on the number of streams considered around a unit operation and whether holdups are modeled or not. For instance, if all streams are considered around a unit operation without modeling material holdup, then $N_{\text{restraining}}$ would be one. Consequently, it may differ from the values listed in the aforementioned look-up tables, depending on whether all material and energy streams are taken into account or not. As a result, we obtain 31 CDOF as a maximum limit for the manipulated variable (MV)s that we could consider to control the plant.

Step 3: Identification of Throughput Manipulator

We identify the throughput manipulator (TPM) of the plant, by determining the primary process path from the main raw material to the main product. For our process, it is the fed oil to biodiesel product path. Therefore, we control the desired production rate of biodiesel by setting the flow controller FC|400, where the MV is the fed-oil flow rate, as shown in Figure 2.2.

Table 2.3.: Restraining and redundant number of streams of process units according to Murthy Konda et al. [140] and Kariwala and Rangaiah [46].

Unit operation	Number of units	$N_{\text{restraining}}$ per unit	$N_{\text{redundant}}$ per unit
CSTR	2	1	0
Distillation column †	3	0	3
Wash column	1	0	0
Condenser	3	2	0
Reboiler	3	1	0
Distillate drum	3	0	0
Cooler	1	1	0
Filter	1	1	0
Pump	4	1	0
Mixer	3	1	0
Splitter	5	1	0
Total		25	9

† Excluding condensers, reboilers, distillate drums, and splitters for reflux.

Step 4: Definition of Quality Controllers

In this step, we define the quality controllers for the FAME and glycerol products. By introducing fresh water into the wash column, glycerol, NaOH, and methanol are extracted from the raffinate, which is the feed of the biodiesel purification unit (FAME column). We thus control the concentration of methanol in the biodiesel product by manipulating the input water to the wash column. Therefore, we set the quality controller QC|400, where we assume the mass fraction of methanol in the biodiesel product is measured and use it as its controlled variable (CV). The flow rate of the input water to the wash column is its MV.

Higher reaction conversions in the transesterifier mean lower unreacted oil entering the FAME column. We thus control the oil glycerides limits in the biodiesel product by achieving the required oil conversion in the transesterifier. High oil conversions are achieved by feeding enough excess methanol to the transesterifier. Thus, we set a cascade controller, where the CV of its primary loop (QC|100) is the oil conversion, and the CV of its secondary loop (QC|101) is the methanol-to-oil mole ratio of the streams entering the transesterifier. The MV of the controller is the flow rate of the input methanol to the plant. This cascade control loop is shown in Figure 2.2.

Achieving the required grade of glycerol product is a single-end composition control case for the glycerol column. Hence, we control glycerol purity by implementing a cascade controller, with purity as the primary CV in QC|600 and the reboiler temperature of the glycerol column as the secondary CV in TC|600. The controller TC denotes temperature controller. Its MV is the flow rate of the input MP steam into the reboiler. We set the maximum reboiler temperature of the controller to the thermal decomposition temperature of glycerol.

Step 5: Controlling the More Severe Controlled Variables

In the IFSH methodology, the more severe CVs are the variables associated with process constraints, e.g., operating and equipment constraints, safety concerns, and environmental regulations.

To minimize losing FAME in the recycled bottom product of the FAME column, we control its recovery by inputting adequate reboiler duty. We thus set a cascade controller, where the CVs of its primary (QC|401) and secondary (TC|400) control loops are the FAME mass fraction in the bottom product and the reboiler temperature, respectively. Its MV is the flow rate of the input thermal oil into the reboiler. We set the maximum limit of the reboiler temperature in the controller to the considered thermal decomposition temperature of methyl oleate.

We achieve the nominal purity of the recycled methanol from the methanol column to the transesterifier by manipulating the flow rate of the column reflux by QC|200. In addition, similar to the FAME column recovery, we target to recycle most of the methanol in the methanol column. Therefore, we control its recovery by also implementing a cascade controller. The CVs of its primary (QC|201) and secondary (TC|200) control loops are the column recovery and the reboiler temperature, respectively. Its MV is the flow rate of the input LP steam into the reboiler.

The nominal temperature of the transesterifier content is maintained by exchanging heat with the flowing medium in the reactor jacket. The jacket medium flows through an external loop in which cold water, hot water, and purge valves open or close according to the required heating or cooling duties of the jacket/reactor system. We model this external loop by considering a temperature change ΔT_{Jacket} of the jacket medium after passing through a pseudo heat exchanger [128, 129]. In this way, we control the heating or cooling modes of the reactor by one control loop with one MV. After the jacket medium exits the jacket, it changes its temperature by ΔT_{Jacket} value after passing through the external heat exchanger, to enter again the jacket. We thus control the reactor temperature by a cascade controller, where the CVs of its primary (TC|100) and secondary (TC|101) control loops are the temperatures of the reactor content and the water medium entering the jacket, respectively. Its MV is ΔT_{Jacket} with extreme values of ± 10 °C.

Finally, we set QC|102 to control the mass fraction of NaOH in the mixture of methanol and $\text{NaOH} \cdot \text{H}_2\text{O}$ entering the transesterifier by manipulating the $\text{NaOH} \cdot \text{H}_2\text{O}$ feed flow rate.

Step 6: Controlling the Less Severe Controlled Variables

Less severe CVs are the variables associated with the material inventory. These CVs are the pressures at the top of the three distillation columns and in the reactors, and the liquid levels in process units. We set pressure controllers (PC) to control column pressures (PC|200, PC|400, and PC|600) by manipulating the refrigerant flow rates entering the condensers, and reactor pressures (PC|100, and PC|500) by manipulating the N_2 gas flow rate leaving the reactors. The level controllers (LC) control liquid levels in the transesterifier (LC|100), neutralizer (LC|500), reflux drums (LC|200, LC|400, and LC|600), reboilers (LC|201, LC|401, and LC|601), and the bottom and top sections of the wash column (LC|300, and LC|301), by manipulating the flow rates of their respective output streams. We implement variable level control for the transesterifier to avoid snowball effects in the

recycle loops. Recycle systems tend to exhibit large variations in the magnitude of their recycle flows in the presence of small disturbances [141]. This high sensitivity of the recycle flow rates is known as the snowball effect. Hence, according to Luyben et al. [141], we implement the variable level control as a cascade controller where the outer loop controls the desired residence time of the reactor content to 1 h and sends level setpoints to the LC in the inner loop. In addition, we add a pH controller (YC|500) for the outlet stream of the neutralizer, where its MV is the flow rate of the $H_3PO_4 \cdot H_2O$ feed stream.

Step 7: Checking the Material Balances and Remaining CDOFs

In the final steps of the IFSH framework, we check the material balances in the plant as well as in its single units by simulating the process. We also check if we can use the remaining CDOFs, which are five (we used 26, cf. stream numbers marked in orange rectangles in Figure 2.2), to enhance the performance of the control system. Based on the defined PWC objectives and structure, no additional control loops are needed.

2.4.2. IFSH Methodology for PWC-B

To design the PWC-B structure, we perform the same steps of the IFSH methodology as for the case of the PWC-A, except for the quality controls. Since quality measurements for product and educt streams are not available, we replace the quality controllers with flow rate ratio controllers (RC). We use the SS values from PWC-A for determining and setting the ratio values in these controllers.

For the transesterifier, we replace QC|100 and QC|101 with RC|100, where the methanol feed flow rate is manipulated to maintain a fixed ratio between the flow rates of the total methanol and $NaOH \cdot H_2O$ mixture, and the oil entering the transesterifier. Likewise, we manipulate the $NaOH \cdot H_2O$ feed flow rate through RC|101 instead of QC|102 by maintaining a fixed ratio between the flow rates of the $NaOH \cdot H_2O$ feed, and the methanol and $NaOH \cdot H_2O$ mixture entering the transesterifier.

For the methanol column, we remove QC|200 and fix the design setpoint for the reflux ratio, and replace QC|201 with RC|200. Similar to PWC-A, the MV of RC|200 is the setpoint of TC|200. RC|200 changes its MV to preserve a fixed ratio between the flow rates of the output bottom and the input feed of the methanol column.

We replace QC|400 in the FAME column with RC|300 to determine the water feed flow rate into the wash column. RC|300 maintains a fixed ratio between the flow rates of water feed and input raffinate into the wash column. RC|400 manipulates the setpoint of TC|400 to maintain a fixed ratio between the flow rates of the output distillate and the input feed of the FAME column.

Similar to the methanol column, RC|600 preserves a fixed ratio between the flow rates of the output bottom and the input feed of the glycerol column by manipulating the setpoint of TC|600.

We provide the process flowsheet for PWC-B in Section A.2 in Appendix A. The used CDOF for this case is 25 because we remove QC|200 and fix the reflux ratio in the methanol column.

PWC-B can be configured in other ways. A common configuration is to use internal temperature controllers for the distillation columns instead of the cascade ratio controllers. However, with the plant disturbances we introduce (cf. Section 2.5), we expect difficulties

to track the product purity setpoints (particularly methanol impurity and glycerol purity) for either configuration.

We summarize the two PWC structures in Table 2.4.

Table 2.4.: Comparison of PWC-A and PWC-B structures.

	PWC-A	PWC-B
Available measurements	Temperature, pressure, flow rate, pH, and concentration	Temperature, pressure, flow rate, and pH
Used CDOF	26	25 (QC|200 is removed)
Material inventory control	Pressure and level controllers for all unit operations	Same as PWC-A
Production rate control	By oil feed flow rate (TMP)	Same as PWC-A
Methanol feed flow rate manipulation	Determined by cascade control of the reaction conversion in the transesterifier	Determined by a ratio controller with the flow rate of the feed oil
Catalyst feed flow rate manipulation	Determined by controlling the NaOH concentration in the methanol-catalyst mixture entering the transesterifier	Determined by a ratio controller with the flow rate of the methanol-catalyst mixture entering the transesterifier
Water feed flow rate manipulation	Determined by controlling methanol impurity in the biodiesel product	Determined by a ratio controller with the flow rate of the raffinate entering the wash column
Acid feed flow rate manipulation	For pH control in the neutralizer	Same as PWC-A
Reboiler duties manipulation	For controlling products purities and column recoveries	Determined by ratio controllers of the column distillate/bottom with feed flow rates

2.5. Simulation Scenarios for Assessment of Process Dynamics and PWC Performance

We first let the plant reach a steady state, after initializing its dynamic model and applying the developed PWC structures while gradually decreasing the purge streams to null. To study its dynamic behavior as well as the performance of the applied PWC structures, we introduce several process disturbances and setpoint tracking scenarios that are commonly found in literature and practice. We perform simulations under the following seven scenarios (one at a time), corresponding to one production rate setpoint change (ST) and six alternative disturbances (SD):

- ST1: setpoint change of biodiesel production rate. The red-dashed line in Figure 2.6f shows the setpoint of the biodiesel production rate over time. The setpoint changes at 1 h over 4 h while being ramped by $\pm 10\%$ from its nominal value until it returns to it at 5 h. Such setpoint changes could be required when the targeted plant capacity changes in accordance with product amount demand. Plant capacity flexibilization for optimizing production costs is also a potential reason for such changes.

- SD1: decrease in the rate coefficients of the transesterifier forward reactions by 20% at time 8 h (t_{k}). This scenario could occur when the quality or type of the fed oil changes. Also, fouling in the reactor is a potential reason for such a disturbance.
- SD2: 30% drop in the overall heat transfer coefficient in the transesterifier reactor/-jacket system at time 13 h (t_{U}). This could occur when fouling in the reactor/jacket system is present.
- SD3: trays fouling and wear in the methanol column. As a result, their separation efficiency decreases. We model this disturbance by eliminating two trays of the column at time 15 h (t_{tray}). Trays fouling and wear are common and occur in practice.
- SD4: column flooding in the FAME column. We model this disturbance by omitting two trays at time 21 h over 0.5 h.
- SD5: foaming in the glycerol column. We model this disturbance by omitting two trays at 25 h over 0.5 h.
- SD6: change in the composition of the fed oil from [0.95 wt% triolein, 0.05 wt% diolein, 0 wt% monoolein] to [0.8 wt% triolein, 0.1 wt% diolein, 0.1 wt% monoolein]. We introduce this disturbance at 27 h (t_{feed}) before the plant reaches a new steady state at 35 h. This disturbance occurs when the fed oil type or quality changes.

The scenarios are introduced at the times depicted in Figure 2.3. The time points are selected to ensure that new steady states are reached in between scenarios. However, it is worth noting that some of the introduced events, such as fouling in the reactor/jacket system of the transesterifier or tray fouling in the methanol column, may require significantly longer durations to manifest in practical situations. Nevertheless, for the purpose of studying the dynamic behavior of the process units under such circumstances, we intentionally introduce these disturbances at the specified time points.

2.6. Simulation Results for Validation of the Dynamic Model and Assessment of the PWC Structures

We implement the process model with the developed PWC structures using the object-oriented modeling language Modelica [58]. The model components can be used with different fluids because we decouple the component equations (e.g., mass and energy balance equations) from thermodynamic property equations (e.g., calculation of specific enthalpy or activity coefficient). The PID controller equations of the PWC structures are part of the DA system of equations within the model. We simulate the process in Dymola 2020 [142] and use the implicit, multi-step Differential Algebraic System Solver (DASSL) [143].

Due to the large number of process variables and control loops present, it is impractical to show the profiles of each process variable and every control loop. Hence, we analyze the dynamic behavior of the plant and the performance of control structures in a plantwide context. We first provide profiles for some process variables of the three main types of unit operations involved in the process, simulated for the case of applying PWC-A. These units are the CSTRs, distillation columns, and a wash column.

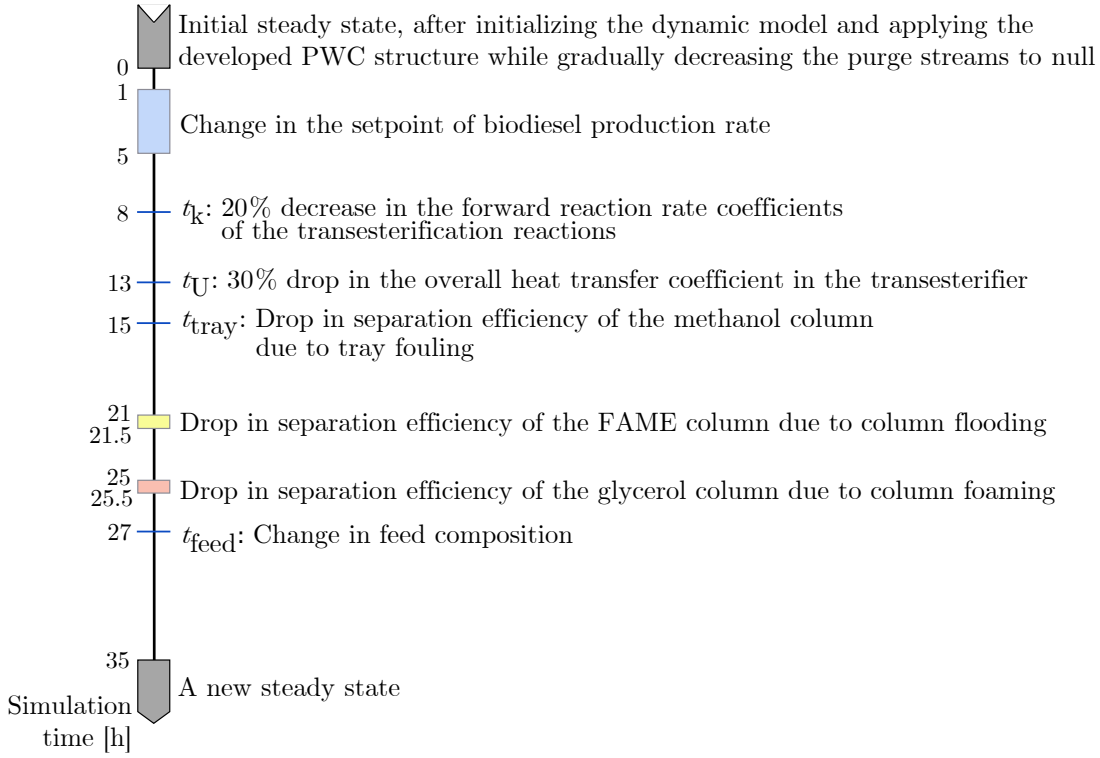

Figure 2.3.: Changes in the setpoint of biodiesel production rate and plantwide disturbances over the simulation time of the plant.

We then study the performance of the two developed PWC structures and compare them by providing and discussing the profile of the process feed and product flow rates, the reboiler duties, as well as some of the more severe and product quality CVs in the plant. In addition, based on Vasudevan and Rangaiah [144] and Kariwala and Rangaiah [46], we provide three measures to quantitatively compare the dynamic performance of the two PWC structures. The performance measures correspond to the overall settling time, the total plant accumulation, and the total deviation from the production target.

We also compare the SS simulation results of the model with that of Aspen Plus. We implemented a similar process with the same inputs and operating conditions in Aspen Plus v11 [101], which we also provide at `permalink.avt.rwth-aachen.de/?id=135903`. The main models used in the Aspen Plus process are the RCSTR, RadFrac, and Extract for the transesterifier, the distillation columns, and the wash column, respectively. We selected the NRTL model as the base method with the default Route ID for properties. We provide results for mole fraction, flow rate, and temperature profiles in Section A.3 in Appendix A for each of the aforementioned three main unit operations comparing both models. The results are very close, demonstrating the validity of our model. Nonetheless, there are some differences in the results due to mainly the different used numerical integration schemes.

2.6.1. Dynamic Behavior of the Main Unit Operations

Figure 2.4 shows the net reaction rate profiles of the considered three transesterification reactions in the transesterifier. In the blue-shaded region, we perform setpoint changes in the biodiesel production rate. In this region, the reaction rates follow the feed flow rate

profiles, which are provided in Figures 2.6a–e. At t_k, a drop in the forward reaction rate coefficients results in a proportional drop in the reaction rates. The disturbance at t_U (drop in overall heat transfer coefficient in the transesterifier) does not affect the reaction rates. The disturbance in the light-brown region has also no effect because there are no recycle streams from the glycerol column to the transesterifier. In the last disturbance at t_{feed}, because the composition of the fed oil has more diolein and less triolein, the triolein transesterification (Reaction (A.1a)) shifts more toward the reverse reaction direction. Therefore, its net reaction rate decreases. For diolein transesterification (Reaction (A.1b)), although the fed oil has more diolein, the net reaction rate decreases because more monoolein is fed, which drives the reaction more into the backward direction. For the last reaction, since monoolein input increases, the reaction is shifted to the forward direction, and thus the net reaction rate increases as indicated in Figure 2.4 for Reaction (A.1c).

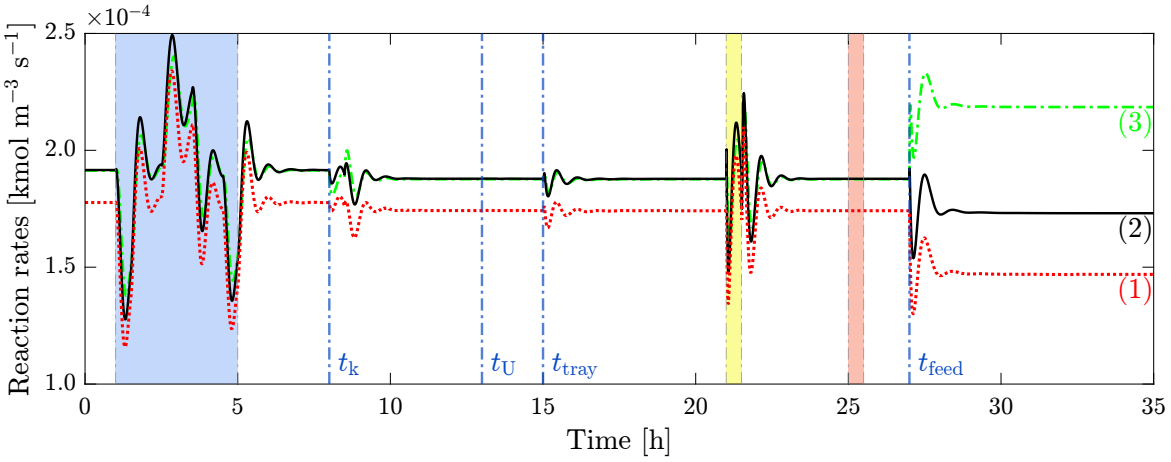

Figure 2.4.: Net reaction rate profiles of the three alkali-catalyzed transesterification reactions in the transesterifier, simulated under the disturbances and setpoint changes provided in Figure 2.3. The reactions are indicated by the number of their respective rate coefficient subindex j in A.1 in Appendix A. The dotted-red, solid-black, and dashed-dotted-green lines correspond to reactions (A.1a), (A.1b), and (A.1c), respectively.

For the distillation columns, we provide the temperature profile of the methanol column in Figure 2.5a. The temperature values increase in the direction from stage one, the condenser, to stage eleven, the reboiler. At t_k, due to the drop in the forward reaction rate coefficients, less methanol reacts in the transesterifier and thus more enters the column. Therefore, lower reboiler temperatures are needed to attain the required column recovery and methanol purity in the distillate stream. This explains the decrease in the temperature values in Figure 2.5a. At t_{tray}, the number of trays in the column is decreased by two. Therefore, higher temperature values are needed to preserve the required purity and recovery. However, the purity controller increases the reflux rates and thus the temperature values decrease back to their previous SS values. In the last disturbance, due to the increase in the rate of Reaction (A.1c), more methanol reacts in the transesterifier, thus, less fraction enters the column. Therefore, higher temperature values are needed to keep the desired recovery and purity. This can be seen in Figure 2.5a at t_{feed}, where the temperature values increase to reach a new steady state.

In Figure 2.5b, we show the activity coefficient profile of methanol in the extract phase in the wash column. The values of the activity coefficient decrease by going from stage one

to stage six. The raffinate enters the column at the sixth stage. In the final disturbance at t_{feed}, more glycerol is being produced in the transesterifier, since monoolein mass fraction in the fed oil increases. Therefore, a higher amount of glycerol enters the wash column and is extracted to the extract phase. Glycerol is a polar species and higher amounts of it increase the attractive forces among the polar species in the mixture. Therefore, the activity coefficient values of the polar species decrease in the extract phase and so does that of methanol, as shown in Figure 2.5b.

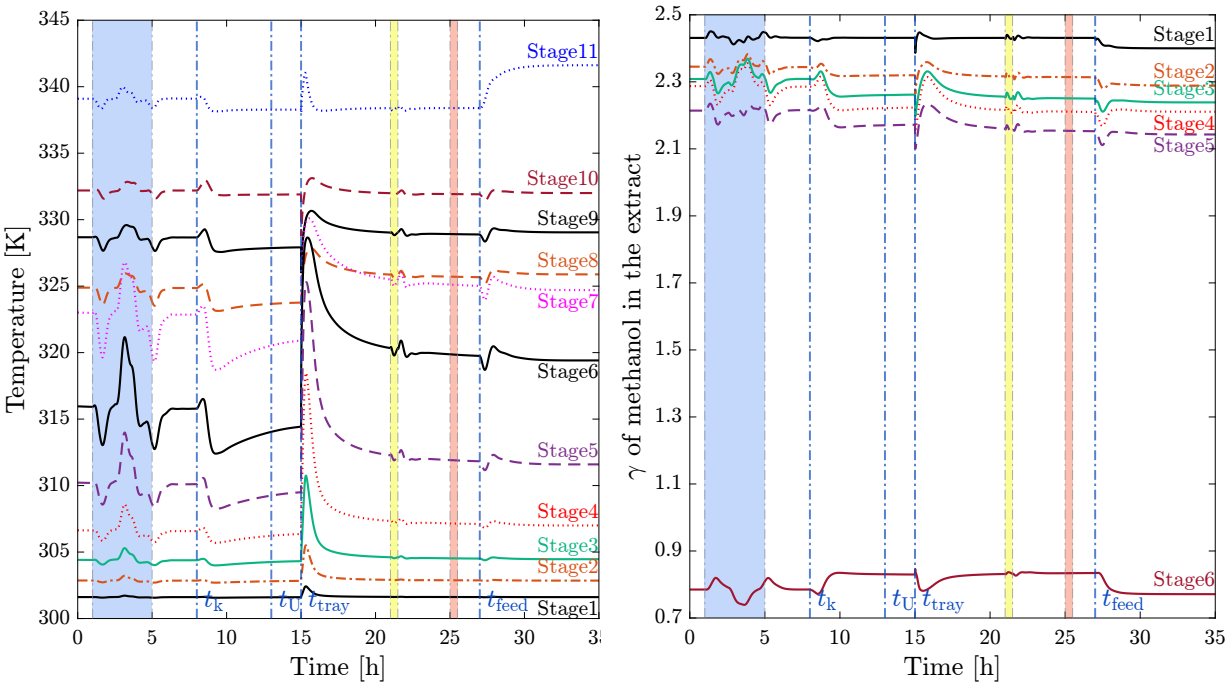

(a) Temperature profile in the methanol column. Stage 11 is the reboiler.

(b) Methanol activity coefficient (γ) profile in the extract phase of the wash column.

Figure 2.5.: Process variable profiles in two main unit operations of the process, simulated under the disturbances and setpoint changes provided in Figure 2.3.

2.6.2. Performance of the PWC Structures

We provide the results for all disturbances in Section A.4 in Appendix A. In this section, we provide the profiles only for scenarios ST1, SD1, and SD6. The disturbances of tray fouling in the methanol column SD3 and flooding in the FAME column SD4 have less interpretable results. For SD3, higher reboiler duties in the methanol column are required to maintain the desired methanol recovery and purity in the column. For SD4, higher mass fraction of monoolein impurity is present in the biodiesel product. However, it stays significantly below its maximum limit. There are no effects on the process dynamics for the drop in the overall heat transfer coefficient scenario SD2. Also, since there are no recycles from the glycerol purification section, the disturbance of foaming in the glycerol column SD5 does not affect the plant.

2.6.2.1. Scenario ST1: Change in Biodiesel Production Rate Setpoint

Figure 2.6 provides the results for the scenario ST1 for both PWC structures, PWC-A (solid-black curves) and PWC-B (dashed-dotted-green curves). The biodiesel production rate is the plant throughput. Its setpoint is shown in the red-dashed line in Figure 2.6f. The flow rates of all feeds are MVs. The oil feed flow rate (Figure 2.6c) is the TPM and is manipulated based on the changes in the biodiesel production rate setpoint. For both PWC structures, its profiles look similar because they have the same FC|400. For PWC-A, the methanol (Figure 2.6a) and $NaOH \cdot H_2O$ (Figure 2.6b) feed flow rates are manipulated according to the required oil conversion (88%) in the transesterifier and NaOH mass fraction in their fed mixture stream, respectively. For PWC-B, they are manipulated according to RC|100 and RC|101, respectively, and thus follow the oil feed flow rate. Therefore, for both PWC structures, the flow rates of the three transesterifier feeds are proportional to that of the biodiesel production rate.

Glycerol product flow rates (Figure 2.6g) are proportional to that of biodiesel because they are produced in the same reaction direction. Since the addition of acid is dependent on the fed $NaOH \cdot H_2O$, its and the formed solids flow rates (Figure 2.6e and Figure 2.6i, respectively) are also proportional to that of biodiesel, for PWC-A and PWC-B. The profiles of water-methanol product (Figure 2.6h) follow the profiles of $NaOH \cdot H_2O$ and methanol feeds. Therefore, they are also proportional to the produced biodiesel profile.

For PWC-B, since the addition of water feed (Figure 2.6d) is controlled by RC|300, its flow rate profile is proportional to that of the fed raffinate into the wash column. Thus, it is proportional to the produced biodiesel flow rate. On contrary, for PWC-A, when low production rates are required, higher water flow rates are fed to the wash column and vice versa. Lower production rates of biodiesel result in lower formation rates of FAME in the transesterifier. Therefore, the outlet stream of the transesterifier will have higher fractions of methanol, since the consumption rate of methanol is proportional to the formation rate of FAME. As a result, for PWC-A, more water will be needed for methanol extraction in the wash column to achieve the required methanol concentration in the biodiesel product, which is controlled by QC|400.

In Figures 2.6j–l, the reboiler duties are proportional to the production rate of biodiesel, as the stream flow rates in the reboiler units are proportional to it.

For PWC-A, all quality controllers (Figures 2.6m–p) are able to return the corresponding CVs to their setpoints while achieving tight control for methanol recovery and glycerol purity. We set the setpoint for methanol mass fraction in the biodiesel product to 0.0013. While there is no direct quality control in PWC-B, the indirect control for the quality CVs by ratio controllers can return these CVs to their corresponding setpoints. Nevertheless, RC|600 is unable to preserve the required purity of the final product glycerol at all times, reflecting the effects of changes in production load.

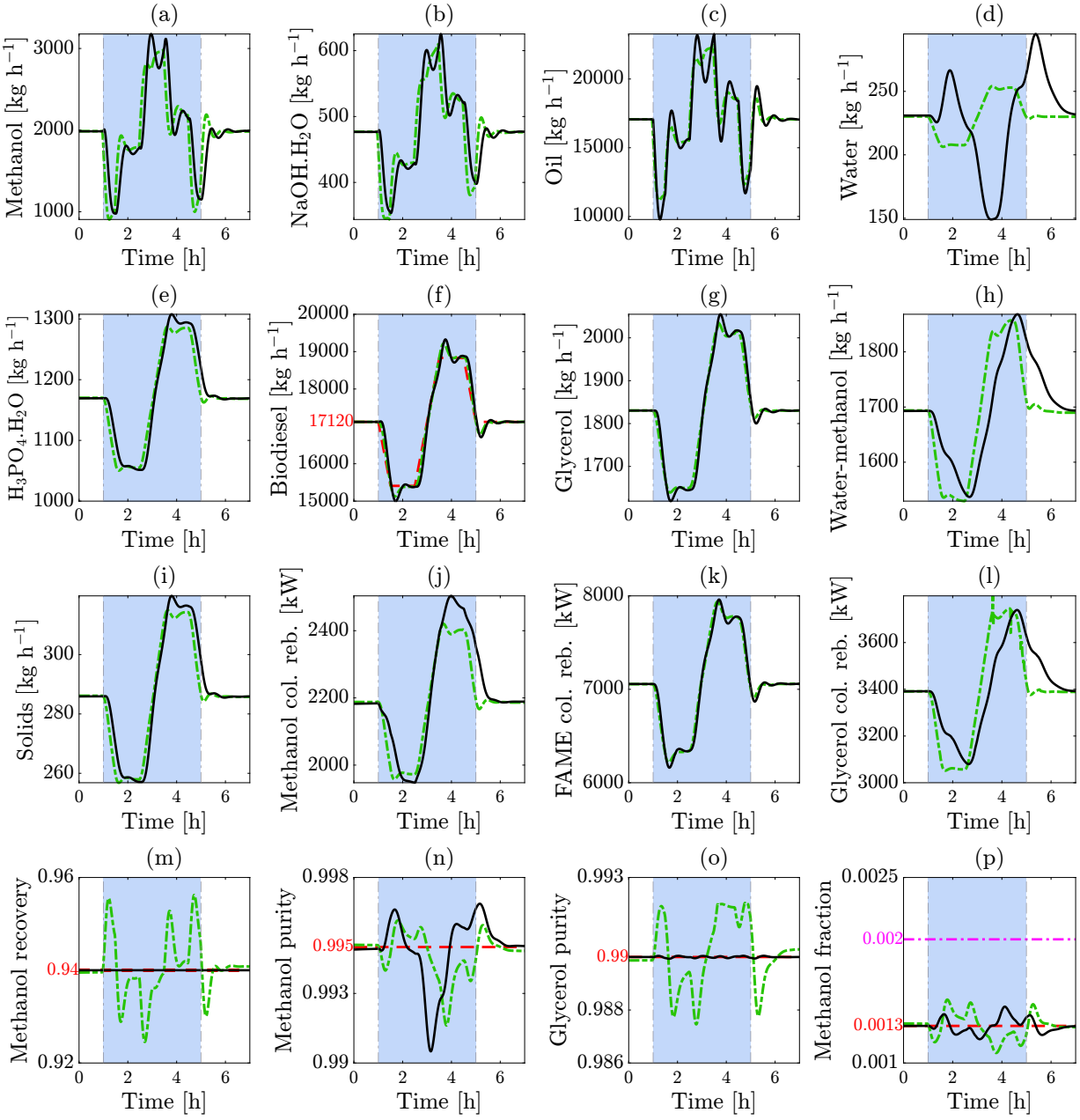

Figure 2.6.: The profiles for the scenario ST1 of the change in biodiesel production rate setpoint as provided in Figure 2.3. The load changes take place in the blue-shaded region. (a)–(e): feed mass flow rates. (f)–(i): product mass flow rates. (j)–(l): reboiler duties. (m): methanol recovery in the methanol column. (n): methanol mass fraction in the methanol column distillate. (o): glycerol mass fraction in the glycerol column bottom. (p): methanol mass fraction in the biodiesel product. The solid-black and dashed-dotted-green curves are for the results of PWC-A and PWC-B, respectively. The dashed-red and dashed-dotted-magenta lines are the setpoints and bounds, respectively.

2.6.2.2. Scenario SD1: 20 % Decrease in the Forward Reaction Rate Coefficients

Figure 2.7 provides the results for the scenario SD1 for both PWC structures. For PWC-A, more $NaOH \cdot H_2O$ (Figure 2.7b) starts to enter the plant to compensate for the drop in the reaction rate coefficients at t_k and preserve the required oil conversion in the reactor. Methanol feed flow rate (Figure 2.7a) increases then returns to its previous SS value, because its needed amount to achieve the required oil conversion is compensated by the increase in $NaOH \cdot H_2O$ while preserving the required methanol recovery and purity in the methanol column. For PWC-B, since the forward reaction rates decrease, less methanol reacts in the transesterifier and thus more enters the methanol column. With a fixed ratio in RC|200, the required methanol recovery cannot hence be achieved. This is shown by the drop in the dashed-green curve in Figure 2.7m. However, its purity increases (Figure 2.7n) because more methanol enters the column. Since less methanol is recovered in the methanol column, more methanol feed is fed to preserve the ratio in RC|100 between the total oil, and methanol and $NaOH \cdot H_2O$ mixture entering the transesterifier. This also explains the increase in $NaOH \cdot H_2O$ feed flow rate, which is manipulated by RC|101 in the case of PWC-B. Since both PWC structures have the same FC|400, they have similar behavior in controlling the desired biodiesel production rate (Figure 2.7f), and thus in manipulating the fed oil flow rates (Figure 2.7c).

Since more methanol leaves the transesterifier due to the decrease in the forward reaction rates, more enters the wash column and thus appears in the distillate of the FAME column. To preserve the required methanol fraction in the biodiesel product, more water enters the wash column for the PWC-A, as can be seen in Figure 2.7d. However, the ratio controller RC|300 in PWC-B manipulates the fed water flow rate according to a preserved ratio with the fed raffinate and thus fails to feed a sufficient amount of water to preserve the required setpoint of methanol in the biodiesel product. This is shown in Figure 2.7p, where the dashed-green curve increases to approach the maximum allowed mass fraction of methanol.

For both PWC structures, the increase in $NaOH \cdot H_2O$ flow rates leads to an increase in the needed amount of acid for neutralization. As a result, more water-methanol and solids products (Figure 2.7h and Figure 2.7i, respectively) are produced. By preserving the required purity of the glycerol product (Figure 2.7o), its flow rate profile (Figure 2.7g) should follow the controlled biodiesel production rate because it is formed proportionally to FAME formation. This is the case for PWC-A. In contrast, for PWC-B, since more water is fed to the glycerol purification section, the RC|600 increases the produced glycerol product while decreasing its purity. Therefore, in this disturbance scenario, PWC-B fails to achieve the required glycerol product purity, track the setpoint of methanol mass fraction in the biodiesel product (rather shifts to its upper abound), and preserve the desired methanol recovery in the methanol column.

For both PWC structures, higher reboiler duties are needed in the methanol and glycerol columns (Figure 2.7j and Figure 2.7l, respectively) because more water enters the columns, thus increasing the enthalpies of vaporization in the reboilers. Since for PWC-B, the required oil conversion is not achieved by the addition in the fed $NaOH \cdot H_2O$ as for PWC-A, more residual oil, especially triolein, leaves the transesterifier and ends in the reboiler of the FAME column. This increases the heat duty in the reboiler as shown in Figure 2.7k.

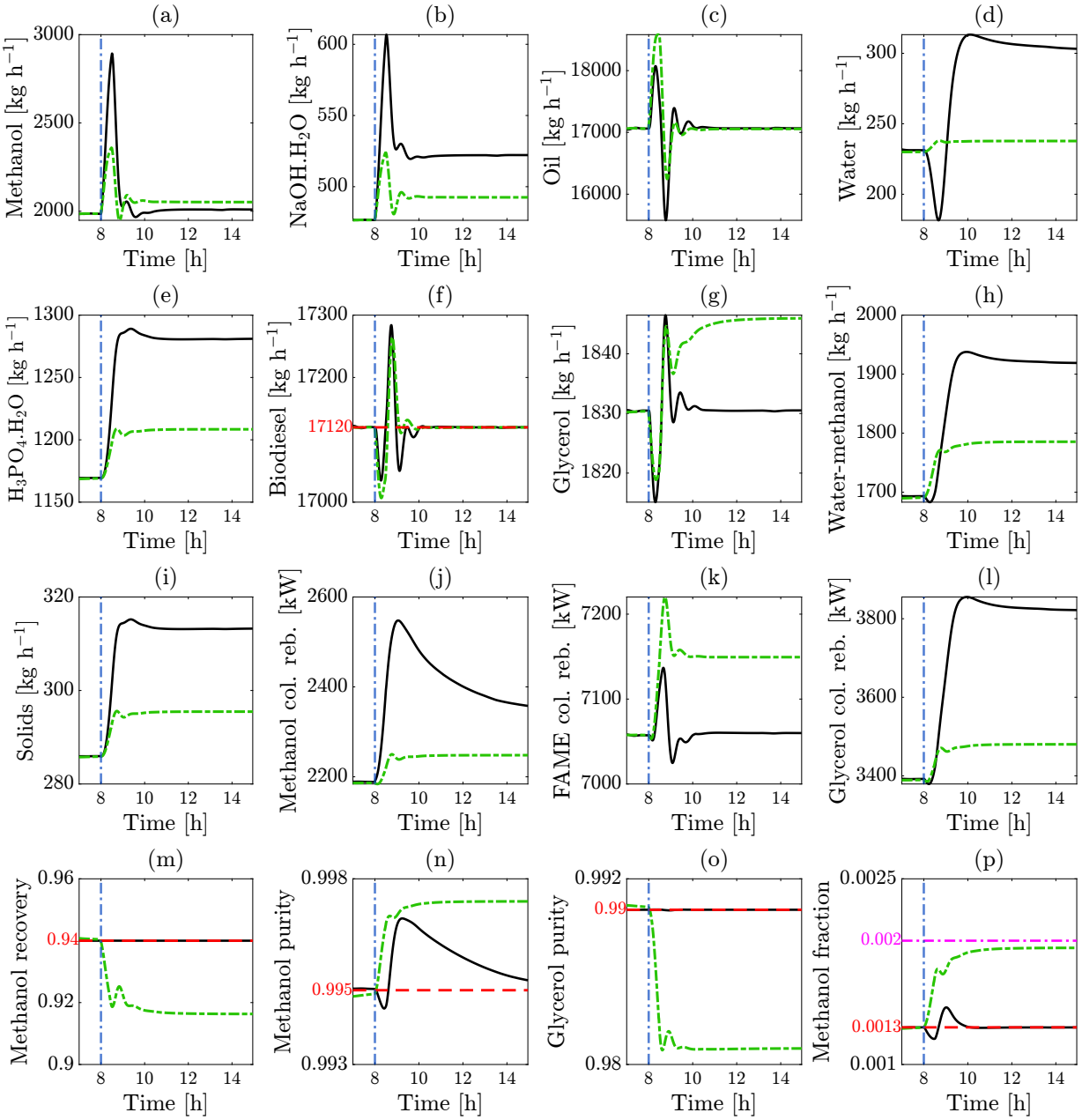

Figure 2.7.: The profiles for the scenario SD1 of 20% decrease in the forward reaction rate coefficients of the transesterification reactions as provided in Figure 2.3. The disturbance takes place at $t_k = 8$ h (vertical dashed-dotted-blue line). (a)–(e): feed mass flow rates. (f)–(i): product mass flow rates. (j)–(l): reboiler duties. (m): methanol recovery in the methanol column. (n): methanol mass fraction in the methanol column distillate. (o): glycerol mass fraction in the glycerol column bottom. (p): methanol mass fraction in the biodiesel product. The solid-black and dashed-dotted-green curves are for the results of PWC-A and PWC-B, respectively. The dashed-red and dashed-dotted-magenta lines are the setpoints and bounds, respectively.

2.6.2.3. Scenario SD6: Change in the Oil Feed Composition

Figure 2.8 provides the results for the scenarios SD6 for both PWC structures. In this last disturbance, we increase the diolein and monoolein mass fractions in the fed oil. Therefore, less methanol and $NaOH \cdot H_2O$ fraction are needed to achieve the same oil conversion. In PWC-A, since the oil conversion is directly controlled by QC|100, the fed methanol and $NaOH \cdot H_2O$ flow rates are adjusted accordingly and hence decreased. This also explains the drop in the fed acid flow rate (Figure 2.8e) and thus the formed solids (Figure 2.8i) for PWC-A. In contrast, in the case of PWC-B, since there is no direct control for the oil conversion in the transesterifier, more methanol is present in the reactor and thus fed into the methanol column. Therefore, the methanol recovery decreases, and its purity increases (Figure 2.8m and Figure 2.8n, respectively). Hence, both methanol and $NaOH \cdot H_2O$ feed flow rates increase as explained in the previous disturbance scenario for PWC-B.

Increasing the diolein and monoolein mass fractions in the fed oil results in an increase in glycerol formation in the transesterifier (cf. reaction rates in Figure 2.4). This explains the increase in glycerol product flow rates in Figure 2.8g for both PWC structures. As aforementioned, glycerol increases the polarity of the extract mixture in the wash column. Therefore, the activity coefficient value of methanol in the extract phase decreases (cf. Figure 2.5b). Thus, less water is needed for methanol extraction. This explains the decrease in the fed water flow rate for PWC-A in Figure 2.8d. On the other hand, since the fed water flow rate is manipulated by a fixed ratio in RC|300 for PWC-B, it increases with the increase of the input raffinate to the wash column. The input raffinate increases because more glycerol is being produced while having the same amount of the produced biodiesel.

The produced water-methanol follows the profiles of the fed water into the wash column, acid, and $NaOH \cdot H_2O$. For PWC-A, less water, acid, and $NaOH \cdot H_2O$ are fed, which is the opposite for PWC-B. This explains the product flow rate profiles for both PWC structures in Figure 2.8h.

In the case of PWC-B, increasing the diolein and monoolein mass fractions in the fed oil, while also increasing the methanol and $NaOH \cdot H_2O$ feeds flow rates, results in an increase in the oil conversion. Therefore, less residual oil ends in the reboiler of the FAME column. This explains the decrease in the reboiler duty of the FAME column in Figure 2.8k for PWC-B. On contrary, it increases for PWC-A, because the overall amount of residual oil increases for the same desired oil conversion in the transesterifier. For both PWC structures, the reboiler duties of the methanol and glycerol columns (Figure 2.8j and Figure 2.8l, respectively) follow the profiles of the fed water into the columns. As aforesaid, when more water enters the columns (cf. Figure 2.8b, Figure 2.8d and Figure 2.8e), the enthalpies of vaporization in the reboilers increase and thus their duties.

Since in the case of PWC-B higher amount of methanol is fed (Figure 2.8a), while having lower recoveries in the methanol column, a higher amount of methanol enters the wash column. The ratio controller RC|300 that manipulates the fed water flow rate (Figure 2.8d) follows the total amount of the input raffinate and not that of methanol only. Therefore, higher concentrations of methanol remain in the raffinate stream that enters the FAME column. As a result, the mass fraction of methanol in the final biodiesel product increases from the previous SS value and gets beyond the permitted bound, as shown in Figure 2.8p. Moreover, the ratio controller RC|600 could not bring the glycerol mass fraction to the desired purity in the produced glycerol product. Therefore, under this disturbance, the implemented PWC-B could not satisfy the quality constraints on the final products.

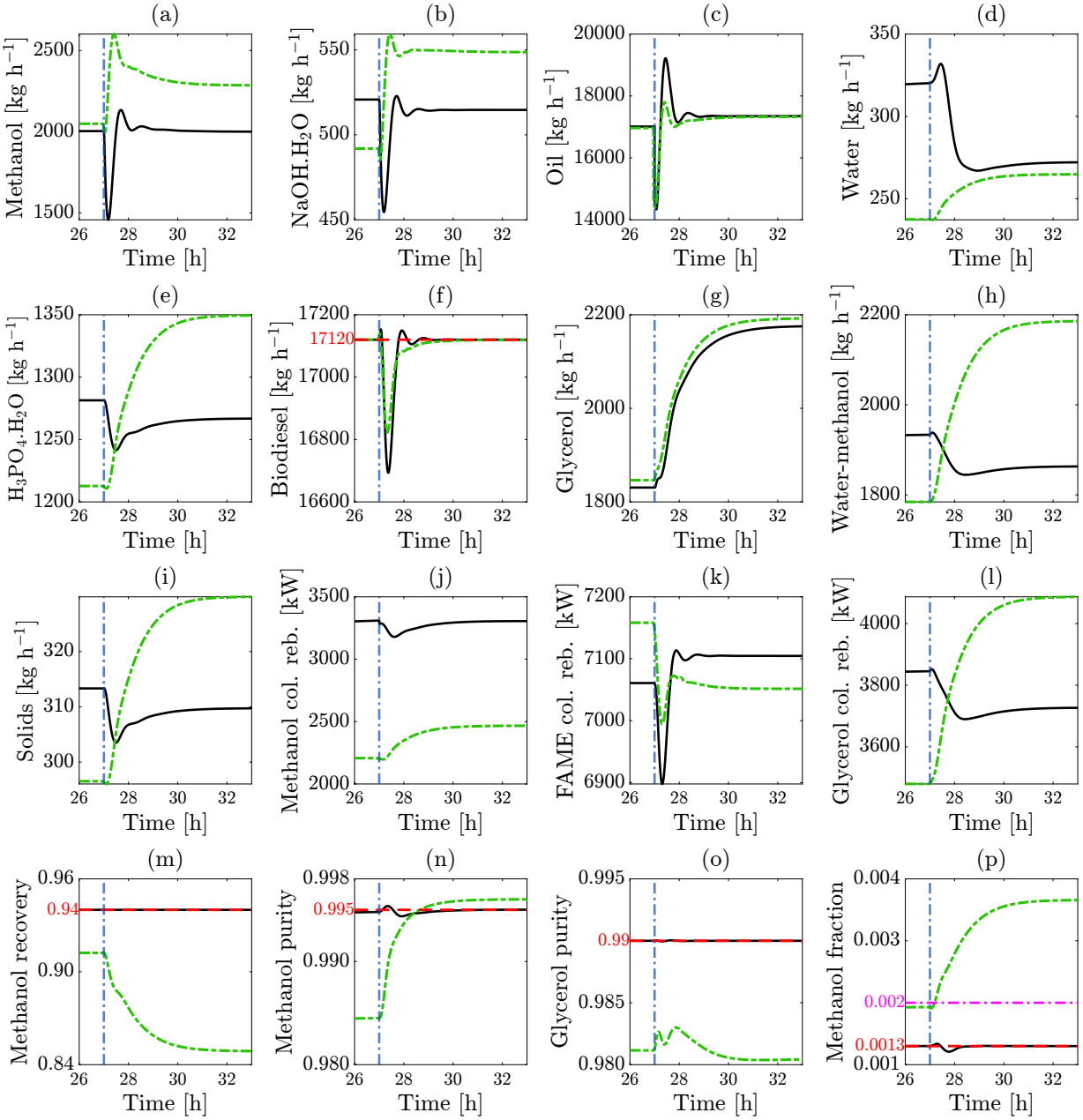

Figure 2.8.: The profiles for the scenario SD6 of the change in the fed oil composition as provided in Figure 2.3. The disturbance takes place at $t_{\text{feed}} = 27$ h (vertical dashed-dotted-blue line). (a)–(e): feed mass flow rates. (f)–(i): product mass flow rates. (j)–(l): reboiler duties. (m): methanol recovery in the methanol column. (n): methanol mass fraction in the methanol column distillate. (o): glycerol mass fraction in the glycerol column bottom. (p): methanol mass fraction in the biodiesel product. The solid-black and dashed-dotted-green curves are for the results of PWC-A and PWC-B, respectively. The dashed-red and dashed-dotted-magenta lines are the setpoints and bounds, respectively.

2.6.2.4. Quantitative Measures of Dynamic Performance

We present measures to quantitatively assess the dynamic performance of PWC-A and PWC-B. A suitable performance measure should capture essential process behavior, and be easily measurable and reliable. We use three performance criteria which are: (a) the accumulation-based settling time, which is the time required for the overall accumulation in process units to settle [46]; (2) the integral of the overall accumulation [145]; and (3) the integral of the deviation from the production target [144]. Table 2.5 provide the results of the three criteria for both PWC-A and PWC-B.

The provided values in Table 2.5 are for applying the disturbances solely and not consecutively as shown in Figure 2.3. The settling times for both PWC structures are similar for all disturbances except for SD6. It is higher for PWC-B. This can be explained by the feed and product flow rate profiles in Figure 2.8, in particular, the methanol feed flow rate. As aforementioned, SD2 and SD5 have no effects on the process dynamics. This explains their zero values of settling times and deviations from the production target. For both PWC structures, the production rate follows its target well (cf. Figure 2.6f, Figure 2.7f, and Figure 2.8f), as the integral of the deviation from the production target for all scenarios is significantly small compared to the production target. The highest value is for PWC-A for ST1 and is less than 1.2 % of the total nominal production amount over 5.4 h.

Table 2.5.: Quantitative performance assessment of the developed PWC structures. The results for PWC-B are shown in parentheses.

Scenario	Accumulation-based settling time [h]	Integral of the overall accumulation [kmol]	Integral of the deviation from the production target [kg]
ST1	5.4 (5.4)	188 (188)	1079 (961)
SD1	2.8 (2.8)	204 (194)	101 (95)
SD2	0 (0)	188 (188)	0 (0)
SD3	1.6 (1.6)	189 (187.6)	32 (37)
SD4	2 (2)	188 (188)	268 (283)
SD5	0 (0)	188 (188)	0 (0)
SD6	3.5 (4)	190 (210)	191 (158)

Recall that due to the interconnected unit operations with PWC loops and recycle streams from the methanol and FAME columns, the analysis of the dynamic behavior of process variables and control loops should be carried out in a plantwide context. Overall, the applied PWC-A assumes that the control structure has an information-rich measurement configuration, which makes it highly suitable for the plant and yields satisfactory performance. The PWC-B, which relies solely on conventional measurement, is capable of satisfactorily handling scenarios involving changes in biodiesel production setpoint. Its control loops exhibit similar behavior to those of PWC-A. However, for the second and last disturbance scenarios, the control structure fails to meet the necessary standards for the final product quality, particularly the maximum allowable methanol concentration in the biodiesel product, due to a lack of measurements. These two disturbances involve changes in the reaction rates and fed oil composition that directly affect the quality of the products produced. As a result, by utilizing the IFSH method for two measurement-availability scenarios, we can provide insights into the need for process analytics. Specifically, the importance of inline concentration measurements for process control could be demonstrated,

which is motivated by recent advancements in process analytics and spectrometry. Conversely, in situations where few conventional measurements are available, the importance of developing dynamic models for use in model-based control and estimation applications was shown. This underscores the significance and relevance of our developed model and implemented PWC structures for benchmark purposes.

While having information-rich measurements would be desirable, this does not correspond to current industrial practice. Thus, alternative control techniques should be considered to overcome the aforementioned limitations in the absence of information-rich measurements. Modern concepts, such as hierarchical control strategies including MPC, state estimation, and soft sensors, are promising solutions. Herein, the system observability needs to be considered. Notably, dynamic models, such as our proposal, need to be utilized for such model-based control and estimation methods.

2.7. Conclusion

We develop a detailed mechanistic dynamic model with rigorous thermodynamics for a biodiesel production plant via the production route of homogeneous alkali-catalyzed transesterification of vegetable oil. The model is implemented in Modelica with modular and hierarchical building blocks and provided open-source. Because we decouple the equations of the model components, the model could be adapted for other processes and used for modeling and simulating chemical processes in general. Therefore, using other production-route alternatives like homogeneous acidic or heterogeneous, utilizing other vegetable oils, or adding the oil (waste cooking oil) pretreatment process should be straightforward.

Moreover, we build a similar process in Aspen Plus and show that its SS results are very close to that of the proposed Modelica dynamic Model. Commercial tools like Aspen Plus are often used in academia and industry for process modeling and simulation. However, their model equations are not accessible and editable. In contrast, our proposed dynamic model is open-source and modular with full control on model equations. Such models are needed for optimization and model-based studies as well as for benchmark purposes. Notably, the proposed model shares many features with general chemical processes, particularly, it has the reaction, separation, and recycle parts. This underlines its generic value and significance as an open-source model.

We develop and implement two PWC structures based on the IFSH methodology. The PWC structures are based on decentralized PID controllers. The first control structure is based on the assumption of having information-rich measurement configurations (quality measurements), motivated by recent advances in process analytical technology and spectroscopy. In the other structure, we consider that only conventional measurements are available. Thus, a structure that more matches current industrial practice. We study the dynamic behavior of the plant and conduct comparisons between the two applied PWC structures by simulating it under several plantwide disturbances and production rate setpoint changes. The plantwide analysis of the process variable profiles and control loops shows how the process units are interconnected with recycle streams and control loops and their interrelated dynamic behavior. The first PWC structure is adequate for the plant and performs satisfactorily in terms of setpoint tracking and disturbance rejection. The second PWC structure fails to satisfy product quality constraints at all times and thus cannot achieve the PWC objectives of the plant. Its behavior deviates from the first PWC

structure, especially for the drop in the forward reaction rate coefficients and change in feed composition disturbances. This performance comparison between the two PWC structures and the limitations of the one that is based on conventional measurements motivate the importance of more advanced control strategies. Model-based control and estimation techniques in hierarchical control structures can be potential solutions to overcome the aforementioned limitations of conventional decentralized PID controllers. This reflects the importance of developing dynamic models of biodiesel production processes that can be utilized for such model-based control.

The developed model and PWC frameworks may be used to support the scaleup of biodiesel production processes, for instance, in terms of sizing of equipment, and identification of potential bottlenecks (e.g., availability of reactants, reactor residence time, catalyst alternatives, and important recycle streams). The model can also be employed as a digital twin for biodiesel production plants as well as for model-based experimental design applications. However, experimental validation of the model is still needed and can be conducted as future work.

We design the process and fix some setpoint values based on reported operating parameters in the literature. Some of those reportedly optimal values were determined for single process units (e.g., transesterifier) and not in a plantwide context. It is thus suggested to apply numerical optimization for the synthesis and design of sustainable biodiesel processes in a plantwide context. Optimal control problems can be formed, for instance, to minimize methanol usage, energy consumption, wash water usage, or waste streams. Moreover, eNMPC methods may be employed to operate the process flexibly based on economical objectives while satisfying all operational and quality constraints. Mass integration synthesis along with HI can also be conducted for process optimization. Furthermore, the process model may be extended with respect to the characterization of the oil feed as well as the upstream processing like the pretreatment of waste cooking oil or preparation of algae oil.

In the subsequent chapters, we build upon this model and the base layer control structures, extending them for optimization- and control-oriented purposes. Our goal is to develop and implement offline DO and online control strategies for the optimal flexible operation of the biodiesel production process. Notably, the model serves not only as the controller and optimization model but also as the plant model for the underlying biodiesel production process, as all our work is conducted in silico.

3. Optimal Design and Flexible Operation of a Fully Electrified Biodiesel Production Process

Figure 3.1 provides a graphical overview of the focus of this chapter within the broader framework illustrated in Figure 1.2. This chapter addresses the integration of process design and optimal operation by developing and solving offline DO strategies. Specifically, we explore flexibility-oriented process designs that incorporate buffer tanks to facilitate and enhance the flexible operation of the biodiesel production process under consideration.

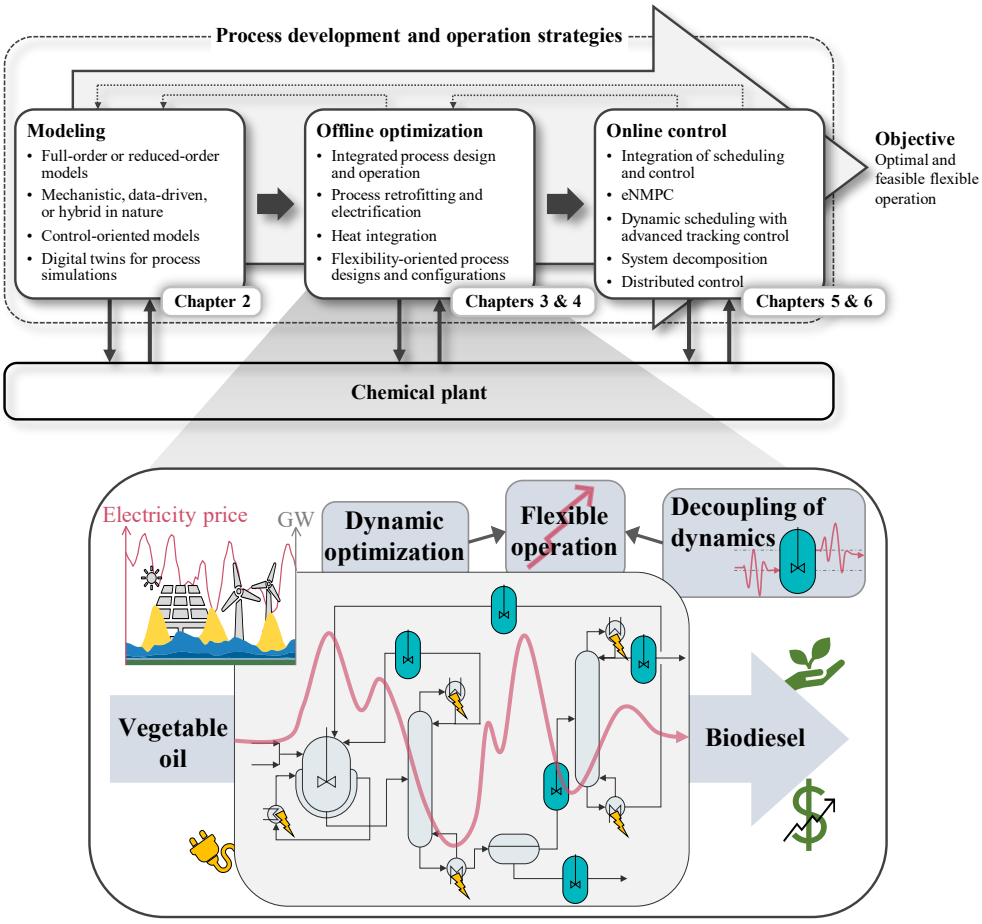

Figure 3.1.: Graphical illustration highlighting the focus of Chapter 3, emphasizing the offline DO and flexibility-oriented process design phase within the modeling and optimization framework presented in Figure 1.2 in Chapter 1.

3.1. Introduction

Flexible operations in chemical processes not only allow for continuous adjustments in production rates to leverage fluctuating energy prices [17, 146], but also enable flexibility in product purities and types, with varying products and grades requiring different power levels and diverse feedstocks available [23, 147]. However, most conventional chemical processes are designed for continuous operation around SS operating points, which necessitates a constant energy and feedstock supply, thereby posing significant challenges for flexible operation [23]. Therefore, this paradigm shift requires a reevaluation of the conventional process design and operation to enable greater flexibility in accommodating variable energy availability. Simultaneously, achieving optimal flexible operation necessitates trajectory optimization, which entails optimizing the process degrees of freedom over a specified time horizon to maximize profit or minimize carbon footprint while satisfying operational constraints and meeting product quality requirements [23]. Several DO techniques, including direct sequential [148, 149] and full discretization methods [150], enable such trajectory optimization. The potential of optimal flexible trajectories has been investigated in several load-shifting applications for electricity-intensive processes like air separation units [21, 33], water desalination plants [40, 41], chlor-alkali electrolyzers [42, 43], and multi-energy systems [151, 152]. However, numerical solutions to these optimization problems can be challenging, with computational costs increasing with model size and complexity, length of considered time horizon, and temporal resolution.

Chemical plants are composed of several unit operations, most prominently involving reaction and separation. These different unit operations exhibit varying levels of operational flexibility, making it difficult to utilize the plant's full flexibility potential or adjust its load as a whole. For instance, the production flexibility of a unit operation may be limited by the operational constraints, particularly level limits, of the downstream processes. Incorporating intermediate and final storage units for the products may allow individual units to operate at different flexibility levels within their respective limits. Such a solution is simple yet effective as it also avoids the need to retrofit the unit operation sizes. Nonetheless, the exchange between upstream and downstream processing through these storage units must be coordinated optimally. This operational complexity and flexibility-oriented process design have not been fully comprehended in existing chemical processes involving reaction, separation, and recycle parts that consider some degree of process flexibility [61, 153]. Despite the added complexity, this strategy may become one of the new paradigms for chemical process design and operation in the era of renewable-powered chemical production.

Biodiesel production processes are an exemplary case of classical chemical plants that involve reaction and separation processes along with multiple material recycle streams [1, 36]. Moreover, biodiesel is a "renewable" fuel derived from biomass that has the potential to replace fossil-based diesel [36]. However, its production costs are higher than those associated with producing conventional diesel [52]. Thus, reducing total manufacturing costs and leveraging fluctuating energy prices through flexible operations are critical to ensuring its economic viability. Therefore, designing an optimal and flexible electrified biodiesel production process would not only explore DSM in a classical chemical plant but also unify sustainability concepts from various research areas. This integration is a key aspect for future industrial biofuel and chemical synthesis using renewable energy.

We investigate a process for the homogeneous transesterification of vegetable oil using

an alkali catalyst to produce biodiesel. Our process design builds upon the work presented in Chapter 2, in which we develop a rigorous first-principle model in Modelica with two PWC structures, and make it available as open-source. We electrify the process using heat pumps and electric coils. The process has a main reaction part, several separation processes, and two recycle streams. It produces two final products with specific quality requirements, as glycerol is a by-product. The process involves operational limits and stringent quality standards, which pose challenges to exploiting process flexibility. As the process educts are in the liquid state, they are suitable for intermediate and final storage without requiring additional liquefaction. Moreover, the process provides an opportunity to explore how operational flexibility affects HI across multiple units.

To investigate the potential of flexibility-oriented designs and operations of the process, we examine three different process configurations using intermediate and final buffer tanks and compare the operating profits obtained from their respective economic DO strategies with that of a conventional optimal SS operation. The three process configurations differ based on the number and the location of the buffer tanks incorporated. We employ the three DO strategies offline, utilizing local gradient-based optimization. We aim to illustrate that, when electrifying chemical processes and utilizing renewable electricity, novel operational strategies rooted in flexibility through dynamic operation may emerge as the new standard for chemical plant operations. Realizing this transition would require the utilization of advanced modeling and optimization techniques, along with a reevaluation of process design considerations, to fully exploit the potential of flexible operation. Furthermore, we demonstrate that intermediate buffer tanks not only decouple dynamics between different process parts but also facilitate the implementation of a distributed optimization strategy with smaller problem sizes, leading to enhanced computational performance.

The chapter is structured as follows. First, we introduce the biodiesel production process under consideration and provide a summary of our modeling approach. Next, we discuss the several configurations examined to achieve process flexibilization, along with the corresponding optimization problem assumptions and formulations. We further elaborate on the considered operational scenario and implementation before presenting and discussing the results. Lastly, we draw conclusions based on our findings.

3.2. Biodiesel and Glycerol Production Process

Figure 3.2 depicts the flowsheet of the entire process, including all buffer tanks and optimization variables. In Section 3.3, we elaborate on the use of buffer tanks and optimization strategies. For completeness, we present a summary of the process description in this section, excluding buffer tanks, and briefly discuss our modeling methodology and underlying assumptions. We refer the reader to Chapter 2 for more detailed information on the process description and modeling.

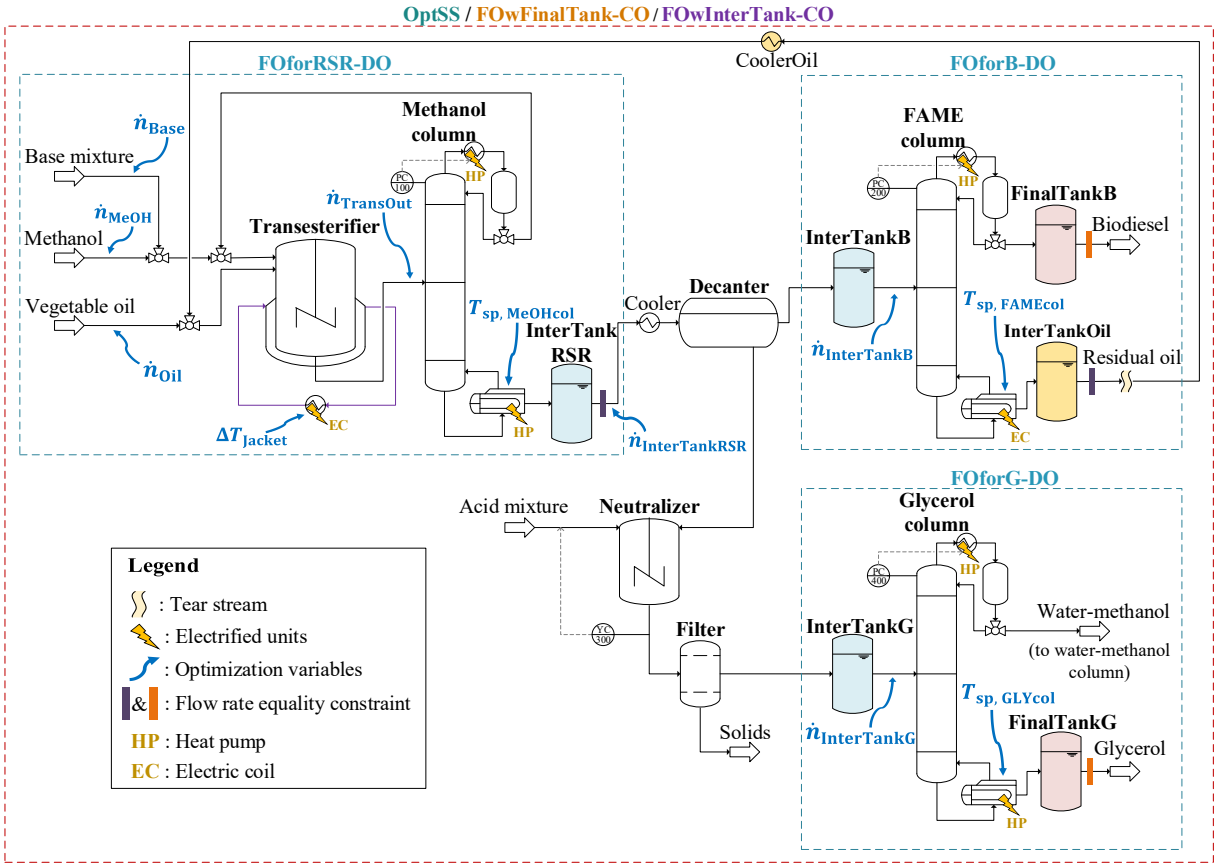

Figure 3.2.: Superstructure flowsheet of the considered configurations of the biodiesel production process. We denote by $\dot{n}_{\text{Oil}}$, $\dot{n}_{\text{MeOH}}$, and $\dot{n}_{\text{Base}}$ the molar flow rates of the vegetable oil, methanol, and base mixture feeds, respectively. The outlet molar flow rates of the transesterifier and buffer tanks `InterTankRSR`, `InterTankB`, and `InterTankG`, are indicated by $\dot{n}_{\text{TransOut}}$, $\dot{n}_{\text{InterTankRSR}}$, $\dot{n}_{\text{InterTankB}}$, and $\dot{n}_{\text{InterTankG}}$, respectively. The temperature change of the transesterifier jacket medium after passing through the external heat exchanger is ΔT_{Jacket}. The temperature setpoints of the column reboilers are indicated by $T_{\text{sp,MeOHcol}}$, $T_{\text{sp,FAMEcol}}$, and $T_{\text{sp,GLYcol}}$, respectively. All buffer tanks are excluded for the SS optimization case, OptSS, while the DO FOwFinalTank-CO includes only the final buffer tanks `FinalTankB` and `FinalTankG`. The distributed optimization subproblems FOforRSR-DO, FOforB-DO, and FOforG-DO include all buffer tanks, whereas the DO FOwInterTank-CO exclude `InterTankOil`. The cooler, CoolerOil, is only considered for the distributed optimization case.

3.2.1. Process Flowsheet

The oil feed composition consists of 95 wt% triolein and 5 wt% diolein [1, 36]. We use methanol for transesterification and sodium hydroxide (NaOH) solution as a catalyst. They are fed into the transesterifier, which converts oil and methanol into FAME and glycerol. The resulting products are then separated and purified. The methanol column recovers the unreacted methanol to recycle it to the reactor. The bottom product is cooled and sent to a decanter to separate most of the glycerol, water, the dissolved NaOH, and methanol from FAME and unreacted oil. The light product is then further purified in the FAME column, producing biodiesel that meets European quality standards [122]. The residual

oil is recycled back into the reactor after being mixed with fresh oil. The decanter bottom is sent into a neutralizer unit, where it is neutralized using a phosphoric acid solution to remove dissolved NaOH species [82]. The solution is then filtered to remove the formed salt in a filter unit. The remaining liquid is purified in a glycerol column to remove water and methanol from glycerol with a pharmaceutical-grade purity of 99 wt% [1, 46].

3.2.2. Process Modeling

Before presenting the electrification approach, we briefly summarize the considered modeling formulation and assumptions for the unit operations and thermodynamics. In addition, we provide the base-layer control considered and further modeling aspects.

3.2.2.1. Unit Operations

We describe the transesterifier as a perfectly-mixed CSTR using energy and material balances. We model the reaction system based on the well-studied reversible three-step transesterification system in the literature [1, 86]. We model the transesterifier jacket as a series of equivalent CSTs. We utilize MESH models for the decanter and each stage of the distillation columns. Our approach includes several assumptions, such as the perfect mixing of vapor and liquid phases, and that the tray holdup only accounts for the liquid phase since the vapor holdup is typically insignificant [130]. We use a quasi-steady-state approximation for the energy balances at the trays, which allows reformulating the model to an index-1 DAE system [130].

Regarding the methodology employed for sizing the main unit operations, particularly the distillation columns, we refer the reader to refs. [154], [155], and [156]. For the transesterifier, we employ a sizing approach based on a one-hour residence time, ensuring it operates at half of its capacity during nominal operation. We utilize residence times of five seconds for the column trays and 30 seconds for the condensers and reboilers. The sizing of other units follows similar heuristics [154–156]. Across all units with holdups, the sizing is such that they operate at approximately half of their capacity during nominal operation.

3.2.2.2. Chemical System and Thermodynamics

We consider ten species, including triolein, diolein, methanol, water, NaOH, and phosphoric acid, as feeds. Monoolein is an intermediate educt. The products are methyl oleate (FAME), glycerol, and monosodium phosphate (solids product). We use the DIPPR temperature-dependent correlations to determine the molar heat capacities [110]. We then determine species enthalpies, entropies, and Gibbs free energies through analytical integration. We determine the vapor pressures using the extended Antoine correlation [133]. To account for non-ideality in the liquid phase, we use the NRTL model [109]. The Racket equation is used to determine liquid-mixture molar densities [132]. We employ isofugacity conditions to describe the LLE and VLE, assuming that the number of existing phases is known.

3.2.2.3. Base-Layer Control System

A base-layer control system consisting of PI controllers (cf. Figure 3.2) is implemented to determine the condenser cooling duties for the design pressure values at the top of the distillation columns by pressure controllers (PCs), and the acid feed flow rate based on a fixed pH value at the outlet of the neutralizer by a pH controller (YC). We control the liquid levels in the distillate drums, reboiler kettles, decanter, and neutralizer by cascade controllers for fixed residence times. Temperature controllers are employed to control the reboiler temperatures to their setpoints by manipulating the reboiler heating duties. The temperature setpoints are determined by an optimizer.

3.2.2.4. Buffer Tanks

We consider energy and material holdups for buffer tanks with half-full nominal liquid levels. We assume the tanks to be thermally insulated.

3.2.2.5. Water-Methanol Waste Stream

To account for the water-methanol waste stream (cf. Figure 3.2) in the optimization calculations, we assume the presence of a downstream purification unit that separates water and methanol (water-methanol column). The energy cost incurred by this unit, as well as the revenue generated by its purified methanol product, are considered contributors to the overall energy cost and product revenue. Therefore, based on SS simulations of a rigorous model for the water-methanol column, we fit an equation that describes the total electrical power demand of this purification unit and its methanol product flow rate as a function of the water-methanol waste flow rate and its methanol mass fraction. An equation that relates the purity of the purified methanol as a function of this mass fraction is also fitted. We include those empirical equations along with the corresponding coefficient of determinations in (B.1) in Appendix B.

3.2.3. Electrification of Process Units

The condensers and reboilers of the distillation columns, as well as the heating unit of the transesterifier, are the power-consuming components. In the following, we explain how we electrify these units in this work.

Condensers

We model the needed electric power for cooling in distillation column condensers through an ideal vapor-compression refrigeration cycle. We use a single-stage compression with an isentropic efficiency of 0.8 [157, 158]. We opt for ammonia as a refrigerant due to its high coefficient of performance (COP) compared to other refrigerants, and widespread use in industrial systems [159, 160]. To enhance heat transfer during the refrigeration process, air fans are employed. We determine their needed electrical power by a linear correlation with the transferred heat [161]. The resulting COP values are around 2.7.

Reboilers

To electrify the distillation column reboilers, we utilize heat pumps or electric coils with different systems employed based on the required heat sink temperature. We model the heat pumps similarly to the refrigeration cycles used for the condensers. The methanol

column reboiler operates within a temperature range of around 65 °C, for which we use a single-stage heat pump with cyclopentane as the working fluid. Such systems are characterized by high COP values for the given source and sink temperatures compared to other fluids [162, 163]. As a result, the COP values are around 3.5. For the glycerol column reboiler, which operates within a temperature range of around 140 °C, we employ a two-stage cascade heat pump as described in refs. [164] and [165]. We use cyclopentane as the working fluid for the low-temperature stage, while water is used for the high-temperature stage, as suggested by ref. [166]. The cascade structure enables the single stages to operate at different pressure and temperature ranges, which are appropriate for the specific refrigerant. The COP values for this system are around 2. Additionally, all heat pumps are equipped with an internal heat exchange system, which reduces the mass flow of the working fluid and thereby improves the COP, as noted by refs. [158] and [167]. Furthermore, the compression process is carried out in two steps with intercooling, which further enhances the COP and reduces the thermal stress on the compressors due to lower temperatures [164, 168]. The temperature operating range of the FAME column reboiler is around 295 °C. We thus employ an internal electric coil with a power-to-heat efficiency of 99 % as a suitable heating source for such temperature values [166, 169, 170].

Transesterifier

To regulate the temperature inside the transesterifier, its jacket medium circulates through an external loop, with valves controlling the flow of hot or room-temperature water, as well as purging, depending on the desired heating or cooling mode. Heating is achieved using an electric coil, so the electrical power consumption of the transesterifier is attributed to the heating mode only. We model this by applying complementarity constraints (CCs) as follows:

$$\dot{Q} = \dot{Q}_\mathrm{h} - \dot{Q}_\mathrm{c}\,, \tag{3.1a}$$

$$\dot{Q}_\mathrm{c} \cdot \dot{Q}_\mathrm{h} = 0\,, \quad \dot{Q}_\mathrm{c} \geq 0\,, \quad \dot{Q}_\mathrm{h} \geq 0\,, \tag{3.1b}$$

where $\dot{Q}_\mathrm{c}$ and $\dot{Q}_\mathrm{h}$ are the cooling and heating power demand, respectively. The overall power demand $\dot{Q}$ depends on the process inputs and variables. We model the external loop of the transesterifier jacket medium by a heat exchanger through which the jacket medium changes its temperature by ΔT_Jacket. We thus control the cooling or heating modes via a single control loop with one MV [1].

Using (3.1b) to model the transesterifier heating duty in optimization results in mathematical programs with CCs, which are challenging for NLP solvers [171, 172]. To allow for the use of standard NLP solvers and DAE integrators, we thus reformulate (3.1b), using the Fischer-Burmeister function with the smoothing term ϵ [172, 173], to a smooth nonlinear complementary problem (NCP) function as follows:

$$\dot{Q}_\mathrm{c} + \dot{Q}_\mathrm{h} \coloneqq \sqrt{\dot{Q}_\mathrm{c}^2 + \dot{Q}_\mathrm{h}^2 + \epsilon}\,. \tag{3.2}$$

This NCP function is equivalent to an equality path constraint that can be incorporated directly into the integrator and solved along with the DAE system of the process model when using sequential optimization methods, unlike full discretization methods [172, 174]. In this work, we use single-shooting [54, 148] as a direct sequential approach to solve the implemented DO problems. Without the smoothing term ϵ, (3.2) leads to a nonsmooth DAE system, requiring special treatment for integration and sensitivity analysis. The value

of ϵ should be sufficiently small to ensure accurate convergence of the DAE system to the exact solution, yet not overly small impeding the NLP solver's ability to explore the search space beyond the initial guess [172, 175].

3.3. Process Optimization for Flexible Operation Using Buffer Tanks

In this section, we present the considered process configurations and optimizations for incorporating buffer tanks to enable flexible dynamic operation, along with the benchmark standard SS operation. We first provide the general mathematical formulations of the implemented DO problems. Afterward, we discuss the approach for solving the SS optimization problem for the benchmark process design, as well as the DO considered for different flowsheet configurations using the intermediate and final buffer tanks. For all considered optimizations, we provide the buffer tanks and process units included, process modifications, and all controls and constraints in Table 3.1.

3.3.1. Mathematical Formulation

Based on the modeling approach and the smooth approximation (3.2) for the transesterifier heating duty, the developed process models for all considered optimizations are smooth DAE systems of index-1. Accordingly, we solve, in all considered process configurations, DO problems on a finite time horizon $\mathcal{T} = [t_0, t_f]$ of the following form:

$$\min_{\mathbf{u},\mathbf{x},\mathbf{y}} \ \Phi(\mathbf{u}, \mathbf{x}, \mathbf{y}, p_{\text{el}}, \mathbf{v}) = \int_{t_0}^{t_f} -L(\mathbf{u}(t), \mathbf{x}(t), \mathbf{y}(t), p_{\text{el}}(t), \mathbf{v})\, \mathrm{d}t\,, \tag{3.3a}$$

$$s.t. \quad \mathbf{M}\dot{\mathbf{x}}(t) = \mathbf{f}(\mathbf{u}(t), \mathbf{x}(t), \mathbf{y}(t), p_{\text{el}}(t), \mathbf{v}),\ \forall t \in \mathcal{T}\,, \tag{3.3b}$$

$$\mathbf{0} = \mathbf{g}(\mathbf{u}(t), \mathbf{x}(t), \mathbf{y}(t), p_{\text{el}}(t), \mathbf{v}), \forall t \in \mathcal{T}\,, \tag{3.3c}$$

$$\mathbf{0} = \mathbf{h}(\mathbf{x}(t_0), \mathbf{y}(t_0), p_{\text{el}}(t_0), \mathbf{v})\,, \tag{3.3d}$$

$$\mathbf{0} \geq \mathbf{c}(\mathbf{u}(t), \mathbf{x}(t), \mathbf{y}(t), p_{\text{el}}(t), \mathbf{v}),\ \forall t \in \mathcal{T}\,, \tag{3.3e}$$

where $\mathbf{f} : \mathcal{X} \to \mathbb{R}^{n_x}$ and $\mathbf{g} : \mathcal{X} \to \mathbb{R}^{n_y}$ describe the DAE system of the process model with the non-singular and constant matrix $\mathbf{M} \in \mathbb{R}^{n_x \times n_x}$, while $\mathcal{X} := \mathbb{R}^{n_x} \times \mathbb{R}^{n_y} \times \mathbb{R}^{n_u} \times \mathbb{R} \times \mathbb{R}^{n_v}$. The initial conditions are indicated by $\mathbf{h} : \mathbb{R}^{n_x} \times \mathbb{R}^{n_y} \times \mathbb{R} \times \mathbb{R}^{n_v} \to \mathbb{R}^{n_x}$, and $\mathbf{c} : \mathcal{X} \to \mathbb{R}^{n_c}$ represents the path and endpoint constraints. We denote the control, state, and algebraic variables by $\mathbf{u} : \mathcal{T} \to \mathbb{R}^{n_u}$, $\mathbf{x} : \mathcal{T} \to \mathbb{R}^{n_x}$, and $\mathbf{y} : \mathcal{T} \to \mathbb{R}^{n_y}$, respectively. The predefined time-variant parameter, which is the electricity prices, is given by $p_{\text{el}} : \mathcal{T} \to \mathbb{R}$, while $\mathbf{v} : \mathcal{T} \to \mathbb{R}^{n_v}$ are the predefined time-invariant parameters, which are the production rate demands and material prices. The initial and final times are denoted by $t_0 \in \mathbb{R}$ and $t_f \in \mathbb{R}$, respectively. The objective function Φ generally consists of the operating profit $L : \mathcal{X} \to \mathbb{R}$, but depending on the considered optimization case, L can consist of the operating costs only or the power consumption instead of the cost. In the following sections, we define L for each of the considered process configurations and the corresponding optimization problems.

Table 3.1.: Summary of the included buffer tanks and units, process modifications, control variables, and operational constraints for the implemented process configurations. Due to the thermal degradation limits of biodiesel and glycerol products, the maximum temperatures in the FAME and glycerol column reboilers are 300 °C and 150 °C, respectively. The maximum temperature changes of the transesterifier jacket medium ΔT_{Jacket} are limited to ±10 °C. Time-variant is indicated by TV. We denote by LL and EC the liquid levels and equality constraints, respectively. Purities are in kg/kg.

	OptSS	FOwFinal-Tank-CO	FOwInter-Tank-CO	FOwInter-Tank-DO
Additional process units and modifications				
FinalTankB and FinalTankG	–	✓	✓	✓
InterTankRSR, InterTankB, and InterTankG	–	–	✓	✓
InterTankOil and CoolerOil	–	–	–	✓
Tearing the residual oil recycle stream	–	–	–	✓
Controls	Constant	TV	TV	TV
$\dot{n}_{\text{Oil}}$ [kmol/h]	✓	✓	✓	✓
$\dot{n}_{\text{MeOH}}$ [kmol/h]	✓	✓	✓	✓
$\dot{n}_{\text{Base}}$ [kmol/h]	✓	✓	✓	✓
$\dot{n}_{\text{TransOut}}$ [kmol/h]	✓	✓	✓	✓
ΔT_{Jacket} [K], limited to ±10 °C	✓	✓	✓	✓
$T_{\text{sp,MeOHcol}}$ [K]	✓	✓	✓	✓
$T_{\text{sp,FAMEcol}}$ [K], upper bound of 300 °C	✓	✓	✓	✓
$T_{\text{sp,GLYcol}}$ [K], upper bound of 150 °C	✓	✓	✓	✓
$\dot{n}_{\text{InterTankRSR}}$ [kmol/h]	–	–	✓	–
$\dot{n}_{\text{InterTankB}}$ [kmol/h]	–	–	✓	✓
$\dot{n}_{\text{InterTankG}}$ [kmol/h]	–	–	✓	✓
Path and endpoint constraints				
Transesterifier LL [m]	✓	✓	✓	✓
FinalTankB and FinalTankG LL [m]	–	✓	✓	✓
InterTankRSR, InterTankB, and InterTankG LL [m]	–	–	✓	✓
InterTankOil LL [m]	–	–	–	✓
InterTankRSR content purities	–	–	–	✓
Path constraints				
Decanter and neutralizer LL [m]	✓	✓	✓	–
Columns: reboilers, distillate drums, and trays LL [m]	✓	✓	✓	✓
EN 14214 [122] biodiesel purities	✓	✓	✓	✓
99 wt% glycerol purity	✓	✓	✓	✓
Biodiesel production demand [kg/h] (EC)	✓	✓	✓	✓
Glycerol production demand [kg/h] (EC)	✓	✓	✓	✓
InterTankRSR outlet [kg/h] (EC)	–	–	–	✓
InterTankOil outlet [kg/h] (EC)	–	–	–	✓
Endpoint constraints				
Transesterifier content purities	–	✓	✓	✓
InterTankRSR, InterTankB, and InterTankG content purities	–	–	✓	✓

3.3.2. Steady-State Optimization via Dynamic Terminal-State Optimization

We consider here the base case that we use for comparison purposes, which corresponds to a standard process design leading to a SS optimization. In this process configuration,

all buffer tanks in the flowsheet in Figure 3.2 are excluded. All controls, which are depicted by the blue arrows, are considered except for the `InterTankRSR`, `InterTankB`, and `InterTankG` outlet molar flow rates ($\dot{n}_{\text{InterTankRSR}}$, $\dot{n}_{\text{InterTankB}}$, and $\dot{n}_{\text{InterTankG}}$, respectively). Also, the CoolerOil unit and the flow rate equality constraints after `InterTankRSR` and `InterTankOil` are excluded here. We denote by OptSS (optimal steady-state operation) the SS optimization case.

We aim to determine an optimal constant operation benchmark that produces the required production rates of biodiesel and glycerol, and satisfies all operational requirements while minimizing power consumption and material costs and maximizing product revenues. To achieve this, we could set the right-hand side of (3.3b) of the DAE system in (3.3) equal to zero and solve the resulting SS optimization problem. However, we use here an alternative approach via optimizing the dynamic terminal-state of the DAE system, which is obtained by integrating for an extended period and using constant control variables. This approach is considered more robust in the literature, e.g., refs. [176] and [131]. Therefore, the controls $\mathbf{u}$ in (3.3) are considered constant in the SS optimization. Moreover, p_{el} is excluded from (3.3a) since the results are independent of any specific electricity price profile. Instead, a fixed price $p_{\text{el, fixed}}$ is utilized, representing the average electricity price over the considered time horizon. In this case, L is defined as:

$$L(t) = \sum_{i=1}^{n_{\text{Prod}}} \dot{m}_i(t) v_i - p_{\text{el, fixed}} W_{\text{Tot}}(t) - \sum_{j=1}^{n_{\text{Feed}}} \dot{m}_j(t) v_j \,, \tag{3.4a}$$

$$W_{\text{Tot}}(t) = W_{\text{Trans}}(t) + W_{\text{Mc}}(t) + W_{\text{Fc}}(t) + W_{\text{Gc}}(t) + W_{\text{WMc}}(t) \,, \tag{3.4b}$$

where $\dot{m}_i$ and $\dot{m}_j$ indicate the production and consumption rates of products and feeds, with the corresponding specific material prices, denoted by v_i and v_j, respectively. The n_{Prod} products are biodiesel, glycerol, solids, and purified methanol by the water-methanol column (cf. Figure 3.2 and Section 3.2.2.5). The n_{Feed} feeds are vegetable oil, methanol, base mixture, and acid mixture. The total power demand is given by W_{Tot}. The power demands of the transesterifier, methanol, FAME, glycerol, and water-methanol columns are indicated by W_{Trans}, W_{Mc}, W_{Fc}, W_{Gc}, W_{WMc}, respectively.

We use a final time t_f of two days, which is sufficiently large for the DAE system to obtain a new quasi SS, starting at the initial DAE state defined by (3.3d). We selected the time horizon by forward simulation of the model, ensuring that a SS is obtained. By optimizing the terminal-state of the DAE system using constant controls, we obtain one feasible SS solution. However, there may be multiple solutions, and the found one may not necessarily be stable. Therefore, we perform a stability check by linearizing the DAE system at the found SS solution and using the indirect method of Lyapunov. We observe that all the real parts of the eigenvalues of the linearized system matrix are negative, indicating that the DAE system is stable at the found SS solution.

3.3.3. Process Configurations and Dynamic Optimization for Flexible Operation

To enable flexible process operation, we add final and/or intermediate buffer tanks. We aim to dynamically operate the process by solving (3.3) for the different buffer tank configurations while producing the same amount of biodiesel and glycerol as the SS operation

benchmark within the considered time horizon. The controls $\mathbf{u}$ are time-variant variables, and p_{el} is kept in (3.3a). Accordingly, the operating profit L is defined as follows:

$$L(t) = \sum_{i=1}^{n_{\mathrm{Prod}}} \dot{m}_i(t) v_i - p_{\mathrm{el}}(t) W_{\mathrm{Tot}}(t) - \sum_{j=1}^{n_{\mathrm{Feed}}} \dot{m}_j(t) v_j \,. \tag{3.5}$$

First, we discuss the configuration of adding final buffer tanks exclusively, before moving on to the use of intermediate tanks. Furthermore, in Section 3.3.3.3, we demonstrate how intermediate buffer tanks enable the implementation of distributed optimization as an alternative to centralized monolithic approaches, potentially enhancing the computational efficiency of optimization problem solving. Additionally, flexibility potential exists not only in production rates but also in the purity of final products. In Section 3.3.3.4, we elaborate on how product purity specification can be used to achieve more process flexibility, particularly for the glycerol product.

3.3.3.1. Process Flexibilization via Final Buffer Tanks Only

As shown in Figure 3.2 and Table 3.1, we include in this case only the two final buffer tanks, namely `FinalTankB` and `FinalTankG`, in the process flowsheet. All intermediate buffer tanks are excluded here. Final buffer tanks are essential when aiming for flexible operation while simultaneously meeting specific production demands, such as biodiesel and glycerol production in our study. We solve (3.3) for this configuration, investigating the operational flexibility that can be achieved through the use of final buffer tanks only. The operating profit L is defined here as in (3.5). We represent the optimization for this case as FOwFinalTank-CO (flexible operation with final tanks - centralized optimization).

We impose additional endpoint constraints for the liquid levels in `FinalTankB` and `FinalTankG` (cf. Table 3.1) to guarantee that the optimizer does not exploit the initial holdups in the tanks to satisfy production demands. Therefore, the liquid levels have to be maintained at their initial values at the end of the time horizon. Our analysis aims to investigate the production flexibility of both biodiesel and glycerol products while ensuring that their respective demands are met.

3.3.3.2. Process Flexibilization via Final and Intermediate Buffer Tanks

Various unit operations have different potentials for flexibility, depending on their operational requirements and positions in the process. For instance, a unit operation's ability to be flexible in production, and thus in its power consumption, may be limited by downstream processes. In particular, liquid level limits in downstream processes may impede the production flexibility potentials of upstream processes. As a solution, the incorporation of additional intermediate buffer tanks can decouple the dynamics between process parts and consequently render full exploitation of the production flexibility of the overall process.

In this work, the output production rate of the methanol column bottom is restricted by the liquid level limits in the downstream processes, notably, the decanter and columns. Thus, we incorporate the buffer tank `InterTankRSR` to realize the full potential of production flexibility for the methanol column (cf. Figure 3.2 and Table 3.1). Consequently, the outlet flow rate of `InterTankRSR` is a new control variable in the DO problem.

Furthermore, to enable varying the production rates through the other downstream power-consuming units, namely the FAME and glycerol columns, we include the buffer tanks, `InterTankB` and `InterTankG`, respectively. As a result, the outlet flow rates of these tanks need to be manipulated, making them new controls in the DO problem (cf. Figure 3.2 and Table 3.1). For all intermediate buffer tanks, we add endpoint constraints for their liquid levels as well as for the purities of their content species (cf. Table 3.1) to ensure that the state at the final time is equal to its initial value.

We denote the optimizer that solves (3.3), where the operating profit L is defined as in (3.5), for the entire process including all intermediate buffer tanks by FOwInterTank-CO (flexible operation with intermediate and final tanks - centralized optimization). In this case, the convergence of the NLP solver is sensitive to the initial guess and the scaling of controls and constraints. In DO problems with large-scale DAE systems, the optimization algorithm is particularly susceptible to encountering ill-conditioning issues, which adversely impact convergence. Utilizing distributed optimizers for different parts of the process leads to DO problems with smaller DAE systems, thus, reducing the number of variables that the user needs to initialize and scale. Consequently, the optimization algorithm is less prone to non-convergence and is computationally more efficient.

3.3.3.3. Process Flexibilization via Buffer Tanks and Distributed Optimization

In addition to fully exploiting production flexibility, the added intermediate buffer tanks can also facilitate the implementation of multiple distributed optimizers for different process parts, rather than relying on a centralized monolithic optimizer for the entire process. Given the high computational cost and convergence challenges associated with large-scale DO problems, we propose another optimization strategy for employing intermediate buffer tanks. We introduce an additional buffer tank for the residual oil recycle (cf. Figure 3.2 and Table 3.1), and employ three distributed optimizers instead of a centralized monolithic one.

By introducing an additional buffer tank, `InterTankOil`, and the water-operating cooler, CoolerOil, for the residual oil recycle, we fix its flow rate and temperature, thereby, allowing to tear this recycle stream (cf. Figure 3.2 and Table 3.1). Consequently, we can decouple the upstream processes of the `InterTankRSR` tank from its downstream processes. However, to enable this, we need additional constraints. Specifically, we constrain the outlet flow rates of `InterTankRSR` and `InterTankOil` tanks to fixed flow rates and impose path constraints on the species purities of the `InterTankRSR` outlet (cf. Table 3.1). Therefore, we can implement the three optimizers FOforRSR-DO, FOforB-DO, and FOforG-DO (flexible operation for the reaction-separation-recycle/biodiesel/glycerol process - distributed optimization), as shown in Figure 3.2. Collectively, we refer to them as FOwInterTank-DO (flexible operation with intermediate and final tanks - distributed optimization). This approach involves solving three DO problems of (3.3), with smaller DAE systems, leading to fewer non-convergence issues and less computational cost. However, it is important to note that these additional constraints are restrictive. Notably, fixing the flow rate of the residual oil recycle stream results in less efficient material consumption of the oil feed. This increases the overall material costs compared to the FOwInterTank-CO case where we have full degrees of freedom. In Section 3.6, we examine whether these restrictions are

significant. The operating profits for the three problems are given by:

$$L_{\text{FOforRSR-DO}}(t) = -p_{\text{el}}(t)\left(W_{\text{Trans}}(t) + W_{\text{Mc}}(t)\right) - \sum_{j=1}^{n_{\text{Feed, FOforRSR-DO}}} \dot{m}_j(t) v_j \,, \tag{3.6a}$$

$$L_{\text{FOforB-DO}}(t) = \dot{m}_{\text{B}}(t) v_{\text{B}} - p_{\text{el}}(t) W_{\text{Fc}}(t) \,, \tag{3.6b}$$

$$L_{\text{FOforG-DO}}(t) = \sum_{i=1}^{n_{\text{Prod, FOforG-DO}}} \dot{m}_i(t) v_i - p_{\text{el}}(t)\left(W_{\text{Gc}}(t) + W_{\text{WMc}}(t)\right) \,, \tag{3.6c}$$

such that the acid feed is not included in $L_{\text{FOforRSR-DO}}$; B indicates biodiesel; and the products in $L_{\text{FOforG-DO}}$ are glycerol, solids, and purified methanol by the water-methanol column.

It is worth noting that the additional `InterTankOil` serves the sole purpose of facilitating the decoupling of process parts and enabling distributed optimizations. Consequently, it does not provide any additional flexibility benefits for the centralized monolithic optimization case. In our process, the two recycle streams from the methanol and FAME columns are already buffered within the transesterifier, rendering intermediate buffer tanks unnecessary for these streams. Furthermore, the presence of `InterTankOil` is a practical necessity. Without it, achieving the decoupling of various process sections (by decoupling their dynamics) and fixing the residual oil recycle stream would be unattainable. Essentially, the considered distributed optimization approach relies on the existence of `InterTankOil`.

The distributed optimization approach we employ is based on a sequential algorithm, wherein only the downstream processes are influenced by the upstream ones, and not vice versa. In a sequential algorithm, subproblems are addressed in a predetermined order. After the optimization of the initial subproblem is completed, the results are shared with the subsequent subproblems. Subsequent subproblems are constrained by the fixed solutions obtained from the previous subproblems. Additionally, we utilize independent, non-cooperative algorithms, where each subproblem seeks to minimize an individual cost function, focusing solely on its specific objective. In our case, FOforRSR-DO remains unaffected by the output of FOforB-DO due to the fixed recycle stream of residual oil. In contrast, both FOforB-DO and FOforG-DO receive as inputs the outlet streams determined by FOforRSR-DO. Additionally, FOforB-DO and FOforG-DO are concurrently addressed once FOforRSR-DO is finalized. As a result, the utilization of parallel computing for solving FOforB-DO and FOforG-DO holds the potential for significant benefits, particularly when considering the real-time application of optimal control strategies in a moving-horizon fashion, such as MPC.

3.3.3.4. Flexible Purity Production

Enforcing the purity constraints of the final products at the outlet streams of the buffer tanks, `FinalTankB` and `FinalTankG`, enables the flexibilization of the produced product purities at their inlet streams. Specifically, a higher degree of freedom is given to the optimizer to vary the purity at the buffer tank inlet streams while satisfying its requirements at the outlet side. Producing higher purities in distillation columns is associated with higher power consumption. As a result, flexibilizing the produced purities of biodiesel and glycerol products leads to additional savings in energy costs. Thus, we impose the required purity limits for both biodiesel and glycerol products at the outlet streams of the

corresponding final buffer tanks. However, flexibility in purity production is more significant when having purity limits for a single species only. That is the case for the glycerol product in our study, where we only control glycerol species purity. In contrast, there are, practically, purity limits for FAME, methanol, water, glycerol, and monoolein for the biodiesel product.

3.4. Operational Scenario

Here, we introduce the considered demand-response scenario for all optimization cases, that is, how we define $p_{el}(t)$ and $\mathbf{v}$. We conduct simulations over a time horizon of one day, during which constant production demands of 20 t/h for biodiesel and 2.12 t/h for glycerol are required. We use historical electricity price data from the German day-ahead spot market for September 3, 2022 [177], which is depicted in Figure 3.3. We use constant prices for raw materials and final products, which are provided in Table B.1 in Appendix B. For all DO problems, we discretize the control variables at an equidistant interval of one hour, while the constraints are discretized at 30-minute intervals.

3.5. Implementation

We solve all optimization problems to local NLP convergence with direct single shooting [54, 148] using our open-source framework DyOS [53]. Using NIXE Is eXtrapolated Euler (NIXE) [178] as a DAE integrator and Sparse Nonlinear OPTimizer (SNOPT) [179] as an NLP, the DO problems are solved sequentially. The Modelica model is coupled to DyOS as a FMU [180] generated by Dymola [142]. As FMU only supports ODEs, Dymola performs numerical reduction and symbolic reformulation of the DAE system to provide an FMU. In addition, we use Dymola for model linearization and for calculating the eigenvalues of the linearized system matrix. We set the DAE integrator, NLP feasibility, and optimality tolerances to 10^{-4}.

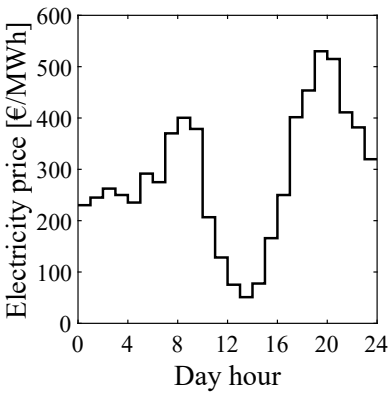

Figure 3.3.: German day-ahead electricity prices for September 3, 2022 [177].

3.6. Results and Discussion

We present production rates and the total power demand results for all the considered process configurations first, before we discuss how the buffer tanks are utilized to enhance the production and, thus, power consumption flexibility. Afterward, we demonstrate how glycerol product purity can vary based on energy costs. We also evaluate the economic performance of the considered optimizations and compare them with the SS operation benchmark OptSS. Lastly, we compare the computational performance of FOwInterTank-DO and FOwInterTank-CO. We provide additional results in Section B.3 in Appendix B, including profiles for all controls, production rates, tank levels, and product purities.

3.6.1. Production Rate and Power Demand

The biodiesel production rates are presented in Figure 3.4a for all considered process configurations. We observe that all DO optimizations, as compared to OptSS, enable production flexibility based on electricity prices. We see how the production rate profiles are opposite to that of the electricity prices. The DO optimizers promptly increase the production rates to move away from the nominal starting point due to lower electricity prices during this period. Subsequently, the production rates are adjusted according to prices to optimize the operating profit while adhering to operational constraints, particularly level limits. The intermediate buffer tanks provide significant additional flexibility, as evident from the profiles of FOwInterTank-CO and FOwInterTank-DO compared to that of FOwFinalTank-CO. For instance, between time periods 10 and 17, the use of intermediate tanks enables considerably higher production rates. On the other hand, FOwFinalTank-CO cannot fully leverage the low prices or always maintain production rates at minimum levels during high prices. During periods around 8, 10, and 23, FOwFinalTank-CO operates at high production rates, even exceeding the nominal rate, despite high prices. In contrast, FOwInterTank-CO and FOwInterTank-DO maintain the production rate at its minimum operating limit. In addition, the production in FOwInterTank-DO is identical to that of FOwInterTank-CO, indicating that the use of distributed optimizers rather than a centralized monolithic one has a similar flexibility potential. Moreover, by comparing the profiles of FOwFinalTank-CO with those of FOwInterTank-CO and FOwInterTank-DO, it is evident that the dynamics in the latter cases are buffered due to the intermediate buffer tanks.

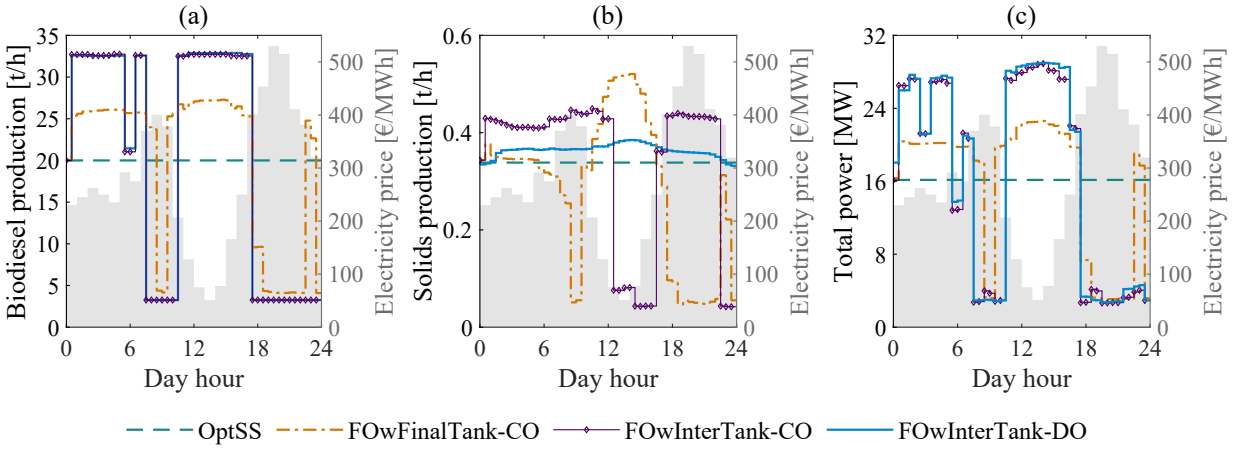

Figure 3.4.: Production rates and total power demand for all optimizers. (a): biodiesel production rates; (b): solids production rates; (c): total power consumption rates. The shaded areas illustrate the electricity price profile, which corresponds to the secondary axes.

The production rate profiles for the glycerol product and water-methanol waste (cf. Figure B.2 in Appendix B) are similar to that of biodiesel. However, during periods of increased production (e.g., between 10 and 17), more water enters the glycerol purification section for FOwInterTank-DO compared to the other DO cases. This is due to the additional purity constraints on the `InterTankRSR` outlet stream that are needed when separating the upstream processes of `InterTankRSR` from the downstream ones. Therefore, during periods of increased production, higher amounts of water-methanol waste are

produced for FOwInterTank-DO compared to FOwFinalTank-CO and FOwInterTank-CO, resulting in higher power demands for both glycerol and water-methanol columns.

Figure 3.4b shows the production rates of solids, the product obtained from the filter unit. Although the produced amount is relatively insignificant compared to the primary products, it provides insights into how the buffer tanks affect the process dynamics, especially the `InterTankRSR`. For FOwFinalTank-CO, the production rate is similar to that of biodiesel since this case only considers the final buffer tanks. However, for FOwInterTank-CO, the production rate is the opposite and follows the electricity price profile. The solids product is a downstream product directly after the `InterTankRSR`, without any buffer tanks in between. In FOwInterTank-CO, all intermediate buffer tanks have full degrees of freedom, enabling `InterTankRSR` to deliver high flow rates to the downstream buffer tanks, `InterTankB`, and `InterTankG`, during periods of high prices, and vice versa. On the other hand, `InterTankB` and `InterTankG` operate oppositely as they are responsible for achieving flexible production rates for biodiesel and glycerol, respectively, as shown in Figure 3.4a. Therefore, before the prices increase, `InterTankRSR` fills these tanks, explaining the high flow rates of the solids product during high prices. During low-price periods, the outlet stream of `InterTankRSR` decreases, allowing `InterTankRSR` to refill while `InterTankB` and `InterTankG` are not utilized as much as during high prices. Section 3.6.2 provides further elaboration on the buffer tank utilization. Conversely, for FOwInterTank-DO, the solids production rate is mostly unaffected by the flexibilization of the other process parts. When using distributed optimizers and fixing the outlet flow rate of `InterTankRSR`, all process units between `InterTankRSR` and its downstream buffer tanks, `InterTankB` and `InterTankG`, operate almost constantly. Slight variations in the production rates occur due to changes in the species purities of the `InterTankRSR` outlet. As those species purities are not fixed, the outlet streams from the decanter vary according to their degree of separation. It is noteworthy how distributed optimizers can decouple the dynamics of various process parts using intermediate buffer tanks, allowing different parts of the process to operate at varying degrees of flexibility.

The total power consumption rates are illustrated in Figure 3.4c, which resemble the biodiesel production rate profiles. Additionally, we see how FOwInterTank-CO and FOwInterTank-DO decrease the power consumption rates at periods around 3 and 6, as compared to FOwFinalTank-CO. This again demonstrates the effectiveness of intermediate buffer tanks in exploiting slight variations in prices. We provide the power demand profiles of all unit operations in Figure B.3 in Appendix B.

For the three process parts, Table 3.2 provides the production rates of their respective products, namely, the methanol column bottom, biodiesel product, and glycerol product. We compare their minimum and maximum achievable values to the corresponding values in the SS operation. This analysis enables a quantitative assessment of the extent of flexibility improvement within the examined process configurations for flexible operation. The results underscore the substantial impact of intermediate buffer tanks on augmenting production flexibility, primarily in the direction of increasing production rates. Notably, differences between configurations employing intermediate buffer tanks and that relying solely on final tanks are relatively modest when examining reductions in production rates. Moreover, we observe that the potential for reducing production rates in the three columns is similar. However, in terms of increasing production rates, the glycerol column demonstrates a notably higher degree of flexibility compared to the other columns, particularly when intermediate tanks are utilized.

Table 3.2.: Quantitative evaluation of the improved production rate flexibility across the various process configurations under consideration. For the three process parts, this assessment presents their corresponding minimum and maximum achievable production rates: the methanol column bottom, biodiesel product, and glycerol product. These values are compared with the corresponding nominal values in the SS operation. Relative differences between these values and those of the SS operation are presented in parentheses.

	OptSS	FOwFinalTank-CO		FOwInterTank-CO		FOwInterTank-DO	
Production rate [t/h]		min	max	min	max	min	max
Bottom of methanol column	24.55	4.82 (−80 %)	32.56 (33 %)	4.68 (−81 %)	45.5 (85 %)	4.71 (−81 %)	46.53 (89 %)
Biodiesel	20	4.03 (−80 %)	27.28 (36 %)	3.25 (−84 %)	32.75 (64 %)	3.24 (−84 %)	32.9 (64 %)
Glycerol	2.12	0.44 (−79 %)	2.9 (37 %)	0.44 (−79 %)	4.41 (108 %)	0.44 (−79 %)	4.41 (108 %)

3.6.2. Buffer Tank Levels

The liquid levels and controls of `InterTankRSR`, `InterTankB`, and `FinalTankB` in Figure 3.5 demonstrate how the final and intermediate buffer tanks enable high degrees of production flexibility. In Figure 3.5a, `FinalTankB` levels increase when electricity prices are low and decrease otherwise. The tank holdup is utilized during high-price periods to ensure that the required biodiesel demand is met, despite the decrease in production rates (Figure 3.4a). The changes in the levels are steeper for FOwInterTank-CO and FOwInterTank-DO than for FOwFinalTank-CO, highlighting the additional flexibility that intermediate buffer tanks provide.

For the glycerol product, the profiles for `FinalTankG` (cf. Figure B.4 in Appendix B) resemble those of `FinalTankB`. In contrast, `InterTankB` (Figure 3.5c) or `InterTankG` (cf. Figure B.4 in Appendix B) exhibit the opposite behavior of final tanks. These intermediate tanks supply the required flow rates for downstream units to operate at the desired capacity. Therefore, they are utilized during low-price periods and filled during high-price periods. For example, during the period between 10 and 17, `InterTankB` is used to operate at high outlet flow rates (Figure 3.5e) so that the FAME column operates at maximum capacity. Consequently, the levels in `InterTankB` decrease while they increase in `FinalTankB`.

Unlike `InterTankB` or `InterTankG`, `InterTankRSR` is utilized similarly to the final tanks. It is filled during low-price periods and utilized otherwise (Figure 3.5b). `InterTankRSR` fills `InterTankB` and `InterTankG` before low-price periods so that the latter tanks are utilized during high-price periods. This is evident from the `InterTankRSR` control variable profile (only in the FOwInterTank-CO case), which shows high flow rate values during high-price periods and vice versa (Figure 3.5d).

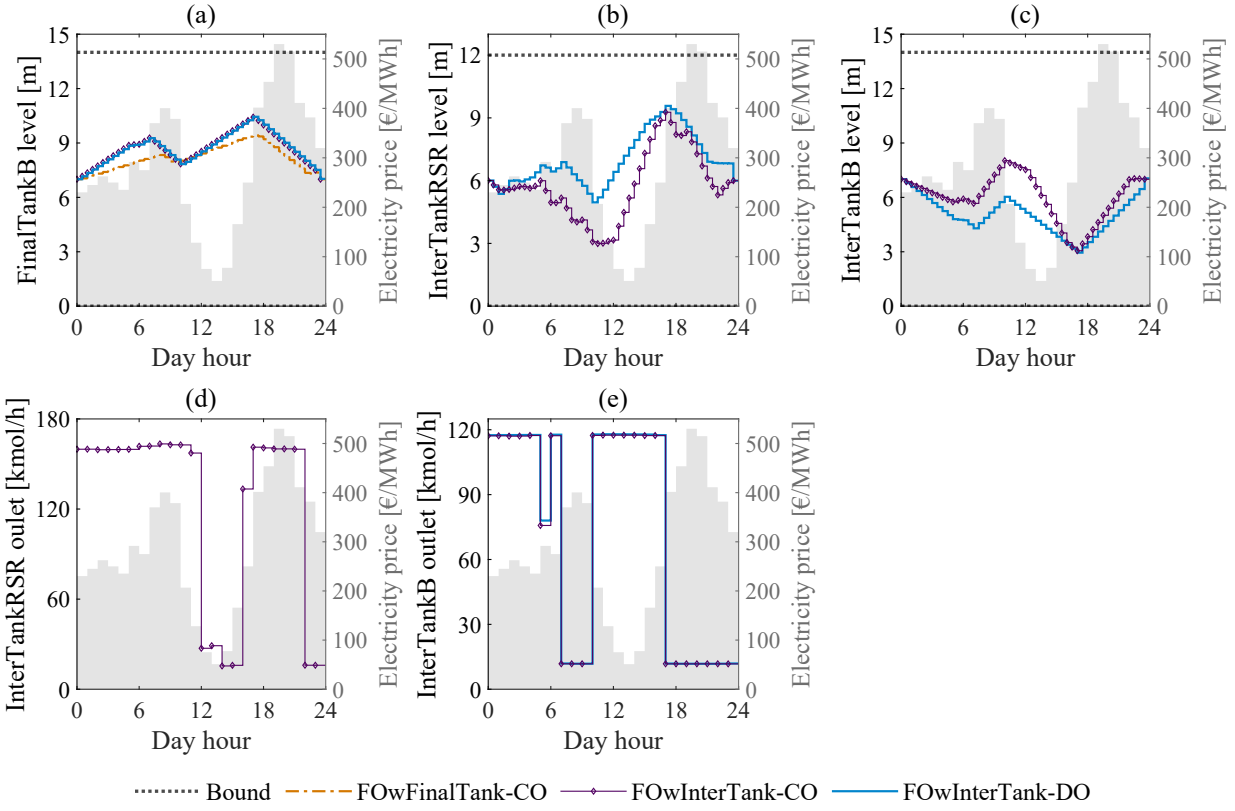

Figure 3.5.: (a), (b), and (c) show the liquid levels in `FinalTankB`, `InterTankRSR`, and `InterTankB`, respectively. The control variables for `InterTankRSR` and `InterTankB`, which are the outlet flow rates, are shown in (d) and (e), respectively. For FOwInterTank-DO, the `InterTankRSR` outlet flow rate is an equality constraint. Therefore, only FOwInterTank-CO has it as a control variable. The secondary axes correspond to the electricity prices, which are depicted in shaded areas.

3.6.3. Flexible Purity Production

Figure 3.6 shows the variability of the produced purity of the glycerol product, which enables additional operational flexibility. The figure depicts the purities before and after `FinalTankG`, as well as the reboiler temperature setpoint of the glycerol column, which is an optimization control variable. The temperature setpoints increase during low-price periods and decrease otherwise for all DO cases (Figure 3.6a), resulting in added power demand flexibility. During periods of lowest price, specifically between 10 and 17, the temperature setpoints reach their maximum allowable limit (glycerol thermal degradation limit) to maximize the power demands of the glycerol column during those periods. This leads to higher glycerol purities being produced and stored in `FinalTankG` (Figure 3.6b). On the other hand, lower purities are produced during high-price periods and mixed with the higher-purity content in `FinalTankG`, resulting in glycerol being delivered at the tank outlet with purities above the required limit (Figure 3.6c). The purity profiles at the inlet of `FinalTankG` (Figure 3.6b) mirror the reboiler temperature profiles, particularly how they decrease and then increase during the period of highest prices, i.e., between 17 and 24. During this period, the purities decrease to below 97.5 wt% (for FOwInterTank-DO), while they remain above the minimum limit at the `FinalTankG` outlet (Figure 3.6c).

Furthermore, we observe that the purities at the `FinalTankG` outlet around 17 are not at the minimum limit (Figure 3.6c), in contrast to other periods. Just before this period, i.e., between 10 and 17, the purities at the inlet reach their highest operational limit (due to temperature limit), resulting in slightly higher purities at the outlet during the period around 17. Consequently, during the next period when the prices are high (between 17 and 24), the tank inlet purities can be minimized while maintaining the outlet purities above the minimum limit.

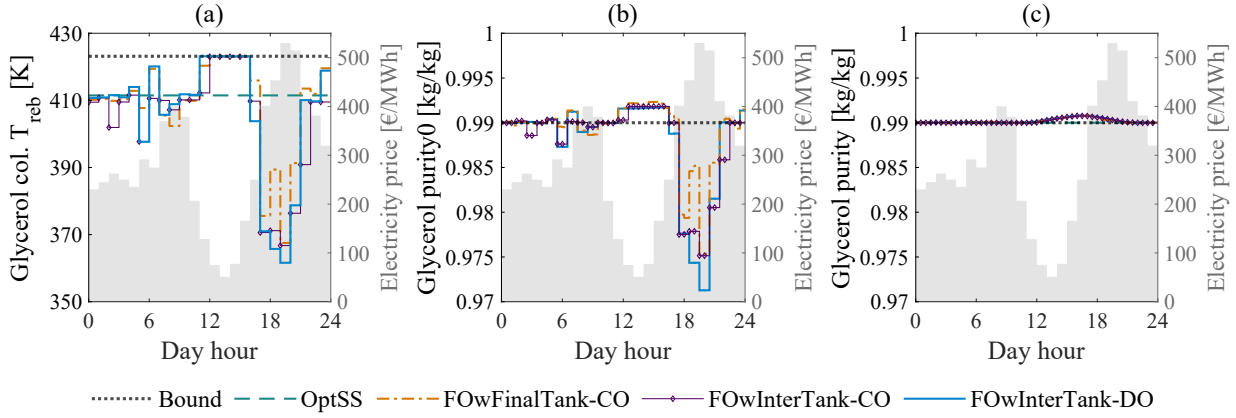

Figure 3.6.: (a) shows the temperature setpoint of the glycerol column reboiler, which is an optimization control variable. (b) and (c) illustrate the glycerol purity in the inlet and outlet streams of `FinalTankG`, respectively. It can be observed from (b) that lower purities are produced during high-price periods and vice versa, while the delivered product purity (in (c)) meets the minimum limit of 99 wt%. The profile of the electricity prices is represented by the shaded area, which corresponds to the secondary axis.

3.6.4. Economic Evaluation

In Table 3.3, we present the total operating profits, energy costs, and material costs for all optimization case studies. The energy costs for three parts of the process are provided: RSRprocess (reaction-separation-recycle process), which includes the transesterifier and methanol column, Bprocess (biodiesel process) for the FAME column, and Gprocess (glycerol process) for the glycerol and water-methanol columns. Additionally, all costs and profits for the DO strategies are given relative to the SS optimization benchmark.

We find that FOwFinalTank-CO incurs 20 % less total energy cost relative to OptSS, while FOwInterTank-CO and FOwInterTank-DO result in 29 % and 28 % less total energy cost, respectively. The total energy cost savings are similar for the implementation of distributed optimizers FOwInterTank-DO compared to the centralized monolithic FOwInterTank-CO. However, there are differences in the savings for different process parts, particularly for the RSRprocess and Gprocess. We observe that tearing the recycle oil stream and fixing its flow rate, while imposing purity limits on the `InterTankRSR` outlet and also fixing its flow rate, leads to less power consumption in the methanol column for FOwInterTank-DO compared to FOwInterTank-CO. However, as explained in Section 3.6.1, more water entering the glycerol purification process for FOwInterTank-DO results in additional power consumption in the glycerol and water-

methanol columns. This explains the higher energy cost incurred for FOwInterTank-DO compared to FOwInterTank-CO and FOwFinalTank-CO.

Table 3.3.: Total operating profit, and energy and material costs for each optimizer. Energy costs for different parts of the process are given. RSRprocess energy includes the transesterifier and the methanol column power demands. Bprocess energy indicates the FAME column power demand, while Gprocess energy indicates that of the glycerol and downstream water-methanol columns. The economic performance (savings) relative to the SS operation case, OptSS, is given in parentheses.

	OptSS	FOwFinalTank-CO	FOwInterTank-CO	FOwInterTank-DO
RSRprocess energy cost [k€]	11.4	10.4 (9.3 %)	9 (22 %)	8.2 (28 %)
Bprocess energy cost [k€]	77.8	64.6 (17 %)	56.4 (28 %)	56.5 (27 %)
Gprocess energy cost [k€]	22.3	14.4 (36 %)	14.4 (36 %)	16.1 (28 %)
Total energy cost [k€]	111.5	89.4 (20 %)	79.8 (29 %)	80.8 (28 %)
Total material cost [k€]	563.9	556.8 (1.3 %)	556.3 (1.4 %)	562.9 (0.2 %)
Total profit [k€]	639.8	667 (4.3 %)	678.6 (6.1 %)	672.4 (5.1 %)

A comparison of the RSRprocess energy costs for FOwFinalTank-CO with that of FOwInterTank-DO and FOwInterTank-CO reveals significant differences in terms of savings, emphasizing the additional operational flexibility that `InterTankRSR` offers for the methanol column. In the case of Bprocess, the savings for both FOwInterTank-CO and FOwInterTank-DO are significantly higher than FOwFinalTank-CO, indicating the added flexibility of `InterTankRSR` when combined with `InterTankB`. It is worth noting that the intermediate tanks do not lead to additional energy savings for the Gprocess, as demonstrated by the comparison of energy costs between FOwFinalTank-CO and FOwInterTank-CO.

We find only slight savings in material costs for the DO cases compared to the SS benchmark, which is expected since the material prices remain unchanged. However, when comparing FOwInterTank-DO to FOwFinalTank-CO or FOwInterTank-CO, we observe fewer material cost savings for FOwInterTank-DO due to the restrictive consideration of tearing the recycle oil stream and fixing its flow rate. Fixing the recycle stream results in less efficient utilization of the expensive oil raw material, which is also the process TPM. Thus, the additional material cost incurred for FOwInterTank-DO can be explained by the less efficient use of the oil feed.

After analyzing the total operating profits, it is evident that material costs exceed energy costs, resulting in considerably lower additional profits by an order of magnitude, as compared to energy costs savings. We also observe that FOwInterTank-DO results in 1 % less additional profit (relative to OptSS) compared to FOwInterTank-CO. In Section 3.6.5, we compare the computational costs and comment on the NLP solver convergence for FOwInterTank-CO and FOwInterTank-DO assessing the significance of this 1 % reduction in savings.

Furthermore, it is noteworthy that when undertaking economic comparisons between the considered configurations, the inclusion of buffer tanks may influence the overall cost, particularly when factoring in the investment cost associated with these tanks. The process designs for configurations considering flexible operation differ from the SS counterpart

solely by the inclusion of the buffer tanks. Moreover, these process designs exhibit differences among themselves based on the incorporation of these tanks. Consequently, a more comprehensive analysis, encompassing the capital costs involved in integrating these buffer tanks, might be necessary for a more precise comparison. Nevertheless, it is important to emphasize that such storage tanks are typically cost-effective and easily integrable into chemical plants, making the anticipated payback period for this investment relatively short.

3.6.5. Solution Times

We provide the CPU times required to solve the DO problems under consideration in Figure 3.7. A comparison of the solution times for FOwFinalTank-CO and FOwInterTank-CO reveals that the addition of intermediate buffer tanks and implementation of a centralized monolithic optimizer results in a 108 % increase in solution time. On the other hand, the total solution time for FOwInterTank-DO is 85 % and 93 % less than that of FOwFinalTank-CO and FOwInterTank-CO, respectively, highlighting the effectiveness of implementing distributed optimizers and solving DO problems with smaller-scale DAE systems in terms of computational cost. Notice that FOforRSR-DO must be solved before FOforB-DO and FOforG-DO, which are solved in parallel afterward.

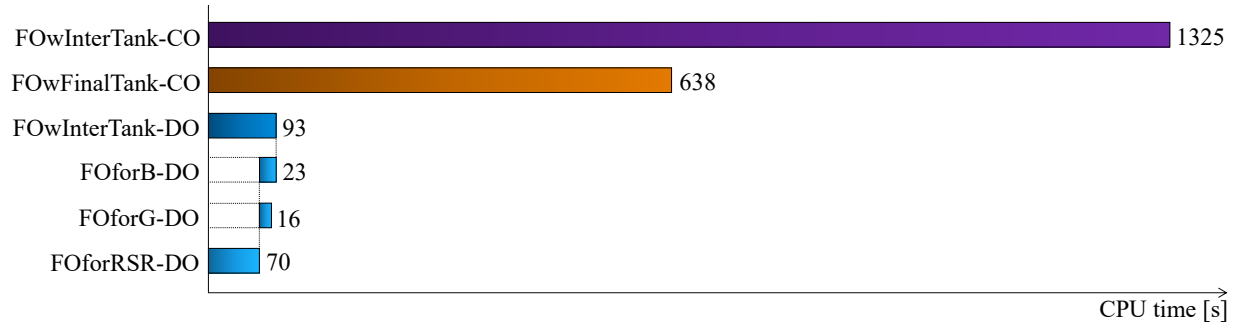

Figure 3.7.: CPU times for solving the DO problems of the considered optimizers. After solving FOforRSR-DO, FOforB-DO and FOforG-DO run in parallel. Collectively, these three optimizers are referred to as FOwInterTank-DO.

Furthermore, implementing a centralized monolithic optimizer for the entire process leads to DO problems with large-scale DAE systems. NLP convergence for such problems, particularly for FOwInterTank-CO, is highly sensitive to the initial guess and variable scaling, resulting in ill-conditioning issues and consequently non-convergence. However, for the FOwInterTank-DO distributed optimizers, the NLP solvers converge robustly and are easier to initialize and scale due to the significantly smaller DAE systems involved in their DO problems.

Therefore, although the FOwInterTank-DO yields 1 % less addition in the total operating profit than FOwInterTank-CO, it is preferable to implement the former, especially for online applications, due to the significant reduction in solution time and the easier convergence of the NLP solvers in its DO problems.

3.7. Conclusion

We investigate the operational flexibility potential of electrified biodiesel production by proposing different process configurations using buffer tanks and solving offline DO problems. The examined process comprises reaction, separation, and recycle components, indicating the application potential of its operational flexibility for a broad range of chemical processes. By incorporating both intermediate and final buffer tanks, we fully exploit the flexibility potential of the process, leading to total energy savings of up to 29 % relative to the SS benchmark. Furthermore, we demonstrate that intermediate buffer tanks facilitate the implementation of distributed optimization, resulting in superior computational performance. Nonetheless, it is essential to acknowledge that different electricity price profiles may lead to varying energy cost savings, particularly given the considerable electricity price fluctuations in our case study. While the considered dynamic operation methods and the concept of incorporating buffer tanks for maximizing flexibility potential and facilitating distributed optimization may not directly transfer to all chemical processes, our study underscores that when electrifying chemical processes with renewable electricity, conventional SS operation may no longer be the most suitable approach. Instead, novel operational strategies based on flexibility through dynamic operation may become the new paradigm for chemical plant operations. Achieving this shift requires the use of advanced modeling and optimization techniques to implement suitable control strategies. Furthermore, reevaluating design considerations becomes crucial to enhance flexibility and fully realize the potential of dynamic operation.

It is worth noting that flexible operation can reduce the operational lifespan of process equipment and potentially lead to increased maintenance requirements. This is particularly evident in the case of mechanically-driven units, such as compressors, pumps, and valves, which may experience shorter operational lifespans. In our study, we do not consider the influence of dynamic operation on the durability of process equipment. Furthermore, we perform the sizing of process units and buffer tanks heuristically and based on literature findings. Alternatively, one could formulate these also as optimization variables/problems to be solved alongside the DO problems for flexible operation. This would involve employing stochastic programming and presents an interesting avenue for future work. Decisions regarding the sizing and configuration of process units typically demand longer time horizons than the one considered in our study. However, extending the time horizon can complicate the optimization problem significantly, rendering it intractable. In such scenarios, the utilization of stochastic programming in conjunction with distributed optimization, while considering a select set of representative electricity price profiles for a specific time period, could potentially provide a promising solution. Nevertheless, it is important to acknowledge that addressing this aspect might entail handling considerably large problem sizes due to the necessity of considering multiple operational scenarios, particularly for electricity price profiles.

Although our current process design lacks consideration of HI, it is important to note that the integration of heat across multiple units is common in complex and modern chemical plants. Notably, the considered process incorporates three distinct distillation columns, each with specific energy duties, creating an opportunity for HI among these columns. Such integration would increase the overall interconnectivity of the process, influence the degrees of freedom available for optimization, and introduce added complexity to the implementation of the distributed optimization approach. To address these aspects,

Chapter 4 investigates the implications of HI on process flexibility, particularly exploring the degrees of freedom available to optimization.

To electrify the process, we utilize separate heat pumps for refrigeration and heating in reboilers, multiple heat pump stages, and multistage compression, based on literature research. In light of this, future work should focus on implementing process design optimization to determine optimal structures, as well as heat pump integration.

Applying online DO for DSM, specifically eNMPC, to the considered process would greatly enhance our understanding of the real-time applicability of the proposed flexibility-oriented process design and flexibilization strategies. The use of distributed optimization promises good computational performance and should be considered for online applications. In Chapter 5 and Chapter 6, we present and apply eNMPC with distributed control to optimize the flexible operation of the process. Additionally, hierarchical control structures with optimal scheduling and lower-level tracking control can be explored as future work. Finally, in cases where optimization problems are computationally expensive and encounter convergence issues, it would be worthwhile to investigate model reduction techniques, such as incorporating surrogate models, and explore algorithm and implementation improvements.

4. Optimal Flexible Operation of Electrified and Heat-Integrated Biodiesel Production

We proceed in this chapter by further examining the offline DO stage within the modeling and optimization framework shown in Figure 1.2. As illustrated in Figure 4.1, we focus on exploring the impact of HI within the considered biodiesel production process on the degrees of freedom available for optimization. Specifically, we implement offline DO strategies while considering different process configurations for HI to assess their operational flexibility.

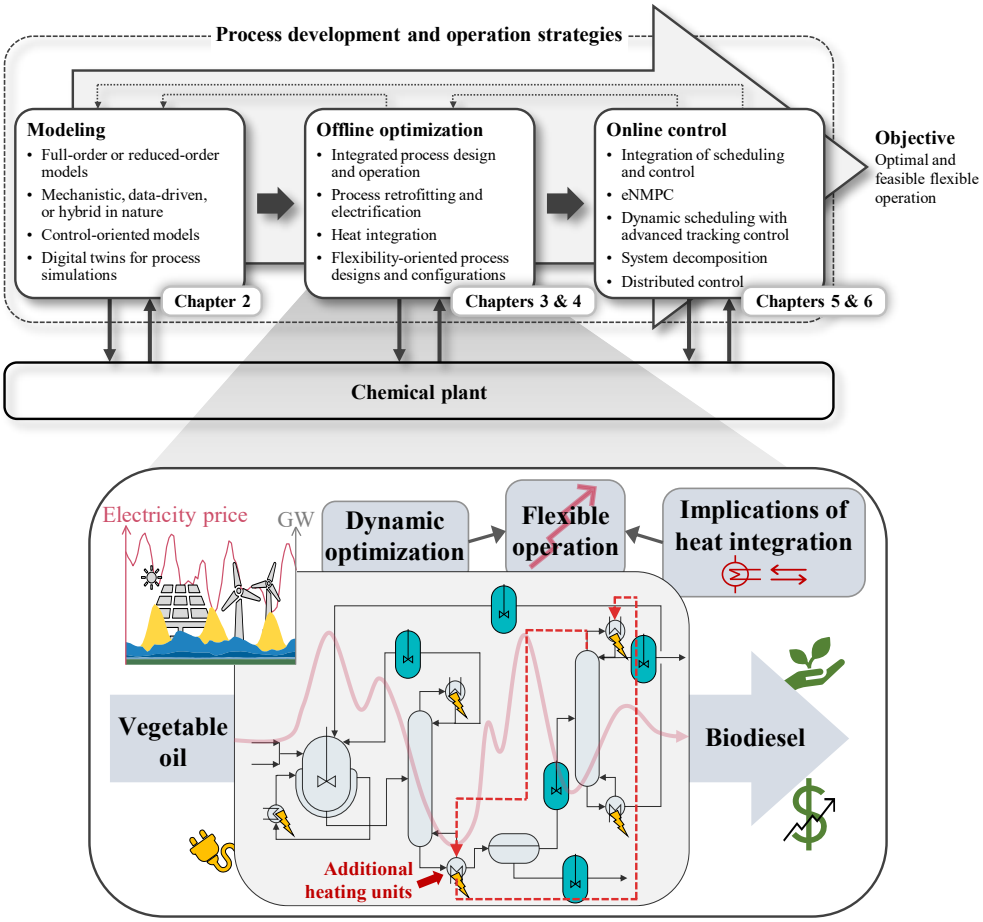

Figure 4.1.: Graphical illustration highlighting the focus of Chapter 4 within the modeling and optimization framework outlined in Figure 1.2. The chapter investigates the implications of HI on the operational flexibility of the biodiesel production process under consideration.

4.1. Introduction

In Chapter 3, we propose electrifying biodiesel production and investigate its optimal flexible operation using intermediate and final buffer tanks. We explore the operational flexibility of three process configurations and compare the outcomes of their DO strategies with those of an optimal SS operation while considering a typical demand-response scenario. Our findings underscore that, as expected, intermediate buffer tanks facilitate the full realization of process flexibility potential, leading to heightened economic performance in dynamic operations. However, this process design do not incorporate HI. The integration of heat across multiple units is a prevalent practice in complex and modern chemical plants, aiming for energy efficiency, i.e., minimal external energy supply. Despite this, the optimal flexible operation in heat-integrated chemical processes with the aid of buffer tanks remains underexplored. HI introduces additional intricacies and interdependencies among unit operations, potentially making the flexible operation more intricate and constraining the optimization options [61].

Herein, we examine how HI impacts the flexible operation of the considered biodiesel production process, particularly in terms of the degrees of freedom available for optimization. We present three different process configurations for HI. In the initial two configurations, complete HI is applied to all three distillation columns within the process. We investigate the flexible operation of the process, both with and without external heating units for the reboilers. Since these additional heating units are only relevant in the context of flexible operation, particularly concerning DSM, our objective is to assess the effect of these external heat sources on the process flexibility in dynamic operation.

Furthermore, we introduce a third configuration allowing the implementation of two distributed optimizers, each dealing with a smaller problem. This contrasts with the centralized approach used in the other configurations. Within this setup, VRC [62, 63] is applied to one column, while the other two columns are heat-integrated. This configuration stems from the potential demonstrated by distributed optimizers in terms of computational performance, as highlighted in Chapter 3. The three configurations are subsequently benchmarked against their respective SS operations, as well as against a dynamic operation of a previous configuration from Chapter 3 without HI. While our evaluation of the three configurations is based on economic objectives, the inclusion of additional units in each configuration may have varying implications for sustainability in terms of overall energy consumption and capital costs.

The structure of the chapter unfolds as follows. We begin with detailing the configurations employed for HI within the biodiesel production process. Following this, we present the formulation of the solved optimization problems before elaborating on their implementation and the operational scenario considered. Lastly, we present and discuss the findings derived from this study, before drawing our conclusions.

4.2. Biodiesel Production Application

In Chapter 2, we introduce and detail the biodiesel production process under consideration, presenting its dynamic model and making it readily accessible as open source. In Chapter 3, we explore its flexible operation for DSM, investigating different process configurations and optimization methodologies. Herein, we use the process configuration that incorporates

both intermediate and final buffer tanks and extend it to accommodate HI. Consequently, we focus only on explaining these specific configurations along with their corresponding optimization strategies.

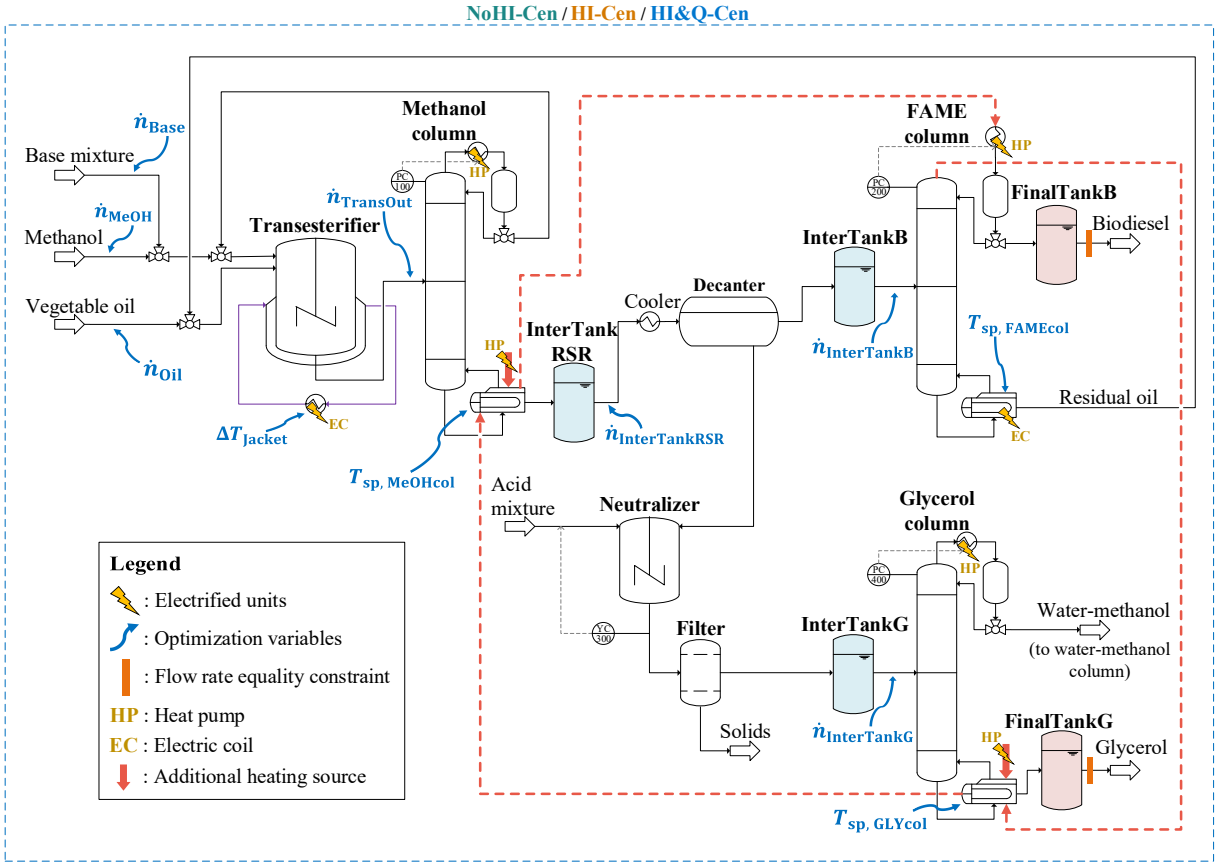

Figure 4.2.: Biodiesel process flowsheet including both intermediate and final buffer tanks and incorporating a centralized optimization approach. The configurations with full heat integration adopt this flowsheet, wherein the heat-integrated three columns are interconnected by the dashed-red streams depicted.

4.2.1. Process Configurations with Full Heat Integration

Figure 4.2 illustrates the considered process with full HI across the three distillation columns within the system. The heat exchange in the transesterifier system primarily operates in cooling mode, utilizing room-temperature water, while its electrified heating mode (cf. Section 3.2.3), if activated at all, is negligible compared to the power demand of the columns. The transesterifier is thus not considered in the HI. We provide a succinct explanation here regarding the necessity of the buffer tanks depicted, and we direct readers to Chapter 3 for more detailed description.

The potential for flexibility varies among different unit operations, determined not only by their operational limits but also by their locations within the process. To exemplify, limitations on liquid levels in downstream processes can impede the flexibility of production in upstream processes. An effective remedy involves the incorporation of intermediate

buffer tanks between distinct sections of the process, enabling the uncoupling of their dynamics and thereby facilitating the maximal utilization of overall production flexibility. In the context of this study, we introduce the buffer tank `InterTankRSR` to fully unlock the production flexibility potential of the methanol column. This is essential as the output production rate of this column is constrained by liquid level limitations in downstream processes, specifically the decanter and columns. Moreover, `InterTankB` and `InterTankG` enable variable production rates within the other downstream power-consuming units, namely the FAME and glycerol columns, respectively. Additionally, `FinalTankB` and `FinalTankG` are indispensable in enabling flexible production of both purities and flow rates while simultaneously fulfilling the demands for final products.

We investigate two distinct process configurations, both of which incorporate complete HI across the three distillation columns. The vapor outlet of the FAME column undergoes heat exchange with the bottoms of the glycerol column and subsequently the methanol column, serving as the essential heat source for evaporating their respective bottoms. We impose constraints on the temperature differences of the outlet streams of the heat exchangers, stipulating a minimal temperature difference of 10 °C. The differing element between the two configurations lies in the presence or absence of supplementary external heating sources for the reboilers of the methanol and glycerol columns. These configurations are denoted as HI-Cen and HI&Q-Cen, respectively, with the added heating sources indicated by red arrows pointing toward the reboilers (cf. Figure 4.2). The optimization variables are highlighted by arrows, wherein $T_{\mathrm{sp,MeOHcol}}$ and $T_{\mathrm{sp,GLYcol}}$ are exclusive to HI&Q-Cen configuration, acting as additional optimization variables. For both configurations, a centralized optimization approach is employed, entailing the resolution of the corresponding optimization problems articulated in Section 4.3.

4.2.2. Process Configuration with Vapor Recompression and Heat Integration

Considering the high computational demands and challenges in achieving convergence when addressing large-scale DO problems, we propose an alternative configuration for HI that allows for the use of a distributed optimization approach. In Chapter 3, we demonstrate that by introducing the buffer tank, `InterTankOil`, alongside the cooler, CoolerOil, we can fix and thus tear the residual oil recycle, as depicted in Figure 4.3. This, in turn, allows for the decoupling of the upstream processes of `InterTankRSR` from its downstream processes. Consequently, we perform HI exclusively for the FAME and glycerol columns while employing VRC for the methanol column (cf. Figure 4.3). Our method involves direct VRC for the methanol column, utilizing the vapor leaving from the top of the column. This vapor is compressed, condensed within the reboiler, and partially refluxed back to the column after pressure reduction via a valve. To ensure balanced heat input, particularly due to compressor-generated heat, a trim condenser becomes necessary [62].

By leveraging this approach, we can implement two separate distributed optimizers for the two distinct process parts, as illustrated in Figure 4.3. This stands in contrast to relying on a centralized optimizer, as for the cases of HI-Cen and HI&Q-Cen. These distributed optimizers are designated as VRC&HI-RSR and VRC&HI-BG, collectively referred to as VRC&HI-Dec for this specific process configuration. This methodology involves tackling two distinct DO problems, encompassing smaller DAE systems. Consequently, this ap-

proach mitigates non-convergence concerns and reduces overall computational costs.

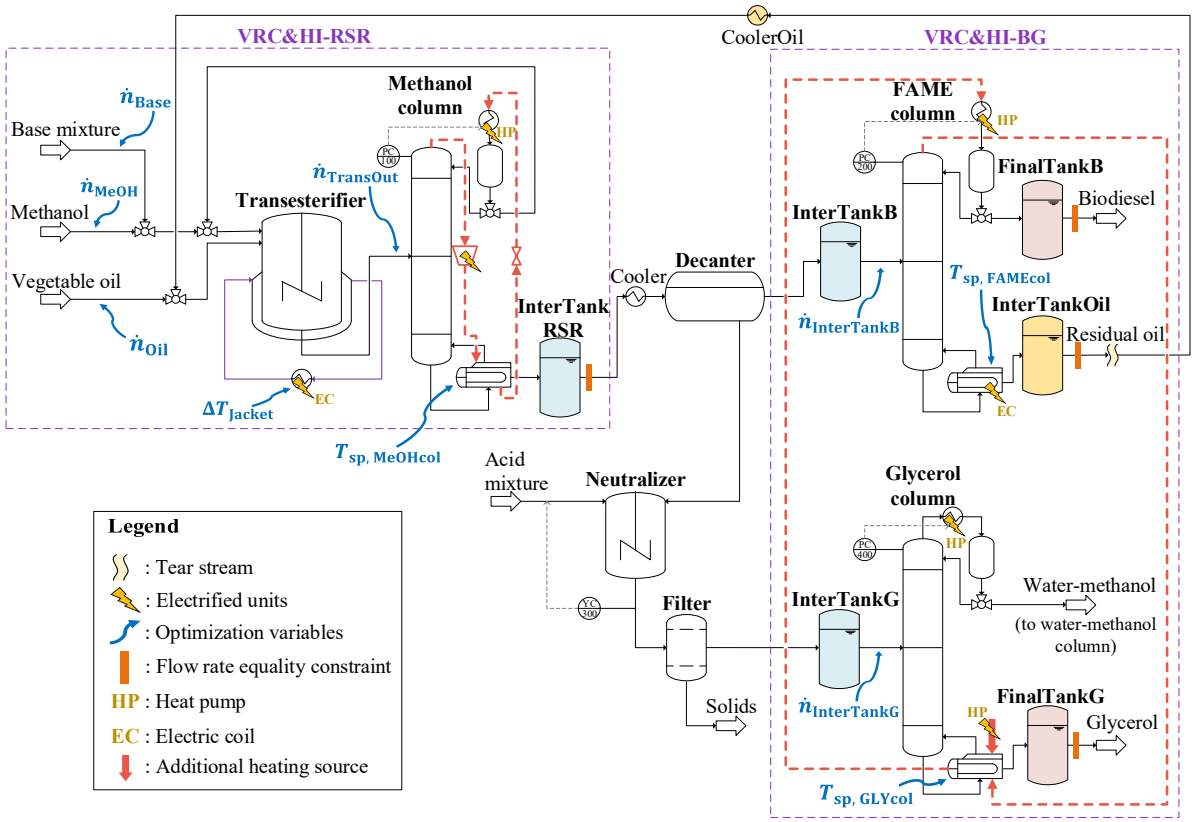

Figure 4.3.: Biodiesel process flowsheet incorporating intermediate and final buffer tanks and employing a distributed optimization approach. The configuration with vapor recompression and heat integration adopts this flowsheet. As indicated by dashed-red streams, the methanol column utilizes vapor recompression, while the other two columns are heat-integrated. Two distributed optimizers are considered here (VRC&HI-RSR and VRC&HI-BG).

4.3. Dynamic Optimization Problem

In all the process configurations under consideration, our objective is to maximize the operating profit of the process while satisfying all operational constraints within a finite time horizon. Our assessment of operating profit includes the revenue generated by all process products, accounting for all material and energy costs, where electricity prices fluctuate as a time-variant parameter. The optimization variables (cf. Figure 4.2) encompass feed flow rates ($\dot{n}_{\mathrm{Oil}}$, $\dot{n}_{\mathrm{MeOH}}$, and $\dot{n}_{\mathrm{Base}}$), the temperature change of the transesterifier jacket fluid ($\Delta T_{\mathrm{Jacket}}$), temperature setpoints for the column reboilers ($T_{\mathrm{sp,MeOHcol}}$, $T_{\mathrm{sp,FAMEcol}}$, and $T_{\mathrm{sp,GLYcol}}$), and outlet flow rates from the transesterifier and intermediate buffer tanks ($\dot{n}_{\mathrm{TransOut}}$, $\dot{n}_{\mathrm{InterTankRSR}}$, $\dot{n}_{\mathrm{InterTankB}}$, and $\dot{n}_{\mathrm{InterTankG}}$). Purity limits for final biodiesel and glycerol products, along with their required production rates, serve as path constraints. Liquid levels within the reactors, decanter, column trays, distillate drums, reboilers, and all buffer tanks are also subject to path constraints. Furthermore, buffer tanks have endpoint

constraints, regulating liquid levels and content purity, preventing optimizers from exploiting initial tank conditions, and ensuring convergence to a similar state as the process's initial state. For a comprehensive understanding of optimization problem formulations and mathematical definitions, we direct readers to Chapter 3.

4.4. Scenario and Implementation

In the simulations of all considered optimization strategies, the demand-response scenario spans a one-day time frame, during which a constant production demand of 20 t/h for biodiesel and 2.12 t/h for glycerol must be met. To capture the electricity price dynamics, we utilize historical data from the German day-ahead spot market for September 3, 2022 [177], which is depicted in Figure 3.3 in Section 3.4. Raw material and final product prices remain constant throughout. Within the domain of all DO problems, the optimization variables are discretized at uniformly spaced intervals of one hour, while the constraints undergo discretization at 30-minute intervals.

In terms of additional benchmarks, we establish a comparison between the dynamically operated three configurations and their corresponding SS counterparts. Furthermore, we compare these configurations against an optimally flexible operation scenario, similar to the one depicted in Figure 4.2, but excluding the incorporation of HI. We refer to this scenario as NoHI-Cen, where we also employ a centralized optimization approach.

Using our open-source optimization framework DyOS [53], we employ direct single-shooting [148] for solving all optimization problems under consideration. The DAE integrator utilized is NIXE [178], while SNOPT [179] is employed as the (local) optimization solver. The underlying model comprises 182 differential and 10336 algebraic variables and is developed in Modelica and integrated into DyOS as a FMU. We configure the DAE integrator tolerances at 10^{-5}, and the solver feasibility and optimality tolerances at 10^{-4}.

4.5. Results and Discussion

In order to assess the extent of operational flexibility within the three proposed process configurations for HI, we start by discussing the results pertaining to the production rates of biodiesel and glycerol, in addition to the total power consumption of the process. Following this, we undertake a comparative analysis of their economic performances against the NoHI-Cen configuration, considering energy and material costs, as well as profits. Furthermore, we conduct a parallel evaluation relative to their respective SS operations. Lastly, we evaluate the computational performances, particularly the CPU-time savings arising from implementing the distributed optimization approach VRC&HI-Dec.

4.5.1. Production Rates and Power Demand

Comparing the biodiesel production rate results depicted in Figure 4.4a with those of the NoHI-Cen configuration, it becomes evident that the three HI configurations exhibit reduced operational flexibility. Specifically, the NoHI-Cen configuration showcases the capacity to operate at notably reduced levels, especially during time intervals between 17.5 and 24. This behavior arises due to the constraints imposed by the HI of process columns, notably the FAME and glycerol columns, which in turn limit the degrees of

freedom available for optimization. As opposed to the NoHI-Cen configuration, where the biodiesel production rates can attain these lower limits, the HI configurations display fewer instances of reaching maximal production rates, such as during the periods spanning 5.5 to 7.5.

Analyzing the production profile of the HI-Cen configuration in Figure 4.4a, it becomes apparent that biodiesel production flexibility is comparatively diminished in comparison to the HI&Q-Cen and VRC&HI-Dec configurations. This observation underscores the advantages of employing external heating sources to enhance the production flexibility of biodiesel. Moreover, the profile of the VRC&HI-Dec configuration exhibits higher flexibility in contrast to the HI&Q-Cen configuration. This illustrates that heat-integrating solely the glycerol and FAME columns while simultaneously utilizing an additional heating source, confers enhanced production flexibility compared to the full HI of all three columns.

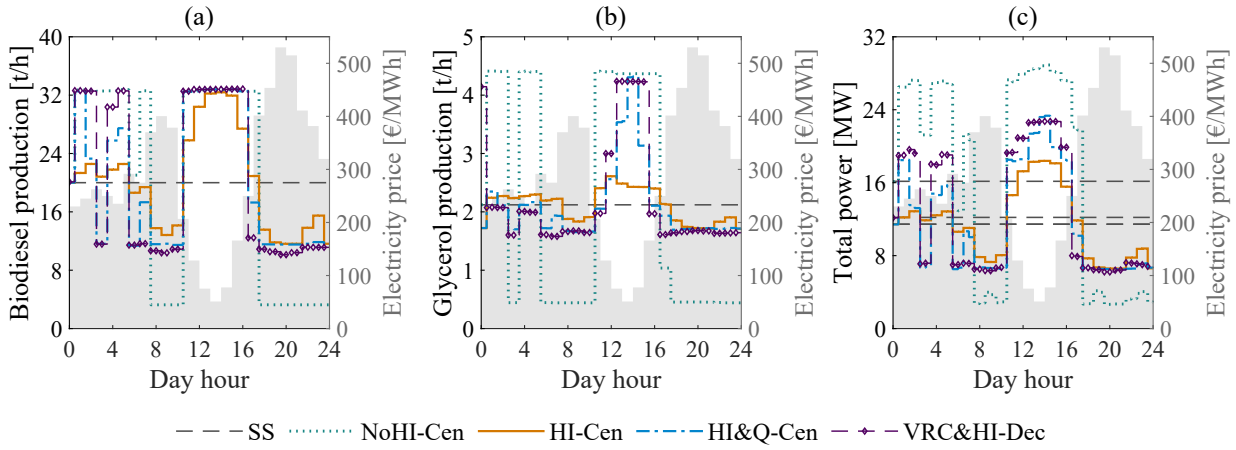

Figure 4.4.: Production rates and overall power demand results for all examined configurations, both in dynamic operation and their corresponding SS counterparts. (a), (b), and (c) show the production rates of biodiesel and glycerol and the overall power consumption, respectively. SS represents the steady-state operations. The power demand results for steady-state operations in (c) correspond to NoHI-Cen, HI-Cen, and HI&Q-Cen, shown in descending order of values, respectively. The shaded regions within the graphs illustrate the electricity price profile corresponding to the secondary axes.

Examining Figure 4.4b, the flexibility in glycerol production is significantly reduced for the HI configurations in comparison to NoHI-Cen. Within the glycerol column, the flow rates are tightly limited to the extent of heat transfer occurring in the column reboiler that engages in thermal exchange with the vapor outlet stream of the FAME column. This interplay imposes limitations, especially evidenced by the incapacity to reduce flow rates beyond specific thresholds, a notable contrast to the NoHI-Cen configuration. Furthermore, the power consumption of the glycerol column during nominal operations is approximately half that of the NoHI-Cen configuration, leading to a decreased necessity for extensive flexibility in glycerol production.

Additionally, the pronounced advantages stemming from the incorporation of supplementary heating sources become clearly apparent. This holds particularly true during the period between 11.5 to 15.5 in Figure 4.4b. During this interval, the flexibility in glycerol production rates experiences a significant sudden increase in both the HI&Q-Cen and VRC&HI-Dec configurations. Incorporating the supplementary heating sources facilitates

increasing the flow rates within both the methanol and glycerol columns, enabling them to approach higher thresholds. The necessary heating duties for vaporizing these increased flow rates through their respective reboilers are met by the supplementary heating sources. That goes beyond the constraints solely imposed by the extent of heat exchange with the vapor outlet stream of the FAME column, as observed in the HI-Cen configuration.

The examination of total power consumption, as depicted in Figure 4.4c across the three HI configurations, stems from the identical analysis applied to biodiesel and glycerol production rates. In general, there is a noticeable reduction in flexibility when compared to the NoHI-Cen configuration. Notably, the enhanced flexibility observed in HI&Q-Cen and VRC&HI-Dec in comparison to HI-Cen aligns with the increased flexibility observed in the production rates. This alignment becomes particularly pronounced during the timeframe from 11.5 to 15.5, wherein the increased glycerol production rates contribute to an additional layer of flexibility.

4.5.2. Economic Evaluation

Table 4.1 provides an overview of the total profit, energy cost, and material cost associated with each considered HI configuration, compared against those of NoHI-Cen. As anticipated, the incorporation of HI across all configurations yields substantial reductions in energy costs, with VRC&HI-Dec displaying the least pronounced decrease. Noteworthy is that while material costs experience an increase, the overall profits remain superior to those of the NoHI-Cen baseline.

Table 4.1.: Operating profit, energy cost, and material cost for each optimizer. The savings relative to NoHI-Cen are given in parentheses.

	NoHI-Cen	HI-Cen	HI&Q-Cen	VRC&HI-Dec
Energy cost [k€]	80	67 (17 %)	65 (18 %)	68 (14 %)
Material cost [k€]	556	560 (−0.6 %)	558 (−0.2 %)	563 (−1.2 %)
Profit [k€]	679	688 (1.4 %)	692 (2 %)	685 (1 %)

In Table 4.2, we present a comparative evaluation of profit and cost outcomes for each HI configuration in relation to their corresponding SS operations. Within all HI configurations, the attained savings, though significant, fall short of those realized by NoHI-Cen. This underscores the additional constraints that HI introduces, thereby constricting the available optimization degrees of freedom. In comparison to HI-Cen, both HI&Q-Cen and VRC&HI-Dec yield heightened energy cost savings, emphasizing the elevated flexibility stemming from the incorporation of external heating sources. Furthermore, VRC&HI-Dec surpasses HI&Q-Cen in energy cost savings due to its distinct configuration wherein HI is confined to the FAME and glycerol columns, thus expanding optimization options. Additionally, it is worth highlighting that the increase in total profit for the HI configurations is comparatively more restrained compared to NoHI-Cen.

Table 4.2.: Savings of energy and material costs and increase in profit for each optimizer relative to its corresponding SS operation.

	NoHI-Cen	HI-Cen	HI&Q-Cen	VRC&HI-Dec
Energy cost	29 %	16 %	17 %	19 %
Material cost	1.4 %	0.7 %	1.1 %	0.2 %
Profit	6.1 %	2.4 %	2.9 %	2.7 %

4.5.3. Computational Performance

In Figure 4.5, we provide the CPU times required for solving the DO problems associated with the three HI configurations. As anticipated, the adoption of a distributed optimization strategy in VRC&HI-Dec yields a notable reduction in CPU time, amounting to approximately threefold savings when compared to HI-Cen or HI&Q-Cen. Additionally, in the process of configuring and scaling the optimization problems for VRC&HI-Dec, a lesser degree of effort was expended, owing to the comparatively smaller DAE systems. This, in turn, led to improved convergence during the problem-solving phase.

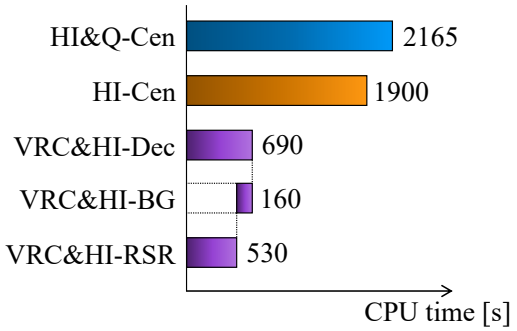

Figure 4.5.: CPU times for solving the dynamic optimization problems of the considered process configurations.

4.6. Conclusion

We show how HI increases the interconnectivity within the biodiesel production process, thereby limiting the degrees of freedom available for optimization during flexible operation. Process configurations incorporating HI show significant reductions in operational flexibility compared to the one without HI, mainly due to constraints imposed by heat integrating the process columns. In these columns, product flow rates are closely tied to the heat transfer occurring in the column reboilers, which exchange heat with the vapor outlet streams of other columns. This interdependence restricts the ability to adjust flow rates beyond specific thresholds, a limitation not observed in the configuration without HI. Conversely, adding supplementary heating sources to the reboilers allows for higher flow rates in the process columns, enabling them to reach upper operational limits. These heating sources provide the necessary energy to vaporize the increased flow rates, thus surpassing the constraints imposed by heat exchange alone, as observed in the HI configuration without additional heating units.

While incorporating external heating sources for the reboilers is unnecessary when optimizing for SS profitability, we demonstrate that this configuration, as applied to biodiesel production, delivers superior results in dynamic operation, especially when considering DSM. Furthermore, despite that the configuration employing a distributed optimization approach involves a lesser extent of HI and subsequently fewer energy cost savings, its

superior computational performance renders it more suitable for online applications. This is especially relevant for eNMPC, which will be the focus of Chapter 5 and Chapter 6. It is worth noting that the results obtained from our investigation in the context of biodiesel production may not necessarily apply to other chemical processes to the same extent. Different processes may encounter limitations due to constraints on educts storage or may have fewer degrees of freedom in optimization. Nevertheless, it is crucial to emphasize that the selection of HI process configurations necessitates a departure from conventional process designs, especially when considering dynamic operation applications.

5. Distributed Economic Nonlinear Model Predictive Control for Flexible Electrified Biodiesel Production: Sequential Architectures

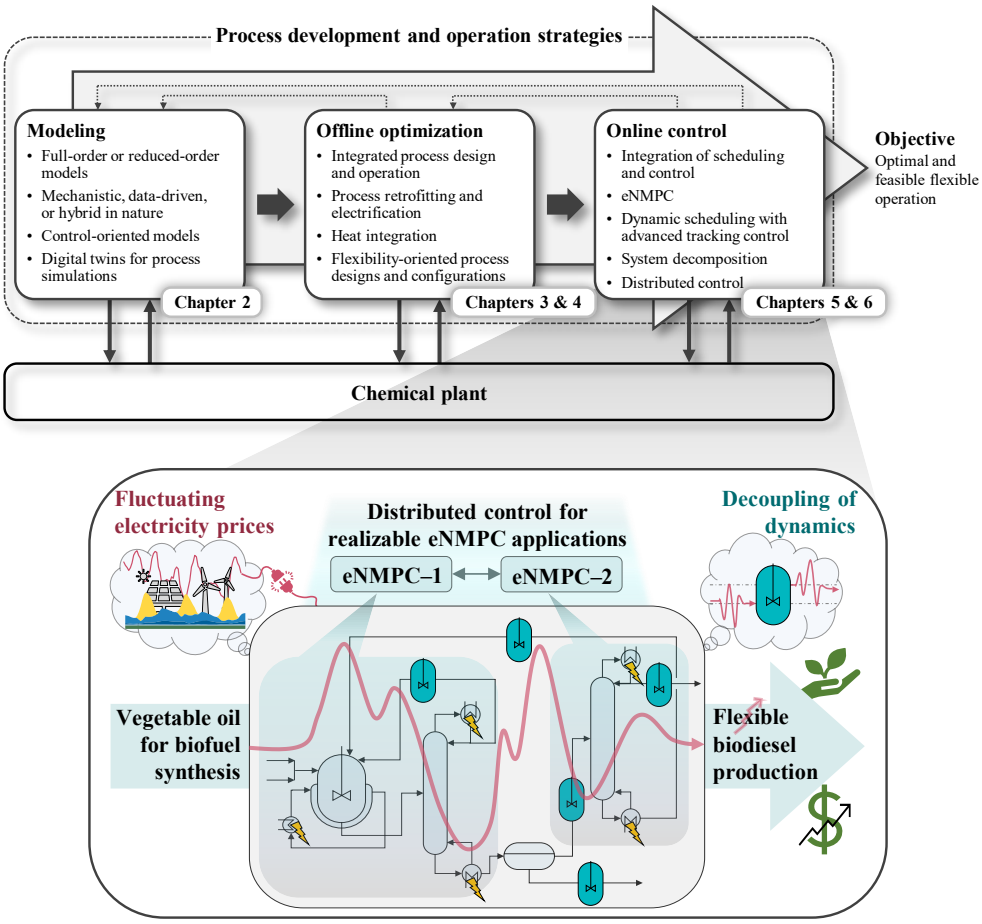

Figure 5.1.: Graphical illustration highlighting the focus of Chapter 5, which addresses the third stage of online control within the framework depicted in Figure 1.2.

As illustrated in Figure 5.1, this chapter advances to the third stage of the flowchart shown in Figure 1.2, focusing on the online control of the biodiesel production process under consideration. Specifically, we introduce a sequential DeNMPC approach for optimal

flexible operation and evaluate its performance against benchmark operational strategies.

5.1. Introduction

The operational time scales of some chemical plants align with the frequency of renewable energy supply fluctuations, leading to prolonged periods of transient states during dynamic operations [23]. Thus, to achieve optimal and feasible flexible operations of such plants, it is crucial to incorporate process dynamics and constraints into frequent scheduling decisions [181], as hypothetically illustrated in Figure 5.2. eNMPC emerges as an effective approach for integrated decision-making in chemical plants across various time scales [32]. Unlike traditional hierarchical automation tasks in chemical plants, eNMPC maximizes economic performance while directly controlling the process [20]. Employing a receding horizon approach, eNMPC solves online DO problems with an economic objective over a sufficiently extended time horizon, utilizing an open-loop process model while accounting for process constraints. Several studies in the literature explore the methodological [182–186] and application [131, 187–189] aspects of eNMPC. Ellis et al. [32] provide a comprehensive overview of the principles, methodologies, and practical implications of eNMPC, addressing both closed-loop stability and performance for nonlinear systems. Notably, the real-time tractability of eNMPC is particularly critical for its applications in chemical processes, where it encompasses DO problems involving large-scale nonlinear systems. Therefore, implementing real-time tractable eNMPC necessitates efficient strategies, such as fast update schemes [190, 191], model reduction techniques [172, 192–194], and/or system decomposition with non-centralized control [66, 187].

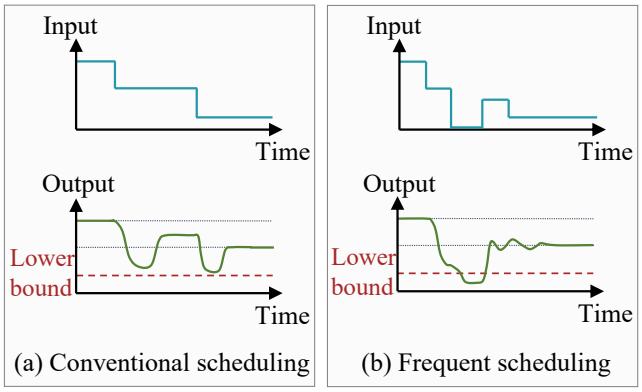

Figure 5.2.: Illustration of a hypothetical process. (a) Feasible operation under conventional scheduling, wherein the process stabilizes at steady states during infrequent decision intervals. (b) Frequent scheduling resulting in temporary constraint violations in the output, as the process fails to reach steady states between scheduling setpoints.

To reduce the computational complexity of eNMPC, an effective approach involves decomposing its optimization problem into smaller subproblems comprising smaller subsystems, while employing local controllers. Several studies present reviews and methods on non-centralized control [66–68, 187, 195, 196]. Scattolini [66] reviews several strategies developed for controlling multiple subsystems, highlighting decentralized and distributed control as primary approaches. Decentralized control operates with no information exchange between subsystems, disregarding the dynamics and coupling between them during optimization. This approach can result in system instability and suboptimal performance due to inadequate consideration of subsystem interactions. In contrast, distributed control allows communication between subsystems, primarily employing sequential or iterative communication protocols [66, 187]. In sequential, non-iterative algorithms, subproblems

are addressed in a fixed order. The optimization results of one subproblem are exchanged with the other subproblems. Therefore, only limited information is available to subproblems that are solved first. For the missing information, results from the previous time step can be used as an estimation. Subproblems addressed subsequently are constrained by the fixed solutions of preceding ones [187, 197]. In contrast, iterative algorithms solve interconnected subproblems iteratively until a termination criterion is met [67, 187]. Besides communication protocols, distributed control algorithms vary based on the objective function used in each subproblem [66, 67]. In independent algorithms, each subproblem minimizes an individual cost function, focusing solely on its own objective, progressing toward a Nash equilibrium [198]. In contrast, cooperative algorithms optimize a global cost function in each subproblem, leading to solutions close to the Pareto front. While integrating global cost functions in linear systems is well-established [198, 199], it remains challenging for large-scale nonlinear systems. One approach involves exchanging sensitivities of individual objectives among the subproblems, incorporating them into the objective functions of other subproblems [195]. Nonetheless, generating and considering sensitivities augment the computational complexity of each subproblem.

In addition to considering distributed control strategies for the practical implementation of eNMPC, integrating process designs that consider operational flexibility is essential for fully capitalizing on the capabilities of eNMPC, particularly in accommodating variable energy supply. Chemical plants typically involve multiple unit operations with varying operational limits. Incorporating buffer tanks for intermediate and final products between unit operations enables their full operational flexibility within their respective limits during dynamic operation [2]. Buffer tanks for final products facilitate flexible operation within chemical plants while meeting production demand. Figure 5.3a and Figure 5.3b illustrate (in hypothetical scenarios) how buffer tanks enable dynamic operation upstream of them while fulfilling both the required production rates and purity specifications of the final products. Figure 5.3c further demonstrates how buffer tanks effectively decouple dynamics between their upstream and downstream processes. This decoupling not only enhances operational flexibility but also facilitates decomposing the system into subsystems, enabling the implementation of distributed control strategies [2].

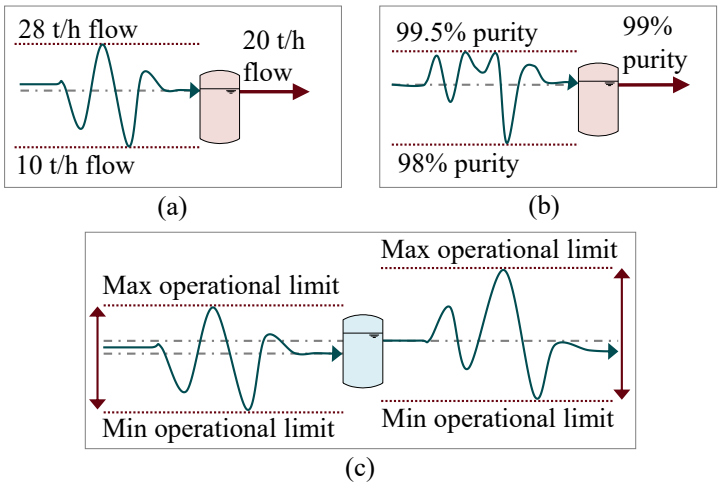

Figure 5.3.: Hypothetical scenarios illustrating how buffer tanks decouple dynamics between upstream and downstream processes, thereby facilitating enhanced dynamic operation while satisfying operational constraints.

The application of eNMPC for demand response applications in chemical processes, particularly those involving reaction, separation, and recycle components, has received limited attention in the existing literature. Moreover, the exploration of DeNMPC schemes in

chemical plants encompassing process design modifications, such as incorporating buffer tanks for flexible operation, remains unexplored. In this chapter, we present and implement a DeNMPC scheme employing sequential algorithms for the flexible operation of an electrified and renewable-powered biodiesel production process under fluctuating electricity prices. This investigation not only demonstrates the application of DeNMPC to a classical chemical process characterized by a large-scale nonlinear system but also bridges various sustainability aspects by utilizing renewable energy for biofuel production. The modeling, design, and flexible operational strategies of the biodiesel production process we examine builds on the previous chapters. In Chapter 2, we introduce the process model and PWC structures, while in Chapter 3, we conduct offline DO studies, demonstrating the potential of buffer tanks to enable and improve flexible operation for demand response. The process comprises a primary reaction unit, multiple separation units, and two recycle streams. By incorporating intermediate and final buffer tanks within the process, we enable straightforward process segmentation and the practical application of DeNMPC for optimal flexible operation. We benchmark our DeNMPC approach against three reference operational strategies, including optimal SS operation, offline DO, and conventional scheduling with simple quasi-stationary models, and assess it under operational disturbances. These disturbances involve sudden and unexpected changes in production demand and feed composition, representing practical scenarios within the process. Furthermore, we integrate two stability formulations from the literature into our DeNMPC scheme, aiming to evaluate their impact on closed-loop performance under operational disturbances affecting the process within the specific context of our biodiesel production application. In Chapter 6, we further explore DeNMPC with iterative architectures and introduce compensation schemes for computational delays inherent in solving the optimization problems, considering system couplings within the DeNMPC framework.

The chapter unfolds as follows. We first provide a succinct overview of the process description, flexibilization, segmentation, modeling, and configurations for the operational strategies considered, referring readers to Chapter 2 and Chapter 3 for a more comprehensive description. Afterward, we detail the implementation of the DeNMPC scheme, including the distributed control approach, mathematical formulation, and appended stability formulations. Subsequently, we explain the operational scenarios, disturbances, and strategies explored, along with the numerical implementation. Lastly, we present and discuss the results, before drawing conclusions.

5.2. Biodiesel Production Process

Figure 5.4 illustrates the flowsheet of the biodiesel production process under consideration, encompassing all buffer tanks for operational flexibility alongside optimization variables.

5.2.1. Process Description

The biodiesel production process is designed to produce FAME, with glycerol as a by-product, through the transesterification of vegetable oil with methanol in the presence of an alkali catalyst within the transesterifier unit. Downstream, the products undergo further separation and purification. Methanol is recovered and recycled to the transesterifier via the methanol column. FAME, representing the biodiesel product, is purified in the FAME

column, while any unreacted oil is recycled to the transesterifier from the bottom of this column. Glycerol, the heavier product from the decanter, undergoes additional purification in the glycerol column after neutralization and filtration. The biodiesel product must adhere to European quality standards [122], while our target purity for glycerol is 99 wt% [1, 46]. We implement a base-layer control system (cf. Figure 5.4) primarily comprising pressure controllers at the top of the distillation columns and level controllers for unit holdups. The entire process is electrified using electric coils and heat pumps.

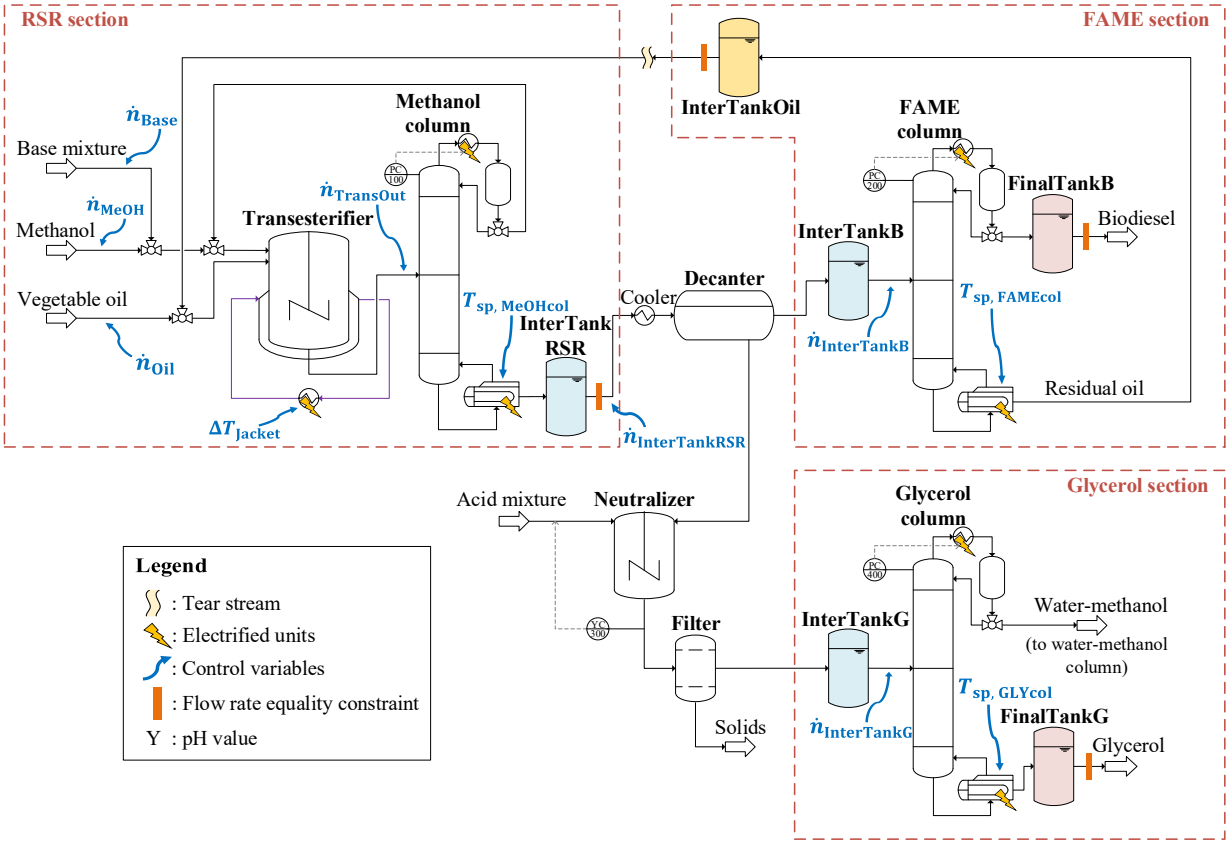

Figure 5.4.: Flowsheet of the considered biodiesel production process, incorporating buffer tanks to facilitate flexible operation.

5.2.2. Buffer Tanks for Flexible Operation and Process Segmentation

To facilitate flexible production while meeting the required demands for both biodiesel and glycerol, we incorporate two final buffer tanks, designated as `FinalTankB` and `FinalTankG`, for each respective product, as illustrated in Figure 5.4. These two tanks correspond to the tanks depicted in Figure 5.3a and Figure 5.3b, representing essential components for a process configuration that enables dynamic production of the final products while satisfying their specified requirements.

Additionally, while the intermediate buffer tanks prefixed with "`Inter`" (cf. Figure 5.4) are not strictly necessary for operational flexibility, they significantly broaden the operational window of all unit operations within the process, thereby enhancing operational

flexibility [2]. As visually depicted in Figure 5.3c, these tanks enable unit operations both upstream and downstream to operate at their limits, particularly concerning level constraints, during flexible operations. This approach fully exploits the flexibility potential of the overall process. For a detailed understanding of the design, location, and functionality of these tanks, we direct readers to Section 3.3.3 in Chapter 3.

Furthermore, the intermediate buffer tank `InterTankOil` enables tearing the residual oil recycle stream (cf. Figure. 5.4) entering the reaction-separation-recycle (RSR) section, thus stabilizing its flow rate. By additionally stabilizing the outlet stream of `InterTankRSR`, we effectively disconnect the RSR subprocess from its downstream counterparts, the FAME and Glycerol subprocesses. This segmentation facilitates distributed optimization across the three process sections, as opposed to a centralized monolithic approach, thereby enabling tractable online optimization.

5.2.3. Process Modeling

We model the transesterifier as a CSTR and each stage of the distillation columns using MESH equations. We use the NRTL model for nonidealities and DIPPR correlations [110] for temperature dependence. We consider energy and material holdups for modeling the buffer tanks and assume them to be thermally insulated. The power demand for heating and cooling modes of the transesterifier is modeled through a smooth NCP function, with the heating mode attributed solely to electric power consumption [2, 200]. The resulting mechanistic model constitutes an index-1 DAE system. For detailed information on the sizing approaches employed for the unit operations, we direct readers to Chapter 2 and Chapter 3.

5.2.4. Operational Degrees of Freedom

Optimization variables within the process (operational degrees of freedom for the DeNMPC) are indicated by blue arrows in Figure 5.4. Molar flow rates of the vegetable oil, methanol, and base mixture feeds are denoted by $\dot{n}_{\mathrm{Oil}}$, $\dot{n}_{\mathrm{MeOH}}$, and $\dot{n}_{\mathrm{Base}}$, respectively. We indicate by $\dot{n}_{\mathrm{TransOut}}$, $\dot{n}_{\mathrm{InterTankRSR}}$, $\dot{n}_{\mathrm{InterTankB}}$, and $\dot{n}_{\mathrm{InterTankG}}$ the outlet molar flow rates of the transesterifier and the buffer tank `InterTankRSR`, `InterTankB`, and `InterTankG`, respectively. The temperature change of the transesterifier jacket medium after passing through an external heat exchanger is denoted by $\Delta T_{\mathrm{Jacket}}$ [1, 2]. The temperature setpoints of the three column reboilers are represented by $T_{\mathrm{sp,MeOHcol}}$, $T_{\mathrm{sp,FAMEcol}}$, and $T_{\mathrm{sp,GLYcol}}$, respectively.

5.2.5. Process Configurations

In addition to the DeNMPC approach, we consider three reference operational strategies: optimal SS operation, offline DO, and conventional scheduling using simple quasi-stationary models. We discuss these strategies in Section 5.4.2. With regard to the buffer tanks included in the process, we use distinct process configurations aligned with each operational strategy under examination in this study.

5.2.5.1. Configuration for Optimal SS Operation

We consider here a process configuration designed for SS operation without any flexibilization strategy. Consequently, in this configuration, devoid of flexibility considerations, all buffer tanks illustrated in Figure 5.4, along with their associated optimization variables, are omitted.

5.2.5.2. Configuration for Offline DO

In this setup, we consider a centralized optimization approach for the entire process, incorporating all necessary buffer tanks to enhance operational flexibility. Hence, we incorporate all buffer tanks depicted in Figure 5.4, along with their corresponding optimization variables. The only exception is `InterTankOil`, as its primary function is to facilitate decoupling of the RSR section from the FAME section by stabilizing the flow rate of the residual oil recycle stream. Therefore, the residual oil recycle stream is not torn, and `InterTankOil` is omitted from this configuration, as we refrain from segmenting the process into subprocesses in this configuration.

5.2.5.3. Configuration for Conventional Scheduling with Simple Quasi-Stationary Models

This configuration involves simple scheduling without considering process dynamics or employing complex models. Consequently, the intermediate tanks within the process cannot be accommodated. Thus, we solely consider the final tanks, `FinalTankB` and `FinalTankG`. As a result, all intermediate buffer tanks, along with their optimization variables, are disregarded in this configuration.

5.2.5.4. Configuration for DeNMPC

In this setting, we include all buffer tanks, including `InterTankOil`, facilitating the segmentation of the process into three distinct sections, as explained in Section 5.2.2. Consequently, the residual oil recycle stream is torn, and the outlet flow of `InterTankOil` is fixed. Here, we consider all optimization variables, except for the outlet flow rate of the intermediate buffer tank `InterTankRSR`, which is constrained and maintained at a fixed value.

5.3. Distributed Economic Nonlinear Model Predictive Control Scheme

In the following, we elaborate on the considered optimization approach for DeNMPC and the coupling of DeNMPC subsystems, present the mathematical formulation of eNMPC, and discuss two extensions using stability formulations from the literature, which we employ in our numerical studies.

5.3.1. Distributed Control

As elaborated in Section 5.2.2, we introduce buffer tanks to facilitate the independent optimization of various sections within the biodiesel production process, namely the RSR, FAME, and Glycerol sections (cf. Figure 5.4). The only interlinking process dynamics involve fluctuations at the outlet stream of the RSR section and the oil recycle stream from the FAME column to the RSR section, both of which are mitigated in the buffer tanks. Consequently, we employ the sequential algorithm within a distributed control strategy as a simple and appropriate approach for the segmented biodiesel production process. Furthermore, we utilize independent, non-cooperative objective functions due to the computational impracticality of integrating the full process dynamics and considering analytical sensitivities for a global cost function in optimizing each subproblem.

As illustrated in Figure 5.5, the DeNMPC consists of three eNMPC controllers: $\text{eNMPC}_{\text{RSR}}$, $\text{eNMPC}_{\text{FAME}}$, and $\text{eNMPC}_{\text{Glycerol}}$, corresponding to the three sections of the process. The optimization of the process sections follows a specific sequence: first, the RSR section (sequence one) undergoes optimization, followed by simultaneous optimization of the FAME and Glycerol sections (sequence two). Since the RSR section is optimized initially, information regarding the operation of the FAME section is not yet available, leading to the exclusion of fluctuations in the oil recycle stream from consideration. Neglecting these fluctuations during the optimization of the RSR section could potentially result in process instability. To address this, the buffer tank `InterTankOil` serves to mitigate purity fluctuations and maintain a fixed flow rate of the recycle stream (cf. Section 5.2.2 and Figure 5.5). Fluctuations in the composition and temperature of the residual oil stream are disregarded in optimization, assuming the residual oil stream to be at a steady state. The FAME and Glycerol sections, being downstream processes and non-interconnecting, are optimized in parallel and independently of each other.

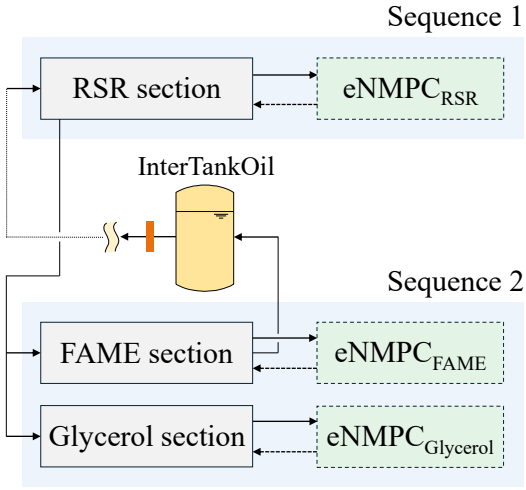

Figure 5.5.: Sequential algorithm for DeNMPC of biodiesel production. The RSR section (sequence 1) is optimized initially, followed by the simultaneous optimization of the FAME and Glycerol sections (sequence 2). The buffer tank `InterTankOil` facilitates the decoupling of the interlinking stream between the FAME and RSR sections, enabling the application of the sequential algorithm.

5.3.2. System Coupling for Distributed Control

The concept of distributed control necessitates the exchange of simulation results among subsystems. Input data from other subsystems must span the entire prediction horizon of the optimized subsystem. Otherwise, the optimization process requires estimation of the missing input data. When subproblems are solved sequentially, the results of sequences

optimized first (the RSR section) are required for subsequent sequences (the FAME and Glycerol sections). Here, we explain the coupling of subproblems using the sequential approach with a two-subproblem example. The information exchange is depicted schematically in Figure 5.6. The same logic applies to more sequences.

As depicted in Figure 5.6a, the prediction horizon of sequence one ($\Delta_{\mathrm{h},1}$) must be at least as long as that of sequence two ($\Delta_{\mathrm{h},2}$) to encompass the entire prediction horizon of sequence two with input data. At time t_n, both sequences are optimized, with the sampling time of sequence one ($\Delta_{\mathrm{s},1}$) longer than that of sequence two ($\Delta_{\mathrm{s},2}$) . Therefore, at time t_{n+1}, sequence one is not yet re-optimized, while sequence two will be. As the control trajectory of sequence one remains fixed from the previous optimization step, the predicted state trajectory can be updated with a forward simulation starting at time t_{n+1}. The input data of sequence two is updated with the new simulation results (cf. Figure 5.6b). As indicated by this scheme, the sampling time of any subsequent sequence must be equal to or shorter than that of the earlier sequences ($\Delta_{\mathrm{s},2} \leq \Delta_{\mathrm{s},1}$). Otherwise, sequence one would be updated more frequently, resulting in deviating input data from sequence one to sequence two. Consequently, the control trajectory of sequence two would not adapt to the new input data, potentially leading to instability and degraded performance, particularly in sequence two.

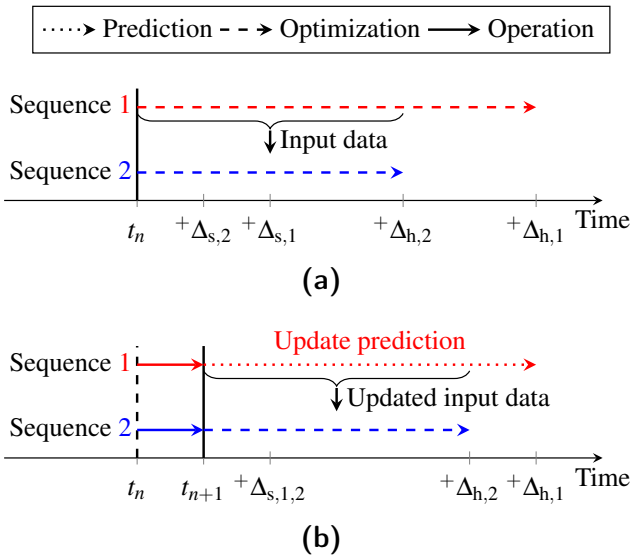

Figure 5.6.: Prediction horizons ($\Delta_{\mathrm{h},1,2}$) and sampling times ($\Delta_{\mathrm{s},1,2}$) for sequential coupling in distributed optimization. The prediction horizon of sequence one must exceed that of sequence two to provide the necessary input data. Given the shorter sampling time of sequence two compared to sequence one, the predicted input data of sequence one at time t_{n+1} should be updated based on the system state at that time. Note that after advancing one more time step, the illustrations in (b) will resemble those in (a).

5.3.3. Mathematical Formulation

For each of the three eNMPC controllers, $\mathrm{eNMPC}_{\mathrm{RSR}}$, $\mathrm{eNMPC}_{\mathrm{FAME}}$, and $\mathrm{eNMPC}_{\mathrm{Glycerol}}$, illustrated in Figure 5.5, we repeatedly solve an online DO problem with an economic objective on a rolling horizon spanning the finite time interval $\mathcal{T} = [t_n,\, t_n + \Delta_{\mathrm{h}}]$. The DO problem is based on the current (e.g., measured or estimated) system state $\tilde{\mathbf{x}}(t_n)$ at time t_n, utilizing the DAE system of the process model. The resulting optimal control problem,

starting at t_n and corresponding to the n-th time step, is formulated as follows:

$$\min_{\mathbf{x},\mathbf{y},\mathbf{u}} \quad \int_{\tau=t_n}^{\tau=t_n+\Delta_\mathrm{h}} l_\mathrm{stage}(\mathbf{x}(\tau),\mathbf{y}(\tau),\mathbf{u}(\tau),\mathbf{p}(\tau),\mathbf{d}(\tau))\,\mathrm{d}\tau \;+\; \sum_{j=1}^{n_\mathrm{u}} w_j \sum_{\theta=2}^{n_{c,j}} (u_{j,\theta}-u_{j,\theta-1})^2\,, \tag{5.1a}$$

$$\text{s.t.} \qquad \dot{\mathbf{x}}(\tau) = \mathbf{f}(\mathbf{x}(\tau),\mathbf{y}(\tau),\mathbf{u}(\tau),\mathbf{p}(\tau),\mathbf{d}(\tau))\,, \quad \forall\,\tau\in[t_n,\,t_n+\Delta_\mathrm{h}]\,, \tag{5.1b}$$

$$\mathbf{0} = \mathbf{g}(\mathbf{x}(\tau),\mathbf{y}(\tau),\mathbf{u}(\tau),\mathbf{p}(\tau),\mathbf{d}(\tau))\,, \quad \forall\,\tau\in[t_n,\,t_n+\Delta_\mathrm{h}]\,, \tag{5.1c}$$

$$\mathbf{0} = \mathbf{h}(\tilde{\mathbf{x}}(t_n),\mathbf{y}(t_n),\mathbf{p}(t_n),\mathbf{d}(t_n))\,, \tag{5.1d}$$

$$\mathbf{0} \geq \mathbf{c}_\mathrm{p}(\mathbf{x}(\tau),\mathbf{y}(\tau),\mathbf{u}(\tau),\mathbf{p}(\tau),\mathbf{d}(\tau))\,, \quad \forall\,\tau\in[t_n,\,t_n+\Delta_\mathrm{h}]\,, \tag{5.1e}$$

$$\mathbf{0} \geq \mathbf{c}_\mathrm{t}(\mathbf{x}(t_n+\Delta_\mathrm{h}),\mathbf{y}(t_n+\Delta_\mathrm{h}),\mathbf{u}(t_n+\Delta_\mathrm{h}),\mathbf{p}(t_n+\Delta_\mathrm{h}),\mathbf{d}(t_n+\Delta_\mathrm{h}))\,, \tag{5.1f}$$

$$\mathbf{u}(\tau) = \mathbf{u}(t_n+\Delta_\mathrm{c})\,, \quad \forall\,\tau\in[t_n+\Delta_\mathrm{c},\,t_n+\Delta_\mathrm{h}]\,, \tag{5.1g}$$

where $\mathbf{f}:\mathcal{X}\to\mathbb{R}^{n_\mathrm{x}}$ and $\mathbf{g}:\mathcal{X}\to\mathbb{R}^{n_\mathrm{y}}$ encapsulate the DAE system with $\mathcal{X}:=\mathbb{R}^{n_\mathrm{x}}\times\mathbb{R}^{n_\mathrm{y}}\times\mathbb{R}^{n_\mathrm{u}}\times\mathbb{R}^{n_\mathrm{p}}\times\mathbb{R}^{n_\mathrm{d}}$. The initial conditions are governed by $\mathbf{h}:\mathbb{R}^{n_\mathrm{x}}\times\mathbb{R}^{n_\mathrm{y}}\times\mathbb{R}^{n_\mathrm{p}}\times\mathbb{R}^{n_\mathrm{d}}\to\mathbb{R}^{n_\mathrm{x}}$, while $\mathbf{c}_\mathrm{p}:\mathcal{X}\to\mathbb{R}^{n_{\mathrm{c_p}}}$ and $\mathbf{c}_\mathrm{t}:\mathcal{X}\to\mathbb{R}^{n_{\mathrm{c_t}}}$ represent the path and economic endpoint constraints, respectively. We denote the state, algebraic, and control variables by $\mathbf{x}:\mathcal{T}\to\mathbb{R}^{n_\mathrm{x}}$, $\mathbf{y}:\mathcal{T}\to\mathbb{R}^{n_\mathrm{y}}$, and $\mathbf{u}:\mathcal{T}\to\mathbb{R}^{n_\mathrm{u}}$ respectively. The parameters and disturbances are represented by $\mathbf{p}:\mathcal{T}\to\mathbb{R}^{n_\mathrm{p}}$ and $\mathbf{d}:\mathcal{T}\to\mathbb{R}^{n_\mathrm{d}}$, while the control and prediction horizons are Δ_c and Δ_h, respectively. The index-1 DAE system of the process model enables the direct specification of state initial conditions. The objective function comprises the integral of an economic stage cost function l_stage and a penalty term aimed at penalizing large adjustments in control variables, using the weights $\mathbf{w}\in\mathbb{R}^{n_\mathrm{u}}$. These weights can be adjusted to prioritize the economic component of the objective function over the penalty term. Control variables, represented by u_j, $j\in[1,\,n_\mathrm{u}]$, are discretized employing $n_{c,j}$ elements, where $(u_{j,\theta}-u_{j,\theta-1})^2$ penalizes changes between consecutive discretization points $\theta-1$ and θ. We employ direct single shooting [148] for solving (5.1). Therefore, through the incorporation of this convex penalty term, we aim to achieve smoother profiles for control variables, thereby facilitating the numerical integration of the DAE system during optimization by reducing fluctuations in control variable trajectories.

5.3.4. eNMPC Stability Formulations

With the core concept of eNMPC, where nonconvex economic terms replace traditional tracking objectives, the controller no longer targets predefined SS setpoints. Consequently, the stability analysis methods traditionally employed for tracking controllers are not directly applicable to eNMPC [182]. Recent research has introduced strategies aimed at ensuring closed-loop stability within eNMPC [182, 201, 202]. However, their applicability does not always guarantee closed-loop stability [65]. We employ here two stability formulations from existing literature on eNMPC, each rooted in distinct assumptions. Our goal is to assess their relevance and evaluate their impact on closed-loop performance. Particularly, we seek to compare the performance of DeNMPC with and without the inclusion of these stability terms under operational disturbances affecting the process.

5.3.4.1. Terminal Costs and Constraints

The first stability formulation entails introducing terminal constraints and costs into the eNMPC problem [182]. To incorporate terminal costs, we extend the stage cost function (5.1a) with a function $V_\mathrm{f}(\mathbf{x}(t_n + \Delta_\mathrm{h}))$, which evaluates the final states at the end of the prediction horizon. Additionally, we incorporate terminal constraints on the states by adding $\mathbf{x}(t_n + \Delta_\mathrm{h}) \in \mathbb{X}_\mathrm{f}$ to (5.1f).

When enforcing terminal equality constraints to ensure the final state matches the optimal steady state ($\mathbb{X}_\mathrm{f} = \mathbf{x}_\mathrm{SS}$), the terminal costs can be set to zero ($V_\mathrm{f} = 0$) [201]. For terminal inequality constraints, with $\mathbb{X}_\mathrm{f}$ defining a suitable compact region encompassing the steady state, incorporating a terminal cost becomes essential [182]. Employing terminal region and terminal cost is preferred over terminal equality constraints as it expands the feasible set of initial conditions and potentially enhances closed-loop performance. Hence, we opt for employing a terminal region with a terminal cost instead of terminal equality constraints. However, determining the terminal region and corresponding cost is challenging due to the absence of a generalized formulation for either term. Amrit et al. [182] suggest utilizing the deviation of the final state from the optimal steady state as the terminal cost function:

$$V_\mathrm{f}(\mathbf{x}(t_n+\Delta_\mathrm{h})) = \frac{1}{2}(\mathbf{x}(\mathrm{t_n} + \Delta_\mathrm{h}) - \mathbf{x}_\mathrm{SS})^\mathrm{T}\mathbf{P}(\mathbf{x}(\mathrm{t_n} + \Delta_\mathrm{h}) - \mathbf{x}_\mathrm{SS}) + \mathbf{p}^\mathrm{T}(\mathbf{x}(\mathrm{t_n} + \Delta_\mathrm{h}) - \mathbf{x}_\mathrm{SS})\,. \quad (5.2)$$

The two terms denote quadratic and linear cost functions, where $\mathbf{P}$ acts as a positive definite weighting matrix and $\mathbf{p}$ as a weighting vector.

This stability approach imposes stringent system requirements, demanding dissipativity concerning the optimized stage costs and state controllability [32, 182, 201]. These prerequisites are system-specific and challenging to ensure in general applications, often proving difficult to verify in practice, especially in eNMPC problems involving large-scale nonlinear DAE systems [202, 203]. Consequently, validating such underlying assumptions for our biodiesel production application makes guaranteeing closed-loop stability inherently challenging.

5.3.4.2. Tracking Cost Constraints

Unlike the first approach, the second stability formulation does not rely on dissipativity with respect to the optimized stage costs. Instead, this formulation incorporates dissipation through a Lyapunov inequality, constructed using conventional tracking cost terms [203]. Thus, in this approach, we add a stabilizing inequality constraint as follows:

$$\begin{aligned}\int_{\tau=t_n}^{\tau=t_n+\Delta_\mathrm{h}} l_\mathrm{tr}(\mathbf{x}(\tau), \mathbf{u}(\tau))_n \,\mathrm{d}\tau \;\leq\; &\int_{\tau=t_{n-1}}^{\tau=t_{n-1}+\Delta_\mathrm{h}} l_\mathrm{tr}(\mathbf{x}(\tau), \mathbf{u}(\tau))_{n-1} \,\mathrm{d}\tau \\ &- \delta \cdot l_\mathrm{tr}(\mathbf{x}(t_{n-1}), \mathbf{u}(t_{n-1})) \cdot \Delta_\mathrm{s}\,, \end{aligned} \quad (5.3a)$$

$$l_\mathrm{tr}(\mathbf{x}(\tau), \mathbf{u}(\tau)) = \|\mathbf{x}(\tau) - \mathbf{x}_\mathrm{SS}\|^2 + \lambda \cdot \|\mathbf{u}(\tau) - \mathbf{u}_\mathrm{SS}\|^2\,. \quad (5.3b)$$

The integrated tracking cost function l_tr at time step n, typically utilized in tracking controllers, is constrained with an upper bound. This upper bound is derived from the tracking cost function of the previous time step $n-1$. The additional term, including

$\delta \in (0, 1]$, determines the level of restriction, with stricter constraints for $\delta = 1$ and less strict constraints as δ approaches zero. Consequently, the right-hand side remains a fixed value during every optimization step, updated iteratively to establish the upper bound for integrated tracking costs. Therefore, in this formulation, we augment the eNMPC problem with (5.3) by adding it to (5.1f).

When comparing the two stability approaches, we anticipate that the tracking cost constraints in (5.3) will facilitate a more gradual enforcement of the stabilizing term, leading to a gradual convergence toward the steady state. Notably, the parameter δ can be adjusted to balance economic performance with stabilizing objectives during closed-loop operation. This contrasts with the first approach, which employs terminal costs and region constraints, leading to an immediate and direct penalization toward the steady state from the outset. In scenarios requiring continuous flexible operation, such as our demand response application, the second stability approach is expected to yield a better balance between closed-loop performance and stability compared to the first approach. However, for applications where the primary objective is to ensure closed-loop stability, the first approach may be more suitable due to its more restrictive imposition of constraints.

5.4. Operational Scenarios and Strategies

In this section, we first elaborate on the operational scenarios considered, namely, how we define the parameter $\mathbf{p}(\tau)$ and disturbance $\mathbf{d}(\tau)$ values in (5.1). Subsequently, we outline the operational strategies evaluated in our simulations, including the DeNMPC strategy and benchmarks as references for comparison.

5.4.1. Operational Scenarios

We conduct simulations over a time horizon of one day. Under nominal conditions, we assume a constant biodiesel product demand of 20 t/h, and correspondingly, a glycerol demand of 2.12 t/h (by stoichiometry and mass balance), throughout the day. All operational schemes presented below must adhere to these nominal product demands. To capture the dynamics of electricity prices, we utilize historical data from the German day-ahead spot market on September 3 and 4, 2022 [177], as depicted in Figure 5.7. Despite the simulation timeframe being one day (indicated by the gray area in Figure 5.7), we require data from the subsequent day due to the receding prediction horizon in the DeNMPC strategy.

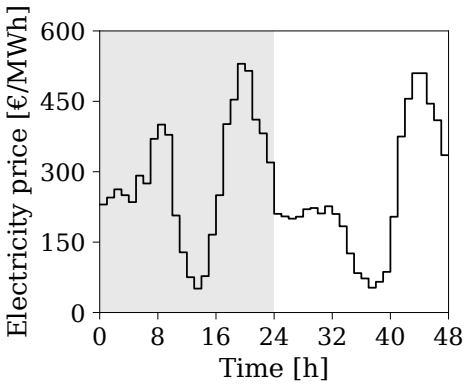

Figure 5.7.: Electricity prices from the German day-ahead spot market for September 3 and 4, 2022 [177].

To evaluate the performance of the DeNMPC strategy with the sequential algorithm concerning its ability to manage changes in required production demand and how this transfer occurs online between subsystems within the distributed optimization approach, we consider a scenario where the production demand for biodiesel increases by 20 % at

12 h and subsequently returns to its nominal value at 18 h. This load disturbance is only known at the time of occurrence, thus remaining unforeseen by the DeNMPC algorithm until both 12 h and 18 h. Therefore, it is not accounted for within its prediction horizon before it takes place.

To assess the performance of DeNMPC with and without the inclusion of the two stability formulations introduced in Section 5.3.4, we consider a disturbance involving a change in the composition of the vegetable oil feed in the process. The oil feed is initially modeled with a nominal composition of 95 wt% triolein, 5 wt% diolein, and 0 wt% monoolein, which changes to 80 wt% triolein, 10 wt% diolein, and 10 wt% monoolein. This feed disturbance occurs at 12 h and is only known to the DeNMPC after 30 min from its initiation. Such a disturbance may arise due to a change in oil type or variations in oil quality, possibly resulting from an oil pretreatment process upstream. During plant operation, the inlet feed composition is not measured online but through laboratory samples taken at regular intervals, with a measurement time of 30 min.

5.4.2. Operational Strategies

We consider four operational strategies: the DeNMPC strategy and three benchmarks. The first two benchmarks represent lower and upper bounds, respectively, illustrating the extent of achievable flexibility. The lower bound represents SS operation without any flexibilization, while the upper bound reflects the best attainable flexibilization through offline DO. The third benchmark entails a simple scheduling approach, demonstrating the benefits and importance of integrating process dynamics into scheduling decisions. The process configurations, control variables, and operational constraints for each of the operational strategies considered are summarized in Table C.1 in Appendix C.

5.4.2.1. Optimal Steady-State Operation

In this strategy, we consider the process configuration tailored for constant operation (cf. Section 5.2.5.1). Our objective is to establish an optimal benchmark for constant operation by minimizing both power consumption and material costs while ensuring that the production rates of biodiesel and glycerol meet specified requirements and that all operational constraints are met. Notably, we do not need to consider electricity price fluctuations within this strategy, as we target minimal energy demands regardless of the electricity price profile. This SS operation serves as a baseline for profit, representing the lower bound, as any economically optimal dynamic operation should surpass the performance of the best SS counterpart [201]. The results obtained from this strategy are used to initialize the system states and controls for all subsequent operational strategies.

5.4.2.2. Offline Dynamic Optimization

The offline DO strategy entails the configuration for centralized DO outlined in Section 5.2.5.2. We consider a similar approach for centralized optimization as presented in Chapter 3. This strategy serves as a lower bound for cost (an upper bound for profit), representing the best achievable operational flexibility, where both energy and material costs are minimized. It is solved offline to establish a benchmark for nominal operation, while taking into account the electricity price dynamics for the entire day, depicted in gray

in Figure 5.7. We discretize the control variables at one-hour intervals, aligning with the electricity price dynamics. Endpoint constraints are imposed on the liquid levels and compositions of all buffer tanks, as well as the transesterifier, ensuring that the final states at the end of the optimization duration match the initial states. These endpoint constraints prevent the optimization from leveraging initial holdups within the process units.

It is important to note that although the offline DO approach is computationally tractable, it is not applied online, unlike DeNMPC. As a result, the offline DO approach cannot account for real-time process disturbances or plant-model mismatch. Furthermore, it relies on centralized, monolithic optimization, which results in higher CPU times (approximately one hour). The convergence of the NLP solver in this approach is also particularly sensitive to the initial guess and the scaling of control variables and constraints. In DO problems involving large-scale DAE systems, the optimization algorithm is more prone to ill-conditioning, which can negatively impact convergence. In contrast, the DeNMPC approach utilizes distributed optimization, leading to smaller-scale DO problems with fewer DAE variables. This reduces the number of variables that need to be initialized and scaled, making the optimization algorithm in the DeNMPC strategy less prone to non-convergence and more computationally efficient.

5.4.2.3. Optimal Quasi-Stationary Scheduling

To underscore the significance of integrating scheduling and control within the presented DeNMPC scheme, we introduce an optimal quasi-stationary scheduling (QSS) approach as a third benchmark, utilizing the process configuration for simple scheduling outlined in Section 5.2.5.3. This approach employs a simplified model based on SS optimizations in scheduling calculations, reflecting a conventional approach in chemical plants where the dynamics of the process and its control system are disregarded in scheduling decisions. Given that electricity prices fluctuate hourly, whereas the time constants within the considered biodiesel production process can extend to six hours (cf. Section 2.6.2.4 in Chapter 2), the process is likely to remain in a transient state for prolonged periods during dynamic operations, potentially leading to infeasible operation (cf. Figure 5.2) when employing such a basic approach for frequent scheduling tasks.

In this scheduling approach, we utilize linear regression to model the overall power consumption of the process as a function of the biodiesel production rate. For the reference dataset, multiple SS optimizations (based on the strategy outlined in Section 5.4.2.1) are conducted at various biodiesel production rate setpoints, with the glycerol production rate scaled proportionally to the biodiesel production rate. The linear regression of the total electricity usage W_{el} as a function of the biodiesel production rate $\dot{m}_{\mathrm{B}}$ is depicted in Figure C.1a in Appendix C. Biodiesel production rate setpoints for the scheduling optimization are discretized hourly over the 24-hour time horizon, aligning with the electricity price profile p_{el}. The optimal production setpoints are determined offline by minimizing

the total electricity costs C_{el}:

$$\min_{W_{\mathrm{el}},\dot{m}_{\mathrm{B}},L_{\mathrm{FinalTankB}}} \quad C_{\mathrm{el}} = \sum_{\theta=0}^{23} W_{\mathrm{el},\theta} \cdot p_{\mathrm{el},\theta}\,, \tag{5.4a}$$

$$\text{s.t.} \quad W_{\mathrm{el},\theta} = f(\dot{m}_{\mathrm{B},\theta})\,, \qquad \forall\theta \in \{0,..,23\}\,, \tag{5.4b}$$

$$\rho_{\mathrm{B}} \cdot A \cdot (L_{\mathrm{FinalTankB},\theta+1} - L_{\mathrm{FinalTankB},\theta}) = (\dot{m}_{\mathrm{B},\theta} - \dot{m}_{\mathrm{B,SP}}) \cdot \Delta_\theta\,, \qquad \forall\theta \in \{0,..,23\}\,, \tag{5.4c}$$

$$7\,\mathrm{t/h} \leq \dot{m}_{\mathrm{B},\theta} \leq 26\,\mathrm{t/h}\,, \qquad \forall\theta \in \{0,..,23\}\,, \tag{5.4d}$$

$$0 \leq L_{\mathrm{FinalTankB},\theta} \leq L_{\mathrm{FinalTankB,max}}\,, \qquad \forall\theta \in \{0,..,23\}\,, \tag{5.4e}$$

$$L_{\mathrm{FinalTankB},0} = 0.5 \cdot L_{\mathrm{FinalTankB,max}}\,, \tag{5.4f}$$

$$L_{\mathrm{FinalTankB},24} = 0.5 \cdot L_{\mathrm{FinalTankB,max}}\,. \tag{5.4g}$$

The biodiesel buffer tank level $L_{\mathrm{FinalTankB}}$ is determined using a discretized mass balance that links consecutive time points θ and $\theta + 1$ (cf. (5.4c)). We assume a constant density of biodiesel ρ_{B}, with A representing the cross-sectional area of the tank. The outlet flow of the tank $\dot{m}_{\mathrm{B,SP}}$ is set to meet the biodiesel production demand of 20 t/h, as outlined in Section 5.4.1. Due to cooling limitations in the transesterifier system, we constrain $\dot{m}_{\mathrm{B},\theta}$ to 26 t/h (cf. (5.4d)). Since we maintain the temperature of the transesterifier content at a fixed setpoint using a cascade PI controller (cf. Section 2.4 in Chapter 2) in this strategy, stabilization for higher production rates is not guaranteed over prolonged durations. Physical constraints, such as minimal holdups, impose a lower limit of 7 t/h on the production rate (cf. (5.4d)). The buffer tank level is bounded by the maximum tank level $L_{\mathrm{FinalTankB,max}}$ (cf. (5.4e)), and it must be at the initial level at 50 % of $L_{\mathrm{FinalTankB,max}}$ after 24 hours (cf. (5.4f) and (5.4g)).

After solving (5.4), we obtain an optimal quasi-stationary schedule for the biodiesel production rate ($\dot{m}_{\mathrm{B}}$), which we then incorporate into a control law. This control law is also derived from SS optimizations and encompasses the control variables fitted as functions of $\dot{m}_{\mathrm{B}}$. The resulting fits and functions are depicted in Figure C.1 in Appendix C. Notably, temperature control in the transesterifier and the FAME and glycerol column reboilers is excluded from this control law, as their temperatures exhibit minimal deviations from their optimal nominal values. Instead, PI controllers are implemented for their control (cf. Section 2.4 in Chapter 2).

5.4.2.4. DeNMPC Operation

For the closed-loop simulations in the DeNMPC strategy, we assume full-state feedback with no plant-model mismatch. The optimized controls are instantaneously transferred to the plant model, neglecting computational time delays for solving the optimization problems of the DeNMPC. In other words, we assume zero computational time, meaning that the control variables are computed instantaneously at each eNMPC step during the closed-loop simulations. We initialize the control variables for all eNMPC optimizations using the solution of the optimal SS operation (cf. Section 5.4.2.1). Additionally, we set the holdups of all buffer tanks to start with half-full levels. Table 5.1 provides the prediction and control horizons, sampling times, and control discretizations for the three eNMPC controllers. To reduce the risk of intermediate constraint violations, we discretize the constraints to twice the extent as the controls are discretized. Ensuring a sufficiently

long prediction horizon is one requirement among several to preserve the stability and economic performance of eNMPC [32, 202]. Over a short prediction horizon, economic advantages such as the transient usage of buffer tanks are not fully realized, leading to shortsighted operation [32]. Additionally, we opt for control horizons two hours shorter than prediction horizons. With a shorter control horizon, the last control is applied over the entire remaining prediction horizon, combining performance and stability advantages with reduced computational costs. Moreover, we set the prediction horizon of sequence one (RSR section) to be one hour longer than that of sequence two (FAME and Glycerol sections) to ensure that sequence one encompasses the entire prediction horizon of sequence two with input data (cf. Section 5.3.2). We define the economic stage costs l_{stage} in (5.1a) for the three eNMPC controllers as follows:

$$l_{\text{stage,RSR}}(\tau) = p_{\text{el}}(\tau)\left(W_{\text{Trans}}(\tau) + W_{\text{Mcol}}(\tau)\right) + \sum_{i=1}^{n_{\text{Feed}}} \dot{m}_i(\tau) v_i \,, \tag{5.5a}$$

$$l_{\text{stage,FAME}}(\tau) = p_{\text{el}}(\tau) W_{\text{Fcol}}(\tau) - \dot{m}_{\text{B}}(\tau) v_{\text{B}} \,, \tag{5.5b}$$

$$l_{\text{stage,Glycerol}}(\tau) = p_{\text{el}}(\tau)\left(W_{\text{Gcol}}(\tau) + W_{\text{WMcol}}(\tau)\right) - \sum_{i=1}^{n_{\text{Prod, G}}} \dot{m}_i(\tau) v_i \,, \tag{5.5c}$$

where $\dot{m}_i$ and v_i indicate the production rate and specific price (cf. Section B.2 in Appendix B) of stream i, respectively. The power demands of the transesterifier, methanol, FAME, glycerol, and water-methanol (cf. Section B.1 in Appendix B) columns are indicated by W_{Trans}, W_{Mcol}, W_{Fcol}, W_{Gcol}, W_{WMcol}, respectively. The terms n_{Feed} and $n_{\text{Prod,G}}$ correspond to the RSR section feeds and Glycerol section products, respectively. These three economic stage costs in (5.5) are utilized as per the methodology outlined in Section 5.3.1, where non-cooperative objective functions are employed within the DeNMPC algorithm.

Table 5.1.: Settings for the three eNMPC controllers, including the control and prediction horizons, as well as the sampling times and control discretizations.

	$\text{eNMPC}_{\text{RSR}}$	$\text{eNMPC}_{\text{FAME}}$	$\text{eNMPC}_{\text{Glycerol}}$
Control horizon [h]	10	9	9
Prediction horizon [h]	12	11	11
Sampling time [min]	15	15	15
Control discretization [min]	30	15	15

The control variables $\mathbf{u}$ and the path and endpoint constraints in (5.1e) and (5.1f) are detailed in Table C.1 in Appendix C. Path constraints include required purity limits and production rates for final biodiesel and glycerol products. The operational windows for unit operations featuring holdups, including column trays, are constrained by their respective minimum and maximum liquid level limits. We employ economic endpoint constraints pertaining to levels and purities in unit operations with holdups, including buffer tanks, to prevent the optimization from capitalizing on initial tank conditions and to ensure recursive eNMPC feasibility. These endpoint constraints are enforced at the end of each prediction horizon in every eNMPC optimization step. Additionally, point constraints are enforced at the end of the day (at 24 h in Figure 5.7). These point constraints, including levels and

purities in unit operations with holdups (cf. Table C.1 in Appendix C), are utilized for comparison purposes with the other benchmark strategies.

5.5. Performance Comparison for Operational Strategies

We use two metrics for the evaluation and comparison of the alternative operational strategies.

5.5.1. Electricity Cost Normalization

For the economic assessment of the operational strategies under consideration, we examine the cumulative electricity costs at the end of the day (highlighted in gray in Figure 5.7). However, given that the process involves multiple unit operations with holdups, notably the transesterifier and buffer tanks, different material holdups and compositions influence the overall electricity demand. While we enforce endpoint constraints on both liquid levels and holdup purities within the dynamic operational strategies, we additionally account for the total production to normalize electricity costs within each process section. This normalization ensures fair evaluation of different production amounts in the economic assessment of the operational strategies. In calculating total production, we consider the primary products of each of the three process sections: the bottom stream of the methanol column, the biodiesel product, and the glycerol product for the RSR, FAME, and Glycerol sections, respectively. We utilize the total production from the nominal SS operation as a reference for normalization. Consequently, we normalize the total electricity costs C_{el} of each process section by the ratio of the total reference production $m_{\mathrm{prod,ref}}$ from the SS operation to the actual total production m_{prod} achieved by the respective section under the dynamic operational strategy. Thus, the electricity costs of the three process sections over the operational period are normalized as follows:

$$C_{\mathrm{el,norm}} = C_{\mathrm{el}} \cdot \frac{m_{\mathrm{prod,ref}}}{m_{\mathrm{prod}}} \,. \tag{5.6}$$

5.5.2. Control Action

For the feed disturbance scenario outlined in Section 5.4.1, we introduce an additional criterion to evaluate the performance of the DeNMPC strategy, with and without the incorporation of the previously introduced stability formulations. We consider quantifying the level of total control action $\Sigma_{\Delta u}$ executed by the eNMPC controllers for each control variable as follows:

$$\Sigma_{\Delta u} = \sqrt{\sum_{\theta} (u_\theta - u_{\theta-1})^2} \,. \tag{5.7}$$

The squared difference between successive control setpoints $(u_\theta - u_{\theta-1})^2$ serves as a measure of the control action applied within a single step. The summation over all setpoints θ indicates the accumulation of control steps executed by the eNMPC controllers. This formulation of $\Sigma_{\Delta u}$ is closely related to the stabilizing control move penalty, introduced in the form of a tracking cost term in (5.1a).

5.6. Numerical Implementation

We model the process DAE system in Modelica and export it as an FMU [180], serving as both the DeNMPC and plant models within our closed-loop simulations. For the RSR, FAME, and Glycerol sections, the DAE systems of the corresponding process models consist of 81, 68, and 56 differential variables, and 3541, 2540, and 1997 algebraic variables, respectively. The closed-loop system, including the DeNMPC framework, is implemented in Python, utilizing our open-source optimization framework DyOS [53] through its Python interface. Within DyOS, we employ direct single shooting and use the sequential quadratic programming (SQP) solver SNOPT [179] and the DAE integrator NIXE [178] for solving optimization problems and process simulations, respectively. The DAE integration tolerances are set to 10^{-4}, while the NLP feasibility and optimality tolerances are set to $5 \cdot 10^{-4}$. We limit the major SQP iterations of SNOPT to 20. It is important to note that the selection of NLP tolerances is strongly influenced by the scaling of the objective function and constraints. In our case, given the scaling we apply, the DAE integration tolerances are significantly finer—more than two orders of magnitude smaller—than the NLP tolerances, as the variables in the NLP formulation are scaled down. We also experimented with finer DAE integration tolerances, but although the closed-loop simulation results remained consistent, the computational times increased unnecessarily. All computations are executed on an Intel(R) Core(TM) i7-1270P processor running at 4.8 GHz with 32 GB RAM.

5.7. Results and Discussion

We begin by presenting the results of the QSS strategy, illustrating the anticipated infeasible operation when utilizing such simplistic models for frequent scheduling tasks in chemical plants. Subsequently, we discuss the results of the DeNMPC strategy by comparing them to those obtained from benchmark references. Next, we outline the computational costs associated with the three eNMPC controllers and the two sequences within the sequential distributed optimization approach. Following this, we examine the performance of the DeNMPC controller under the load disturbance. Finally, we evaluate the DeNMPC performance under the feed disturbance while incorporating the stability formulations introduced previously.

5.7.1. Quasi-Stationary Scheduling

In this strategy, the simplified scheduling model fails to capture process dynamics or consider the full complexity of the production process, as it omits intermediate process steps and does not model unit operations. Consequently, operational constraints such as physical level limits in unit operations and limitations of cooling capacity in the transesterifier cannot be integrated into the scheduling optimization. This is expected to result in operations that violate constraints (cf. Figure 5.2), as illustrated in Figure 5.8 (labeled as QSS-Regular), where both the holdup in the decanter and the reboiler of the FAME column exceed their respective level limits.

However, an alternative scheduling-based approach can be implemented by imposing tighter operating windows during scheduling calculations. For example, if the biodiesel production rate is constrained between 80 % and 120 % of its nominal value (i.e., 16 t/h $\leq$

$\dot{m}_{B,\theta} \leq 24\,t/h$ in (5.4)), the operational limits are not surpassed (shown as QSS-Limited in Figure 5.8). Nevertheless, this reduced production flexibility drives the process to operate closer to the nominal SS operating point, resulting in higher energy costs and consequently fewer savings. Moreover, despite achieving adherence to operational limits through the implementation of tighter production bounds, it is anticipated to encounter feasibility issues again in the presence of disturbances.

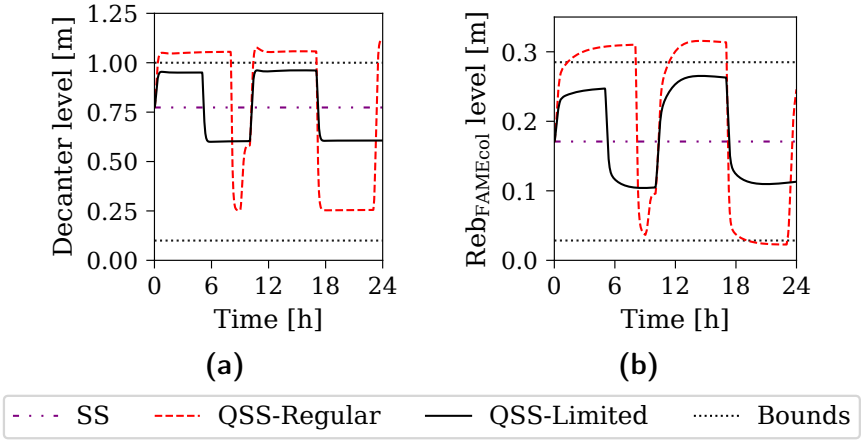

Figure 5.8.: Limitations of the QSS approach. Results with regular production rate limits (QSS-Regular) and tighter limits (QSS-Limited). Liquid levels in the decanter (a) and the reboiler of the FAME column (b) exceed their bounds for the regular production rate limits.

5.7.2. Comparison of DeNMPC with Benchmark Strategies

We first conduct an economic evaluation, comparing the energy costs of the considered strategies. Next, we present results for the production rates of the final products and total power consumption. Subsequently, we discuss the role of the different buffer tanks within the process and how the DeNMPC controller utilizes them.

5.7.2.1. Energy Costs

Table 5.2 presents the energy costs and their savings compared to those of the optimal SS operation after normalization using (5.6) for both the overall process and each of its three sections. The upper bound of energy cost savings is the offline DO strategy, resulting in significant savings of 27 % in total. While the QSS-Regular approach yields total savings of 14 %, it is an unrealizable strategy due to the resulting infeasibilities, as previously discussed in Section 5.7.1. Note that we do not consider the resulting infeasible operations when determining the corresponding energy costs for the QSS-Regular approach. For the case where we limit the operational window of the production rate (QSS-Limited), the total savings are reduced to 6 %, indicating a significant reduction in operational flexibility. Conversely, the DeNMPC operation results in total savings of 20 % while simultaneously guaranteeing that all operational constraints are satisfied. These results underscore the superior capabilities of DeNMPC over the conventional scheduling approach for frequent scheduling tasks, particularly in demand response applications. DeNMPC not only achieves feasible operation but also enables enhanced flexible operation and thus higher energy cost savings.

Table 5.2.: Normalized energy costs for all operational strategies, both total and for each of the three process sections. The savings compared to the SS operation are indicated in parentheses.

	Normalized energy costs [k€]			
	RSR	FAME	Glycerol	Total
SS	12	78	20	109
Offline DO	9 (21 %)	57 (27 %)	13 (31 %)	80 (27 %)
QSS-Regular	10 (16 %)	66 (15 %)	18 (9 %)	94 (14 %)
QSS-Limited	11 (8 %)	72 (7 %)	19 (2 %)	102 (6 %)
DeNMPC	11 (8 %)	60 (22 %)	16 (17 %)	87 (20 %)

Upon examining the results of the individual process sections, the RSR section demonstrates the lowest savings compared to the other two process sections for all operational strategies. This discrepancy arises because the RSR section encompasses the feed streams into the process, where material costs primarily contribute to the optimization objective function. Moreover, the savings achieved through the DeNMPC operation in the RSR section are significantly lower than those of the offline DO counterpart, notably equivalent to the QSS-Limited approach. In the DeNMPC approach, we restrict the number of SQP iterations in the NLP solver to ensure computationally tractable problems. Since material costs dominate the objective function of the $\text{eNMPC}_{\text{RSR}}$ optimization problems, achieving higher energy cost savings and approaching the offline DO results would necessitate more major SQP iterations. This accounts for the considerable discrepancy between the savings of the DeNMPC operation and those of the offline DO counterpart. In contrast, there are no material costs in the objective functions of $\text{eNMPC}_{\text{FAME}}$ and $\text{eNMPC}_{\text{Glycerol}}$ (cf. (5.5)), resulting in fewer discrepancies in their respective results between the DeNMPC operation and the offline DO counterpart.

5.7.2.2. Production and Power Consumption

As illustrated in Figure 5.9a and Figure 5.9b, the production rates of both final products, biodiesel and glycerol, exhibit an opposite trend to the electricity price profile across all dynamic operations. These dynamic strategies, in contrast to the SS operation, enable production flexibility based on electricity prices. Initially, all dynamic operations swiftly ramp up production rates to diverge from the nominal starting point during periods of lower electricity prices. Subsequently, production rates are adjusted in response to price fluctuations to optimize operating costs while adhering to operational constraints, particularly level limits.

The profiles shown for the QSS approach corresponds to the scenario where stricter bounds are imposed on biodiesel production rates (i.e., QSS-Limited). Although both offline DO and QSS-Limited encompass the full-day electricity price profile, the stricter operational window enforced by the simple scheduling approach significantly reduces production flexibility. Conversely, the DeNMPC operation facilitates greater production flexibility, with production rate profiles resembling those of the offline DO counterpart, especially during the period of lowest prices, i.e., between 10 h and 17 h.

However, in the DeNMPC operation, production rates do not consistently align with the trajectories of the offline DO counterpart. Particularly, during the initial periods of the

day, DeNMPC operation exhibits lower production rates. This discrepancy arises because the higher electricity prices during the final hours of the day are initially unknown due to the 12-hour prediction horizon. Consequently, only the lower electricity prices between 12 h and 16 h are incorporated into the prediction horizon, resulting in diminished production in the initial hours relative to the offline DO approach. Moreover, the 12-hour prediction horizon in the DeNMPC operation accounts for the deviations in the profiles around 9 h and 17 h from its offline DO counterpart. Furthermore, during the final hours of the day, the DeNMPC operation demonstrates an increase in production rates, especially for biodiesel, compared to the offline DO results. This increase is necessary to compensate for the total amount of produced products and fulfill the endpoint constraints imposed at the end of the day. Offline DO benefits from knowledge of the complete electricity price profile, allowing for increased production initiation followed by reduction at the end during high-price periods.

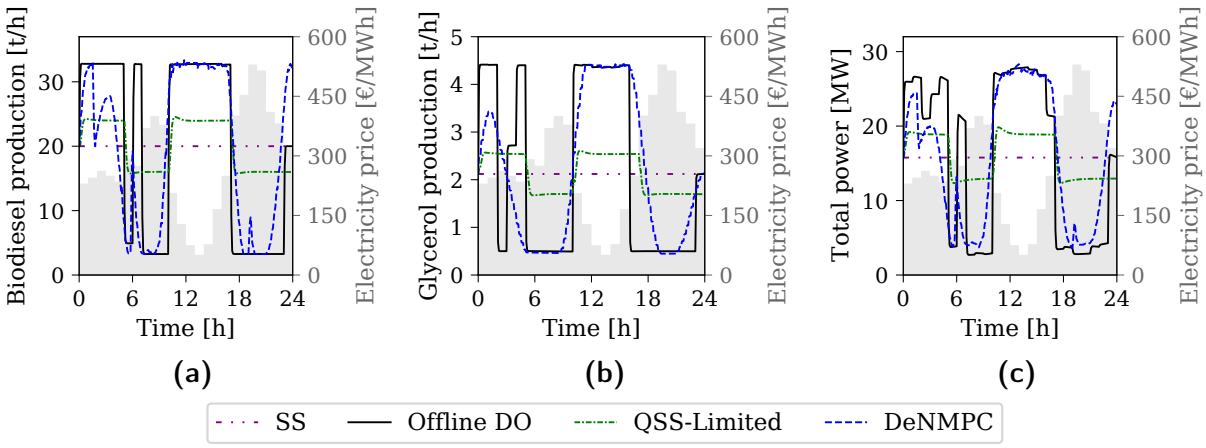

Figure 5.9.: Production rates of biodiesel (a) and glycerol (b), along with total power consumption (c), for the operational strategies under consideration. The gray area represents the electricity price profile.

The total power consumption rates are depicted in Figure 5.9c, closely mirroring the production rates, with distillation columns, particularly the biodiesel purification column, demanding the highest energy input. Since power consumption is directly related to production rates, the analysis of the behavior of the profiles in Figure 5.9c is similar to that of production rates, particularly for biodiesel production. The 12-hour prediction horizon in the DeNMPC operation limits its ability to anticipate final prices at the end of the day, leading to decreased power consumption at the beginning and increased consumption at the end compared to the offline DO counterpart. Ultimately, this results in increased energy costs for the DeNMPC operation compared to the offline DO approach, as previously discussed in Section 5.7.2.1.

5.7.2.3. Buffer Tanks

Figure 5.10 demonstrates the utilization of final and intermediate buffer tanks within the dynamic operation strategies under consideration, as exemplified by the liquid levels in `FinalTankB`, `InterTankB`, and `InterTankRSR`, facilitating significant production flexibility. During periods of low electricity prices, production is increased, and the excess is stored in

tanks for utilization during high-price intervals. In Figure 5.10a, the levels of `FinalTankB` rise during periods of low electricity prices and decrease otherwise. The reserve capacity of the tank is employed during high-price intervals to ensure that the required biodiesel demand is met, despite the decrease in production rates (cf. Figure 5.9a). In the DeNMPC operation, absolute values of `FinalTankB` levels are shifted to lower values compared to the offline DO results due to divergent operation patterns at the beginning and end of the 24-hour period. As discussed in Section 5.7.2.2, production rates are lower for the DeNMPC operation due to the 12-hour prediction horizons, resulting in reduced tank levels during the first five hours. Between 22 h and 24 h, production for the DeNMPC operation is increased compared to offline DO to meet the 24-hour point constraints on tank levels. Nevertheless, the rate of change of the `FinalTankB` levels for the DeNMPC strategy closely resembles that of the offline DO counterpart, particularly in the period between 9 h and 18 h. Conversely, the tank is barely utilized by the QSS-Limited approach due to the limited operational window of biodiesel production.

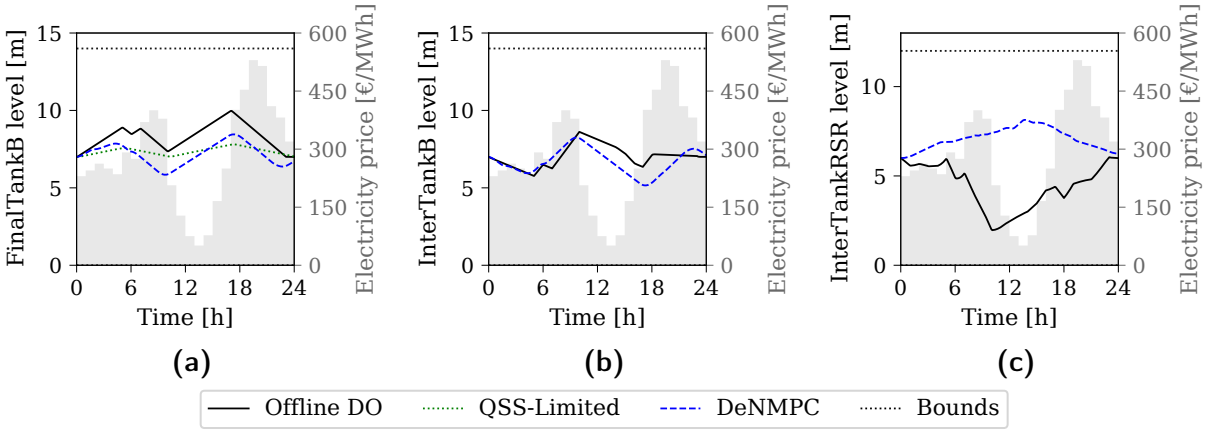

Figure 5.10.: Liquid levels in `FinalTankB` (a), `InterTankB` (b), and `InterTankRSR` (c) for the considered operational strategies. The intermediate buffer tanks `InterTankRSR` and `InterTankB` are absent in the QSS approach. The gray area represents the electricity price profile.

For glycerol production, profiles for `FinalTankG` resemble those of `FinalTankB`. In contrast, `InterTankB` (depicted in Figure 5.10b) or `InterTankG` exhibit the opposite behavior of final tanks. These intermediate tanks supply the required flow rates for downstream units to operate at the desired capacity. Therefore, they are utilized during low-price periods and filled during high-price periods. For instance, during the period between 10 h and 17 h, `InterTankB` is utilized to operate at high outlet flow rates so that the FAME column operates at increased production capacity. Consequently, levels in `InterTankB` and `InterTankG` decrease while they increase in `FinalTankB` and `FinalTankG`.

Unlike `InterTankB` or `InterTankG`, `InterTankRSR` is utilized differently for the DeNMPC operation compared to its offline DO counterpart as illustrated in Figure 5.10c. This is because the outlet flow of `InterTankRSR` is a control variable for the offline DO, while it is fixed for the DeNMPC operation (cf. TableC.1 in Appendix C). Since the outlet flow of `InterTankRSR` is fixed for the DeNMPC operation, the tank acts as a final buffer tank, reaching its maximum level during periods of the lowest electricity prices. With its outlet flow as a control variable in the offline DO strategy, `InterTankRSR` fills `InterTankB`

and `InterTankG` before low-price periods so that the latter tanks are utilized during such periods, offering higher degrees of freedom compared to the DeNMPC operation.

5.7.3. Computational Costs

In Table 5.3, we provide the CPU times required for solving the online DO problems within the DeNMPC strategy. As detailed in Section 5.3.1, the optimization steps within the DeNMPC scheme are sequenced, with $\text{eNMPC}_{\text{RSR}}$ being solved first in sequence one, followed by $\text{eNMPC}_{\text{FAME}}$ and $\text{eNMPC}_{\text{Glycerol}}$ being solved concurrently in sequence two. Hence, the CPU times relevant to our DeNMPC scheme correspond to sequence 1 and sequence 2 in Table 5.3. For sequence one, we consider the CPU times for solving $\text{eNMPC}_{\text{RSR}}$, while for sequence two, we take into account the maximum values between the CPU times for $\text{eNMPC}_{\text{FAME}}$ and $\text{eNMPC}_{\text{Glycerol}}$. The mean CPU times for both sequences in the sequential approach are notably lower than the sampling times, with none of the maximum values exceeding the sampling times. Despite disregarding computational delays within our DeNMPC scheme, these CPU times are non-negligible, necessitating consideration of computational delays in closed-loop simulations. Nonetheless, employing an appropriate delay compensation scheme [71, 204] within the DeNMPC algorithm can effectively render it practically applicable in real-time scenarios.

Table 5.3.: CPU times within the considered DeNMPC scheme. Sequence 1, addressed prior to sequence 2, involves solving $\text{eNMPC}_{\text{RSR}}$, while in sequence 2, $\text{eNMPC}_{\text{FAME}}$ and $\text{eNMPC}_{\text{Glycerol}}$ are concurrently solved, taking into account the maximum CPU times between them within sequence 2.

	CPU time [s]		
	Mean	Maximum	Standard deviation
$\text{eNMPC}_{\text{RSR}}$	179	387	87
$\text{eNMPC}_{\text{FAME}}$	67	121	27
$\text{eNMPC}_{\text{Glycerol}}$	67	164	37
Sequence 1	179	387	87
Sequence 2	83	164	30

5.7.4. DeNMPC under Load Disturbance

In the load disturbance scenario described in Section 5.4.1, we also adjust the glycerol demand to maintain plant feasibility during operation. Specifically, we scale the glycerol demand proportionally to the biodiesel demand, increasing it by 20 % between 12 h and 18 h. Additionally, we update the SS reference and constraints, including the outlet flow of `InterTankRSR`, which represents the production demand of the RSR section, to the optimal SS values corresponding to the new biodiesel load during this period.

As indicated in Table 5.4, the overall energy cost savings for this scenario decrease to 15 %, compared to 20 % for the nominal operation results (cf. Table 5.2). This reduction stems from the diminished margin of operational flexibility when the load is increased, resulting in less flexibilized power consumption and consequently lower energy cost savings.

Table 5.4.: Normalized energy costs for the DeNMPC operation under the load disturbance and for the corresponding SS operation, presented both in total and for each of the three process sections. The savings compared to the corresponding SS operation are indicated in parentheses.

	Normalized energy costs [k€]			
	RSR	FAME	Glycerol	Total
SS	12	80	20	112
DeNMPC	11 (9 %)	66 (17 %)	18 (11 %)	95 (15 %)

Figure 5.11 provides a comparison between the results of the DeNMPC strategy under the load disturbance and those of the nominal operation counterpart for durations after 12 h, as the disturbance occurs at this time. It is evident that the operation is minimally affected by the change in production demand. Intermediate and final buffer tanks, particularly `InterTankB` and `FinalTankB`, play a crucial role in mitigating the effects of the disturbance. The buffer tank holdup (cf. Figure 5.11a) is utilized to counteract the demand change and facilitates a gradual adaptation of production rates. Between 12 h and 17 h, production is already operating at maximum capacity, even without the increased demand (cf. Figure 5.11b). The additional demand is accommodated by `FinalTankB` being filled at a reduced rate. Surplus biodiesel demand is produced during periods around 18 h and 22 h, leveling the lower tank level to meet the 24-hour point constraint.

The implemented DeNMPC scheme, employing the sequential optimization approach, demonstrates its effectiveness in managing sudden and unexpected shifts in biodiesel load. The buffer tanks are pivotal in maintaining operational flexibility and stability during such disturbances in real-time scenarios characterized by uncertainty.

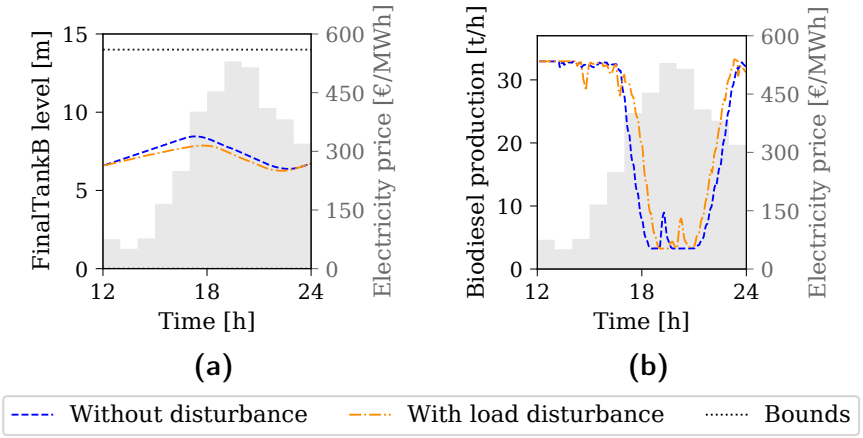

Figure 5.11.: Profiles depicting the `FinalTankB` liquid level (a) and biodiesel production rate (b) for the DeNMPC operation. A comparison is made between the results for the nominal operation without any disturbance and those with the load disturbance, which entails a sudden and unexpected increase in biodiesel demand by 20 % between 12 h and 18 h. The gray area illustrates the electricity price profile.

5.7.5. DeNMPC with Stability Formulations under Feed Disturbance

For the feed disturbance outlined in Section 5.4.1, we compare in Table 5.5 and Figure 5.12 the outcomes of the DeNMPC strategies with and without the inclusion of the previously introduced stability terms. For the terminal region constraints (cf. Section 5.3.4.1), we use (5.2) as a terminal cost and select $\mathbb{X}_\mathrm{f}$ such that the terminal states are limited to a maximum deviation of 20 % from the steady state ($0.8 \cdot \mathbf{x}_\mathrm{SS} \leq \mathbf{x}(t_n + \Delta_\mathrm{h}) \leq 1.2 \cdot \mathbf{x}_\mathrm{SS}$). Regarding the formulation with tracking cost constraints (cf. Section 5.3.4.2), we heuristically set δ in (5.3) to 0.5, 0.1, and 0.1 for $\mathrm{eNMPC}_\mathrm{RSR}$, $\mathrm{eNMPC}_\mathrm{FAME}$, and $\mathrm{eNMPC}_\mathrm{Glycerol}$, respectively. This selection is based on multiple runs assessing the convergence and robustness of the NLP solver. A stricter value for $\mathrm{eNMPC}_\mathrm{RSR}$ is set due to its greater degrees of freedom in satisfying the constraint, attributed to the inlet feed streams into the RSR section as control variables.

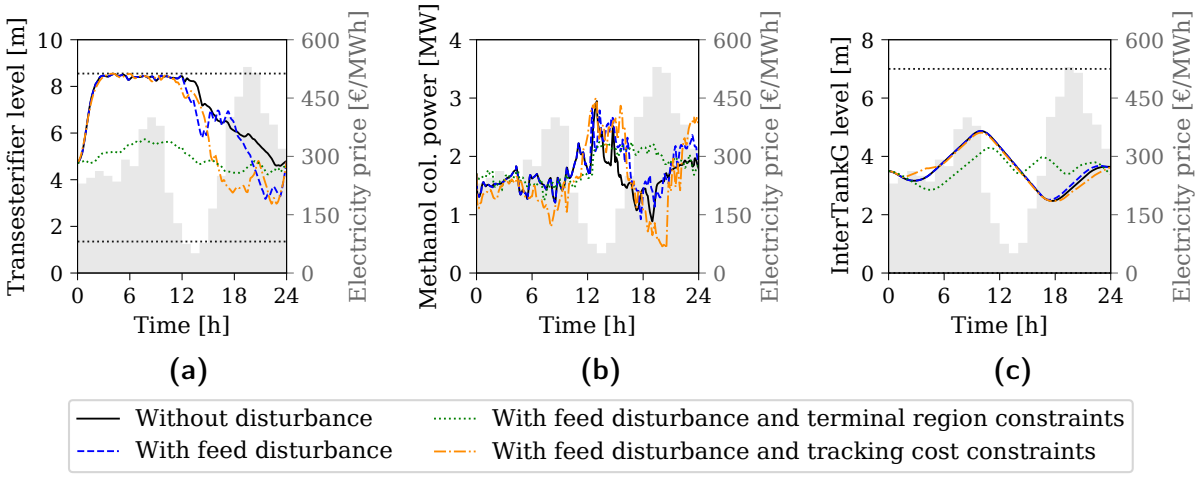

Figure 5.12.: Profiles depicting the transesterifier liquid level (a), methanol power demand (b), and `InterTankG` liquid level (c) for the DeNMPC operation. A comparison is made between the results for the nominal operation without any disturbance and those with the feed disturbance, with and without stability terms. The gray area represents the electricity price profile.

As provided in Table 5.5, the energy cost savings for the RSR section are higher under the feed disturbance compared to the nominal operation counterpart. Altering the feed composition, as outlined in Section 5.4.1, appears to enable greater operational flexibility in the RSR section compared to the nominal operation case. Notably, the DeNMPC strategy with tracking cost constraints achieves significantly higher energy cost savings, reaching 27 %. Examining the profiles in Figure 5.12a, we observe that the DeNMPC with tracking cost constraints employs a gradual approach to the steady state, penalizing the deviation from it gradually to operate around it during the periods after 15 h. This approach is advantageous, particularly during periods of higher electricity prices later in the day. Consequently, adjusting levels in the transesterifier by recycling less methanol from the methanol column during this time reduces power consumption in the methanol column. Conversely, DeNMPC operations without this stability term could not achieve such optimization due to suboptimal optimizations resulting from the limit on major SQP iterations within the NLP solver. Although this limit is also imposed for the optimization of

the DeNMPC strategy with tracking cost constraints, the additional stabilizing constraint leads to enhanced operational flexibility due to the aforementioned reasons. As evidenced in Figure 5.12b, the power consumption of the methanol column exhibits higher flexibility for the strategy with tracking cost constraints. In contrast, the DeNMPC with terminal region constraints operates closer to the steady state from the beginning of the day, hindering flexible operation from capitalizing on fluctuating electricity prices.

Table 5.5.: Normalized energy costs for the DeNMPC operation, with and without stability terms, under the feed disturbance, along with the corresponding SS operation, depicted both in total and for each of the three process sections. The savings compared to the corresponding SS operation are indicated in parentheses.

	Normalized energy costs [k€]			
	RSR	FAME	Glycerol	Total
SS	13.6	77	19.4	110
DeNMPC	11.6 (15 %)	61.9 (20 %)	17.7 (9 %)	91.2 (17 %)
DeNMPC with terminal region constraints	12.5 (8 %)	62.6 (19 %)	20.1 (−4 %)	95.2 (14 %)
DeNMPC with tracking cost constraints	10 (27 %)	63.3 (18 %)	18.2 (6 %)	91.5 (17 %)

In Figure 5.12c, we present the liquid level profile of `InterTankG` to compare the DeNMPC strategies for the Glycerol section. While the DeNMPC operation with tracking cost constraints closely mirrors the behavior of operations without stability terms, the one with terminal region constraints exhibits oscillatory behavior around the steady state. This not only restricts operational flexibility, as observed in the RSR section, but also leads to adverse effects, including increased energy costs compared to the corresponding SS operation (cf. Table 5.5). Furthermore, in all DeNMPC operations under the feed disturbance, operations in the Glycerol section result in higher energy costs compared to nominal operation, attributed to more glycerol species entering the Glycerol section during the disturbance, thereby increasing energy demands for glycerol purification in the glycerol column (cf. Section 2.6.2.3 in Chapter 2).

In the FAME section, the operation and energy cost savings of DeNMPC strategies with stability terms closely resemble those without stability terms. Regarding total energy cost savings, the DeNMPC with tracking cost constraints achieves savings of 17 %, similar to operations without stability terms, while the DeNMPC operation with terminal region constraints results in fewer savings of 14 %.

Furthermore, Table 5.6 provides the values of the $\Sigma_{\Delta u}$ term introduced in Section 5.5.2 for the three DeNMPC operations under the feed disturbance. Overall, $\Sigma_{\Delta u}$ is significantly lower for most control variables in the DeNMPC operations with stability terms compared to those without, demonstrating their stabilizing effects on plant operation. Particularly, the DeNMPC strategy with tracking cost constraints facilitates operational flexibility with energy cost savings similar to those without any stabilization terms while requiring less control action and enhancing closed-loop stability. Notably, the tracking cost term introduced in (5.3) enables gradual imposition of the enforced stabilizing constraints throughout plant operation, with the parameter δ adjustable to find a balance between economic performance and stabilizing objectives for closed-loop operation.

Based on the profiles in Figure 5.12, the energy costs in Table 5.5, and the $\Sigma_{\Delta u}$ values in Table 5.6, the DeNMPC strategy with tracking cost constraints achieves a better balance

between closed-loop performance and stability compared to the approaches using terminal region constraints or no stability formulation. Therefore, considering both economic performance and operational stability, the DeNMPC approach with tracking cost constraints proves to be the most effective among the three strategies compared.

Table 5.6.: Total control action $\Sigma_{\Delta u}$ for the DeNMPC operations under the feed disturbance. The $\Sigma_{\Delta u}$ values of control variables for the controllers incorporating different stability terms are compared to those without stabilization.

	$\Sigma_{\Delta u}$ for DeNMPC without stabilization	$\Sigma_{\Delta u}$ for DeNMPC with terminal region constraints	$\Sigma_{\Delta u}$ for DeNMPC with tracking cost constraints
$\dot{n}_{\mathrm{Oil}}$ [kmol/h]	110	28	86
$\dot{n}_{\mathrm{Base}}$ [kmol/h]	119	52	86
$\dot{n}_{\mathrm{MeOH}}$ [kmol/h]	234	85	190
$\Delta T_{\mathrm{Jacket}}$ [K]	26	18	24
$\dot{n}_{\mathrm{TransOut}}$ [kmol/h]	340	116	398
$T_{\mathrm{sp,MeOHcol}}$ [K]	17	8	14
$\dot{n}_{\mathrm{InterTankB}}$ [kmol/h]	135	143	74
$T_{\mathrm{sp,FAMEcol}}$ [K]	118	38	53
$\dot{n}_{\mathrm{InterTankG}}$ [kmol/h]	130	209	154
$T_{\mathrm{sp,GLYcol}}$ [K]	59	69	35

5.8. Conclusion

We present and apply a DeNMPC scheme with sequential communication protocols to optimize the flexible operation of electrified and renewable-powered biodiesel production. In a demand response scenario with fluctuating electricity prices, our DeNMPC strategy demonstrates significant energy cost savings compared to SS operation while ensuring operational feasibility. Unlike conventional scheduling with quasi-stationary models, which leads to infeasible operation, our approach integrates process scheduling and control tasks, demonstrating the suitability of DeNMPC for frequent scheduling decisions in chemical plants. Furthermore, while the absolute savings compared to SS operation may vary with different electricity price profiles, we expect the relative performance of dynamic operation strategies to remain consistent across these scenarios.

The incorporation of buffer tanks for intermediate and final products within our considered process proves essential for enabling process segmentation into subprocesses by decoupling process dynamics. This segmentation facilitates system decomposition, allowing for the employment of subproblems in a distributed control strategy. Such an approach is crucial for practical eNMPC application in the biodiesel production process under consideration. By utilizing buffer tanks with compatibility constraints, we enable the implementation of DeNMPC with a sequential architecture and non-cooperative objectives, providing a simple yet effective and real-time tractable approach. Furthermore, the buffer tanks mitigate the impact of process disturbances, such as sudden and unexpected changes in production demand, by counteracting these disturbances and enabling gradual adaptation of production rates within process sections. These tanks are instrumental for

maintaining operational flexibility and stabilizing the process under practical disturbances marked with uncertainty.

The presented DeNMPC strategy targets significant dynamic operations under the demand response scenario, yet the stability approach based on terminal region constraints imposes limitations on flexible operation. In contrast, the stability approach with the tracking cost constraints allows for the gradual imposition of enforced stabilizing constraints, balancing closed-loop performance and stability. Notably, the bound of the tracking cost constraint can be adjusted to reduce control action throughout plant operation without overly hindering flexible operation. While we apply two eNMPC stability formulations established from the literature and find the approach with tracking cost constraints promising, their applicability does not necessarily guarantee closed-loop stability. These stability approaches entail system-specific requirements, such as dissipativity and controllability, which can be challenging to ensure in general applications. Such prerequisites are often proving difficult to verify in practice, especially in eNMPC problems involving large-scale nonlinear systems, as in our biodiesel process application. Furthermore, it is important to note that our analysis of the two considered stability formulations does not imply system stability. Rather, it concerns improving numerical conditioning and suppressing excessive control actions.

The examined biodiesel production process encompasses the reaction, separation, and recycle components of a chemical plant, indicating the potential transferability of our study findings to a broader range of chemical processes. Particularly notable is the dual role played by buffer tanks, not only in enhancing operational flexibility but also in facilitating the application of DeNMPC. Such process design, considering operational flexibility, coupled with distributed control, holds promise for application in other chemical processes aiming for dynamic operation, especially under scenarios like demand response applications. However, application-specific operational considerations and challenges may arise, such as the utilization of buffer tanks and the phase of the stored products, whether liquid or vapor. Nevertheless, our study underscores the emergence of novel operational strategies rooted in flexibility-oriented process design as a potential new paradigm in future chemical production. This paradigm emphasizes the integration of process design and operation to enable feasible and efficient operational strategies.

In the presented DeNMPC scheme, we neglect the computational delays for solving the optimization problems. Although the solution CPU times within the sequences of the sequential approach are notably below the sampling times, they are non-negligible, indicating the necessity for considering delay compensation methods. Additionally, further research could explore alternative non-centralized control strategies, such as distributed control with iterative architectures or hierarchical control structures, which may yield superior closed-loop performance compared to the sequential architecture. However, such strategies may also entail higher computational demands, impeding their real-time applicability. In Chapter 6, we address iterative architectures and present computational delay compensation schemes for the DeNMPC framework. Furthermore, utilizing cooperative objective functions in the controller of each process section within the DeNMPC could potentially enhance overall economic performance. However, implementing such cooperative objectives requires information exchange between all process sections, leading to increased computational complexity and costs. Surrogate models (in hierarchical structures) could be employed to reduce computational complexity, although these models may not capture all process dynamics, potentially restricting consideration of all operational limits.

6. Distributed Economic Nonlinear Model Predictive Control for Flexible Electrified Biodiesel Production: Sequential and Iterative Architectures with Computational Delay Compensation

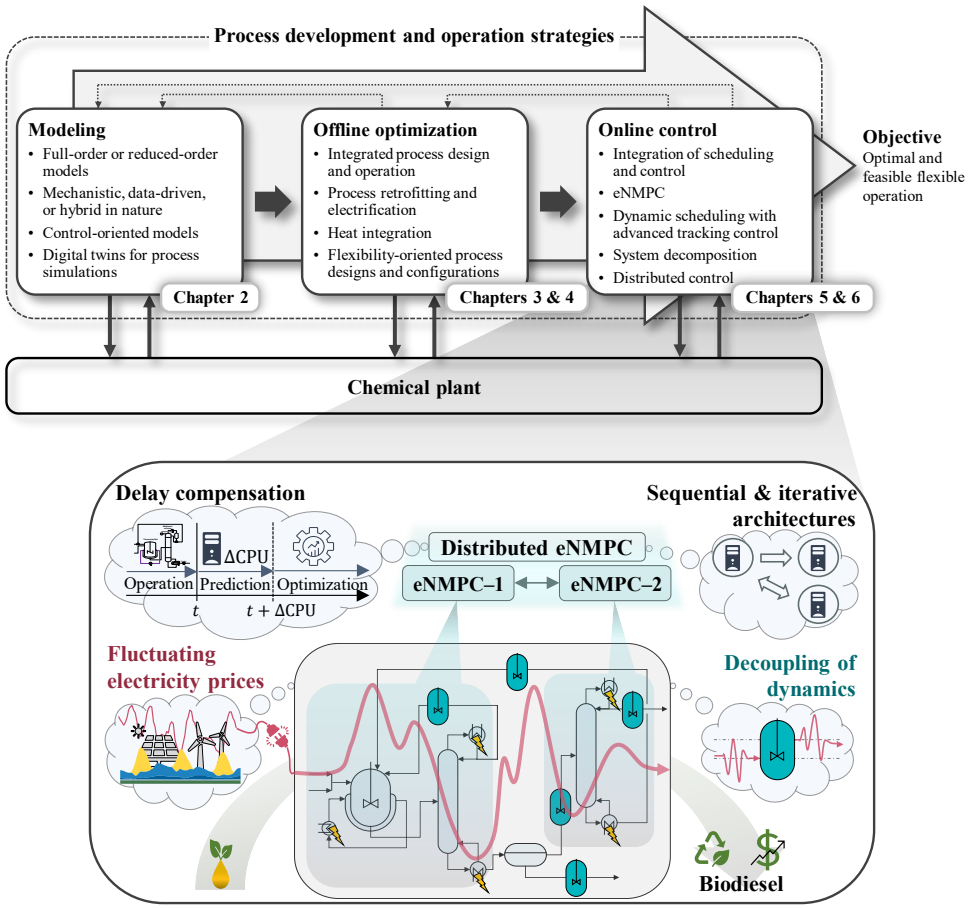

Figure 6.1.: Graphical illustration emphasizing the focus of Chapter 6, which further examines the online control stage within the framework presented in Figure 1.2.

As illustrated in Figure 6.1, this chapter further explores the online control stage depicted in the flowchart in Figure 1.2. Specifically, we focus on developing iterative DeNMPC and comparing its performance with sequential DeNMPC while incorporating computational delay compensation schemes.

6.1. Introduction

An effective strategy for realizing practical eNMPC applications in chemical processes involves utilizing eNMPC with distributed control schemes and system decomposition [4, 66, 68, 187]. In distributed MPC, multiple local controllers with inter-controller communication are cooperatively utilized across the subsystems of a decomposed system. Each local MPC controller addresses a smaller control problem and computes control actions. Overall, closed-loop plant objectives are achieved with a reduced computational burden (CPU times) compared to centralized control solutions [68, 205, 206]. Several studies provide reviews and methodologies on distributed control [26, 66–68, 187, 195], identifying two primary distributed MPC systems based on information communication architectures: sequential distributed MPC and iterative distributed MPC. In sequential distributed MPC, information exchange between neighboring controllers occurs unidirectionally. Consequently, controller subproblems in each MPC step are solved in a predetermined order, with subsequent subproblems constrained by the fixed solutions of preceding ones [4, 68, 187, 197]. Conversely, iterative distributed MPC allows for bidirectional communication where interconnected subproblems are solved repeatedly, exchanging information iteratively within each MPC step until a termination criterion is met [67, 68, 187]. The termination criterion can be defined by reaching a maximum number of iterations, the computational time required for solving the total problem, or the difference in solution trajectories between consecutive iterations being smaller than a predetermined threshold value [205].

While utilizing distributed MPC facilitates tractable eNMPC applications in chemical processes, the computational time required to solve an optimization problem, even within subsystems, is often significant relative to the MPC sampling period. This is particularly relevant in eNMPC, where nonconvex problems involving nonlinear systems of equations are solved at every sampling instant. Consequently, neglecting the computational delay inherent in calculating control variables may result in discrepancies between predicted and actual system states, leading to degradation in closed-loop performance and/or closed-loop instability [64, 65]. Early efforts addressing computational delays in nonlinear MPC involve adapting the MPC problem-solving strategy to explicitly incorporate these delays [69, 70], or prematurely terminating the optimization to maintain closed-loop stability [207, 208]. Grüne et al. [71] propose a model-based predictor with timestamping to manage communication delays between sensors, controllers, and actuators, ensuring stable system operation through prediction consistency. Advances in strategy include NLP sensitivity analysis in managing computational delays, separating the optimization into a pre-feedback nonlinear problem and a post-feedback quick update phase utilizing NLP sensitivities [204, 209, 210]. More recently, Zhou et al. [211] address fractional-order delay issues by proposing compensation methods that integrate predictive simulation to correct control actions before actual system execution, thereby mitigating the impact of delays on system performance. However, research specifically targeting computational delays in economic MPC, particularly

DeNMPC, remains largely underexplored [65, 210, 212].

In Chapter 5, we present a DeNMPC scheme employing sequential communication architectures to optimize the flexible operation of electrified and renewable-powered biodiesel production under fluctuating electricity prices. We underscore the significance of integrating buffer tanks for storing intermediate and final products within the biodiesel production process, not only for enhancing operational flexibility but also for facilitating process segmentation. Employing compatibility constraints, we apply three eNMPC controllers across three process segments, achieving a tractable eNMPC implementation with CPU times shorter than the sampling times. However, we do not account for the computational delays in solving the optimization problems, despite the considerable CPU times incurred. Additionally, we do not consider iterative DeNMPC. In this chapter, we address an iterative DeNMPC approach while considering and presenting computational delay compensation schemes for our DeNMPC. The proposed delay compensation schemes leverage model-based predictive simulation algorithms [69–71], considering subsystem coupling within the DeNMPC for both the sequential and iterative architectures. We provide the DeNMPC framework as open-source software at `permalink.avt.rwth-aachen.de/?id=619269`. Implemented in Python and integrated with the DO framework DyOS, it includes both sequential and iterative communication architectures, computational delay compensation schemes, and all relevant model extensions. We evaluate and compare the two control schemes, assessing their closed-loop performance with delay compensation under a practical disturbance in feed composition. Notably, the considered biodiesel production process shares similarities with many chemical processes, characterized by large-scale nonlinear systems and involving reaction, separation, and recycle components typical in chemical plants. Hence, our study not only explores the application of DeNMPC with computational delay schemes to a representative chemical process but also aims to bridge various sustainability aspects by optimizing biofuel production using renewable energy sources.

The structure of the chapter is as follows. We first present the DeNMPC strategies considered, along with the corresponding process configurations. Afterward, we detail the implementation of the delay compensation schemes for DeNMPC. Subsequently, we elaborate on the operational scenarios, disturbance, and strategies explored. Finally, we present and discuss the results before drawing our conclusions.

6.2. Distributed Control for Flexible Biodiesel Production

Figure 6.2 depicts the considered biodiesel production process with buffer tanks. This process produces biodiesel and glycerol as a by-product through the alkali-transesterification of vegetable oil with methanol. The control variables, indicated by arrows on the flowsheet, include feed flow rates, temperature changes of the transesterifier jacket fluid, temperature setpoints for column reboilers, and outlet flow rates from the transesterifier and intermediate buffer tanks. To apply DeNMPC through system decomposition, we partition the process utilizing the buffer tanks into three segments: the RSR, FAME, and Glycerol sections. Notably, by stabilizing the outlet flow rate of the tank `InterTankRSR`, we decouple the RSR section from downstream processes. We employ three eNMPC controllers correspondingly on the three process subsystems, each with independent, non-cooperative

objective functions due to the computational impracticality of integrating full process dynamics and considering analytical sensitivities for a global cost function in optimizing each subproblem [4, 195]. The communication architectures for the sequential and iterative schemes differ primarily in how the controllers of the RSR and FAME sections interact via the residual oil recycle stream, as illustrated in Figure 6.2. The following sections outline the distributed control strategies, system coupling in both control architectures, and the eNMPC mathematical formulation. For a more comprehensive understanding of the process description, modeling, and strategies for process flexibilization and segmentation using buffer tanks, we refer to the previous chapters.

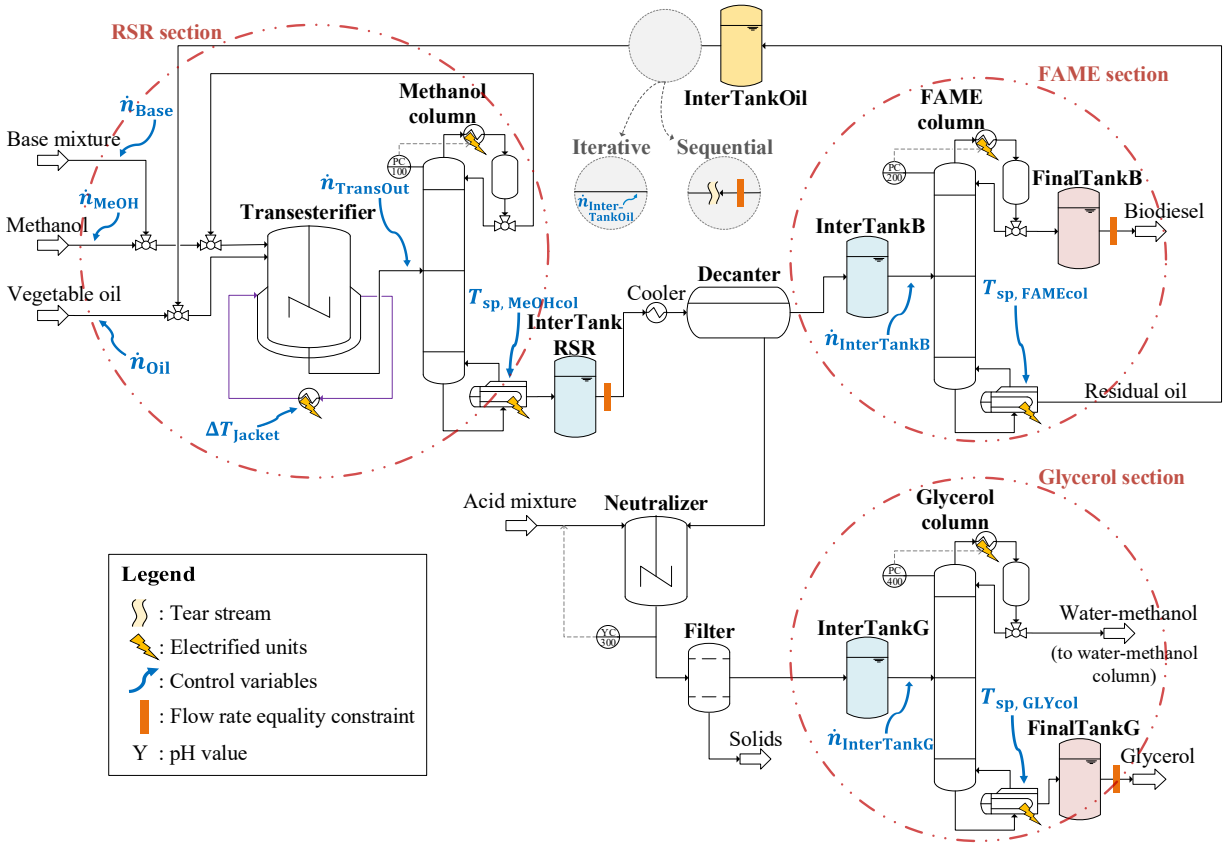

Figure 6.2.: Flowsheet of the biodiesel production process incorporating buffer tanks to enable flexible operation and distributed control. The configurations for the sequential and iterative architectures of the DeNMPC differ primarily in how the residual oil recycle stream from the FAME section connects to the RSR section, as shown downstream of the tank `InterTankOil`.

6.2.1. Distributed Control Strategies

Sequential Architecture

As illustrated in Figure 6.2 and Figure 6.3a, the outlet stream of the tank `InterTankOil` is fixed, and the residual oil recycle stream is torn in the sequential architecture. This configuration allows the RSR section to be optimized without considering downstream process dynamics, meaning that variations in the composition and temperature of the recycle stream from the FAME section are not included in the controller model. Consequently,

the residual oil recycle stream is treated as a fixed input to the RSR section. Without feedback from downstream processes, the RSR section can be optimized independently of the FAME and Glycerol sections. Therefore, the optimization of the process sections follows a predetermined sequence at each MPC sampling instant (cf. Figure 6.3a). The controller $\text{eNMPC}_{\text{RSR}}$ (sequence one) is solved first, followed by the simultaneous run of $\text{eNMPC}_{\text{FAME}}$ and $\text{eNMPC}_{\text{Glycerol}}$ (sequence two). Because the FAME and Glycerol sections are downstream processes and not interconnected, they are optimized in parallel and independently of each other.

Iterative Architecture

In the iterative architecture, we do not tear the residual oil recycle stream (cf. Figure 6.2 and Figure 6.3b) as in the sequential approach. Instead, we treat the outlet flow from `InterTankOil` as a control variable for $\text{eNMPC}_{\text{RSR}}$. Thus, the control variables for $\text{eNMPC}_{\text{RSR}}$ and $\text{eNMPC}_{\text{FAME}}$ in this architecture are those enclosed in the two circles respectively in Figure 6.2, with the addition of $\dot{n}_{\text{InterTankOil}}$ for $\text{eNMPC}_{\text{RSR}}$. This architecture differs from the sequential approach by offering greater flexibility and more degrees of freedom in optimization through manipulation of the recycle stream in $\text{eNMPC}_{\text{RSR}}$.

Consequently, we iteratively solve both $\text{eNMPC}_{\text{RSR}}$ and $\text{eNMPC}_{\text{FAME}}$ in sequence one, incorporating the downstream process dynamics of the FAME section into the optimization of the RSR section. At each MPC sampling instance, multiple optimizations are performed in an alternating manner between the two controllers until a termination criterion is met. The iterative optimization process begins by running $\text{eNMPC}_{\text{RSR}}$, where differential states are initialized, and input data from the FAME section are exchanged based on the results of the previous MPC sampling instance. Next, within the same sampling instance, $\text{eNMPC}_{\text{FAME}}$ is executed, using the recent optimization results from $\text{eNMPC}_{\text{RSR}}$ for input data exchange from the RSR section to the FAME section. We then rerun $\text{eNMPC}_{\text{RSR}}$, using the most recent control variable values as the initial guess and incorporating the updated results from $\text{eNMPC}_{\text{FAME}}$ for input data exchange. This iterative process continues until one of the following termination criteria is satisfied: (a) reaching a maximum number of iterations ($i \leq I_{\max}$), or (b) meeting a convergence condition, which is based on the deviation of control trajectories for both controllers between consecutive iterations $i-1$ and i. This convergence condition is defined as:

$$\sum_{j=1}^{n_u} \sum_{\theta=1}^{n_{c,j}} \frac{|u_{j,\theta,i} - u_{j,\theta,i-1}|}{u_{j,\text{scale}}} \leq \epsilon \,, \tag{6.1}$$

where the control variables u_j, $j \in [1, n_{\text{u}}]$, are scaled by $u_{j,\text{scale}}$ and discretized with $n_{c,j}$ elements. If the cumulative difference in all control trajectories between two consecutive iterations, for both $\text{eNMPC}_{\text{RSR}}$ and $\text{eNMPC}_{\text{FAME}}$, falls below the threshold ϵ, the dynamic operation of the system remains substantially unchanged from iteration $i-1$ to i. Since the only feedback dynamics between the RSR and FAME sections is the oil recycle stream, and with the buffering effect of `InterTankOil`, the solution is expected to converge within a few iterations.

Alternatively, if the maximum number of iterations ($I_{\max}$) is reached before meeting the convergence condition, the solution is still expected to be feasible, though suboptimal. This is because the input data exchange and initial guesses of the control variables are recursively updated based on the latest runs. The consequence of not reaching convergence is merely a suboptimal solution, as the system has not yet fully adapted to the most recent fluctuations

in input data exchange between the two controllers. However, due to the buffering effect of the tanks on process dynamics, these fluctuations are minimal, typically resulting in only a small number of iterations needed for convergence.

Subsequently, $\text{eNMPC}_{\text{Glycerol}}$ is solved sequentially in sequence two since the Glycerol section is a downstream process without a recycle stream, thus not affecting the operation of the RSR section. It is important to note that our DeNMPC approach employs independent, non-cooperative objective functions across the three controllers, as previously mentioned. Consequently, no iterative optimization is required between $\text{eNMPC}_{\text{RSR}}$ and $\text{eNMPC}_{\text{Glycerol}}$, since global system performance is not the objective here. While the operation of the RSR section does affect the Glycerol section, only a single iteration is necessary, as data is transferred unidirectionally from the RSR section to the Glycerol section. After this one-time data transfer, no further communication between the sections is needed. The $\text{eNMPC}_{\text{Glycerol}}$ inputs are updated, and its optimization is run once at the respective MPC sampling instance, without impacting the solution of $\text{eNMPC}_{\text{RSR}}$ or operation of the RSR section.

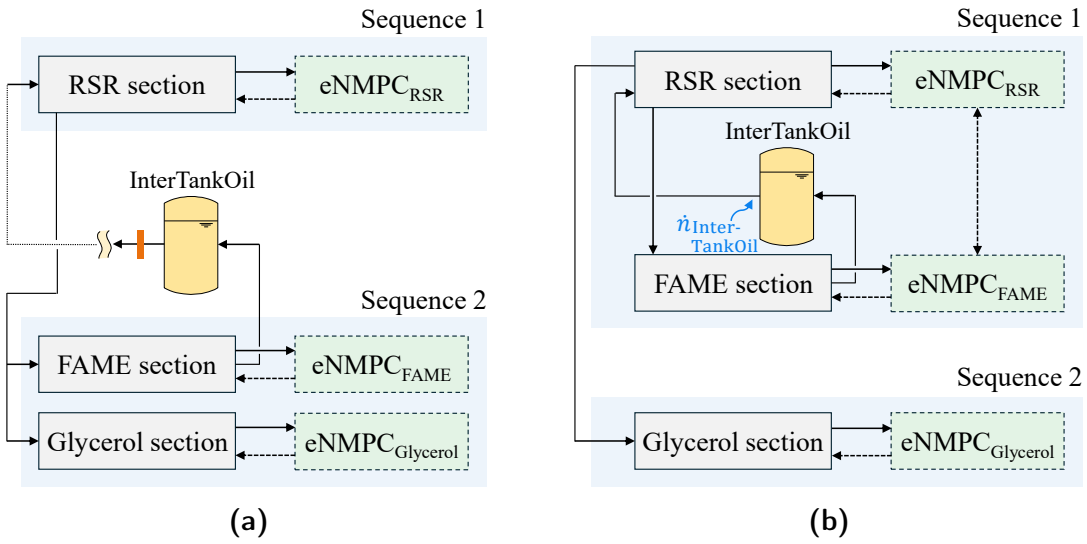

Figure 6.3.: DeNMPC architectures applied to the considered biodiesel production process: (a) sequential; (b) iterative. In the sequential architecture, the RSR section (sequence 1) is optimized first, followed by the concurrent optimization of the FAME and Glycerol sections (sequence 2). In contrast, in the iterative architecture, the RSR and FAME sections are optimized iteratively in the first sequence, with the Glycerol section then optimized sequentially in the second sequence.

6.2.2. System Coupling in Distributed Control

In distributed control, where information exchange occurs between subsystems, the input data from other subsystems should span the entire prediction horizon of the subsystems undergoing optimization. Otherwise, the optimization process would require estimating the missing input data. Below, we outline the coupling algorithms and information exchange for the two DeNMPC strategies.

Sequential Coupling

When subproblems are solved sequentially, the results of earlier sequences (RSR section) are needed for subsequent sequences (FAME and Glycerol sections). To illustrate this coupling with two subproblems, we schematically depict the information exchange in Figure 5.6 in Section 5.3.2. The same logic extends to more sequences. As depicted in Figure 5.6a, the prediction horizon of sequence one ($\Delta_{\mathrm{h},1}$) must cover at least the entire prediction horizon of sequence two ($\Delta_{\mathrm{h},2}$) to provide input data. Notably, the sampling time of any later sequence ($\Delta_{\mathrm{s},2}$) must be equal to or shorter than that of the earlier sequences ($\Delta_{\mathrm{s},1}$). This ensures that sequence one is not updated with a higher frequency than sequence two, avoiding potential instability and performance degradation, especially in sequence two. Meanwhile, at time t_{n+1}, while sequence two undergoes optimization, sequence one remains unchanged. Thus, the predicted state trajectory of sequence one can be updated through forward simulation, starting from t_{n+1}. The input data of sequence two is then updated with these new simulation results (cf. Figure5.6b). We employ this coupling approach in our sequential DeNMPC strategy, where sequence one optimizes the RSR section, and sequence two optimizes the FAME and Glycerol sections concurrently and independently, receiving their input data from the RSR section, as shown in Figure 5.6.

Iterative Coupling

In the iterative architecture, where subproblems are solved within a single sequence iteratively, all coupled subproblems require identical sampling times. Differing sampling times are impractical due to the iterative nature of solving these subproblems, rendering no subsystem capable of independent optimization. Consequently, all subsystems are optimized and updated at the same frequency. As illustrated schematically in Figure 6.4 for two subsystems, each subsystem necessitates input data from others. Therefore, to ensure coverage of the entire prediction horizon for each subproblem, the prediction horizons of all subproblems must be equal. Any discrepancies in prediction horizons would result in incomplete input data from shorter-horizon subproblems to longer-horizon counterparts.

We apply this coupling approach in our iterative DeNMPC strategy to optimize the RSR and FAME sections in sequence one. In Figure 6.4, subsystems one and two represent the RSR and FAME sections, respectively. The input data exchange refers to the transfer of the stream from the RSR section to the FAME section via the decanter when moving from subsystem one to subsystem two, and the transfer of the oil recycle stream when going in the opposite direction. Notably, while we use iterative coupling within sequence one in our iterative DeNMPC strategy, we employ the sequential coupling shown in Figure 5.6 for data exchange between sequences one and two, specifically when transferring data unidirectionally from the RSR section to the Glycerol section.

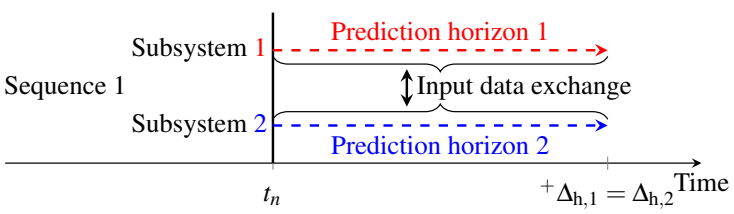

Figure 6.4.: Information exchange in the iterative coupling approach. The prediction horizons of the two subsystems must be equally long to ensure the provision of required input data for each other.

6.2.3. eNMPC Mathematical Formulation

Considering the system coupling in the two distributed architectures described above, we repeatedly solve a DO problem online with an economic objective over a rolling horizon spanning the finite time interval $\mathcal{T} = [t_n, t_n + \Delta_h]$ for each of the three eNMPC controllers: $\text{eNMPC}_{\text{RSR}}$, $\text{eNMPC}_{\text{FAME}}$, and $\text{eNMPC}_{\text{Glycerol}}$, illustrated in Figure 6.3. Therefore, we formulate the resulting optimal control problem based on the current system state $\tilde{\mathbf{x}}(t_n)$ at time t_n and corresponding to the n-th time step, as defined in (5.1) in Section 5.3.3.

6.3. Computational Delay Compensation Scheme

We address the computational delay inherent in solving optimization problems in the proposed DeNMPC by implementing a compensation scheme leveraging model-based predictive simulation [69–71]. First, we explain the scheme for a single controlled system over one MPC sampling time interval in Section 6.3.1. Afterward, we extend the concept to encompass multiple MPC sampling time intervals in Section 6.3.2. Subsequently, we examine the application of delay compensation within DeNMPC in Section 6.3.3. Specifically, we explain how we consider system coupling in both the sequential and iterative architectures within the compensation scheme. Furthermore, in Section 6.3.4, we illustrate an eNMPC implementation without considering delay compensation, which we subsequently use in our numerical studies.

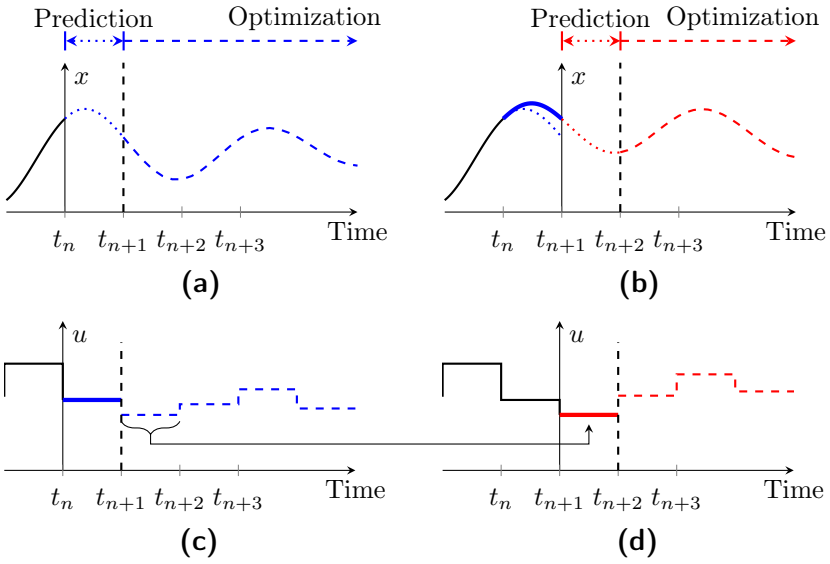

Figure 6.5.: Delay compensation over one MPC sampling time interval. The fixed control trajectory between t_n and t_{n+1} (cf. Figure 6.5c) is determined by the previous optimization (i.e., the previous MPC step) and is used to predict the future state of the system. The predicted future state sets the initial state for the optimization (cf. Figure 6.5a), which should conclude by t_{n+1} to repeat the procedure (cf. Figure 6.5b and Figure 6.5d).

6.3.1. Delay Compensation over One Sampling Time Interval

In Figure 6.5, we schematically illustrate the compensation scheme over one sampling time interval, assuming that the CPU times for controller optimizations are less than the MPC sampling time. The scheme is also outlined in Algorithm 1. We distinguish between system operation (solid lines), controller prediction (dotted lines), and controller optimization (dashed lines). Specifically, system operation depicts the plant operation through the simulation of the plant surrogate model, while controller prediction and optimization represent the forward simulation and optimization run using the controller model, respectively. The scheme uses the controller model to perform forward simulations (predictions) for optimization at a later point in time. Specifically, the optimization time horizon does not start at the current time t_n but rather at a time point t_{n+1} in the future. The control trajectory applied between t_n and t_{n+1} (solid-blue line in Figure 6.5c) is determined in the previous optimization (i.e., the previous MPC step). The state trajectory of the system between t_n and t_{n+1} (dotted-blue line in Figure 6.5a) is predicted by forward simulation of the controller model, starting at the measured state $\tilde{\mathbf{x}}(t_n)$ and utilizing the fixed control trajectory. The predicted state $\mathbf{x}(t_{n+1})$ (corresponding to the dotted line in Figure 6.5a) serves as the initial state for the subsequent optimization. Meanwhile, this optimization, initiated at t_n (i.e., the current MPC step), is targeted to conclude by t_{n+1}. During this optimization, the system progresses from t_n to t_{n+1} (solid-blue line in Figure 6.5b). Notably, the actual state of the system may deviate from the predicted state due to a mismatch between the controller model and the real system (plant surrogate). At t_{n+1}, the optimized control trajectory between t_{n+1} and t_{n+2} is fixed (solid-red line in Figure 6.5d), and the procedure is repeated.

Algorithm 1: Delay compensation scheme over one sampling time interval

Step 1: **System initialization at time t_n:**
- Measure the system state: $\tilde{\mathbf{x}}(t_n)$.
- Fix the control trajectory for $t_n \leq t \leq t_{n+1}$ based on the previous MPC step (solid-blue line in Figure 6.5c).

Step 2: **Controller prediction:**
- Perform forward simulation of the system state from t_n to t_{n+1} using the controller model (dotted-blue line in Figure 6.5a).
- Predict the system state at t_{n+1}: $\mathbf{x}(t_{n+1})$.

Step 3: **Controller optimization:**
- Initialize the optimization using the predicted state $\mathbf{x}(t_{n+1})$ from Step 2.
- Determine the optimal control trajectory over the horizon $[t_{n+1}, t_{n+1} + \Delta_{\mathrm{h}}]$.

Step 4: **System operation:**
- Apply the control trajectory for $t_n \leq t \leq t_{n+1}$, determined in the previous MPC step (solid-blue line in Figure 6.5c).
- The system evolves based on the plant surrogate model (solid-blue line in Figure 6.5b).
- The predicted state at t_{n+1} ($\mathbf{x}(t_{n+1})$) may differ from the actual system state ($\tilde{\mathbf{x}}(t_{n+1})$) due to potential model mismatches.

Step 5: **Progress to time t_{n+1}:** Shift the time horizon forward by one step (cf. Figure 6.5b and Figure 6.5d).

Step 6: **Return to Step 1 and repeat the procedure.**

6.3.2. Delay Compensation over Multiple Sampling Time Intervals

In the previous section, we assume that the controller optimization concludes before t_{n+1}. However, if the required CPU time exceeds the MPC sampling time, a longer time horizon must be considered in the predictive simulation of the compensation scheme. In such cases, multiple sampling time intervals are taken into account, resulting in multiple optimizations running in parallel since the sampling time is shorter than the considered time horizon in the predictive simulation. While we demonstrate the resulting control scheme for a maximum CPU time of two sampling time intervals in Figure 6.6 and Algorithm 2, the same methodology applies for longer CPU times. At t_n, the optimization for time t_{n+2} begins since the maximum CPU time equals two sampling time intervals (cf. Figure 6.6a and Figure 6.6d). During the predictive simulation between t_n and t_{n+2}, the latest available optimized control trajectory is utilized. Notably, only the control trajectory between t_n and t_{n+1}, determined at t_{n-2}, is fixed and applied to the system. As the time t_{n+1} is reached, another optimization, initiated at t_{n-1} and running in parallel, concludes, and the resulting control trajectory is applied between t_{n+1} and t_{n+2} (cf. Figure 6.6b and Figure 6.6e). By t_{n+2}, the optimization initiated at t_n concludes. The optimal control trajectory is then applied to the system and utilized for the predictive simulation of the new optimization (cf. Figure 6.6c and Figure 6.6f).

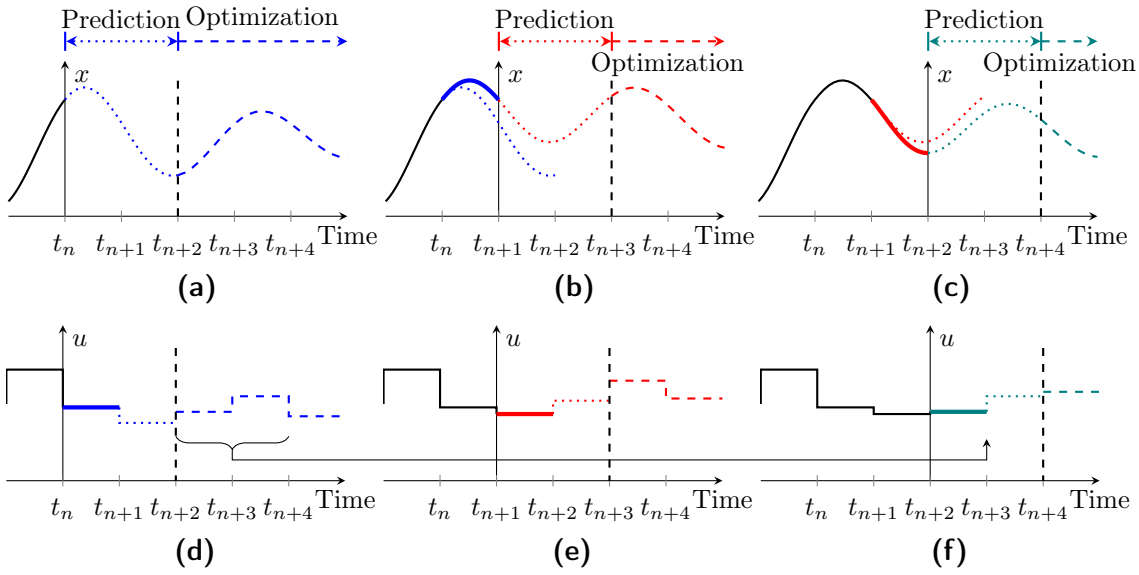

Figure 6.6.: Delay compensation over multiple MPC sampling time intervals. We illustrate the resulting control scheme for a maximum CPU time of two sampling time intervals. The optimization for time t_{n+2} initiates at t_n.

Algorithm 2: Delay compensation scheme over multiple sampling time intervals

Step 1: **System initialization at time t_n:**
- Measure the system state: $\tilde{\mathbf{x}}(t_n)$.
- Fix the control trajectory for $t_n \leq t \leq t_{n+1}$, determined at t_{n-2} in the second previous MPC step (solid-blue line in Figure 6.6d).

Step 2: **Controller prediction:**
- Perform forward simulation of the system state from t_n to t_{n+2} using the controller model (dotted-blue line in Figure 6.6a).
- The control trajectory for $t_n \leq t \leq t_{n+2}$ is based on the second previous MPC step, and is fixed only for $t_n \leq t \leq t_{n+1}$, as mentioned in Step 1 (cf. Figure 6.6d).
- Predict the system state at t_{n+2}: $\mathbf{x}(t_{n+2})$.

Step 3: **Controller optimization:**
- Initialize the optimization using the predicted state $\mathbf{x}(t_{n+2})$ from Step 2.
- Determine the optimal control trajectory over the horizon $[t_{n+2}, t_{n+2} + \Delta_\mathrm{h}]$.

Step 4: **System operation:**

4.1: From t_n to t_{n+1}:
- Apply the control trajectory from t_n to t_{n+1}, determined at t_{n-2} in the second previous MPC step (solid-blue line in Figure 6.6d).
- The system evolves based on the plant surrogate model from t_n to t_{n+1} (solid-blue line in Figure 6.6b).
- The predicted state at t_{n+1} ($\mathbf{x}(t_{n+1})$) may differ from the actual system state ($\tilde{\mathbf{x}}(t_{n+1})$) due to potential model mismatches (cf. Figure 6.6b).

4.2: From t_{n+1} to t_{n+2}:
- Apply the control trajectory from t_{n+1} to t_{n+2}, determined at t_{n-1} in the first previous MPC step (solid-red line in Figure 6.6e).
- The system evolves based on the plant surrogate model from t_{n+1} to t_{n+2} (solid-red line in Figure 6.6c).
- The predicted state at t_{n+2} ($\mathbf{x}(t_{n+2})$) may differ from the actual system state ($\tilde{\mathbf{x}}(t_{n+2})$) due to potential model mismatches (cf. Figure 6.6c).

Step 5: **Progress to time t_{n+2}:** Shift the time horizon forward by two steps (cf. Figure 6.6c and Figure 6.6f).

Step 6: **Return to Step 1 and repeat the procedure.**

6.3.3. Delay Compensation in Distributed Control

We extend the previously discussed concepts of delay compensation to distributed MPC, considering the system coupling approaches outlined in Section 6.2.2.

6.3.3.1. Delay Compensation with Sequential Coupling

We adapt the delay compensation scheme to the sequential coupling approach, as conceptually depicted in Figure 6.7. This illustration considers two sequences with equal sampling times, but the same concept applies to additional sequences and different sampling times. As outlined in Section 6.2.2, the sampling time for sequence two ($\Delta_{\mathrm{s},2}$) must be shorter than or equal to that of sequence one ($\Delta_{\mathrm{s},1}$). At time t_n, sequence one is optimized first with a total delay $\Delta_{\mathrm{CPU},1}$ (cf. Figure 6.7a), accounting for the computational delays for the optimization of both sequences ($\mathrm{CPU}_{\mathrm{seq1}}$ and $\mathrm{CPU}_{\mathrm{seq2}}$). The CPU time of sequence one is less than two sampling time intervals, i.e., $\mathrm{CPU}_{\mathrm{seq1}} < t_{n+2} - t_n$. Therefore, the optimization for sequence one is completed by t_{n+2}. These optimization results then serve as input data for sequence two (cf. Figure 6.7b). Based on this input data, sequence two is optimized between t_{n+2} and t_{n+3}. Subsequently, at t_{n+3}, the optimized control trajectories for both

sequences are simultaneously applied to the system, since the CPU time for sequence two ($\mathrm{CPU}_{\mathrm{seq2}}$) was also considered in the total delay calculation for sequence one. The total computational delay for sequence one is calculated as follows:

$$\Delta_{\mathrm{CPU},1} = \left\lceil \lceil \mathrm{CPU}_{\mathrm{seq1}} \rceil_{\Delta_{\mathrm{s},2}} + \mathrm{CPU}_{\mathrm{seq2}} \right\rceil_{\Delta_{\mathrm{s},1}}, \tag{6.2}$$

where the maximum CPU time for sequence one ($\mathrm{CPU}_{\mathrm{seq1}}$) is rounded up to the nearest sampling time instant of sequence two. In the given illustration, this time corresponds to t_{n+2}, at which the optimization of sequence two is started. Notably, its maximum CPU time ($\mathrm{CPU}_{\mathrm{seq2}}$) is also added in computing $\Delta_{\mathrm{CPU},1}$. The overall resulting delay is then rounded up to the next sampling time instant of sequence one. This corresponds to the next possible time point (t_{n+3} in Figure 6.7b) at which the optimized control trajectories of both sequences are applied to the system.

The computational delay $\mathrm{CPU}_{\mathrm{seq2}}$ is incorporated into $\Delta_{\mathrm{CPU},1}$ to stabilize the operation of the entire system. Without considering $\mathrm{CPU}_{\mathrm{seq2}}$, the optimization of sequence one would conclude and be applied immediately at t_{n+2}. Meanwhile, the control trajectory of sequence two at t_{n+2} would be optimized based on outdated predictions from sequence one. As a result, the current operation of sequence one would not influence the control decisions for sequence two. The presented scheme ensures that each sequence adapts its operations to align with the fixed operations of other sequences.

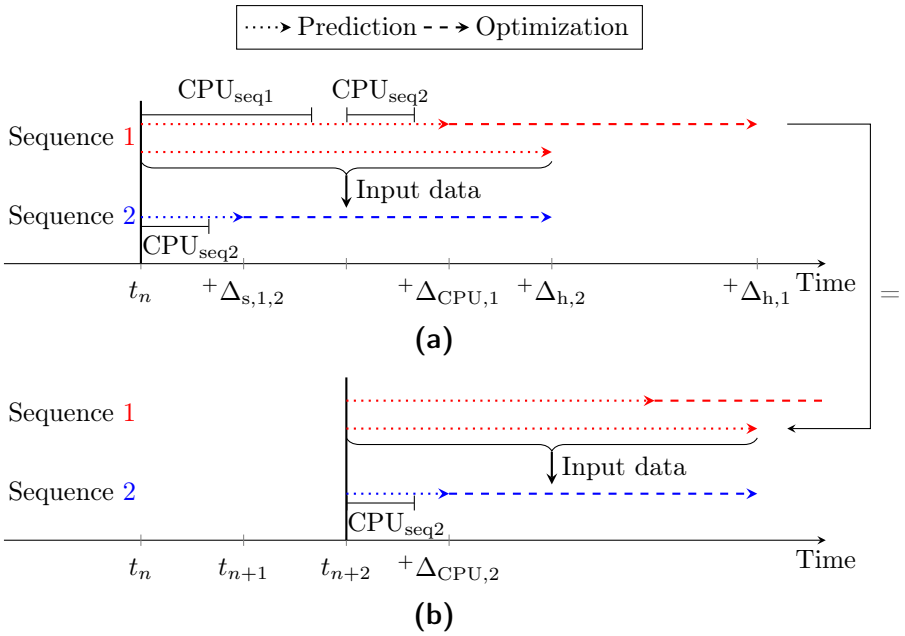

Figure 6.7.: Delay compensation with sequential coupling. In sequence one, the CPU time of sequence two is considered additionally. Once the optimization of sequence one concludes at time t_{n+2}, sequence two is optimized using the optimized input data from sequence one.

Simultaneously with the optimization of sequence one starting at time t_n, the output of sequence one is predicted using previous optimization results. The predicted output provides the necessary input data for the optimization of sequence two, which also begins at time t_n (cf. Figure 6.7a). Notably, the prediction horizon of sequence one ($\Delta_{\mathrm{h},1}$) must be sufficiently long to cover the entire prediction horizon of sequence two ($\Delta_{\mathrm{h},2}$) at each

sampling time. Since sequence two is optimized after sequence one, the computational delay of sequence one does not need to be considered. Thus, the total delay of sequence two is calculated as follows:

$$\Delta_{\mathrm{CPU},2} = \lceil \mathrm{CPU}_{\mathrm{seq2}} \rceil_{\Delta_{\mathrm{s},2}} . \tag{6.3}$$

6.3.3.2. Delay Compensation with Iterative Coupling

In the iterative coupling approach, the coupled subproblems are solved within one sequence with equal sampling times and prediction horizons (cf. Section 6.2.2). For the computational delay of this sequence ($\mathrm{CPU}_{\mathrm{seq}}$), we consider the maximum CPU times of the coupled subproblems ($\mathrm{CPU}_{\mathrm{sub}}$) and the maximum number of iterations (I_{max}):

$$\mathrm{CPU}_{\mathrm{seq}} = I_{\mathrm{max}} \cdot \sum_{\mathrm{sub} \in \mathrm{seq}} \mathrm{CPU}_{\mathrm{sub}} . \tag{6.4}$$

As illustrated in Figure 6.8 for two subsystems, the resulting maximum delay $\mathrm{CPU}_{\mathrm{seq}}$ is considered for the predictive simulation of all subsystems within the sequence.

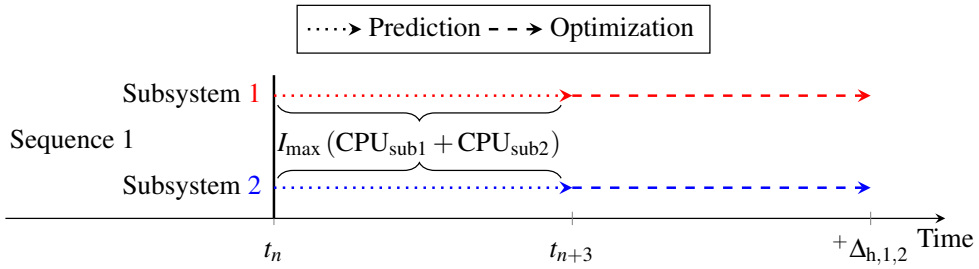

Figure 6.8.: Delay compensation with iterative coupling, illustrated for two subsystems. The maximum CPU times for the coupled subproblems ($\mathrm{CPU}_{\mathrm{sub},1,2}$) and the maximum number of iterations (I_{max}) are considered.

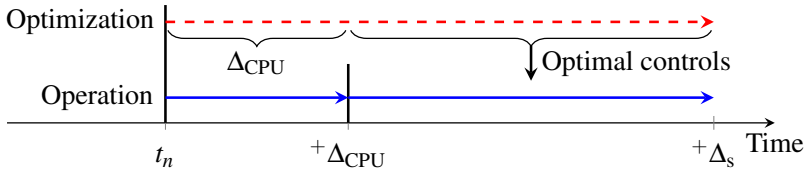

Figure 6.9.: An illustration showing a plant operation scenario where computational delay is considered, but without compensation in the controller model. The optimized controls are applied to the system once the optimization concludes at time $t_n + \Delta_{\mathrm{CPU}}$.

6.3.4. Computational Delay without Compensation

In our numerical studies, we also explore a scenario where we include the computational delay (Δ_{CPU}) in the operation of the plant surrogate during closed-loop simulations but without compensating for it in the controller model. Figure 6.9 schematically depicts this scenario, where the optimization process in the controller model initiates at t_n, but the optimized controls are applied only after the optimization concludes. Meanwhile, the operation of the plant advances based on the controls determined in the previous optimization.

6.4. Operational Scenarios and Strategies

We employ settings similar to those in Chapter 5. Here, we briefly describe the operational scenarios and strategies considered. We use historical data from the German day-ahead spot market on September 3 and 4, 2022 [177] to reflect the dynamics of electricity prices. Our closed-loop simulations span a time horizon of one day, during which we aim to meet constant product demands for biodiesel and glycerol under nominal conditions. Additionally, to compare the performances of the sequential and iterative DeNMPC strategies while considering computational delay compensation, we introduce a disturbance in the feed. Specifically, the composition of the vegetable oil feed undergoes a sudden change at 12 h and is only known (measured) to the DeNMPC controllers 30 min later (cf. Section 5.4.1 in Chapter 5).

In the closed-loop simulations, we employ the same process model for both the DeNMPC controllers and the plant surrogate, assuming full-state feedback with no plant-model mismatch. System states at the beginning of the simulations and the control variables for all eNMPC optimizations are initialized using the solution of an optimal SS operation (cf. Section 5.4.2.1 in Chapter 5). Additionally, we initialize the buffer tank holdups with half-full levels. Table 6.1 lists the prediction and control horizons, sampling times, and control discretizations for the three controllers in both the sequential and iterative strategies. Notably, the prediction horizons in sequence one are set to one hour longer than that in sequence two within both architectures, ensuring sequence one encompasses the entire prediction horizon of sequence two (cf. Section 6.2.2). The economic stage costs l_{stage} in (5.1) for the three eNMPC controllers include the operating costs for each corresponding process section and are defined in (5.5) in Section 5.4.2.4.

Table 6.1.: Settings for the three controllers in both sequential and iterative strategies, including control and prediction horizons, sampling times, and control discretizations.

	Sequential eNMPC			Iterative eNMPC		
	RSR	FAME	Glycerol	RSR	FAME	Glycerol
Control horizon [h]	10	9	9	10	10	9
Prediction horizon [h]	12	11	11	12	12	11
Sampling time [min]	15	15	15	15	15	15
Control discretization [min]	30	15	15	30	15	15

Furthermore, we benchmark our DeNMPC strategies against SS and offline DO counterparts, both utilizing centralized monolithic optimization. These benchmarks represent the lower and upper bounds of achievable operational flexibility. The lower bound represents SS operation without any flexibilization, while the upper bound reflects the best possible flexibilization achieved through offline DO. The SS operation excludes the use of any buffer tanks, whereas offline DO leverages all available buffer tanks through centralized optimization with a full-day prediction horizon. Additional information about these benchmarks can be found in Chapter 3 and Chapter 5. Table D.1 in Appendix D summarizes the process configurations, control variables, and operational constraints for each operational strategy. Notably, we incorporate economic endpoint constraints related to levels and purities in unit operations with holdups, including buffer tanks, to prevent

the optimization from exploiting initial tank conditions and to ensure recursive eNMPC feasibility.

6.5. Numerical Results and Discussion

We implement the process models in Modelica and use our open-source optimization framework DyOS [53] to solve the DO problems, employing direct single shooting. We use SNOPT [179] as the SQP solver and NIXE [178] as the DAE integrator, with integration tolerances set to 10^{-4} and NLP feasibility and optimality tolerances set to $5 \cdot 10^{-4}$. We perform all computations on an Intel(R) Core(TM) i7-1270P processor running at 4.8 GHz with 32 GB RAM.

We begin by presenting the results for both the sequential and iterative DeNMPC strategies under ideal computational conditions, i.e., without accounting for computational delays, as assumed in Chapter 5. In other words, the optimized control actions are computed and applied to the plant model instantaneously at each MPC step during the closed-loop simulations, assuming zero computational time for solving the DeNMPC optimization problems. Under these conditions, we compare the two DeNMPC strategies to the SS operation and offline DO benchmarks (cf. Chapter 5). Following this, we discuss the computational costs for both DeNMPC strategies, highlighting the necessity for delay compensation. Subsequently, we compare the performances of the two DeNMPC controllers under the feed disturbance while considering delay compensation. Finally, we underscore the need for delay compensation by comparing the DeNMPC strategies with counterparts that account for computational delays in the plant surrogate but lack any compensation scheme in the controller models (cf. Section 6.3.4).

6.5.1. Evaluation of the DeNMPC Strategies under Ideal Computational Conditions

As indicated in Table 6.2, both DeNMPC strategies demonstrate considerable energy cost savings compared to the SS operation. The presented energy costs are normalized by the total production amounts of the respective process sections, with the SS operation serving as the reference for normalization (cf. Section 5.5.1 in Chapter 5). Although the DeNMPC strategies operate with half the prediction horizon of the offline DO counterpart (cf. Table 6.1), the discrepancies in the savings are relatively modest. Notably, the sequential and iterative strategies yield similar results under the assumption of ideal computational conditions (i.e., zero computational time) in the closed-loop simulations, both resulting in savings of 20 %.

In Figure 6.10, we present the biodiesel production rates and the liquid levels in the final buffer tank of the biodiesel product (`FinalTankB`) and the intermediate buffer tank in the Glycerol section (`InterTankG`). We aim to demonstrate that both DeNMPC strategies perform similarly within the process sections compared to the presented benchmarks. For a more detailed analysis of the results, particularly the discrepancies between the DeNMPC strategies and the offline counterpart, refer to Section 5.7.2. As shown in Figure 6.10a, the production rates of biodiesel for the DeNMPC strategies exhibit an opposite trend to the electricity price profile, resembling that of the offline DO counterpart and in contrast to

the SS operation. Notably, the iterative strategy results in a smoother profile, primarily due to the non-fixed outlet stream of `InterTankOil`, unlike the sequential strategy.

Table 6.2.: Normalized energy costs for all operational strategies considered, under nominal conditions and without considering computational delay in closed-loop simulations, both total and for each of the three process sections. Savings compared to SS operation are provided in parentheses.

	Normalized energy costs [k€]			
	RSR	FAME	Glycerol	Total
Steady-state	11.8	77.5	19.6	108.9
Offline	9.3 (21 %)	56.8 (26.7 %)	13.5 (31.2 %)	79.6 (26.9 %)
Sequential	10.8 (7.9 %)	60.4 (22.2 %)	16.2 (17.4 %)	87.4 (19.8 %)
Iterative	10.6 (9.4 %)	60.3 (22.3 %)	16.3 (16.9 %)	87.2 (19.9 %)

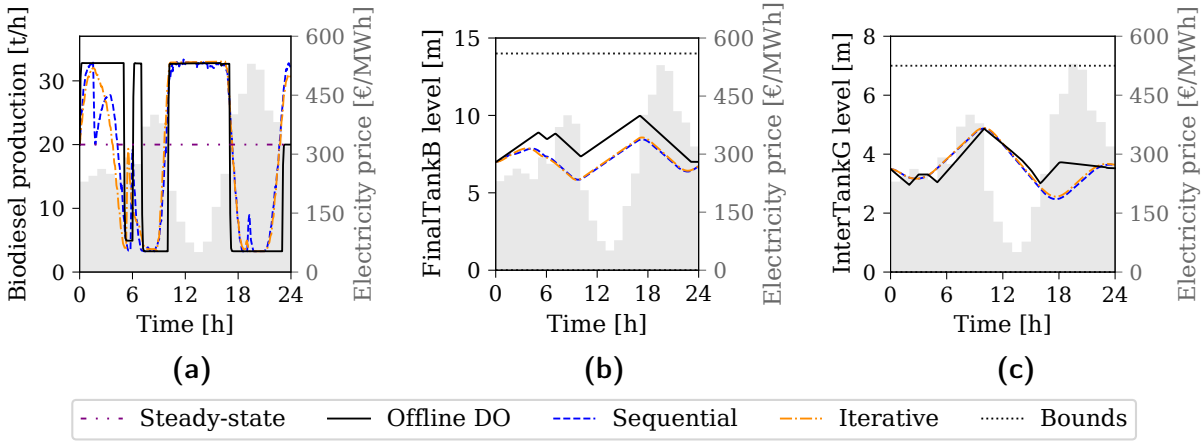

Figure 6.10.: Biodiesel production rate (a) and liquid levels in `FinalTankB` (b) and `InterTankG` (c) for the considered operational strategies. The gray area represents the electricity price profile.

However, because the DeNMPC strategies have a 12-hour prediction horizon, the later increase in electricity prices is initially unknown, leading to production rates that do not fully align with that of the offline DO counterpart, particularly with lower production rates early in the day. This is evident in the absolute values of `FinalTankB` levels in Figure 6.10b, which are shifted to lower values compared to the offline DO results. Furthermore, compared to the offline DO results, the DeNMPC strategies demonstrate increased production rates during the final hours to meet endpoint constraints and achieve the total required production (cf. Figure 6.10a and Figure 6.10b). Additionally, Figure 6.10b and Figure 6.10c illustrate that the two DeNMPC strategies utilize the buffer tanks in the FAME and Glycerol sections similarly. Specifically, excess production is stored in the final buffer tanks during periods of low electricity prices (cf. Figure 6.10b) to be used during higher-price periods. Conversely, the intermediate buffer tanks (cf. Figure 6.10c) exhibit the opposite behavior compared to the final buffer tanks.

Figure 6.11 further illustrates the operational differences between the sequential and iterative DeNMPC strategies. Overall, the iterative strategy demonstrates behavior more

aligned with the offline DO compared to the sequential strategy. This is clear in the profiles of the liquid level in the transesterifier and the temperature setpoint of the FAME column reboiler depicted in Figure 6.11a and Figure 6.11b, respectively. From 14 h onward, the transesterifier liquid level for the sequential strategy decreases compared to the offline DO, unlike the iterative counterpart. Notably, the temperature setpoint of the FAME column reboiler, a control variable, exhibits more fluctuations and diverges more from the offline DO in the sequential strategy than in the iterative approach. This discrepancy primarily arises from the greater degrees of freedom available in the iterative approach for the residual oil recycle stream. In the sequential strategy, fixing the outlet flow rate of `InterTankOil` leads to different behavior with more oscillating control variables due to the imposed constraint. Additionally, for the sequential approach, the state variables, exemplified by the oil purity in the FAME column reboiler in Figure 6.11c, exhibit more fluctuations compared to the iterative counterpart, for the same aforementioned reasons. Utilizing the outlet stream of `InterTankOil` as a control variable in the iterative strategy brings its operation closer to that of a centralized optimization, as demonstrated in comparison to the offline DO.

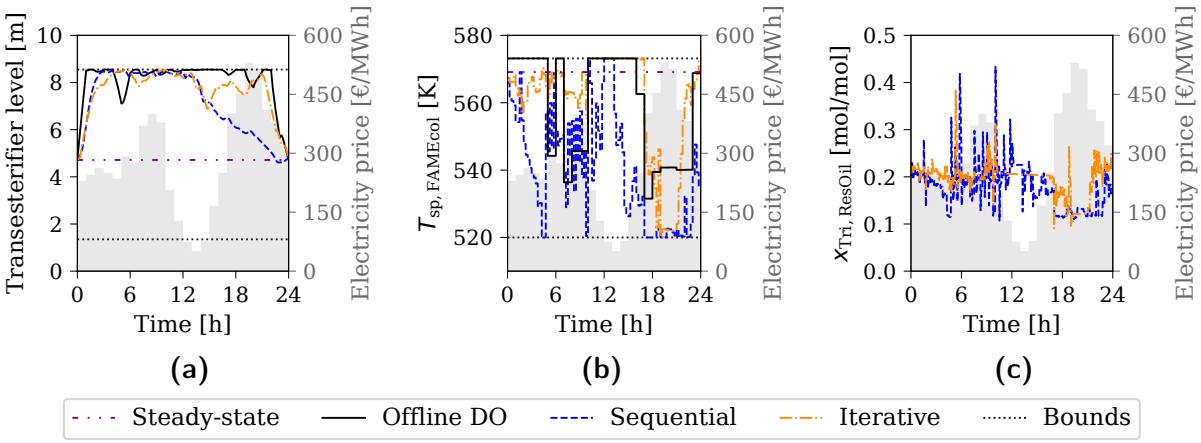

Figure 6.11.: Transesterifier liquid level (a) and temperature setpoint of the FAME column reboiler (b) for all operational strategies considered. Comparison of the oil purity in the reboiler of the FAME column for the two DeNMPC strategies (c). The gray area depicts the electricity price profile.

6.5.2. eNMPC Computational Costs

Table 6.3 outlines the CPU times required to solve the DO problems for the two DeNMPC strategies. In the sequential strategy, the CPU times for solving $\text{eNMPC}_{\text{RSR}}$ are considered for sequence one, while the maximum values between the CPU times for $\text{eNMPC}_{\text{FAME}}$ and $\text{eNMPC}_{\text{Glycerol}}$ are used for sequence two. Conversely, in the iterative strategy, we account for the total CPU times required to solve $\text{eNMPC}_{\text{RSR}}$ and $\text{eNMPC}_{\text{FAME}}$ iteratively in sequence one until either the convergence condition in (6.1) is met or the maximum number of iterations is reached. For sequence two, the CPU times for solving $\text{eNMPC}_{\text{Glycerol}}$ are considered.

Both DeNMPC strategies have mean and maximum CPU times in sequence one less than the sampling time (cf. Table 6.1). Thus, the required computational delay ($\Delta_{\text{CPU},1}$)

for both strategies in the compensation scheme in (6.2) (for coupling two sequences) is 30 min, equivalent to two sampling time intervals. This delay is set to 30 min, rather than 15 min, because our compensation approach for sequential coupling accounts for the delays in subsequent sequences when calculating the delay for preceding ones, as described in Section 6.3.3.1. Thus, the compensation scheme for sequence one includes not only its own 15 min delay but also an additional 15 min to account for the delay in sequence two. Therefore, we implement the compensation scheme presented in Section 6.3.2 over two sampling time intervals in sequence one for both DeNMPC strategies. On the other hand, the compensation scheme over one sampling time interval (cf. Section 6.3.1) is used in sequence two for both strategies, as $\Delta_{\mathrm{CPU},2} = 15\,\mathrm{min}$ in (6.3) (i.e., there are no subsequent sequences after sequence two).

While all required CPU times fall below the eNMPC sampling times, they remain considerable, especially for sequence one in the iterative strategy, emphasizing the need for the delay compensation schemes. Notably, the closed-loop performance of the iterative approach, particularly in sequence one, is anticipated to be more affected by computational delays compared to the sequential approach, as indicated by the CPU time results for sequence one in Table 6.3.

With the scaling used in the convergence condition in (6.1) and since we take the maximum cumulative difference in all control trajectories between $\mathrm{eNMPC_{RSR}}$ and $\mathrm{eNMPC_{FAME}}$, setting $\epsilon = 0.01$ is sufficient to ensure that the dynamic operation of the system remains substantially unchanged in the iterative algorithm. Furthermore, as discussed for the iterative architecture in Section 6.2.1, only a few iterations are required to meet this convergence condition. Accordingly, we set $I_{\max} = 4$. During the closed-loop simulations, this convergence condition is satisfied in all MPC sampling instances for $i \leq I_{\max}$, except for the sampling instance at 10 h, where a value of 0.02 is reached. Nevertheless, all solutions remain feasible. The mean and standard deviation for the number of iterations i are 2.7 and 0.6, respectively, while for the maximum cumulative deviations in the control trajectories in (6.1), the values are both 0.003.

Table 6.3.: Required CPU times for solving the DO problems within the considered DeNMPC strategies. In the sequential strategy, $\mathrm{eNMPC_{FAME}}$ and $\mathrm{eNMPC_{Glycerol}}$ are solved concurrently in sequence two. In the iterative strategy, $\mathrm{eNMPC_{RSR}}$ and $\mathrm{eNMPC_{FAME}}$ are solved iteratively in sequence one until a termination criterion is met.

		CPU time [s]		
		Mean	Maximum	Standard deviation
Sequential	$\mathrm{eNMPC_{RSR}}$	179	387	87
	$\mathrm{eNMPC_{FAME}}$	67	121	27
	$\mathrm{eNMPC_{Glycerol}}$	67	164	37
	Sequence 1	179	387	87
	Sequence 2	83	164	30
Iterative	$\mathrm{eNMPC_{RSR}}$	302	814	121
	$\mathrm{eNMPC_{FAME}}$	53	150	26
	$\mathrm{eNMPC_{Glycerol}}$	47	116	16
	Sequence 1	354	859	127
	Sequence 2	47	116	16

6.5.3. Comparison of the DeNMPC Strategies with Delay Compensation under Feed Disturbance

As shown in Table 6.4, the energy cost savings under the feed disturbance, while considering delay compensation, decrease for the sequential strategy compared to the iterative counterpart, accounting for 13.2 % and 18.5 %, respectively. This discrepancy primarily stems from the lower savings observed in the RSR and FAME sections for the sequential strategy. The iterative optimization within the RSR and FAME sections in the iterative strategy leads to better closed-loop performance and thus higher cost savings, attributed to the increased degrees of freedom available through the manipulation of the residual oil recycle stream. Furthermore, in Chapter 5, the sequential strategy yields 17 % savings for the same disturbance but under ideal closed-loop computational conditions. This difference compared to the current savings under non-ideal computational conditions highlights the impact of computational delay on the closed-loop performance of the sequential strategy.

Table 6.4.: Normalized energy costs for the proposed DeNMPC strategies under the feed disturbance, accounting for computational delay compensation in closed-loop simulations. Total costs and costs for each of the three process sections are presented, with savings compared to the corresponding SS operation provided in parentheses.

	Normalized energy costs [k€]			
	RSR	FAME	Glycerol	Total
Steady-state	13.6	77	19.4	110
Sequential	11.7 (14 %)	66 (14.3 %)	17.8 (8.3 %)	95.5 (13.2 %)
Iterative	11 (19.1 %)	61 (20.8 %)	17.6 (9.3 %)	89.6 (18.5 %)

Figure 6.12 illustrates the superior closed-loop performance of the iterative strategy compared to its sequential counterpart under the current scenario, explaining the reasons behind the lower energy cost savings for the sequential approach. Despite electricity prices remaining low until 18 h, the biodiesel production rate, shown in Figure 6.12a, begins to decline around 15 h in the sequential strategy, unlike in the iterative strategy. This trend is also reflected in Figure 6.12b, where the liquid levels in `FinalTankB` plateau despite the low prices between 15 h and 18 h. In contrast, the iterative strategy adjusts the outlet flow of `InterTankOil` as a control variable in response to the disturbance after it is detected at 12.5 h. As shown in Figure 6.12c, the outlet flow rate of `InterTankOil` increases at 12.5 h compared to the nominal operational scenario for the iterative strategy (depicted by the solid black line).

The considered feed disturbance results in more unreacted oil entering the FAME section, leading to higher residual oil quantities in the bottom of the FAME column, which explains the increase in the outlet stream of `InterTankOil` for the iterative strategy. Conversely, in the sequential strategy, this stream remains fixed, constraining the flexible operation of the FAME section. Specifically, the outlet stream of the intermediate tank `InterTankB` cannot sustain an increased flow rate between 15 h and 18 h, resulting in reduced production through the FAME column, as shown in Figure 6.12a. Without flexibility in adjusting the outlet of `InterTankOil`, the endpoint constraints at 24 h for the levels in `FinalTankB` and `InterTankOil` would not be met due to increased oil quantities in the FAME column bottom. This is evident from the earlier increase in the biodiesel production rate around

19 h in the sequential approach (cf. Figure 6.12a) to fulfill the total production quantity and endpoint constraints. In contrast, production in the iterative counterpart begins to rise later, around 22 h. Notably, in Chapter 5, where computational delays are overlooked, the feed disturbance do not impact closed-loop performance in the sequential strategy as it does in the current scenario.

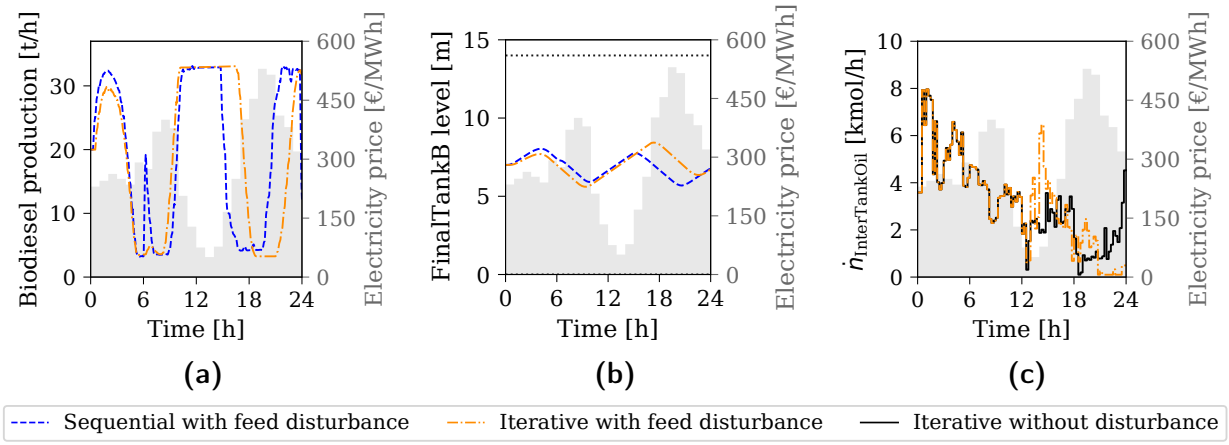

Figure 6.12.: Results for the two DeNMPC strategies under the feed disturbance with delay compensation. Biodiesel production rate (a), liquid level in `FinalTankB` (b), and outlet flow from `InterTankOil` as a control variable in the iterative strategy (c).

Table 6.5.: Total control actions $\Sigma_{\Delta u}$ for the sequential and iterative DeNMPC strategies under the feed disturbance, both with and without compensation for computational delays. The $\Sigma_{\Delta u}$ values of all control variables for the controllers are compared.

	$\Sigma_{\Delta u}$ for sequential		$\Sigma_{\Delta u}$ for iterative	
	Delay comp.	No delay comp.	Delay comp.	No delay comp.
$\dot{n}_{\text{Oil}}$ [kmol/h]	83	110	68	82
$\dot{n}_{\text{Base}}$ [kmol/h]	118	130	105	112
$\dot{n}_{\text{MeOH}}$ [kmol/h]	189	250	198	245
ΔT_{Jacket} [K]	28	26	30	27
$\dot{n}_{\text{TransOut}}$ [kmol/h]	342	320	331	357
$T_{\text{sp,MeOHcol}}$ [K]	16	20	21	19
$\dot{n}_{\text{InterTankB}}$ [kmol/h]	138	128	76	96
$T_{\text{sp,FAMEcol}}$ [K]	80	100	49	98
$\dot{n}_{\text{InterTankG}}$ [kmol/h]	113	118	112	109
$T_{\text{sp,GLYcol}}$ [K]	57	55	55	82
$\dot{n}_{\text{InterTankOil}}$ [kmol/h]	–	–	10	13

6.5.4. Effects of Computational Delay

We further compare the two DeNMPC strategies under the feed disturbance with counterparts that do not incorporate any delay compensation schemes in the control algorithm, while accounting for the computational delay in solving the DO problems in the plant surrogate (cf. Section 6.3.4). Table 6.5 provides the total control actions $\Sigma_{\Delta u}$ executed by

the control variables of the two DeNMPC controllers for strategies with and without delay compensation. This control action metric represents the cumulative control steps executed by the DeNMPC controllers (cf. Section 5.5.2 in Chapter 5). Overall, $\Sigma_{\Delta u}$ is lower for most control variables in both DeNMPC strategies with delay compensation compared to those without, indicating the impact of computational delay on closed-loop stability.

Figure 6.13a and Figure 6.13b depict the temperature setpoint of the FAME column reboiler and the oil purity of its liquid content for the iterative strategy with and without delay compensation, under the feed disturbance. The strategy that neglects computational delay in the controller scheme exhibits greater fluctuations in both the temperature control and purity state variables, demonstrating the stabilizing effects of considering delay compensation.

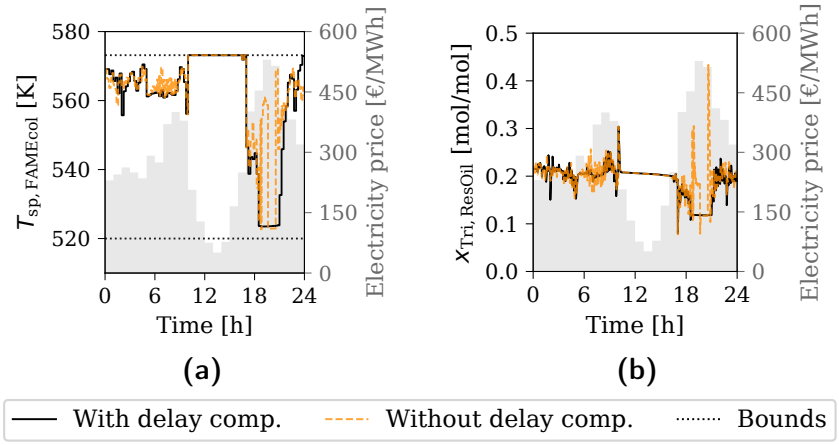

Figure 6.13.: Results for the iterative strategy with and without delay compensation under feed disturbance. Temperature setpoint of the FAME column reboiler (a) and oil purity in the reboiler of the FAME column (b).

Furthermore, when delay compensation is not incorporated, the energy cost savings for the sequential strategy remain similar to those of its counterpart that includes delay compensation. However, for the iterative strategy, the savings drop to 17.7 % (cf. Table 6.4). As mentioned in Section 6.5.2, since the CPU times are higher for the iterative strategy, especially for sequence one, neglecting computational delays impacts it more compared to the sequential counterpart. Notably, the decrease from 18.5 % to 17.7 % for the iterative strategy when neglecting the computational delay is mainly due to the reduced performance of eNMPC$_{\text{RSR}}$. The savings in the RSR section drop to 17.4 %, down from 19.1 %. Therefore, incorporating computational delay compensation in the applied DeNMPC strategies not only improves closed-loop stability but also enhances performance, leading to higher energy cost savings, particularly in the iterative strategy.

Using shorter prediction horizons in the iterative strategy, thereby reducing computational times, could mitigate the effects of not compensating for computational delays in the control algorithm. However, the observed drop in energy cost savings (from 18.5 % to 17.7 %) suggests that the negative impact on closed-loop performance from shorter prediction horizons may be more significant than from neglecting computational delays. In contrast, for the currently applied prediction horizons in the sequential strategy, as mentioned earlier, the energy cost savings remain consistent even without delay compensation due to the relatively low computational times (cf. Table 6.3). While extending prediction

horizons in the sequential strategy could potentially improve closed-loop performance, it may also increase the effects of computational delays, potentially offsetting the performance benefits.

6.6. Conclusion

We present DeNMPC with computational delay compensation, employing both sequential and iterative communication architectures. Notably, our delay compensation scheme considers compensation over multiple sampling time intervals and addresses considerations with both sequential and iterative couplings. We assess the performance of sequential and iterative DeNMPC strategies in optimizing the flexible operation of biodiesel production under fluctuating electricity prices. Under ideal computational conditions (i.e., zero computational time), both DeNMPC strategies yield similar energy cost savings compared to SS operation. Overall, the iterative approach exhibits operation closer to that of a centralized optimization, as demonstrated in comparison to the offline DO, mainly due to utilizing the outlet stream of `InterTankOil` (the oil recycle) as a control variable.

Our numerical findings underscore the significant impact of computational delays on the closed-loop performance of DeNMPC strategies. In particular, accounting for computational delays in closed-loop simulations with compensation schemes reveals superior closed-loop performance of the iterative strategy under practical disturbances compared to the sequential counterpart. This advantage stems from the greater degrees of freedom available in optimization within the iterative architecture with bidirectional communication, allowing for better adaptability to feed disturbances through iterative optimization of the oil recycle stream and data exchange between upstream and downstream processes during closed-loop optimizations.

The proposed delay compensation scheme effectively mitigates the adverse effects of computational delays on closed-loop stability and operational performance. It enables more stable control and enhanced energy cost savings in flexible biodiesel production, particularly for the iterative DeNMPC. However, future research could explore further improvements in delay compensation techniques, investigate more complex control architectures, and examine the applicability of these strategies in other chemical process applications to ensure stability and optimized economic performance. Additionally, while our DeNMPC strategies are based on independent, non-cooperative objective functions, future work might consider employing global objective functions to potentially enhance closed-loop performance further. Although using global objectives demands data exchange within the distributed control framework, leading to higher computational burdens, low-order models in a hierarchical structure offer a promising solution for tractable applications. Specifically, reduced models incorporating only the relevant process dynamics could be used at a higher control level to coordinate data communication among the DeNMPC controllers.

7. Conclusion and Outlook

In this dissertation, we focus on developing and applying the necessary methods and tools to achieve optimal flexible operation of electrified and renewable-powered chemical processes under fluctuating electricity prices. To conclude, we summarize the key findings, draw conclusions, and outline potential directions for future research. Figure 7.1 highlights the dissertation's main findings and perspectives after the development and application of the modeling and optimization framework shown in Figure 1.2, achieving the objectives for optimal flexible operation of electrified biodiesel production.

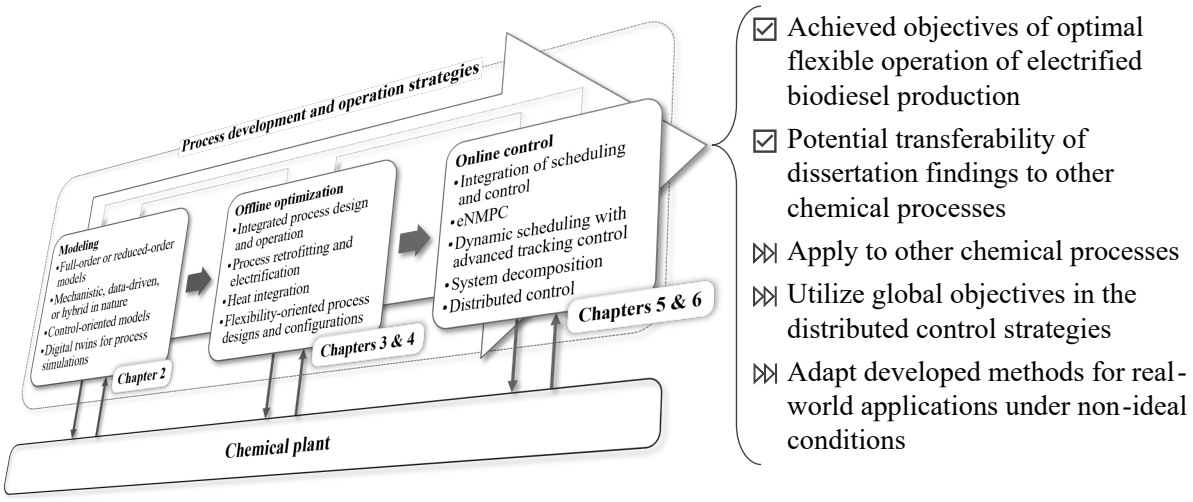

Figure 7.1.: Key findings and perspectives of the dissertation following the development and application of the modeling and optimization framework presented in Figure 1.2, fulfilling the objectives for optimal flexible operation of electrified biodiesel production.

This dissertation explores in depth the stages of model development, offline optimization, and online control within the process systems framework illustrated in Figure 1.2, with the goal of achieving optimal flexible operation. We emphasize the importance of considering the interconnectivity and mutual influences between these stages during both the development and real-time application phases. Starting with the definition of objectives for optimized flexible operation, we systematically address several topics related to the flexible operation of dynamic processes. Specifically, we focus on optimizing in silico the flexible operation of an electrified biodiesel production process—based on the alkali-catalyzed homogeneous transesterification of vegetable oil—under fluctuating electricity prices. As model-based strategies are essential, the first step involves developing mathematical models of the process, tailored to support the desired outcomes. Next, we examine offline DO studies alongside flexibility-oriented process designs, demonstrating that when chemical processes are electrified and powered by renewable energy, novel process designs and operational strategies rooted in flexibility may emerge as a new paradigm for chemical

plant operations. Finally, we integrate scheduling and control through online-tractable eNMPC, leveraging the developed models and offline strategies to achieve optimal flexible operations. We demonstrate that process dynamics must be accounted for to enable both optimal and feasible flexible operation. Neglecting these dynamics results in performance losses, suboptimal, or even infeasible process behavior, hindering effective DSM. This dissertation demonstrates how modeling approaches, optimization methods, and control strategies can be developed and applied to tailor dynamic processes for flexible operations. We illustrate that optimal flexible operation has substantial economic potential and that incorporating flexibility considerations into process design can unlock this potential.

In Chapter 2, we describe the model development phase outlined in Figure 1.2, presenting a modular and rigorous mechanistic dynamic model for the biodiesel production process, which is made available as open-source. Additionally, we apply and compare two PWC structures based on differing assumptions of measurement availability. The first PWC structure assumes access to advanced measurement configurations, including species concentration data from technologies like Raman spectroscopy, while the second relies on conventional measurement setups that monitor standard process variables, reflecting current industry practices. We evaluate the two PWC structures by simulating plant responses under various disturbance scenarios and production rate setpoint changes. While the first PWC structure performs well in terms of setpoint tracking and disturbance rejection, the second structure fails to consistently meet product quality specifications, demonstrating its inadequacy in maintaining the desired control objectives. This performance discrepancy underscores the need for more advanced control strategies, such as model-based control and estimation techniques, to overcome the limitations of conventional PID-based configurations. Thus, Chapter 2 underlines the importance of developing dynamic models that support advanced control strategies, forming the foundation for the offline optimization and online control strategies discussed in the subsequent chapters.

After model development, Chapter 3 and Chapter 4 focus on formulating offline DO strategies for achieving optimal flexible operation while considering flexibility-oriented process designs and configurations. In particular, we investigate how incorporating buffer tanks for storing intermediate and final products within the biodiesel production process can fully unlock production flexibility. We demonstrate that buffer tanks decouple the dynamics between different process sections, allowing each unit operation, and consequently the overall process, to reach its operational limits. Additionally, we show that flexibility extends beyond production rates to include product purities, as higher purification often requires increased energy consumption, particularly in distillation, and vice versa. In Chapter 4, we examine the impact of heat integration on process flexibility, highlighting how the incorporation of additional heating units increases the degrees of freedom for optimization, thus enhancing production flexibility. Specifically, while adding extra heating sources for reboilers may not be relevant when optimizing for SS profitability, we demonstrate that this configuration yields superior results during dynamic operation, especially when considering DSM. Furthermore, we explore configurations that support distributed optimization as opposed to centralized monolithic approaches, driven by the reduced computational burden associated with solving smaller DAE problems through system decomposition. These configurations are enabled by the critical role of buffer tanks in decoupling process dynamics. Consequently, the process configurations facilitating distributed optimization in Chapter 3 and Chapter 4 pave the way for online-tractable control applications, which are the focus of Chapter 5 and Chapter 6.

In Chapter 5 and Chapter 6, we address the final stage of the framework illustrated in Figure 1.2 by implementing DeNMPC to enable real-time control, thereby achieving the final objectives of optimal flexible operation of the biodiesel production process. Chapter 5 presents a DeNMPC scheme with sequential communication protocols under ideal computational conditions and compares it to conventional QSS. In a demand response scenario with fluctuating electricity prices, our DeNMPC strategy achieves substantial energy cost savings compared to SS operation while ensuring operational feasibility. Unlike QSS, which results in infeasible operations, our approach integrates scheduling and control tasks, demonstrating its suitability for frequent scheduling in chemical plants. Chapter 6 extends this work by introducing a DeNMPC scheme with iterative communication architectures and compares it to the sequential approach under non-ideal computational conditions. In this chapter, we incorporate delay compensation schemes into our DeNMPC strategies to address the impact of computational delays. Notably, our compensation scheme considers delays across multiple sampling intervals and addresses both sequential and iterative couplings. The proposed delay compensation scheme effectively mitigates the adverse effects of computational delays on closed-loop stability and operational performance. Our numerical results highlight the significant impact of computational delays on the closed-loop performance of the DeNMPC strategies. Specifically, simulations incorporating delay compensation reveal superior closed-loop performance of the iterative strategy under practical disturbances compared to the sequential approach. This advantage arises from the greater degrees of freedom in optimization and bidirectional communication within the iterative architecture, allowing for better adaptation to disturbances by iterative optimizations.

The biodiesel production process examined in this dissertation shares several characteristics with many chemical processes, including the reaction, separation, and recycle components commonly found in chemical plants. It also features heat integration, a prevalent practice in modern industrial plants, as well as interconnected unit operations with relatively slow process dynamics. These similarities suggest that the findings of this dissertation are transferable to a broader class of chemical processes. Specifically, the modeling and optimization framework presented in Figure 1.2, along with the systematically developed methods and tools, can be effectively applied to other processes aiming for optimal flexible operation or other objectives where modeling- and optimization-based strategies are essential. This underscores the generalizability of the methodologies and approaches developed throughout this work. A key aspect of our methodology is the use of flexibility-oriented process designs to facilitate both optimal and real-time tractable control. Notably, the incorporation of buffer tanks plays a dual role: not only does it enhance operational flexibility, but it also enables the practical implementation of DeNMPC strategies. This is particularly relevant for chemical processes characterized by large-scale nonlinear systems, where distributed optimization through system decomposition facilitates achieving realizable control solutions. Such an integrated approach to process design and operation, which considers both operational flexibility and distributed control, shows great promise for applications in other chemical systems, especially those aiming for dynamic operation, such as DSM scenarios. While the general applicability of these strategies is promising, process-specific operational considerations and challenges may arise, such as the use of buffer tanks and the phase of stored products—whether liquid or vapor. Nevertheless, this dissertation underscores the emergence of novel operational strategies rooted in flexibility-oriented process design as a potential new paradigm for future chemical production.

While this dissertation covers a range of topics, it also uncovers promising avenues for

future research. Given the potential transferability of our findings to other chemical processes, it would be particularly interesting to apply our proposed methods and approaches to optimize the flexible operation of processes involving intermediate or final products in the vapor phase, where storage in buffer tanks would require liquefaction. Since liquefaction incurs additional energy costs, this would introduce a trade-off between enhancing process flexibility to take advantage of variable energy prices and the increased costs associated with liquefaction. Furthermore, our work focuses on retrofitting an existing chemical process for flexible operation by incorporating buffer tanks. Future research could explore integrating optimal process design and flexible operation from the outset, particularly in the context of designing new chemical plants or resizing unit operations to inherently support flexibility. Additionally, while we size the buffer tanks heuristically and based on literature findings, an alternative approach would be to formulate these also as optimization variables to be solved concurrently with the DO problems for flexible operation. This approach would involve employing stochastic programming, presenting an interesting direction for future work.

While our current DeNMPC strategies employ independent, non-cooperative objective functions, future research could explore the use of global objective functions to potentially enhance closed-loop performance. Although implementing global objectives would require increased data exchange within the distributed control framework, resulting in higher computational costs, using low-order models in a hierarchical structure could offer a feasible solution. Specifically, simplified models that capture only the most relevant process dynamics could be employed at a higher control level to facilitate data coordination among DeNMPC controllers. However, these reduced models might not fully capture all system dynamics, potentially limiting the consideration of operational constraints.

In addition to distributed control strategies and system decomposition, future work could explore model-reduction techniques, such as data-driven or hybrid models, or their integration with distributed control to enable real-time tractable control. This is particularly promising due to the trade-off between the high controller performance and model accuracy provided by mechanistic models and the reduced computational effort and enhanced tractability offered by data-driven models. Moreover, determining the required level of optimality (ranging from fast-update approaches to global optimality via local solutions) and the appropriate model complexity for satisfactory process operation remains an open question for future studies on optimal flexible operation.

Since the majority of methods proposed in this dissertation rely on DO, leveraging parallel computing to accelerate DO is another promising direction for future research. Additionally, the use of DO with CCs could be explored for rigorous process design to achieve high operational flexibility, including optimal start-up and shutdown strategies. Another promising research area is the deterministic global optimization of dynamic problems. While local DO is relatively mature and widely applicable, global DO remains computationally intensive and impractical for many real-world applications. Future efforts should target scenarios where local optimization is insufficient—either because a global optimum is necessary or because multiple local optima hinder convergence to a satisfactory solution.

Furthermore, we develop and apply the methods and strategies in this dissertation within idealized settings. To ensure their practical relevance, it is crucial to adapt them for real-world applications, both for small- and large-scale industrial processes operating under nonideal conditions. This transition introduces increased uncertainty, potentially impact-

ing the performance of operational strategies and adding system complexity. Specifically, integrating these tools into actual process control systems for flexible industrial operation will require building confidence in the computational methods and addressing potential security concerns.

Appendix A.

Dynamic Modeling and Plantwide Control of a Production Process for Biodiesel and Glycerol

Herein, we first present the full mathematical model of the process. Subsequently, we provide the process flowsheet for implementing the PWC-B structure. We then compare the SS results of our model simulation with that of Aspen Plus in tabular form.

A.1. Full Process Model

We provide details on the models of the main unit operations and relevant thermodynamic properties.

A.1.1. Unit Operations Models

In this section, we provide the dynamic models of the transesterifier, distillation columns, wash column, and heat exchangers.

A.1.1.1. Transesterifier

We abbreviate triolein, diolein, monoolein, methanol, methyl oleate, and glycerol to TG, DG, MG, ME, MO, and G, respectively. We assume for the alkali-catalyzed transesterification of oil with methanol, the following reversible three-step reaction system [73, 86, 117, 127]:

$$\text{triolein} + \text{methanol} \underset{k_{1\mathrm{r}}}{\overset{k_{1\mathrm{f}}}{\rightleftharpoons}} \text{diolein} + \text{methyloleate}\,, \tag{A.1a}$$

$$\text{diolein} + \text{methanol} \underset{k_{2\mathrm{r}}}{\overset{k_{2\mathrm{f}}}{\rightleftharpoons}} \text{monoolein} + \text{methyloleate}\,, \tag{A.1b}$$

$$\text{monoolein} + \text{methanol} \underset{k_{3\mathrm{r}}}{\overset{k_{3\mathrm{f}}}{\rightleftharpoons}} \text{glycerol} + \text{methyloleate}\,, \tag{A.1c}$$

where $k_{j\mathrm{f}}$ and $k_{j\mathrm{r}}$, $j \in \{1, 2, 3\}$, are the reaction rate coefficients of the respective forward (f) and reverse (r) reactions of reaction j and determined by the Arrhenius equation [213]:

$$k_{j\{\mathrm{f,r}\}} = A_{j\{\mathrm{f,r}\}} \exp\left(\frac{-E_{j\{\mathrm{f,r}\}}}{RT}\right).$$

The pre-exponential factor $A_{j\{\mathrm{f,r}\}}$ and the activation energy $E_{j\{\mathrm{f,r}\}}$ values of the three reactions are taken from Narváez et al. [117] and Aspen Technology [214], and are summarized in Table A.1. The temperature of the reactor content and the universal gas constant are T and R, respectively.

Table A.1.: Pre-exponential factor $A_{j\{\mathrm{f,r}\}}$ and activation energy $E_{j\{\mathrm{f,r}\}}$ values for the three alkali-catalyzed transesterification reactions j, taken from Narváez et al. [117] and Aspen Technology [214].

$j\{\mathrm{f,r}\}$	$A_{j\{\mathrm{f,r}\}} \times 10^{-3}$		$E_{j\{\mathrm{f,r}\}}$ [kJ/mol]
1f	31174	$[\mathrm{L}^2/(\mathrm{mol}^2\,\mathrm{s})]$	56.48
1r	17.26	$[\mathrm{L}/(\mathrm{mol}\,\mathrm{s})]$	43.10
2f	62408595	$[\mathrm{L}^2/(\mathrm{mol}^2\,\mathrm{s})]$	72.80
2r	200324	$[\mathrm{L}/(\mathrm{mol}\,\mathrm{s})]$	67.78
3f	0.897	$[\mathrm{L}^2/(\mathrm{mol}^2\,\mathrm{s})]$	25.94
3r	29.81	$[\mathrm{L}/(\mathrm{mol}\,\mathrm{s})]$	49.79

Following second-order elementary rate laws, the reaction rates r_j are then:

$$r_1 = k_{1\mathrm{f}}\, C_{\mathrm{TG}}\, C_{\mathrm{ME}}\, C_{\mathrm{NaOH}} - k_{1\mathrm{r}}\, C_{\mathrm{MO}}\, C_{\mathrm{DG}}\,,$$

$$r_2 = k_{2\mathrm{f}}\, C_{\mathrm{DG}}\, C_{\mathrm{ME}}\, C_{\mathrm{NaOH}} - k_{2\mathrm{r}}\, C_{\mathrm{MO}}\, C_{\mathrm{MG}}\,,$$

$$r_3 = k_{3\mathrm{f}}\, C_{\mathrm{MG}}\, C_{\mathrm{ME}}\, C_{\mathrm{NaOH}} - k_{3\mathrm{r}}\, C_{\mathrm{MO}}\, C_{\mathrm{G}}\,,$$

where C_i represents the concentration of species i in the reactor. The effect of the catalyst NaOH is considered in the forward reactions only [117, 214].

We model the total and species material balances as follows:

$$\frac{\mathrm{d}N}{\mathrm{d}t} = \dot{N}_{\mathrm{in}} - \dot{N}_{\mathrm{out}}\,,$$

$$\frac{\mathrm{d}n_{\mathrm{TG}}}{\mathrm{d}t} = \dot{n}_{\mathrm{TG}}^{\mathrm{in}} - \dot{n}_{\mathrm{TG}}^{\mathrm{out}} - r_1 V\,,$$

$$\frac{\mathrm{d}n_{\mathrm{DG}}}{\mathrm{d}t} = \dot{n}_{\mathrm{DG}}^{\mathrm{in}} - \dot{n}_{\mathrm{DG}}^{\mathrm{out}} + (r_1 - r_2)\, V\,,$$

$$\frac{\mathrm{d}n_{\mathrm{MG}}}{\mathrm{d}t} = \dot{n}_{\mathrm{MG}}^{\mathrm{in}} - \dot{n}_{\mathrm{MG}}^{\mathrm{out}} + (r_2 - r_3)\, V\,,$$

$$\frac{\mathrm{d}n_{\mathrm{ME}}}{\mathrm{d}t} = \dot{n}_{\mathrm{ME}}^{\mathrm{in}} - \dot{n}_{\mathrm{ME}}^{\mathrm{out}} - (r_1 + r_2 + r_3)\, V\,,$$

$$\frac{\mathrm{d}n_{\mathrm{MO}}}{\mathrm{d}t} = \dot{n}_{\mathrm{MO}}^{\mathrm{in}} - \dot{n}_{\mathrm{MO}}^{\mathrm{out}} + (r_1 + r_2 + r_3)\, V\,,$$

$$\frac{\mathrm{d}n_{\mathrm{G}}}{\mathrm{d}t} = \dot{n}_{\mathrm{G}}^{\mathrm{in}} - \dot{n}_{\mathrm{G}}^{\mathrm{out}} + r_3 V\,,$$

$$\frac{\mathrm{d}n_{\mathrm{NaOH}}}{\mathrm{d}t} = \dot{n}_{\mathrm{NaOH}}^{\mathrm{in}} - \dot{n}_{\mathrm{NaOH}}^{\mathrm{out}}\,,$$

$$\frac{\mathrm{d}n_{\mathrm{H_2O}}}{\mathrm{d}t} = \dot{n}_{\mathrm{H_2O}}^{\mathrm{in}} - \dot{n}_{\mathrm{H_2O}}^{\mathrm{out}}\,,$$

where n_i, $\dot{n}_i^{\text{in}}$, and $\dot{n}_i^{\text{out}}$ are the species mole holdup, input, and output flow rates, respectively. The total input and output mole flow rates of the reactor are $\dot{N}_{\text{in}}$ and $\dot{N}_{\text{out}}$, respectively. We control $\dot{N}_{\text{out}}$ such that the residence time of the reactor content is 1 h. The volume of the reactor content V is determined from the total mole holdup N and the specific molar density of the mixture. The mixture density is determined using the Rackett equation (A.5).

We model the reactor and its jacket by the following energy balances.

$$\frac{\mathrm{d}Nh^{\text{total}}}{\mathrm{d}t} = \dot{N}_{\text{in}} h_{\text{in}}^{\text{total}} - \dot{N}_{\text{out}} h_{\text{out}}^{\text{total}} + U\frac{A}{N_s}\sum_{s=1}^{N_s}\left(T_{J,s} - T\right),$$

$$0 = \dot{N}_{\text{in}}^{\text{Jacket}}\left(h_{\text{in}}^{\text{Jacket},s} - h_{\text{out}}^{\text{Jacket},s}\right) - U\frac{A}{N_s}\left(T_{J,s} - T\right), \quad \forall\, s \in \{1, 2, \ldots, N_s\}.$$

The molar enthalpies of the reactor content, input and output flows are h^{total}, $h_{\text{in}}^{\text{total}}$ and $h_{\text{out}}^{\text{total}}$, respectively. They are determined based on the standard state as a reference state (cf. Section A.1.2.1). The overall heat transfer coefficient and area are U and A, respectively. A segment of the jacket is denoted by s and its content temperature is $T_{J,s}$. The number of jacket segments is N_s. The molar enthalpies of the input and output flows of each jacket segment are represented by $h_{\text{in}}^{\text{Jacket},s}$ and $h_{\text{out}}^{\text{Jacket},s}$, respectively.

A.1.1.2. Distillation Columns

For the columns, equilibrium equations, energy, and material balances are calculated for each stage. All three distillation columns of the process have total condensers. A column has M trays. A tray can generally have a feed, and an input or output heat flux. We model each tray $m \in \{1, 2, \ldots, M\}$ as follows:

$$\frac{\mathrm{d}N_m}{\mathrm{d}t} = L_{\text{in},m} + V_{\text{in},m} - L_{\text{out},m} - V_{\text{out},m} + F_m,$$

$$L_{\text{out},m} = \frac{N_m}{\tau_m}, \tag{A.2a}$$

$$N_m\frac{\mathrm{d}x_{i,m}}{\mathrm{d}t} = L_{\text{in},m}\left(x_{\text{in},i,m} - x_{i,m}\right) + V_{\text{in},m}\left(y_{\text{in},i,m} - x_{i,m}\right) - V_{\text{out},m}\left(y_{\text{out},i,m} - x_{i,m}\right) + F_m\left(z_{i,m} - x_{i,m}\right), \tag{A.2b}$$

$$y_{i,m}P_m = \gamma_{i,m}^{\text{l}} x_{i,m} P_{\text{vp},i,m},$$

$$0 = \sum_i y_{i,m} - \sum_i x_{i,m},$$

$$0 = L_{\text{in},m}\left(h_{\text{in},m}^{\text{l}} - h_{\text{out},m}^{\text{l}}\right) + V_{\text{in},m}\left(h_{\text{in},m}^{\text{v}} - h_{\text{out},m}^{\text{l}}\right) - V_{\text{out},m}\left(h_{\text{out},m}^{\text{v}} - h_{\text{out},m}^{\text{l}}\right) + F_m\left(h_m^{\text{feed}} - h_{\text{out},m}^{\text{l}}\right) + Q_m, \tag{A.2c}$$

where N_m is the total mole holdup on the tray m, $L_{\text{in},m}$ and $V_{\text{in},m}$ are the input liquid and vapor mole flow rates, $L_{\text{out},m}$ and $V_{\text{out},m}$ are the output liquid and vapor mole flow rates, respectively. The hydraulic parameter τ_m is applied for determining $L_{\text{out},m}$. The liquid and vapor mole fractions of species i are $x_{i,m}$ and $y_{i,m}$, respectively, which are equal to

their respective compositions $x_{\mathrm{out},i,m}$ and $y_{\mathrm{out},i,m}$ in the outlet flows. The liquid and vapor species mole fractions in the input flows are $x_{\mathrm{in},i,m}$ and $y_{\mathrm{in},i,m}$, respectively, $P_{\mathrm{vp},i,m}$ is the species vapor pressure, and $\gamma^{\mathrm{l}}_{i,m}$ is its activity coefficient. The total molar enthalpies of the input and output flows are $h_{\mathrm{in},m}$ and $h_{\mathrm{out},m}$, and their superscripts l and v indicate liquid and vapor phases, respectively. The feed mole flow rate is F_m, $z_{i,m}$ is the species mole fraction in the feed, and h^{feed}_m is the total molar enthalpy of the feed. We denote the input or output heat flux by Q_m.

For all trays, except for the feed tray, F_m is null. All trays have zero Q_m, except for the reboiler and condenser trays, it is positive nonzero and negative nonzero, respectively. For the condenser tray, $L_{\mathrm{in},m}$ and $V_{\mathrm{out},m}$ are null because the three columns have total condensers. The reboiler tray has no $V_{\mathrm{in},m}$. The $L_{\mathrm{out},m}$ of the reboiler tray is the bottom product and that of the condenser tray is split between the reflux stream and the distillate product after accumulating in a distillate drum.

The formulation of species material balance (A.2b) and total energy balance (A.2c) equations as well as (A.2a) is a result of the assumption that the tray holdup is only due to the liquid phase. For the energy balance, we apply a quasi-steady-state approximation, resulting in an index-1 DA system [130].

A.1.1.3. Wash Column

The wash column is a liquid-liquid extraction process, where we introduce water as the extraction solvent to remove the polar species from the raffinate stream containing the biodiesel product. Glycerol, water and methanol are extracted from the light oil-based raffinate stream to the heavy water-based extract stream.

The model of a tray $m \in \{1, 2, \ldots, M\}$ of the wash column with M trays reads:

$$\begin{aligned}
\frac{\mathrm{d}N_m}{\mathrm{d}t} &= E_{\mathrm{in},m} + R_{\mathrm{in},m} - E_{\mathrm{out},m} - R_{\mathrm{out},m}\,,\\
E_{\mathrm{out},m} &= \frac{N_m}{\tau_m}\,, && \text{(A.3a)}\\
N_m \frac{\mathrm{d}x^{\mathrm{E}}_{i,m}}{\mathrm{d}t} &= E_{\mathrm{in},m}\left(x^{\mathrm{E}}_{\mathrm{in},i,m} - x^{\mathrm{E}}_{i,m}\right) + R_{\mathrm{in},m}\left(x^{\mathrm{R}}_{\mathrm{in},i,m} - x^{\mathrm{E}}_{i,m}\right)\\
&\quad - R_{\mathrm{out},m}\left(x^{\mathrm{R}}_{\mathrm{out},i,m} - x^{\mathrm{E}}_{i,m}\right)\,, && \text{(A.3b)}\\
\gamma^{\mathrm{R}}_{i,m} x^{\mathrm{R}}_{i,m} &= \gamma^{\mathrm{E}}_{i,m} x^{\mathrm{E}}_{i,m}\,,\\
0 &= \sum_i x^{\mathrm{R}}_{i,m} - \sum_i x^{\mathrm{E}}_{i,m},\\
0 &= E_{\mathrm{in},m}\left(h^{\mathrm{E}}_{\mathrm{in},m} - h^{\mathrm{E}}_{\mathrm{out},m}\right) + R_{\mathrm{in},m}\left(h^{\mathrm{R}}_{\mathrm{in},m} - h^{\mathrm{E}}_{\mathrm{out},m}\right)\\
&\quad - R_{\mathrm{out},m}\left(h^{\mathrm{R}}_{\mathrm{out},m} - h^{\mathrm{E}}_{\mathrm{out},m}\right)\,, && \text{(A.3c)}
\end{aligned}$$

where E and R represent the extract and raffinate phases, respectively. The other variables, subscripts, and superscripts have the same indications as for the distillation column model. We apply a quasi-steady-state approximation for the energy balance (A.3c), resulting in an index-1 DA system. We also use the hydraulic parameter τ_m for determining $E_{\mathrm{out},m}$ in (A.3a). Assuming that the tray holdup is only due to the extract phase, we could formulate (A.3b), (A.3c), and (A.3a) as provided [130].

A.1.1.4. Heat Exchangers

We model the heat exchangers by dividing them into segments and solving energy balances on each segment. The metal wall between the two heat-exchanging streams is carbon steel (CS) with a density ρ_{CS} of 7842 kg/m^3 and a specific heat capacity $c_{p,\mathrm{CS}}$ of 0.49 kJ/(kg K). We denote the first and second streams exchanging heat through the CS wall by S1 and S2, respectively.

For a segment $m \in \{1, 2, \ldots, M\}$ of a heat exchanger with M segments, the model reads:

$$\begin{aligned} e_{\mathrm{CS}}\rho_{\mathrm{CS}}c_{p,\mathrm{CS}}\frac{\mathrm{d}T_{\mathrm{CS},m}}{\mathrm{d}t} &= U_{\mathrm{S2}}\left(T_{\mathrm{S2},m} - T_{\mathrm{CS},m}\right) - U_{\mathrm{S1}}\left(T_{\mathrm{CS},m} - T_{\mathrm{S1},m}\right) , \\ 0 &= \dot{N}_{\mathrm{S1}}\left(h^{\mathrm{in}}_{\mathrm{S1},m} - h^{\mathrm{out}}_{\mathrm{S1},m}\right) + U_{\mathrm{S1}}A_m\left(T_{\mathrm{CS},m} - T_{\mathrm{S1},m}\right) , \\ 0 &= \dot{N}_{\mathrm{S2}}\left(h^{\mathrm{in}}_{\mathrm{S2},m} - h^{\mathrm{out}}_{\mathrm{S2},m}\right) - U_{\mathrm{S2}}A_m\left(T_{\mathrm{S2},m} - T_{\mathrm{CS},m}\right) , \end{aligned}$$

where e_{CS} is the thickness of the metal wall, A_m is the heat transfer area of the segment, and U_{S1} and U_{S2} are the overall heat transfer coefficients on the sides of S1 and S2 streams, respectively.

A.1.2. Models of the Thermodynamic Properties

We first introduce the temperature-dependent equations used to determine the molar heat capacities, enthalpies, entropies, and Gibbs free energies of the system's species in the solid, liquid, and vapor phases. Second, we provide the used correlations for calculating the densities in the three phases. Finally, we provide the applied LLE, VLE, and VLLE models.

A.1.2.1. Heat Capacity, Enthalpy, Entropy, and Gibbs Free Energy Models

For determining the molar heat capacity at a constant pressure c_p, for both the solid and the liquid phases as a function of temperature, we use the DIPPR equation 100 for all species except for monoolein and FAME in the solid phase we use the DIPPR equation 102 [110].
DIPPR equation 100:

$$c^{\mathrm{s\,or\,l}}_{p,i} = C_{1i} + C_{2i}T + C_{3i}T^2 + C_{4i}T^3 + C_{5i}T^4 , \qquad C_{6i} \leq T \leq C_{7i} .$$

DIPPR equation 102:

$$c^{\mathrm{s}}_{p,i} = \frac{C_{1i}T^{C_{2i}}}{1 + C_{3i}/T + C_{4i}T^2} , \qquad C_{6i} \leq T \leq C_{7i} .$$

For the vapor-phase heat capacities, we apply the DIPPR equation 107 by Aly and Lee [215]:

$$c^{\mathrm{v}}_{p,i} = C_{1i} + C_{2i}\left(\frac{C_{3i}/T}{\sinh(C_{3i}/T)}\right)^2 + C_{4i}\left(\frac{C_{5i}/T}{\cosh(C_{5i}/T)}\right)^2 , \qquad C_{6i} \leq T \leq C_{7i} .$$

For each phase, the molar enthalpy h_i and entropy s_i of each species i are explicitly calculated based on analytical integration of:

$$\frac{\mathrm{d}h_i}{\mathrm{d}T} = c_{p,i}\,,$$
$$\frac{\mathrm{d}s_i}{\mathrm{d}T} = \frac{c_{p,i}}{T}\,,$$

using h_i^{ref} and s_i^{ref} at the standard state (25 °C and 1 bar) as reference values.

The molar Gibbs free energy g is then determined as follows:

$$g_i = h_i - Ts_i\,.$$

The solid, liquid, and vapor phases are denoted by s, l, and v, respectively. All the coefficients $C_{b,i}$, $b \in \{1, 2, \ldots, 7\}$, as well as the values of h_i^{ref} and s_i^{ref} are retrieved from DIPPR's Project 801 database [110].

To account for the enthalpy of mixing (h^E) in the liquid phase, we determine the excess Gibbs free energy (g^E) using the NRTL activity coefficient (γ) model, which we provide in Section A.1.2.3:

$$h^E = -RT^2\left[\frac{\partial(g^E/RT)}{\partial T}\right]_{P,x}\,,$$
$$g^E = RT\sum_i x_i \ln\gamma_i\,.$$

We observe that the enthalpy of mixing in liquid mixtures has negligible effects on the simulation results. Moreover, since there are ten chemical species present, determining h^E using the NRTL model increases the size of the DA system of the model drastically (doubling). In the proposed Modelica model we allow for both options, but in the shown simulation results we ignore the enthalpy of mixing.

A.1.2.2. Density Models

The process operates at low pressure values. Thus, for determining the the molar densities (ρ) in the vapor phase, we use the ideal gas law. For all species in the solid phase and for NaH_2PO_4 in the liquid phase, we use the DIPPR molar density equation 100 [110]:

$$\rho_i^{\mathrm{s\,or\,l}} = C_{1i} + C_{2i}T + C_{3i}T^2 + C_{4i}T^3 + C_{5i}T^4\,, \qquad C_{6i} \le T \le C_{7i}\,.$$

We use the DIPPR molar density equation 105 for the remaining species in the liquid phase except for water, we apply the DIPPR molar density equation 116 [110].
DIPPR equation 105:

$$\rho_i^{\mathrm{l}} = C_{1i}/C_{2i}^{1+(1-T/C_{3i})^{C_{4i}}}\,, \qquad C_{6i} \le T \le C_{7i}\,.$$

DIPPR equation 116:

$$\rho_i^{\mathrm{l}} = C_{1i} + C_{2i}\tau^{0.35} + C_{3i}\tau^{2/3} + C_{4i}\tau + C_{5i}\tau^{4/3}\,, \qquad C_{6i} \le T \le C_{7i}\,,$$

where

$$\tau = 1 - \frac{T}{T_{\mathrm{ci}}} \,.$$

We determine the molar density of a liquid mixture (ρ_m^{l}) by applying the Rackett equation [132]:

$$\rho_m^{\mathrm{l}} = \frac{P_{cm}}{RT_{cm}{Z_{cm}}^{1+(1-T_r)^{2/7}}} \,, \tag{A.5}$$

where

$$T_{cm} = \sum_i \sum_j x_i x_j \left(V_{ci} V_{cj}\right) \left(T_{ci} T_{cj}\right)^{1/2} \left(1 - k_{ij}\right) / V_{cm}^2 \,,$$

$$k_{ij} = 1 - \frac{8 \left(V_{ci} V_{cj}\right)^{1/2}}{\left(V_{ci}^{1/3} + V_{cj}^{1/3}\right)^3} \,,$$

$$\frac{T_{cm}}{P_{cm}} = \sum_i x_i \frac{T_{ci}}{P_{ci}} \,,$$

$$Z_{cm} = \sum_i x_i Z_{ci} \,,$$

$$V_{cm} = \sum_i x_i V_{ci} \,,$$

$$T_r = T / T_{cm} \,.$$

For every species i or j, T_{ci} or T_{cj}, P_{ci} or P_{cj}, and V_{ci} or V_{cj} denote the species critical temperature, pressure, and volume, respectively. The species mole fraction in the liquid phase is represented by x_i or x_j, Z_{ci} indicates the species critical compressibility factor, and T_r is the reduced temperature of the mixture. The mixture's critical temperature, pressure, volume, and compressibility factor are denoted by T_{cm}, P_{cm}, V_{cm}, and Z_{cm}, respectively.

A.1.2.3. Equilibrium Models

For describing the LLE, VLE, and VLLE, we apply the isofugacity conditions. In general these are necessary only (i.e., not sufficient) for stable equilibrium. A more rigorous approach would be to minimize the Gibbs free energy globally or follow sophisticated approaches [216–218] that consider (dis)appearing phases. We instead make use of the fact that the number of the existing phases is known and constant in time. We use SS simulations in Aspen Plus to properly initialize the dynamic simulations in Modelica and observe that the isofugacity conditions result in the expected (nontrivial) equilibrium, which we thus assume to be stable. For LLE, where I and II indicate the first and second liquid phases, respectively, isofugacity implies isopotential:

$$\gamma_i^{\mathrm{I}} x_i^{\mathrm{I}} = \gamma_i^{\mathrm{II}} x_i^{\mathrm{II}} \,,$$

where γ_i is the activity coefficient of species i.

The isofugacity condition for VLE, with the ideal gas assumption, gives:

$$y_i P = \gamma_i^{\mathrm{l}} x_i P_{\mathrm{vp},i}\,,$$

where y_i and $P_{\mathrm{vp},i}$ are the mole fraction and vapor pressure of species i in the vapor phase, respectively.

For VLLE, the isofugacity condition is then:

$$y_i P = \gamma_i^{\mathrm{I}} x_i^{\mathrm{I}} P_{\mathrm{vp},i} = \gamma_i^{\mathrm{II}} x_i^{\mathrm{II}} P_{\mathrm{vp},i}\,.$$

By applying the extended Antoine correlation [133] for each species, we determine its vapor pressure:

$$\ln P_{\mathrm{vp},i} = C_{1i} + \frac{C_{2i}}{T + C_{3i}} + C_{4i} T + C_{5i} \ln T + C_{6i}\, T^{C_{7i}}\,, \qquad C_{8i} \leq T \leq C_{9i}\,.$$

All the coefficients $C_{b,i}$, $b \in \{1, 2, \ldots, 9\}$ are retrieved from DIPPR's Project 801 database [110].

We use the NRTL model [109] to determine the activity coefficients in the liquid phase:

$$\ln \gamma_i = \frac{\sum\limits_j x_j \tau_{ji} G_{ji}}{\sum\limits_k x_k G_{ki}} + \sum_j \frac{x_j G_{ij}}{\sum\limits_k x_k G_{kj}} \left(\tau_{ij} - \frac{\sum\limits_m x_m \tau_{mj} G_{mj}}{\sum\limits_k x_k G_{kj}} \right),$$

where

$$G_{ij} = \exp(-c_{ij} \tau_{ij})\,, \qquad \tau_{ij} = a_{ij} + b_{ij}/T\,, \qquad G_{ii} = 1\,, \qquad \tau_{ii} = 0\,,$$

a_{ij}, b_{ij}, and c_{ij} are the binary interaction parameters of the chemical species. The parameters a_{ij} and b_{ij} are unsymmetrical. That means a_{ij} may not be equal to a_{ji}, etc. We retrieve the values of all binary interaction parameters from Albuquerque et al. [119] and Aspen Technology [134].

A.2. Process Flowsheet with PWC-B Configuration

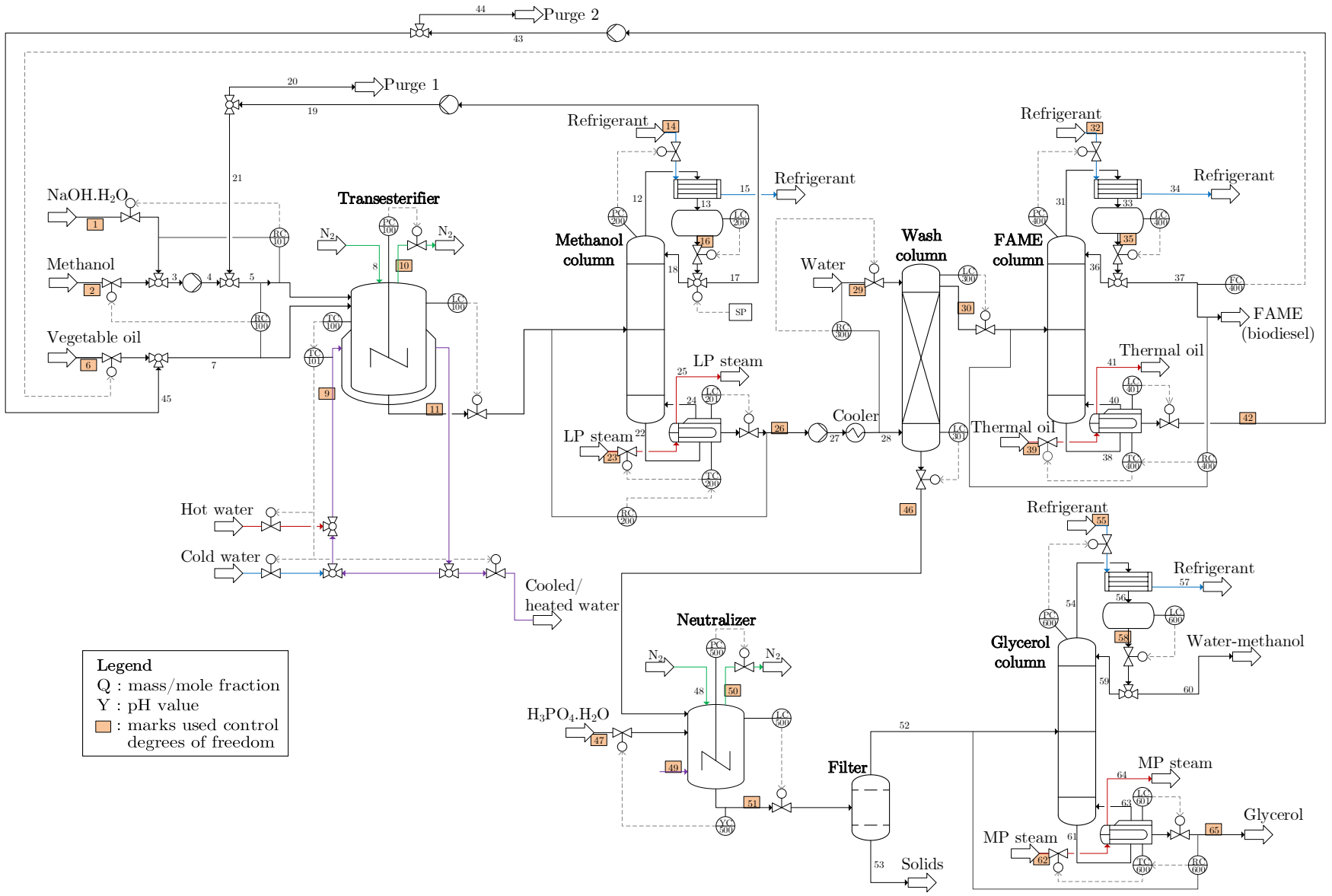

Figure A.1.: Process flowsheet with PWC-B configuration of a biodiesel production plant by oil alkali-catalyzed transesterification. The shown control structure is for the PWC structure having only conventional measurement configurations available.

A.3. Comparison of the Steady-State Simulation Results to That of Aspen Plus

For further validation of the developed Modelica model, we compare its SS simulation results to that of Aspen Plus. We provide the results of mainly the mole fractions, temperatures, and flow rates for the transesterifier, FAME and wash columns.

A.3.1. Transesterifier

Table A.2.: Comparison between the steady-state simulation results of the Modelica model with that of Aspen Plus for the transesterifier unit.

	Modelica	Aspen Plus
x_{TG}	4.62e−3	4.31e−3
x_{DG}	2.20e−3	2.06e−3
x_{MG}	8.40e−3	8.11e−3
x_{ME}	4.09e−1	4.10e−1
x_{NaOH}	1.35e−2	1.35e−2
x_{MO}	3.27e−1	3.28e−1
x_{G}	1.12e−1	1.12e−1
$x_{\mathrm{H_2O}}$	1.23e−1	1.23e−1
$\dot{N}_{\mathrm{out}}$ [kmol/h]	1.76e2	1.76e2
V $\left[\mathrm{m}^3\right]$	2.86e1	2.78e1
$h_{\mathrm{out}}^{\mathrm{total}}$ [kJ/kmol]	−4.62e5	−4.60e5

A.3.2. FAME Column

Table A.3.: Steady-state simulation results of the Modelica model for the FAME column.

Modelica: FAME column							
Stage	1	2	3	4	5	6	7
x_{TG}	3.64e−14	2.10e−10	7.54e−7	2.56e−3	2.67e−3	3.70e−3	2.95e−1
x_{DG}	2.69e−15	2.77e−11	1.89e−7	1.22e−3	1.27e−3	2.30e−3	1.41e−1
x_{MG}	3.97e−4	1.70e−3	5.69e−3	1.86e−2	6.88e−2	4.84e−1	5.29e−1
x_{ME}	1.19e−2	8.24e−6	2.34e−6	2.50e−6	2.15e−9	2.31e−12	2.30e−15
x_{NaOH}	0	0	0	1.32e−14	1.38e−14	1.81e−14	1.52e−12
x_{MO}	9.86e−1	0.9995	9.96e−1	9.79e−1	9.29e−1	5.11e−1	3.70e−2
x_{G}	4.06e−12	4.99e−15	1.35e−15	1.40e−15	0	0	0
$x_{\mathrm{H_2O}}$	2.73e−3	2.46e−8	7.05e−9	8.01e−9	0	0	0
T [K]	2.83e2	4.99e2	5.02e2	5.05e2	5.08e2	5.18e2	5.69e2
L_{out} [kmol/h]	1.17e2	1.62e2	1.62e2	3.18e2	3.05e2	2.32e2	2.76
V_{out} [kmol/h]	0	1.17e2	2.20e2	2.20e2	3.15e2	3.02e2	2.30e2
Q [kW]	−7.29e3	–	–	–	–	–	7.06e3

Table A.4.: Aspen Plus simulation results for the FAME column.

Aspen Plus: FAME column							
Stage	1	2	3	4	5	6	7
x_{TG}	3.46e−14	1.99e−10	7.16e−7	2.41e−3	2.56e−3	3.90e−3	2.89e−1
x_{DG}	2.56e−15	2.64e−11	1.80e−7	1.16e−3	1.23e−3	2.40e−3	1.39e−1
x_{MG}	3.99e−4	1.70e−3	5.71e−3	1.87e−2	6.96e−2	4.90e−1	5.36e−1
x_{ME}	1.18e−2	8.20e−6	2.33e−6	1.88e−6	1.62e−9	1.74e−12	1.73e−15
x_{NaOH}	0	0	0	1.22e−14	1.30e−14	1.87e−14	1.46e−12
x_{MO}	9.85e−1	9.98e−1	9.94e−1	9.78e−1	9.27e−1	5.04e−1	3.66e−2
x_{G}	3.64e−12	4.46e−15	1.21e−15	1.25e−15	0	0	0
$x_{\mathrm{H_2O}}$	2.70e−3	2.43e−8	6.98e−9	7.48e−10	0	0	0
T [K]	2.83e2	4.99e2	5.02e2	5.05e2	5.08e2	5.18e2	5.69e2
L_{out} [kmol/h]	1.17e2	1.62e2	1.61e2	3.15e2	2.96e2	2.05e2	2.62
V_{out} [kmol/h]	0	1.17e2	2.20e2	2.20e2	3.12e2	2.94e2	2.03e2
Q [kW]	−7.29e3	–	–	–	–	–	7.01e3

A.3.3. Wash Column

Table A.5.: Steady-state simulation results of the Modelica model for the wash column.

Modelica: Wash column						
Stage	1	2	3	4	5	6
$x^{\mathrm{E}}_{\mathrm{TG}}$	5.21e−4	5.20e−4	5.17e−4	5.15e−4	4.87e−4	1.25e−5
$x^{\mathrm{E}}_{\mathrm{DG}}$	1.35e−3	1.37e−3	1.35e−3	1.35e−3	1.33e−3	4.56e−8
$x^{\mathrm{E}}_{\mathrm{MG}}$	5.94e−2	8.65e−2	9.91e−2	1.05e−1	1.07e−1	1.42e−6
$x^{\mathrm{E}}_{\mathrm{ME}}$	1.42e−2	1.83e−2	1.98e−2	2.04e−2	2.13e−2	6.09e−2
$x^{\mathrm{E}}_{\mathrm{NaOH}}$	2.45e−11	1.75e−9	1.21e−7	8.26e−6	5.62e−4	4.00e−2
$x^{\mathrm{E}}_{\mathrm{MO}}$	1.47e−4	2.93e−4	3.88e−4	4.42e−4	4.80e−4	3.43e−4
$x^{\mathrm{E}}_{\mathrm{G}}$	9.05e−10	4.76e−8	2.51e−6	1.33e−4	7.01e−3	3.30e−1
$x^{\mathrm{E}}_{\mathrm{H_2O}}$	9.25e−1	8.94e−1	8.81e−1	8.72e−1	8.62e−1	5.68e−1
$x^{\mathrm{R}}_{\mathrm{TG}}$	1.33e−2	1.32e−2	1.31e−2	1.30e−2	1.30e−2	1.30e−2
$x^{\mathrm{R}}_{\mathrm{DG}}$	6.34e−3	6.53e−3	6.50e−3	6.47e−3	6.46e−3	6.45e−3
$x^{\mathrm{R}}_{\mathrm{MG}}$	2.42e−2	3.71e−2	4.35e−2	4.66e−2	4.81e−2	4.87e−2
$x^{\mathrm{R}}_{\mathrm{ME}}$	1.14e−2	1.43e−2	1.53e−2	1.56e−2	1.58e−2	1.60e−2
$x^{\mathrm{R}}_{\mathrm{NaOH}}$	6.86e−14	5.54e−12	4.02e−10	2.81e−8	1.93e−6	1.32e−4
$x^{\mathrm{R}}_{\mathrm{MO}}$	9.43e−1	9.27e−1	9.20e−1	9.17e−1	9.15e−1	9.14e−1
$x^{\mathrm{R}}_{\mathrm{G}}$	3.88e−12	2.06e−10	1.09e−8	5.83e−7	3.11e−5	1.65e−3
$x^{\mathrm{R}}_{\mathrm{H_2O}}$	2.61e−3	2.85e−3	2.95e−3	2.99e−3	2.99e−3	1.90e−3
T [K]	3.32e2	3.33e2	3.33e2	3.33e2	3.33e2	3.33e2
E_{out} [kmol/h]	1.39e1	1.44e1	1.46e1	1.48e1	1.49e1	5.97e1
R_{out} [kmol/h]	6.12e1	6.22e1	6.27e1	6.30e1	6.31e1	6.32e1

Table A.6.: Aspen Plus simulation results for the wash column.

Aspen Plus: Wash column						
Stage	1	2	3	4	5	6
$x^{\mathrm{E}}_{\mathrm{TG}}$	4.81e−4	4.79e−4	4.75e−4	4.73e−4	4.47e−4	1.17e−5
$x^{\mathrm{E}}_{\mathrm{DG}}$	1.26e−3	1.28e−3	1.27e−3	1.26e−3	1.25e−3	4.31e−8
$x^{\mathrm{E}}_{\mathrm{MG}}$	5.77e−2	8.43e−2	9.68e−2	1.03e−1	1.05e−1	1.41e−6
$x^{\mathrm{E}}_{\mathrm{ME}}$	1.42e−2	1.83e−2	1.97e−2	2.03e−2	2.12e−2	6.10e−2
$x^{\mathrm{E}}_{\mathrm{NaOH}}$	2.27e−11	1.64e−9	1.15e−7	8.01e−6	5.54e−4	4.00e−2
$x^{\mathrm{E}}_{\mathrm{MO}}$	1.40e−4	2.77e−4	3.68e−4	4.18e−4	4.57e−4	3.42e−4
$x^{\mathrm{E}}_{\mathrm{G}}$	8.30e−10	4.45e−8	2.38e−6	1.29e−4	6.90e−3	3.30e−1
$x^{\mathrm{E}}_{\mathrm{H_2O}}$	9.26e−1	8.95e−1	8.81e−1	8.75e−1	8.64e−1	5.68e−1
$x^{\mathrm{R}}_{\mathrm{TG}}$	1.24e−2	1.23e−2	1.22e−2	1.22e−2	1.22e−2	1.21e−2
$x^{\mathrm{R}}_{\mathrm{DG}}$	5.95e−3	6.13e−3	6.10e−3	6.08e−3	6.07e−3	6.06e−3
$x^{\mathrm{R}}_{\mathrm{MG}}$	2.34e−2	3.59e−2	4.22e−2	4.52e−2	4.67e−2	4.74e−2
$x^{\mathrm{R}}_{\mathrm{ME}}$	1.13e−2	1.43e−2	1.52e−2	1.56e−2	1.57e−2	1.60e−2
$x^{\mathrm{R}}_{\mathrm{NaOH}}$	6.28e−14	5.13e−12	3.78e−10	2.68e−8	1.88e−6	1.30e−4
$x^{\mathrm{R}}_{\mathrm{MO}}$	9.44e−1	9.29e−1	9.21e−1	9.18e−1	9.16e−1	9.15e−1
$x^{\mathrm{R}}_{\mathrm{G}}$	3.49e−12	1.89e−10	1.02e−8	5.54e−7	3.01e−5	1.62e−3
$x^{\mathrm{R}}_{\mathrm{H_2O}}$	2.58e−3	2.81e−3	2.91e−3	2.95e−3	2.94e−3	1.87e−3
T [K]	3.32e2	3.33e2	3.33e2	3.33e2	3.33e2	3.33e2
E_{out} [kmol/h]	1.39e1	1.44e1	1.46e1	1.47e1	1.48e1	5.96e1
R_{out} [kmol/h]	6.11e1	6.22e1	6.27e1	6.29e1	6.30e1	6.31e1

A.4. Additional Results

We here provide for both PWC-A and PWC-B, simulated under all plant disturbances and setpoint changes, profiles of feed flow rates; product flow rates; heating and cooling duties for individual units and the whole plant; oil conversion in the transesterifier, and column recoveries and purities; and the species mass fraction in the biodiesel product.

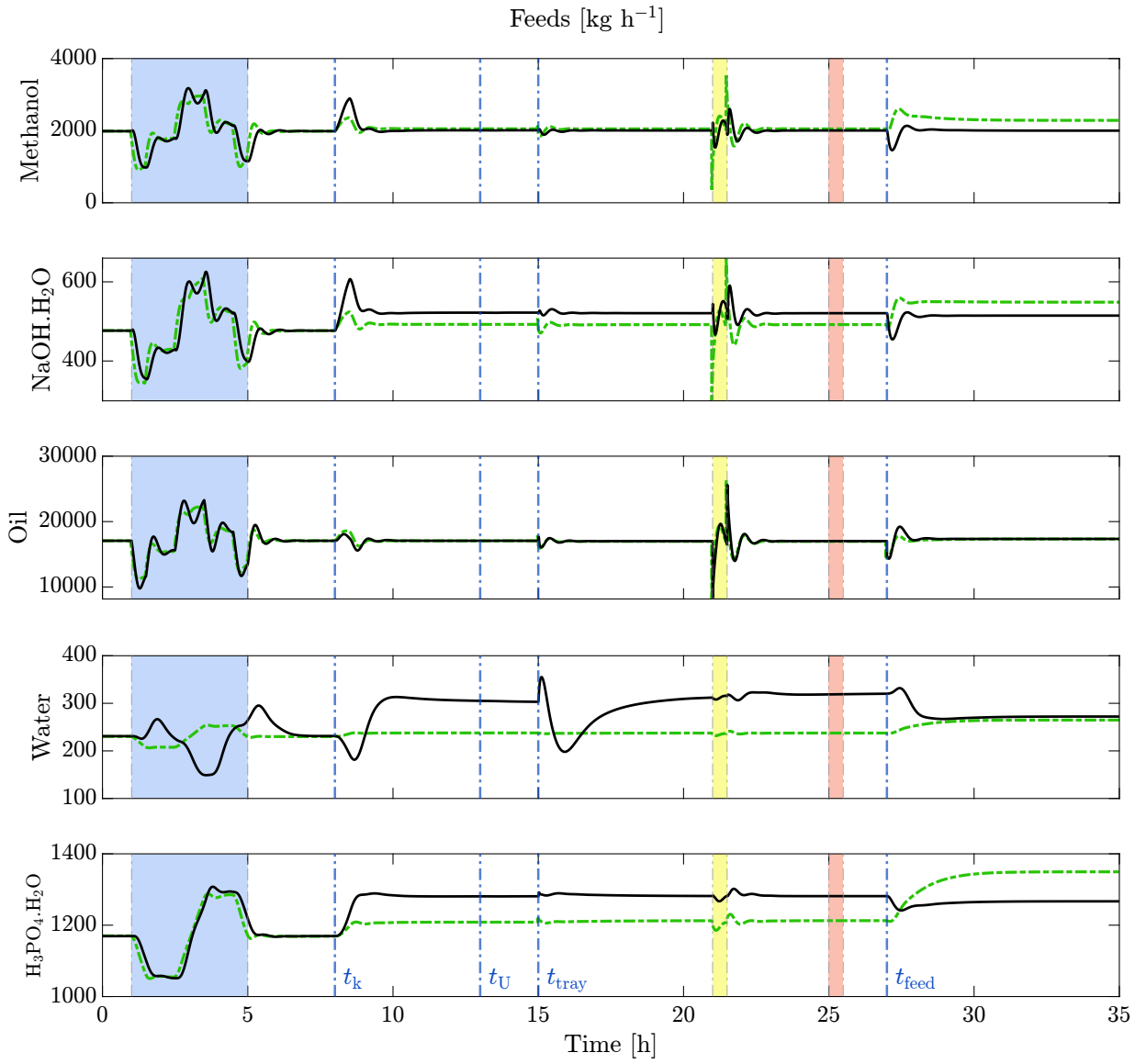

Figure A.2.: Profiles of feed mass flow rates for both PWC-A (solid-black) and PWC-B (dashed-dotted-green), simulated under all disturbances and setpoint changes.

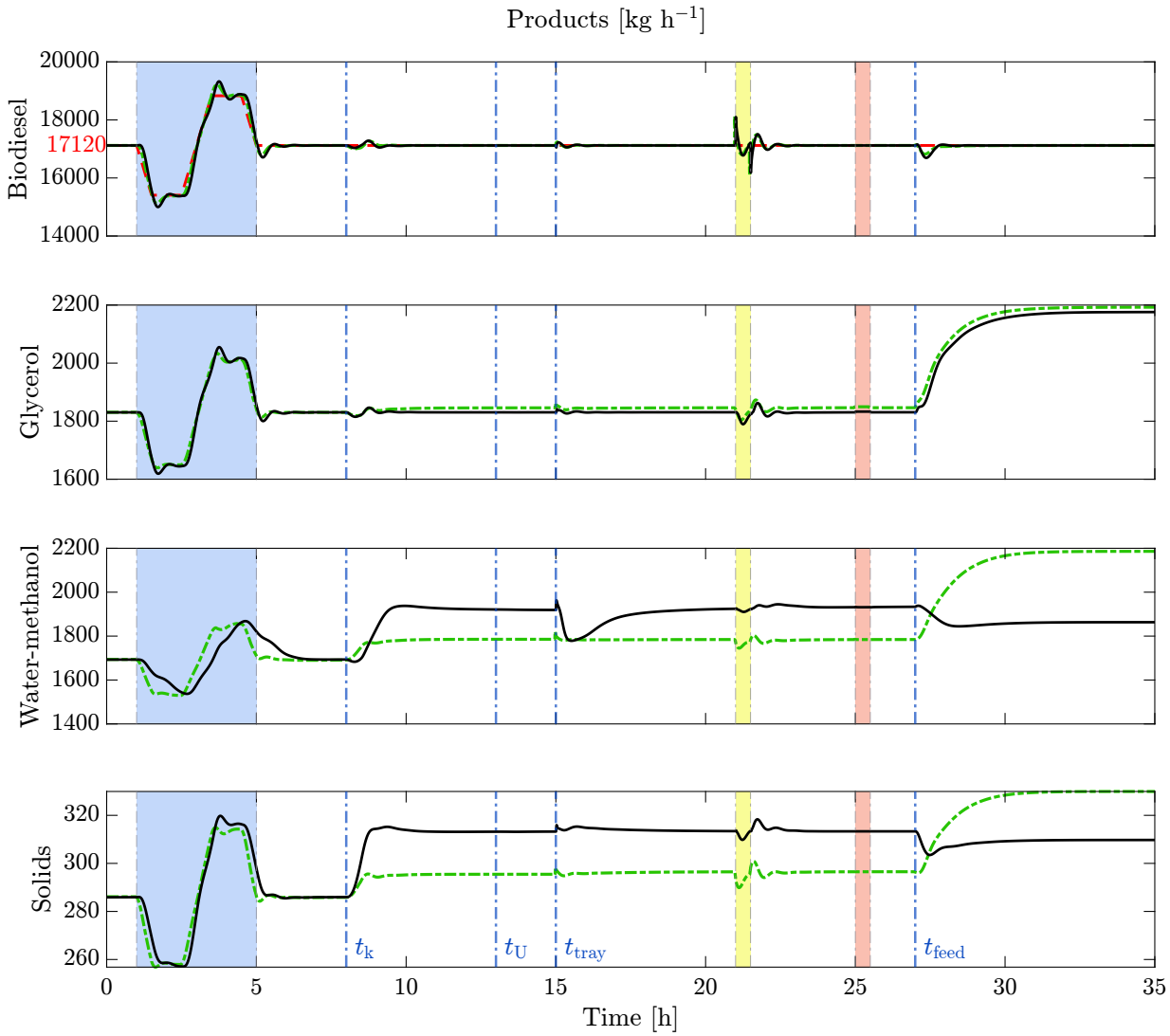

Figure A.3.: Profiles of product mass flow rates for both PWC-A (solid-black) and PWC-B (dashed-dotted-green), simulated under all disturbances and setpoint changes. The setpoint of biodiesel production rate is indicated by the red-dashed line in the top graph.

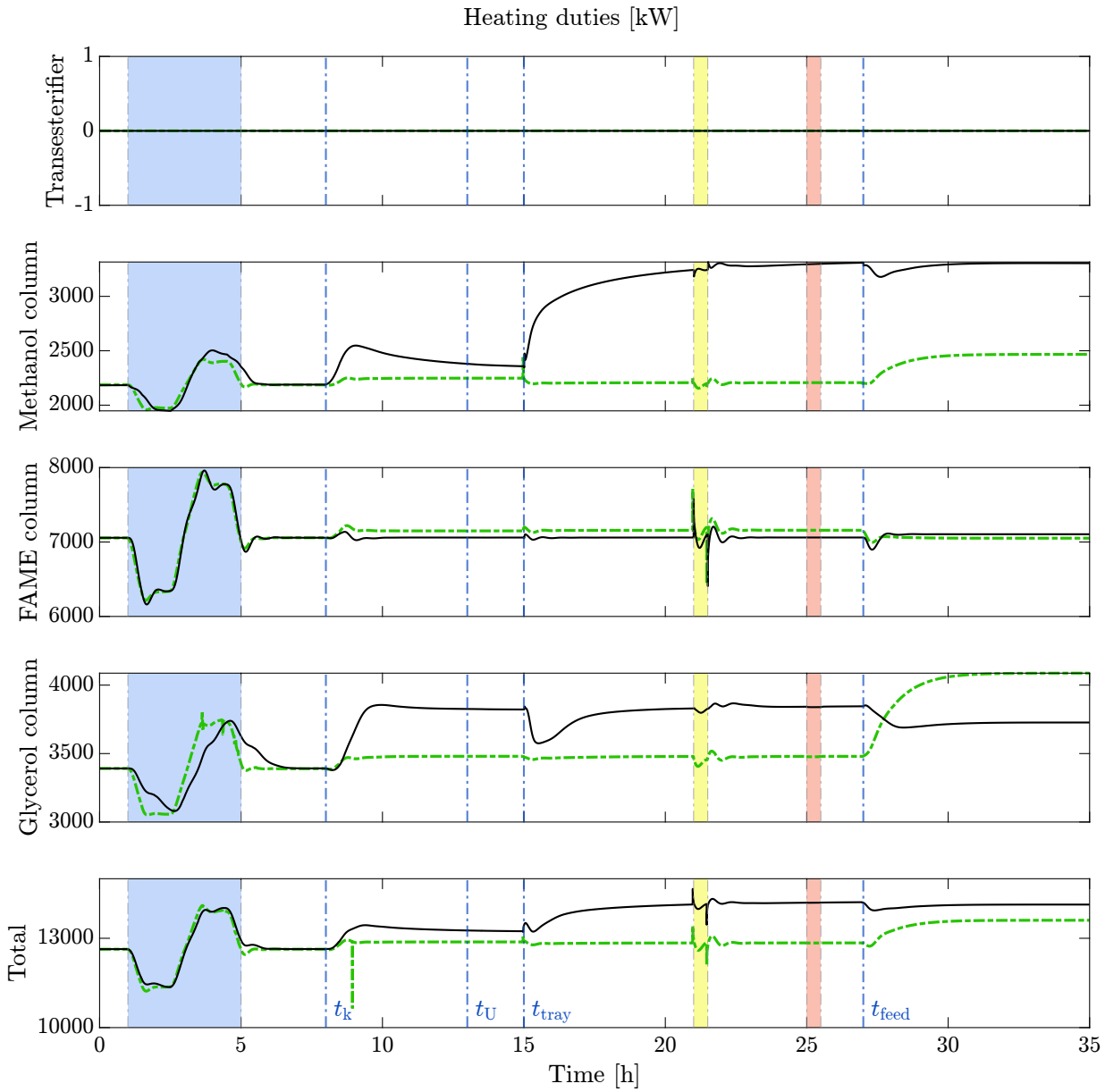

Figure A.4.: Heating duties in the transesterifier and reboilers, as well as that of the whole plant for both PWC-A (solid-black) and PWC-B (dashed-dotted-green), simulated under all disturbances and setpoint changes.

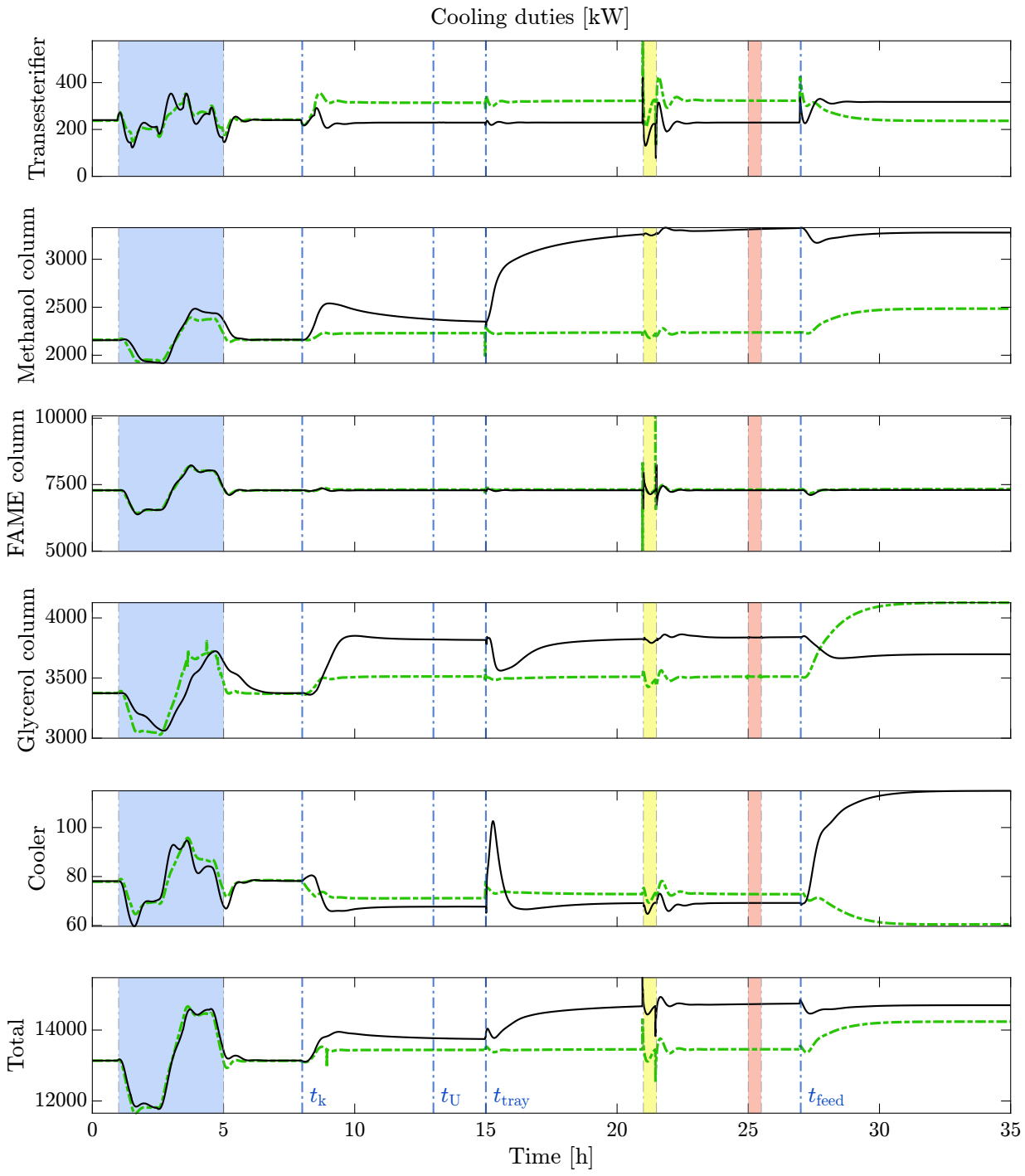

Figure A.5.: Cooling duties in the transesterifier, condensers and cooler, as well as that of the whole plant for both PWC-A (solid-black) and PWC-B (dashed-dotted-green), simulated under all disturbances and setpoint changes.

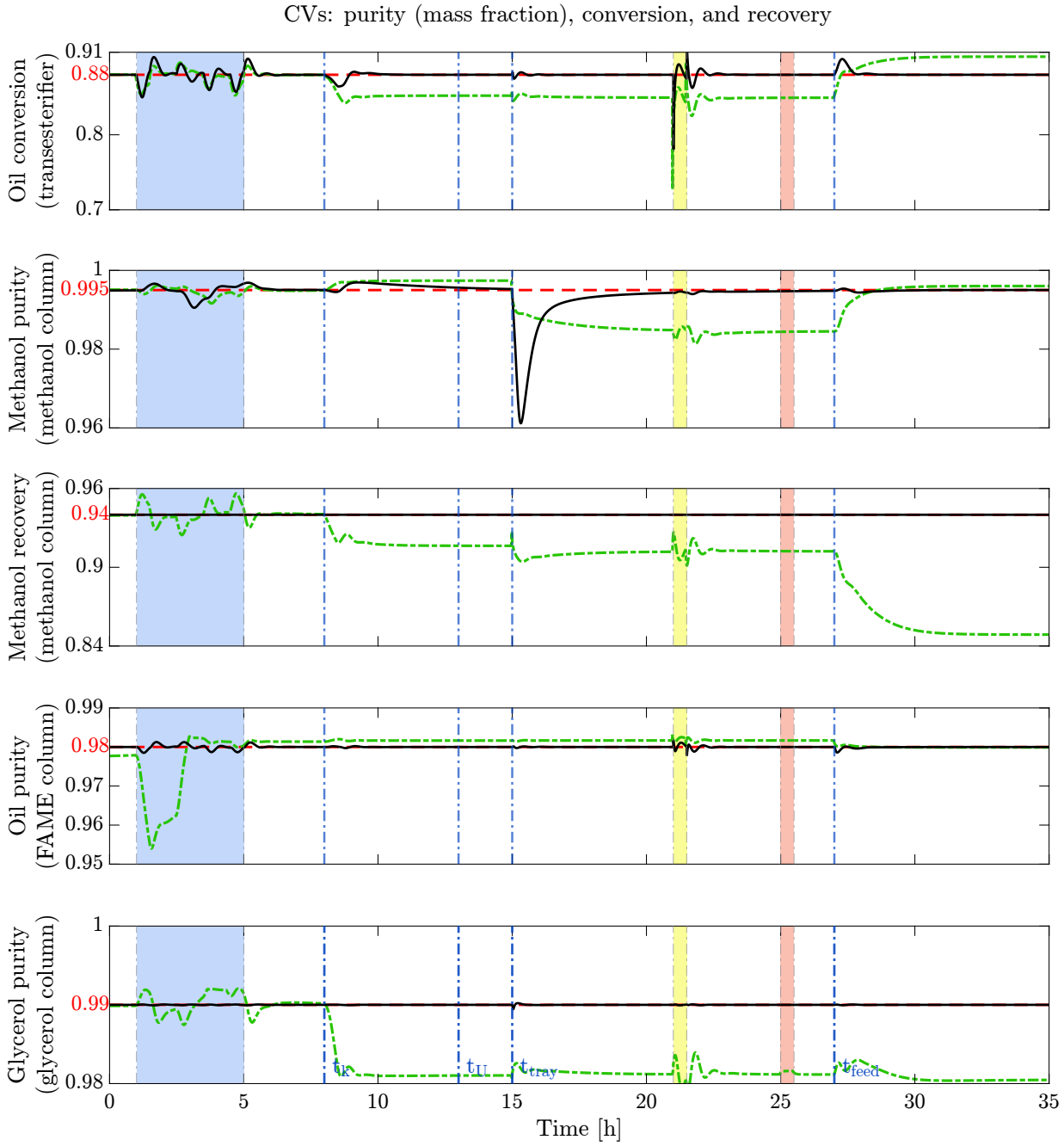

Figure A.6.: CV profiles of oil conversion in the transesterifier and column recoveries and purities for both PWC-A (solid-black) and PWC-B (dashed-dotted-green), simulated under all disturbances and setpoint changes. Design setpoints are indicated by the red-dashed lines.

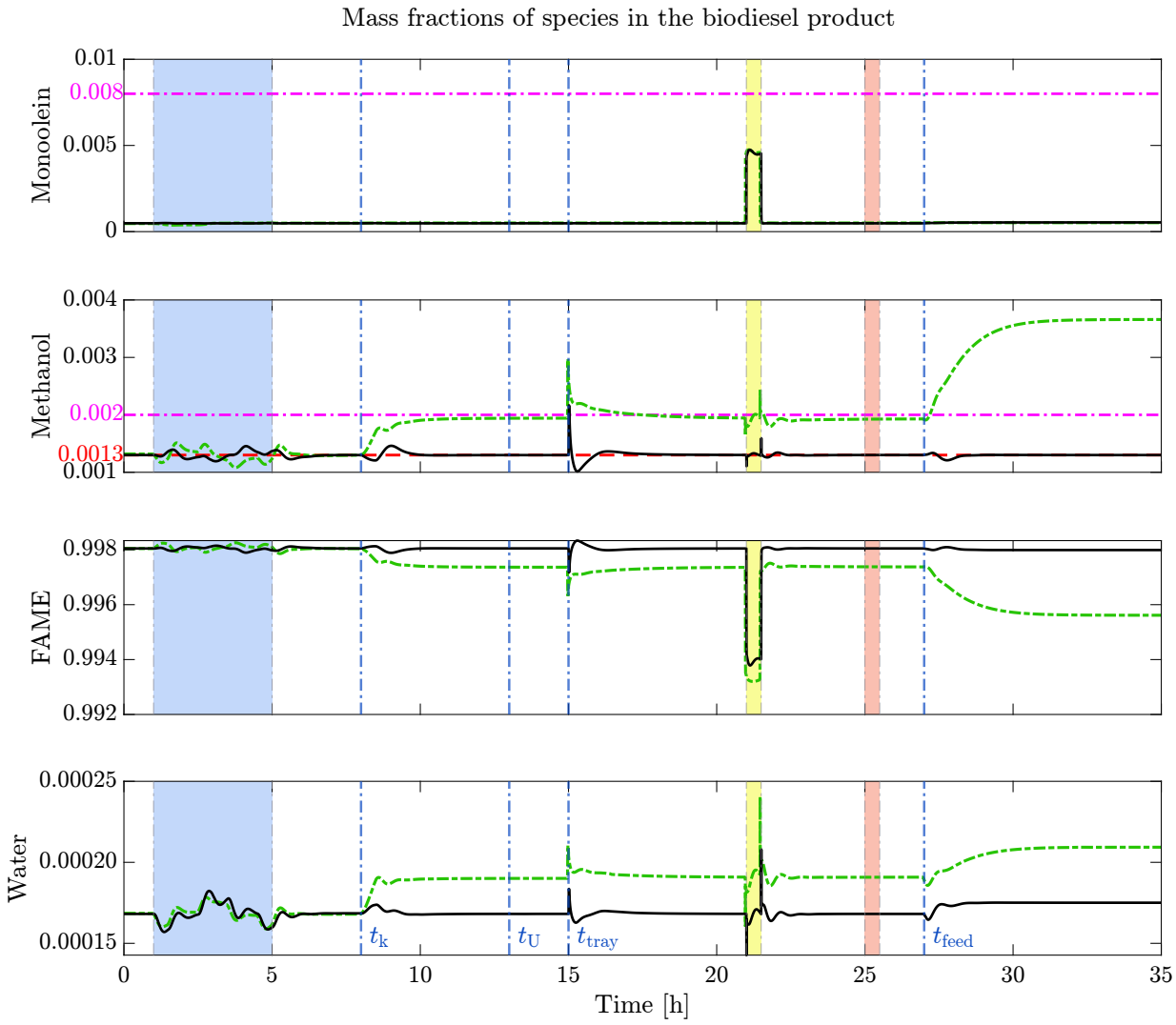

Figure A.7.: Mass fraction profiles of monoolein, methanol, FAME, and water in the biodiesel product stream for both PWC-A (solid-black) and PWC-B (dashed-dotted-green), simulated under all disturbances and setpoint changes. Design setpoints are indicated by the red-dashed lines. The dashed-dotted-magenta lines indicate the bounds.

Appendix B.

Optimal Design and Flexible Operation of a Fully Electrified Biodiesel Production Process

We present here the empirically fitted equations for the purification unit of the water-methanol waste stream (water-methanol column). We provide the prices of raw materials and final products. We also show the profiles of all control variables, transesterifier and buffer tank levels, production rates, and power demand of all process units. In addition, the purities of the final biodiesel product and `InterTankRSR` outlet stream are provided.

B.1. Fitted Equations for the Water-Methanol Column

Using SS simulations of a rigorous model for the purification unit of the water-methanol waste stream (water-methanol column), we fit the following empirical equations:

$$W_{\mathrm{WMc}} = 1.87\,\dot{m}_{\mathrm{WM}}\,w_{\mathrm{MeOH,WM}}\,, \quad R^2 = 0.955\,, \tag{B.1a}$$

$$\dot{m}_{\mathrm{WMc,Dist}} = 1.48\,\dot{m}_{\mathrm{WM}}\,w_{\mathrm{MeOH,WM}}\,, \quad R^2 = 0.996\,, \tag{B.1b}$$

$$\begin{aligned} w_{\mathrm{MeOH,WMc,Dist}} = 1 - \exp\big(&-180\,w_{\mathrm{MeOH,WM}}^3 + 160\,w_{\mathrm{MeOH,WM}}^2 \\ &-55\,w_{\mathrm{MeOH,WM}}\big)\,, \quad R^2 = 0.919\,, \end{aligned} \tag{B.1c}$$

where $\dot{m}_{\mathrm{WM}}$ and $w_{\mathrm{MeOH,WM}}$ are the mass flow rate of the water-methanol waste stream and its methanol mass fraction, respectively. The total power demand of the water-methanol column is denoted by W_{WMc}, while $\dot{m}_{\mathrm{WMc,Dist}}$ is its distillate mass flow rate with the methanol purity $w_{\mathrm{MeOH,WMc,Dist}}$. The R^2 values represent the coefficient of determination for each fitted equation.

B.2. Material Prices

Table B.1.: Specific prices of raw materials and final products.

Material	Price [€/kg]
Vegetable oil (rapeseed oil)	1.1 [219, 220]
Methanol	0.55 [221, 222]
Sodium hydroxide (20 wt%)	0.1 [223]
Phosphoric acid (20 wt%)	0.19 [224]
Biodiesel (EN 14214 [122])	2.57 [225]
Glycerol (99 wt%)	1.4 [226]
Monosodium phosphate (solids)	1 [227]

B.3. Further Profiles

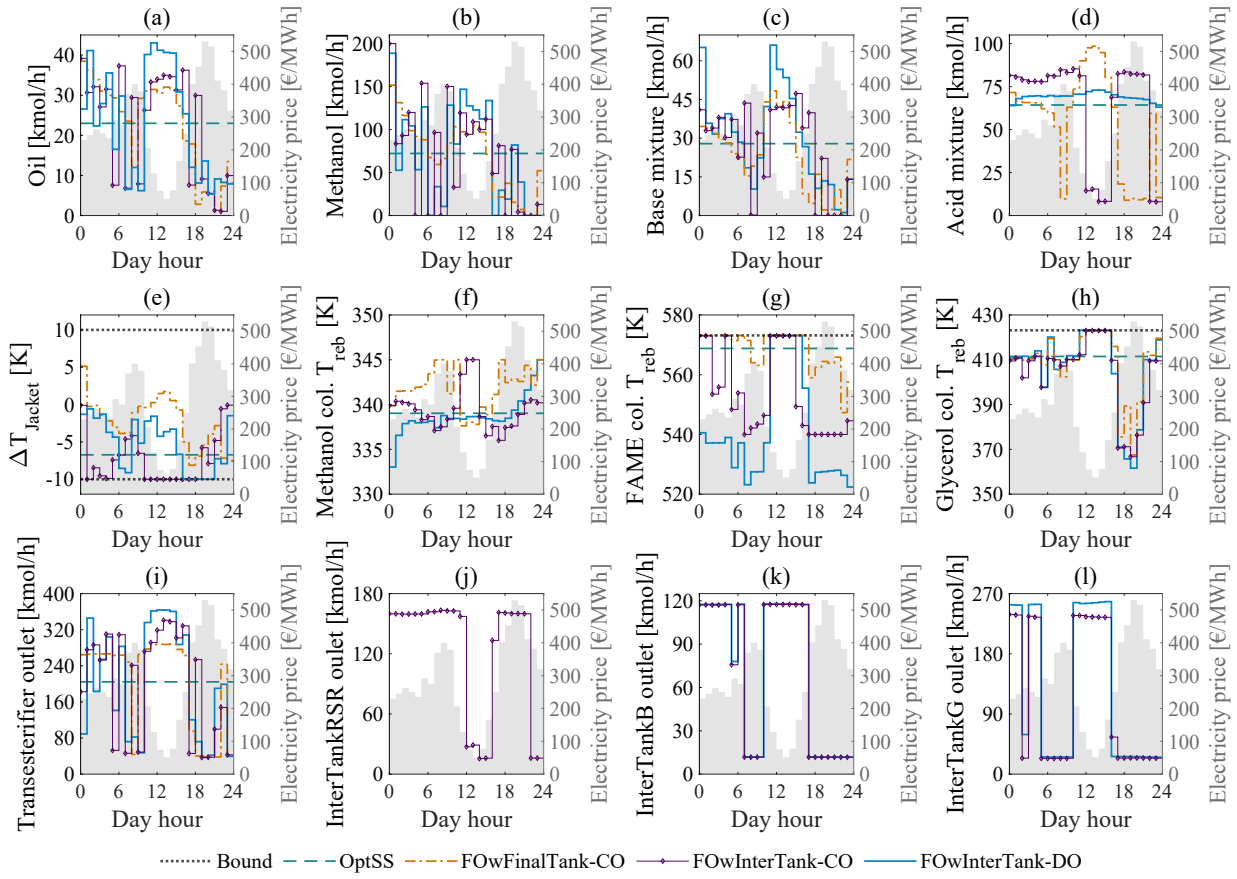

Figure B.1.: Control variable profiles. The acid mixture feed is not a control variable in optimizers. It is manipulated by a pH controller to control the pH of the neutralizer outlet stream. T_{reb} denotes reboiler temperatures, and ΔT_{Jacket} is the temperature change of the transesterifier jacket medium after passing through the external heat exchanger.

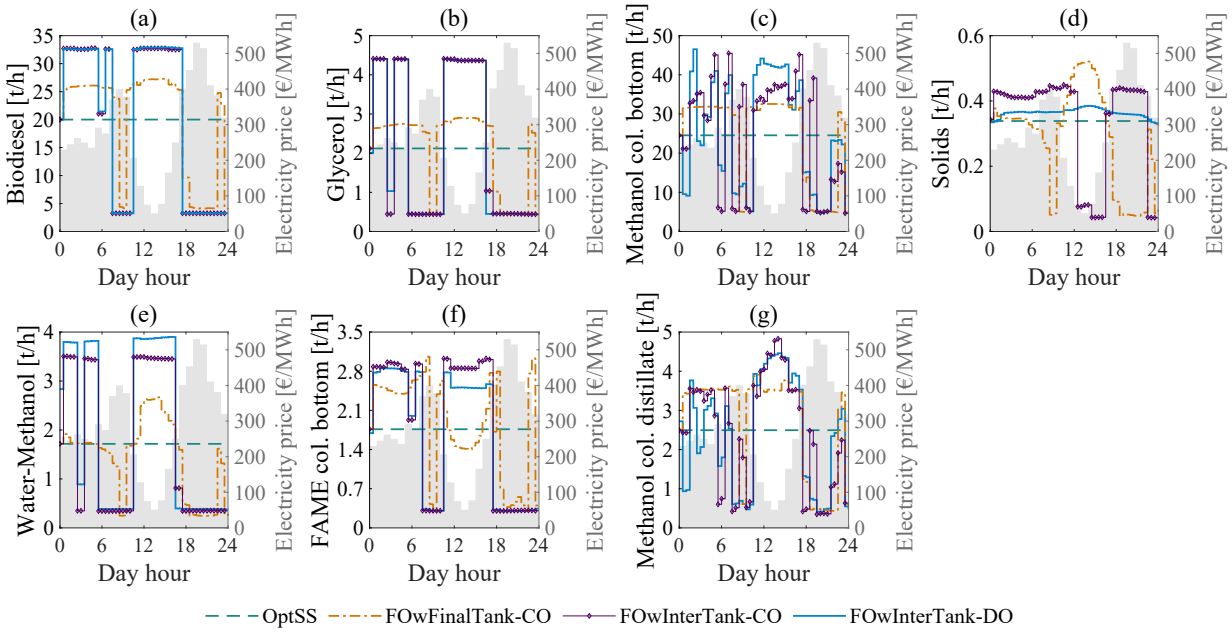

Figure B.2.: Production flow rate profiles for the final products, FAME column bottom, and methanol column outlet streams.

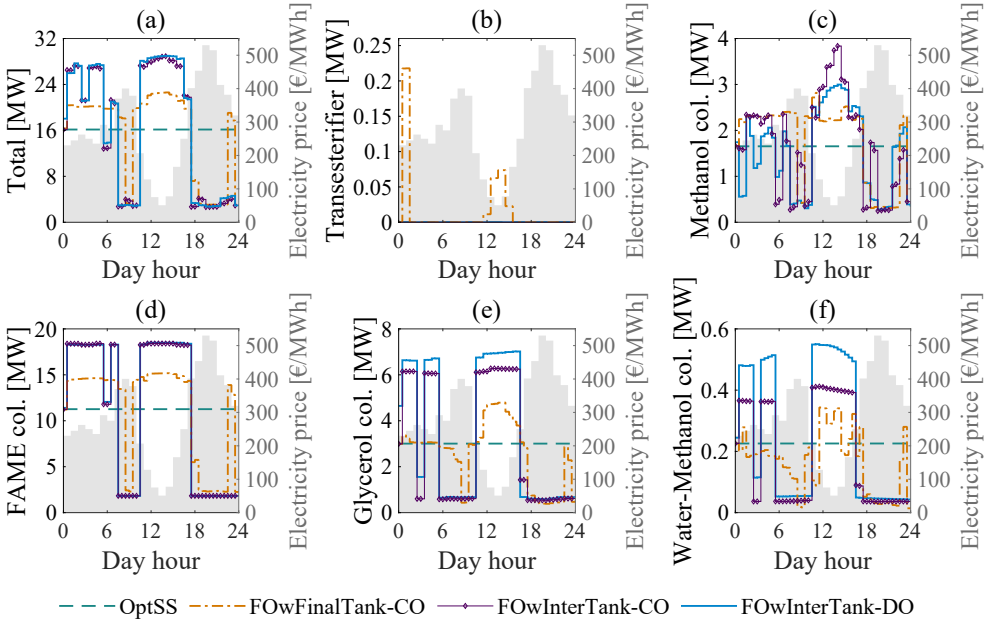

Figure B.3.: Power demands of all process units.

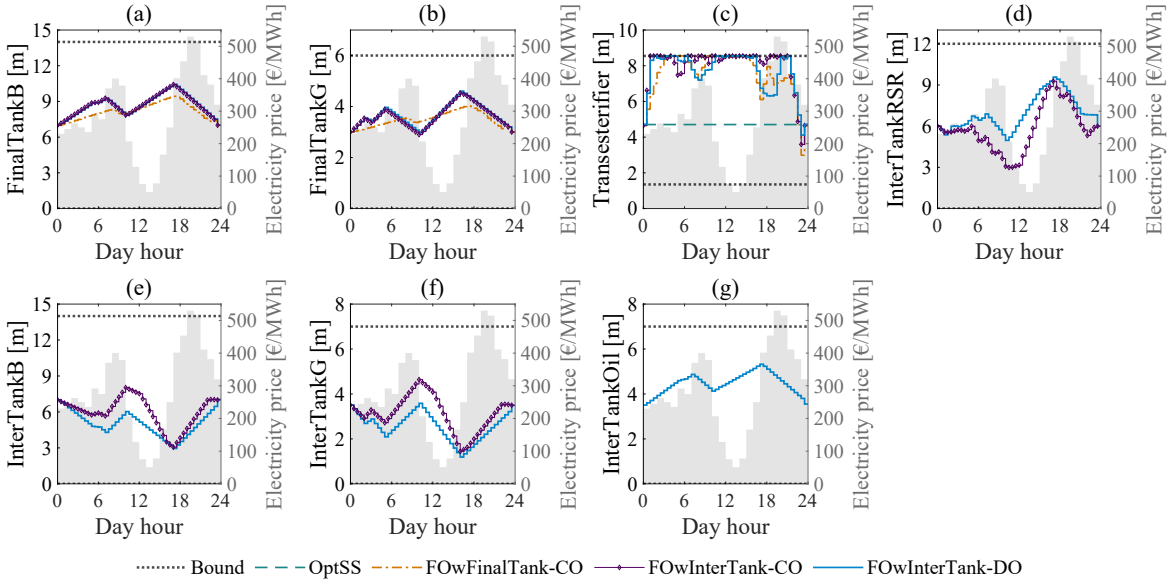

Figure B.4.: Liquid levels in the transesterifier and buffer tanks.

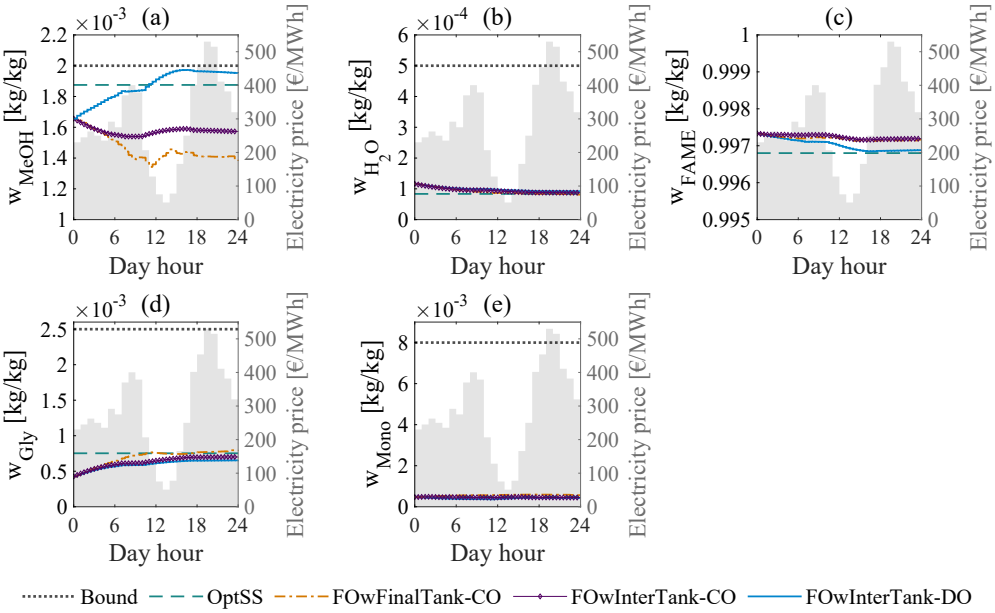

Figure B.5.: Purities in the biodiesel product. MeOH, Gly, and Mono indicate methanol, glycerol, and monoolein, respectively.

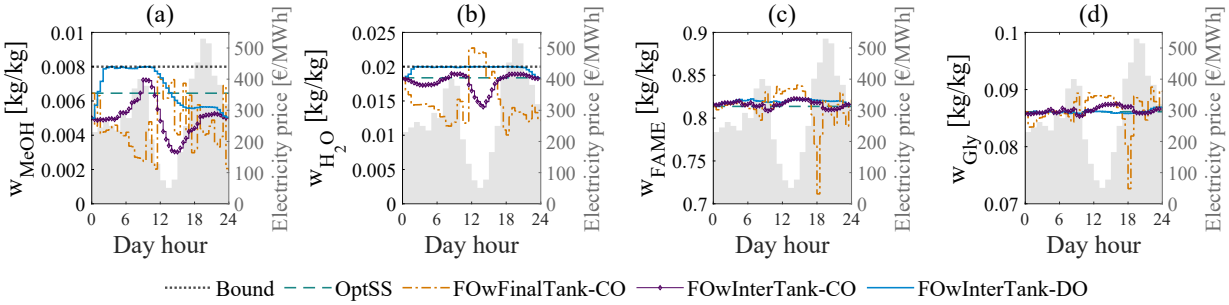

Figure B.6.: Purities in the `InterTankRSR` outlet stream. MeOH and Gly indicate methanol and glycerol, respectively. The bounds are only in the case of FOwInterTank-DO.

Appendix C.

Distributed Economic Nonlinear Model Predictive Control for Flexible Electrified Biodiesel Production: Sequential Architectures

C.1. Model Fitting for Quasi-Stationary Scheduling

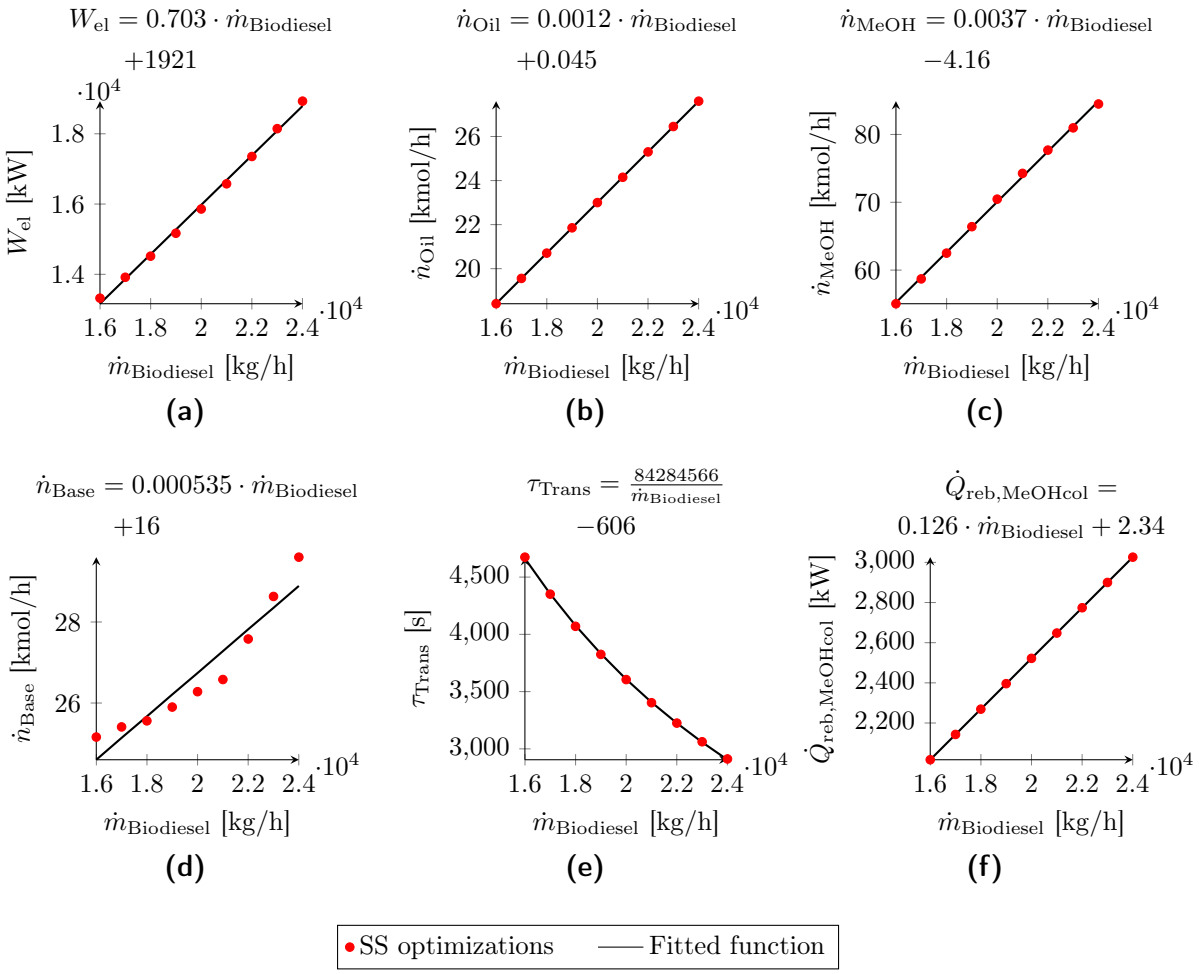

Figure C.1.: Total power consumption (a) and control variables (b)–(f) plotted against the biodiesel production rate, utilized in the QSS approach. All control variables and total power consumption are linearly fitted, except for τ_{Trans}, which is fitted with a hyperbolic function. Here, τ_{Trans} represents the residence time in the transesterifier, and $\dot{Q}_{reb,MeOHcol}$ denotes the reboiler duty in the methanol column.

C.2. Overview of Process Configurations, Control Variables, and Constraints of the Considered Operational Strategies

Table C.1.: Summary of the included buffer tanks, process modifications, control variables, and constraints for the considered operational strategies. Due to the thermal degradation limits of biodiesel and glycerol products, the maximum temperatures in the FAME and glycerol column reboilers are set at $300\,^{\circ}\mathrm{C}$ and $150\,^{\circ}\mathrm{C}$, respectively. The maximum temperature changes of the transesterifier jacket medium $\Delta T_{\mathrm{Jacket}}$ are restricted to $\pm 10\,^{\circ}\mathrm{C}$. Time-variant parameters are denoted by TV, while time-dependent setpoints are represented by SP. Liquid levels and equality constraints are indicated by LL and EC, respectively. Purities are expressed in $\mathrm{kg/kg}$. In DeNMPC, endpoint constraints are enforced at every iteration (I) and as point constraints at the 24-hour time point.

	SS	Offline DO	QSS	DeNMPC
Additional process units and modifications				
FinalTankB and FinalTankG	–	✓	✓	✓
InterTankRSR, InterTankB, and InterTankG	–	✓	–	✓
InterTankOil and tearing the residual oil recycle stream	–	–	–	✓
Control variables	Constant	TV	SP	TV
$\dot{n}_{\mathrm{Oil}}$, $\dot{n}_{\mathrm{MeOH}}$, and $\dot{n}_{\mathrm{Base}}$ [kmol/h]	✓	✓	✓	✓
$\dot{n}_{\mathrm{TransOut}}$ [kmol/h]	–	✓	–	✓
τ_{Trans} [h]	✓	–	✓	–
$\Delta T_{\mathrm{Jacket}}$ [K], limited to $\pm 10\,^{\circ}\mathrm{C}$	✓	✓	–	✓
$T_{\mathrm{sp,MeOHcol}}$ [K]	–	✓	–	✓
$\dot{Q}_{\mathrm{reb,MeOHcol}}$ [MW]	✓	–	✓	–
$T_{\mathrm{sp,FAMEcol}}$ [K], upper bound of $300\,^{\circ}\mathrm{C}$	✓	✓	–	✓
$T_{\mathrm{sp,GLYcol}}$ [K], upper bound of $150\,^{\circ}\mathrm{C}$	✓	✓	–	✓
$\dot{n}_{\mathrm{InterTankRSR}}$ [kmol/h]	–	✓	–	–
$\dot{n}_{\mathrm{InterTankB}}$ and $\dot{n}_{\mathrm{InterTankG}}$ [kmol/h]	–	✓	–	✓
Path constraints				
Distillation columns: reboilers, distillate drums, and trays LL	✓	✓	–	✓
Decanter and neutralizer LL	✓	✓	–	–
Transesterifier LL	✓	✓	–	✓
InterTankRSR, InterTankB, and InterTankG LL	–	✓	–	✓
InterTankOil LL	–	–	–	✓
FinalTankB LL	–	✓	✓	✓
FinalTankG LL	–	✓	–	✓
Biodiesel purities (EN 14214 [122])	✓	✓	–	✓
Glycerol purity (99 wt%)	✓	✓	–	✓
InterTankRSR composition	–	–	–	✓
Biodiesel production demand (EC)	✓	✓	✓	✓
Glycerol production demand (EC)	✓	✓	–	✓
InterTankRSR and InterTankOil outlets [kg/h] (EC)	–	–	–	✓
Endpoint constraints				
Distillation columns: reboilers, distillate drums, and trays LL	–	✓	–	–
Decanter and neutralizer LL	–	✓	–	–
Transesterifier LL	–	✓	–	✓(I, 24 h)
InterTankRSR, InterTankB, and InterTankG LL	–	✓	–	✓(I, 24 h)
InterTankOil LL	–	–	–	✓(I, 24 h)
FinalTankB LL	–	✓	✓	✓(I, 24 h)
FinalTankG LL	–	✓	–	✓(I, 24 h)
Transesterifier and InterTankRSR composition	–	✓	–	✓(I, 24 h)
InterTankB and InterTankG composition	–	✓	–	–
InterTankOil composition	–	–	–	✓(24 h)

Appendix D.

Distributed Economic Nonlinear Model Predictive Control for Flexible Electrified Biodiesel Production: Sequential and Iterative Architectures with Computational Delay Compensation

D.1. Overview of Process Configurations, Control Variables, and Constraints of the Considered Operational Strategies

Table D.1.: Summary of buffer tanks, process modifications, control variables, and constraints for the operational strategies under consideration. Time-varying parameters are designated as TV. Liquid levels and equality constraints are denoted by LL and EC, respectively. Purities are expressed in $\mathrm{kg/kg}$. In DeNMPC, endpoint constraints are enforced at each iteration (I) and as point constraints at $24\,\mathrm{h}$.

	SS	Offline DO	Sequential	Iterative
Additional process units and modifications				
FinalTankB and FinalTankG	–	✓	✓	✓
InterTankRSR, InterTankB, and InterTankG	–	✓	✓	✓
InterTankOil	–	–	✓	✓
Tearing the residual oil recycle stream	–	–	✓	–
Control variables	Constant	TV	TV	TV
$\dot{n}_{\mathrm{Oil}}$, $\dot{n}_{\mathrm{MeOH}}$, and $\dot{n}_{\mathrm{Base}}$ [kmol/h]	✓	✓	✓	✓
$\dot{n}_{\mathrm{TransOut}}$ [kmol/h]	–	✓	✓	✓
τ_{Trans} [h]	✓	–	–	–
$\Delta T_{\mathrm{Jacket}}$ [K], limited to $\pm 10\,^{\circ}\mathrm{C}$	✓	✓	✓	✓
$T_{\mathrm{sp,MeOHcol}}$ [K]	–	✓	✓	✓
$\dot{Q}_{\mathrm{reb,MeOHcol}}$ [MW]	✓	–	–	–
$T_{\mathrm{sp,FAMEcol}}$ [K], upper bound of $300\,^{\circ}\mathrm{C}$	✓	✓	✓	✓
$T_{\mathrm{sp,GLYcol}}$ [K], upper bound of $150\,^{\circ}\mathrm{C}$	✓	✓	✓	✓
$\dot{n}_{\mathrm{InterTankRSR}}$ [kmol/h]	–	✓	–	–
$\dot{n}_{\mathrm{InterTankB}}$ and $\dot{n}_{\mathrm{InterTankG}}$ [kmol/h]	–	✓	✓	✓
$\dot{n}_{\mathrm{InterTankOil}}$ [kmol/h]	–	–	–	✓
Path constraints				
Distillation columns: reboilers, distillate drums, and trays LL	✓	✓	✓	✓
Decanter and neutralizer LL	✓	✓	–	–
Transesterifier LL	✓	✓	✓	✓
InterTankRSR, InterTankB, and InterTankG LL	–	✓	✓	✓
InterTankOil LL	–	–	✓	✓
FinalTankB and FinalTankG LL	–	✓	✓	✓
Biodiesel purities (EN 14214 [122])	✓	✓	✓	✓
Glycerol purity ($99\,\mathrm{wt\%}$)	✓	✓	✓	✓
InterTankRSR composition	–	–	✓	✓
Biodiesel and glycerol production demands (EC)	✓	✓	✓	✓
InterTankRSR outlet [kg/h] (EC)	–	–	✓	✓
InterTankOil outlet [kg/h] (EC)	–	–	✓	–
Endpoint constraints				
Distillation columns: reboilers, distillate drums, and trays LL	–	✓	–	–
Decanter and neutralizer LL	–	✓	–	–
Transesterifier LL	–	✓	✓(I, 24 h)	✓(I, 24 h)
InterTankRSR, InterTankB, and InterTankG LL	–	✓	✓(I, 24 h)	✓(I, 24 h)
InterTankOil LL	–	–	✓(I, 24 h)	✓(I, 24 h)
FinalTankB and FinalTankG LL	–	✓	✓(I, 24 h)	✓(I, 24 h)
Transesterifier and InterTankRSR composition	–	✓	✓(I, 24 h)	✓(I, 24 h)
InterTankB and InterTankG composition	–	✓	–	–
InterTankOil composition	–	–	✓(24 h)	–

Bibliography

[1] M. El Wajeh, A. Mhamdi, and A. Mitsos. Dynamic Modeling and Plantwide Control of a Production Process for Biodiesel and Glycerol. *Industrial & Engineering Chemistry Research*, 62(27):10559–10576, 2023.

[2] M. El Wajeh, A. Mhamdi, and A. Mitsos. Optimal Design and Flexible Operation of a Fully Electrified Biodiesel Production Process. *Industrial & Engineering Chemistry Research*, 63(3):1487–1500, 2024.

[3] M. El Wajeh, A. Mhamdi, and A. Mitsos. Optimal Flexible Operation of Electrified and Heat-Integrated Biodiesel Production. *IFAC-PapersOnLine*, 58(14):513–518, 2024.

[4] M. El Wajeh, M. Granderath, A. Mitsos, and A. Mhamdi. Distributed Economic Nonlinear Model Predictive Control for Flexible Electrified Biodiesel Production—Part I: Sequential Architectures. *Industrial & Engineering Chemistry Research*, 63 (42):17997–18012, 2024.

[5] M. El Wajeh, M. Granderath, A. Mitsos, and A. Mhamdi. Distributed Economic Nonlinear Model Predictive Control for Flexible Electrified Biodiesel Production—Part II: Sequential and Iterative Architectures with Computational Delay Compensation. *Industrial & Engineering Chemistry Research*, 63(42):18013–18026, 2024.

[6] M. El Wajeh, F. Jung, D. Bongartz, C. D. Kappatou, N. Ghaffari Laleh, A. Mitsos, and J. N. Kather. Can the Kuznetsov Model Replicate and Predict Cancer Growth in Humans? *Bulletin of Mathematical Biology*, 84(11):130, 2022.

[7] M. Morobeid. Model Predictive Control of a Biodiesel Purification Unit. Bachelor's thesis, Chair of Process Systems Engineering, RWTH Aachen University, 2022.

[8] J. Jordan. Reduced Dynamic Modeling for Process Columns Based on Artificial Neural Networks and Compartmentalization. Bachelor's thesis, Chair of Process Systems Engineering, RWTH Aachen University, 2023.

[9] A. Lachmund. Dynamic Modeling of a Wash Unit in an Industrial Biodiesel Production Plant. Bachelor's thesis, Chair of Process Systems Engineering, RWTH Aachen University, 2024.

[10] M. Granderath. Economic Nonlinear Model Predictive Control for Optimal Flexible Operation of Biodiesel Production. Master's thesis, Chair of Process Systems Engineering, RWTH Aachen University, 2024.

[11] N. Groll. Dynamic Scheduling with Tracking Nonlinear Model Predictive Control for Flexible Biodiesel Production. Master's thesis, Chair of Process Systems Engineering, RWTH Aachen University, 2024.

[12] V. Klippel. Cooperative Distributed Economic Nonlinear Model Predictive Control for Flexible Chemical Production. Master's thesis, Chair of Process Systems Engineering, RWTH Aachen University, 2024.

[13] A. Weber. Temperature Profiles in Distillation Columns: Behavior under Different Operating Points. Master's thesis, Chair of Process Systems Engineering, RWTH Aachen University, 2025.

[14] Z. J. Schiffer and K. Manthiram. Electrification and Decarbonization of the Chemical Industry. *Joule*, 1(1):10–14, 2017.

[15] A. Mitsos, N. Asprion, C. A. Floudas, M. Bortz, M. Baldea, D. Bonvin, A. Caspari, and P. Schäfer. Challenges in process optimization for new feedstocks and energy sources. *Computers & Chemical Engineering*, 113:209–221, 2018.

[16] J. L. Barton. Electrification of the chemical industry. *Science*, 368(6496):1181–1182, 2020.

[17] Q. Zhang and I. E. Grossmann. Planning and Scheduling for Industrial Demand Side Management: Advances and Challenges. In M. Martín, editor, *Alternative Energy Sources and Technologies: Process Design and Operation*, pages 383–414. Springer International Publishing, Cham, 2016.

[18] Agora Energiewende. Electricity Data. `https://www.agora-energiewende.de`, 2023. Accessed: March 29, 2023.

[19] C. M. Masuku, R. S. Caulkins, and J. J. Siirola. Process decarbonization through electrification. *Current Opinion in Chemical Engineering*, 44:101011, 2024.

[20] M. Baldea and I. Harjunkoski. Integrated production scheduling and process control: A systematic review. *Computers & Chemical Engineering*, 71:377–390, 2014.

[21] A. Caspari, C. Tsay, A. Mhamdi, M. Baldea, and A. Mitsos. The integration of scheduling and control: Top-down vs. bottom-up. *Journal of Process Control*, 91: 50–62, 2020.

[22] D. Dering and C. L. Swartz. A scenario-based framework for the integration of scheduling and control under multiple uncertainties. *Journal of Process Control*, 129:103055, 2023.

[23] M. Cegla, R. Semrau, F. Tamagnini, and S. Engell. Flexible process operation for electrified chemical plants. *Current Opinion in Chemical Engineering*, 39:100898, 2023.

[24] I. Harjunkoski, R. Nyström, and A. Horch. Integration of scheduling and control—Theory or practice? *Computers & Chemical Engineering*, 33(12):1909–1918, 2009.

[25] E. N. Pistikopoulos and N. A. Diangelakis. Towards the integration of process design, control and scheduling: Are we getting closer? *Computers & Chemical Engineering*, 91:85–92, 2016.

[26] P. Daoutidis, W. Tang, and S. S. Jogwar. Decomposing complex plants for distributed control: Perspectives from network theory. *Computers & Chemical Engineering*, 114: 43–51, 2018.

[27] P. M. Castro, I. E. Grossmann, and Q. Zhang. Expanding scope and computational challenges in process scheduling. *Computers & Chemical Engineering*, 114:14–42, 2018.

[28] D. Dering and C. L. Swartz. Integration of Scheduling and Control for Plants Controlled by Distributed MPC Systems. *Industrial & Engineering Chemistry Research*, 63(27):12016–12034, 2024.

[29] Q. Zhang, I. E. Grossmann, C. F. Heuberger, A. Sundaramoorthy, and J. M. Pinto. Air separation with cryogenic energy storage: Optimal scheduling considering electric energy and reserve markets. *AIChE Journal*, 61(5):1547–1558, 2015.

[30] Q. Zhang, A. Sundaramoorthy, I. E. Grossmann, and J. M. Pinto. A discrete-time scheduling model for continuous power-intensive process networks with various power contracts. *Computers & Chemical Engineering*, 84:382–393, 2016.

[31] H. Li and C. L. Swartz. Approximation techniques for dynamic real-time optimization (DRTO) of distributed MPC systems. *Computers & Chemical Engineering*, 118:195–209, 2018.

[32] M. Ellis, H. Durand, and P. D. Christofides. A tutorial review of economic model predictive control methods. *Journal of Process Control*, 24(8):1156–1178, 2014.

[33] A. Caspari, C. Offermanns, P. Schäfer, A. Mhamdi, and A. Mitsos. A flexible air separation process: 2. Optimal operation using economic model predictive control. *AIChE Journal*, 65(11):e16721, 2019.

[34] H. Fukuda, A. Kondo, and H. Noda. Biodiesel fuel production by transesterification of oils. *Journal of Bioscience and Bioengineering*, 92(5):405–416, 2001.

[35] G. Vicente, M. Martinez, and J. Aracil. Integrated biodiesel production: a comparison of different homogeneous catalysts systems. *Bioresource Technology*, 92(3): 297–305, 2004.

[36] Y. Zhang, M. A. Dubé, D. D. McLean, and M. Kates. Biodiesel production from waste cooking oil: 1. Process design and technological assessment. *Bioresource Technology*, 89(1):1–16, 2003.

[37] N. Nazir, N. Ramli, D. Mangunwidjaja, E. Hambali, D. Setyaningsih, S. Yuliani, M. A. Yarmo, and J. Salimon. Extraction, transesterification and process control in biodiesel production from Jatropha curcas. *European Journal of Lipid Science and Technology*, 111(12):1185–1200, 2009.

[38] A. Abbaszaadeh, B. Ghobadian, M. R. Omidkhah, and G. Najafi. Current biodiesel production technologies: A comparative review. *Energy Conversion and Management*, 63(4):138–148, 2012.

[39] I. E. Grossmann and M. Morari. Operability, Resiliency and Flexibility – Process Design Objectives for a Changing World. In *Proceedings of the 2nd International Conference on Foundations of Computer-Aided Process Design*, pages 931–1030, 1984.

[40] A. Ghobeity and A. Mitsos. Optimal time-dependent operation of seawater reverse osmosis. *Desalination*, 263(1):76–88, 2010.

[41] K. Oikonomou and M. Parvania. Optimal Participation of Water Desalination Plants in Electricity Demand Response and Regulation Markets. *IEEE Systems Journal*, 14(3):3729–3739, 2020.

[42] L. C. Brée, K. Perrey, A. Bulan, and A. Mitsos. Demand side management and operational mode switching in chlorine production. *AIChE Journal*, 65(7):e16352, 2019.

[43] J. I. Otashu and M. Baldea. Demand response-oriented dynamic modeling and operational optimization of membrane-based chlor-alkali plants. *Computers & Chemical Engineering*, 121:396–408, 2019.

[44] K. W. Scholl and S. C. Sorenson, editors. *Combustion of Soybean Oil Methyl Ester in a Direct Injection Diesel Engine*, 1993. SAE International.

[45] L. E. Wagner, S. J. Clark, and M. D. Schrock. *Effects of soybean oil esters on the performance, lubricating oil, and water of diesel engines*. Society of Automotive Engineers, Inc.,Warrendale, PA, United States, 1984.

[46] V. Kariwala and G. P. Rangaiah. *Plantwide Control: Recent Developments and Applications*. John Wiley & Sons Ltd, United Kingdom, 2012.

[47] P. U. Okoye, A. Longoria, P. J. Sebastian, S. Wang, S. Li, and B. H. Hameed. A review on recent trends in reactor systems and azeotrope separation strategies for catalytic conversion of biodiesel-derived glycerol. *Science of The Total Environment*, 719:134595, 2020.

[48] A. Demirbas. Biodiesel from vegetable oils via transesterification in supercritical methanol. *Energy Conversion and Management*, 43(17):2349–2356, 2002.

[49] P. Maheshwari, M. B. Haider, M. Yusuf, J. J. Klemes, A. Bokhari, M. Beg, A. Al-Othman, R. Kumar, and A. K. Jaiswal. A review on latest trends in cleaner biodiesel production: Role of feedstock, production methods, and catalysts. *Journal of Cleaner Production*, 355:131588, 2022.

[50] E. Shahid and Y. Jamal. A review of biodiesel as vehicular fuel. *Renewable and Sustainable Energy Reviews*, 12:2484–2494, 2008.

[51] M. Martín and I. E. Grossmann. Simultaneous Optimization and Heat Integration for Biodiesel Production from Cooking Oil and Algae. *Industrial & Engineering Chemistry Research*, 51(23):7998–8014, 2012.

[52] S.N. Gebremariam and J.M. Marchetti. Economics of biodiesel production: Review. *Energy Conversion and Management*, 168:74–84, 2018.

[53] A. Caspari, A. M. Bremen, J. Faust, F. Jung, C. D. Kappatou, S. Sass, Y. Vaupel, R. Hannemann-Tamás, A. Mhamdi, and A. Mitsos. DyOS - A Framework for Optimization of Large-Scale Differential Algebraic Equation Systems. In A. A. Kiss, E. Zondervan, R. Lakerveld, and L. Özkan, editors, *Computer Aided Chemical Engineering: 29 European Symposium on Computer Aided Process Engineering*, volume 46, pages 619–624. Elsevier, 2019.

[54] R. G. Brusch and R. H. Schappelle. Solution of Highly Constrained Optimal Control Problems Using Nonlinear Programing. *AIAA Journal*, 11(2):135–136, 1973.

[55] H. Bock and K. Plitt. A Multiple Shooting Algorithm for Direct Solution of Optimal Control Problems. *IFAC Proceedings Volumes*, 17(2):1603–1608, 1984.

[56] M. Schlegel, K. Stockmann, T. Binder, and W. Marquardt. Dynamic optimization using adaptive control vector parameterization. *Computers & Chemical Engineering*, 29(8):1731–1751, 2005.

[57] F. Assassa and W. Marquardt. Dynamic optimization using adaptive direct multiple shooting. *Computers & Chemical Engineering*, 60:242–259, 2014.

[58] P. Fritzson. *Principles of Object-Oriented Modeling and Simulation with Modelica 3.3: A Cyber-Physical Approach*. Wiley – IEEE Press, Piscataway, NJ 08854, 2nd edition, 2015.

[59] K. A. Esmonde-White, M. Cuellar, C. Uerpmann, B. Lenain, and I. R. Lewis. Raman spectroscopy as a process analytical technology for pharmaceutical manufacturing and bioprocessing. *Analytical and Bioanalytical Chemistry*, 409(3):637–649, 2017.

[60] Z. D. Harms, Z. Shi, R. A. Kulkarni, and D. P. Myers. Characterization of Near-Infrared and Raman Spectroscopy for In-Line Monitoring of a Low-Drug Load Formulation in a Continuous Manufacturing Process. *Analytical Chemistry*, 91(13): 8045–8053, 2019.

[61] C. Chen and A. Yang. Power-to-methanol: The role of process flexibility in the integration of variable renewable energy into chemical production. *Energy Conversion and Management*, 228:113673, 2021.

[62] A. Harwardt and W. Marquardt. Heat-integrated distillation columns: Vapor recompression or internal heat integration? *AIChE Journal*, 58(12):3740–3750, 2012.

[63] L. Guedes do Nascimento, L. P. Costa Monteiro, R. de Cássia Colman Simões, and D. M. Prata. Eco-efficiency analysis and intensification of the biodiesel production process through vapor recompression strategy. *Energy*, 275:127479, 2023.

[64] Y. Su, K. K. Tan, and T. H. Lee. Computation delay compensation for real time implementation of robust model predictive control. *Journal of Process Control*, 23 (9):1342–1349, 2013.

[65] M. Ellis and P. D. Christofides. Handling computational delay in economic model predictive control of nonlinear process systems. In *2015 American Control Conference (ACC)*, pages 2962–2967, 2015.

[66] R. Scattolini. Architectures for distributed and hierarchical Model Predictive Control – A review. *Journal of Process Control*, 19(5):723–731, 2009.

[67] P. D. Christofides, R. Scattolini, Muñoz de la Peña, David, and J. Liu. Distributed model predictive control: A tutorial review and future research directions. *Computers & Chemical Engineering*, 51:21–41, 2013.

[68] M. A. Müller and F. Allgöwer. Economic and Distributed Model Predictive Control: Recent Developments in Optimization-Based Control. *SICE Journal of Control, Measurement, and System Integration*, 10(2):39–52, 2017.

[69] W.-H. Chen, J. O'Reilly, and D. J. Ballance. Model predictive control of nonlinear systems: Computational burden and stability. *IEE Proceedings - Control Theory and Applications*, 147(4):387–394, 2000.

[70] R. Findeisen and F. Allgöwer. Computational Delay in Nonlinear Model Predictive Control. *IFAC Proceedings Volumes*, 37(1):427–432, 2004.

[71] L. Grüne, J. Pannek, and K. Worthmann. A prediction based control scheme for networked systems with delays and packet dropouts. In *Proceedings of the 48h IEEE Conference on Decision and Control (CDC) held jointly with 2009 28th Chinese Control Conference*, pages 537–542, 2009.

[72] S. Tayari, R. Abedi, and A. Rahi. Comparative assessment of engine performance and emissions fueled with three different biodiesel generations. *Renewable Energy*, 147:1058–1069, 2020.

[73] B. Freedman, R. O. Butterfield, and E. H. Pryde. Transesterification kinetics of soybean oil 1. *Journal of the American Oil Chemists' Society*, 63(10):1375–1380, 1986.

[74] V. Mandari and S. K. Devarai. Biodiesel Production Using Homogeneous, Heterogeneous, and Enzyme Catalysts via Transesterification and Esterification Reactions: a Critical Review. *BioEnergy Research*, 15(2):935–961, 2022.

[75] M. N. B. Mohiddin, Y. H. Tan, Y. X. Seow, J. Kansedo, N. M. Mubarak, M. O. Abdullah, Y. S. Chan, and M. Khalid. Evaluation on feedstock, technologies, catalyst and reactor for sustainable biodiesel production: A review. *Journal of Industrial and Engineering Chemistry*, 98:60–81, 2021.

[76] B. L. Salvi and N. L. Panwar. Biodiesel resources and production technologies – A review. *Renewable and Sustainable Energy Reviews*, 16(6):3680–3689, 2012.

[77] G. Santori, G. Di Nicola, M. Moglie, and F. Polonara. A review analyzing the industrial biodiesel production practice starting from vegetable oil refining. *Applied Energy*, 92:109–132, 2012.

[78] C. C. Enweremadu and M. M. Mbarawa. Technical aspects of production and analysis of biodiesel from used cooking oil—A review. *Renewable and Sustainable Energy Reviews*, 13(9):2205–2224, 2009.

[79] M. J. Haas, A. J. McAloon, W. C. Yee, and T. A. Foglia. A process model to estimate biodiesel production costs. *Bioresource Technology*, 97(4):671–678, 2006.

[80] A. H. West, D. Posarac, and N. Ellis. Assessment of four biodiesel production processes using HYSYS.Plant. *Bioresource Technology*, 99(14):6587–6601, 2008.

[81] A. A. Apostolakou, I. K. Kookos, C. Marazioti, and K. C. Angelopoulos. Techno-economic analysis of a biodiesel production process from vegetable oils. *Fuel Processing Technology*, 90(7):1023–1031, 2009.

[82] L. L. Myint and M. M. El-Halwagi. Process analysis and optimization of biodiesel production from soybean oil. *Clean Technologies and Environmental Policy*, 11(3): 263–276, 2009.

[83] G. Santana, P. F. Martins, N. de Da Lima Silva, C. B. Batistella, R. Maciel Filho, and M. R. Wolf Maciel. Simulation and cost estimate for biodiesel production using castor oil. *Chemical Engineering Research and Design*, 88(5):626–632, 2010.

[84] S. Lee, D. Posarac, and N. Ellis. Process simulation and economic analysis of biodiesel production processes using fresh and waste vegetable oil and supercritical methanol. *Chemical Engineering Research and Design*, 89(12):2626–2642, 2011.

[85] S. G. Zavarukhin, V. A. Yakovlev, V. N. Parmon, V. G. Sister, E. M. Ivannikova, and O. A. Eliseeva. Development of a process for refining rape seed oil into biodiesel and high-cetane components of diesel fuel. *Chemistry and Technology of Fuels and Oils*, 46(1):1–8, 2010.

[86] H. Noureddini and D. Zhu. Kinetics of transesterification of soybean oil. *Journal of the American Oil Chemists' Society*, 74(11):1457–1463, 1997.

[87] Y. C. Sharma, B. Singh, and J. Korstad. Latest developments on application of heterogenous basic catalysts for an efficient and eco friendly synthesis of biodiesel: A review. *Fuel*, 90(4):1309–1324, 2011.

[88] D. Kusdiana and S. Saka. Kinetics of transesterification in rapeseed oil to biodiesel fuel as treated in supercritical methanol. *Fuel*, 80(5):693–698, 2001.

[89] G. Vicente, M. Martínez, J. Aracil, and A. Esteban. Kinetics of Sunflower Oil Methanolysis. *Industrial & Engineering Chemistry Research*, 44(15):5447–5454, 2005.

[90] W. A. Wali, A. I. Al-Shamma'a, K. H. Hassan, and J. D. Cullen. Online genetic-ANFIS temperature control for advanced microwave biodiesel reactor. *Journal of Process Control*, 22(7):1256–1272, 2012.

[91] C. S. Bildea and A. A. Kiss. Dynamics and control of a biodiesel process by reactive absorption. *Chemical Engineering Research and Design*, 89(2):187–196, 2011.

[92] Y. H. Shen, J. K. Cheng, J. D. Ward, and C. C. Yu. Design and control of biodiesel production processes with phase split and recycle in the reactor system. *Journal of the Taiwan Institute of Chemical Engineers*, 42(5):741–750, 2011.

[93] B. F. Da Silva, J. E. Schmitz, I. C. Franco, and F. V. Da Silva. Plantwide control systems design and evaluation applied to biodiesel production. *Biofuels*, 12(10): 1199–1207, 2021.

[94] C. S. Bildea and A. A. Kiss. Plantwide Control of a Biodiesel Process by Reactive Absorption. In S. Pierucci and G. B. Ferraris, editors, *Computer Aided Chemical Engineering: 20 European Symposium on Computer Aided Process Engineering*, volume 28, pages 535–540. Elsevier, 2010.

[95] A. Regalado-Méndez, R. Romero, R. Natividad, and S. Skogestad. Plant-Wide Control of a Reactive Distillation Column on Biodiesel Production. In R. Silhavy, R. Senkerik, Z. K. Oplatkova, P. Silhavy, and Z. Prokopova, editors, *Automation Control Theory Perspectives in Intelligent Systems*, pages 107–117, Cham, 2016. Springer International Publishing.

[96] F. S. Mjalli and M. A. Hussain. Approximate Predictive versus Self-Tuning Adaptive Control Strategies of Biodiesel Reactors. *Industrial & Engineering Chemistry Research*, 48(24):11034–11047, 2009.

[97] A. S. Brásio, A. Romanenko, N. C. Fernandes, and L. O. Santos. First principle modeling and predictive control of a continuous biodiesel plant. *Journal of Process Control*, 47:11–21, 2016.

[98] P. T. Benavides and U. Diwekar. Optimal control of biodiesel production in a batch reactor: Part I: Deterministic control. *Fuel*, 94:211–217, 2012.

[99] P. T. Benavides and U. Diwekar. Optimal control of biodiesel production in a batch reactor: Part II: Stochastic control. *Fuel*, 94:218–226, 2012.

[100] P. T. Benavides and U. Diwekar. Studying various optimal control problems in biodiesel production in a batch reactor under uncertainty. *Fuel*, 103:585–592, 2013.

[101] Aspen Technology. Aspen Plus | Process Simulation Software | AspenTech, 2022.

[102] Aspen Technology. Aspen HYSYS | Process Simulation Software | AspenTech, 2022.

[103] A.-F. Chang and Y. A. Liu. Integrated Process Modeling and Product Design of Biodiesel Manufacturing. *Industrial & Engineering Chemistry Research*, 49(3):1197–1213, 2010.

[104] A. S. Brásio, A. Romanenko, J. Leal, L. O. Santos, and N. C. Fernandes. Nonlinear model predictive control of biodiesel production via transesterification of used vegetable oils. *Journal of Process Control*, 23(10):1471–1479, 2013.

[105] M. Reza Talaghat, S. Mokhtari, and M. Saadat. Modeling and optimization of biodiesel production from microalgae in a batch reactor. *Fuel*, 280:118578, 2020.

[106] V. K. Aniya, R. K. Muktham, K. Alka, and B. Satyavathi. Modeling and simulation of batch kinetics of non-edible karanja oil for biodiesel production: A mass transfer study. *Fuel*, 161:137–145, 2015.

[107] L.-H. Cheng, S.-Y. Yen, Z.-S. Chen, and J. Chen. Modeling and simulation of biodiesel production using a membrane reactor integrated with a prereactor. *Chemical Engineering Science*, 69(1):81–92, 2012.

[108] O. Farobie, N. Hasanah, and Y. Matsumura. Artificial Neural Network Modeling to Predict Biodiesel Production in Supercritical Methanol and Ethanol Using Spiral Reactor. *Procedia Environmental Sciences*, 28:214–223, 2015.

[109] H. Renon and J. M. Prausnitz. Local compositions in thermodynamic excess functions for liquid mixtures. *AIChE Journal*, 14(1):135–144, 1968.

[110] Design Institute for Physical Property Data. *DIPPR Project 801, Full Version: Evaluated Standard Thermophysical Property Values*. BYU DIPPR, Thermophysical Properties Laboratory, Provo, 2010.

[111] J. J. Downs and S. Skogestad. An industrial and academic perspective on plantwide control. *Annual Reviews in Control*, 35(1):99–110, 2011.

[112] W. L. Luyben, B. D. Tyréus, and M. L. Luyben. *Plantwide Process Control*. McGraw-Hill, New York, United States, 1998.

[113] S. Skogestad. Control structure design for complete chemical plants. *Computers & Chemical Engineering*, 28(1-2):219–234, 2004.

[114] A. C. de Araújo, M. Govatsmark, and S. Skogestad. Application of plantwide control to the HDA process. I steady-state optimization and self-optimizing control. *Control Engineering Practice*, 15(10):1222–1237, 2007.

[115] A. C. B. de Araújo, E. S. Hori, and S. Skogestad. Application of Plantwide Control to the HDA Process. II Regulatory Control. *Industrial & Engineering Chemistry Research*, 46(15):5159–5174, 2007.

[116] N. V. S. N. Murthy Konda, G. P. Rangaiah, and P. R. Krishnaswamy. Plantwide Control of Industrial Processes: An Integrated Framework of Simulation and Heuristics. *Industrial & Engineering Chemistry Research*, 44(22):8300–8313, 2005.

[117] P. C. Narváez, S. M. Rincón, and F. J. Sánchez. Kinetics of Palm Oil Methanolysis. *Journal of the American Oil Chemists' Society*, 84(10):971–977, 2007.

[118] D. M. Yancy-Caballero and R. Guirardello. Modeling and parameters fitting of chemical and phase equilibria in reactive systems for biodiesel production. *Biomass and Bioenergy*, 81(1):544–555, 2015.

[119] A. A. Albuquerque, F. T. Ng, L. Danielski, and L. Stragevitch. Phase equilibrium modeling in biodiesel production by reactive distillation. *Fuel*, 271(6):117688, 2020.

[120] A. Salehi, A. Karbassi, B. Ghobadian, A. Ghasemi, and A. Doustgani. Simulation process of biodiesel production plant. *Environmental Progress & Sustainable Energy*, 38(6):e13264, 2019.

[121] J. D. Engerer, G. R. Jackson, R. Paul, and T. S. Fisher. Flash Boiling and Desorption From a Macroporous Carbon-Boron-Nitrogen Foam. In *Volume 6B: Energy*. American Society of Mechanical Engineers, 2013.

[122] British Standards Institution. Automotive fuels — Fatty acid methyl esters (FAME) for diesel engines — Requirements and test methods: EN 14214:2008+A1:2009, 2010.

[123] German Union for the Promotion of Oil and Protein Plants. Annual Report 2020/2021: Biodiesel production capacities in Germany in 2020, 2020.

[124] K. M. Ebeling, D. Bongartz, S. Mürtz, R. Palkovits, and A. Mitsos. Thermodynamic and Economic Potential of Glycerol Oxidation to Replace Oxygen Evolution in Water Electrolysis. *Industrial & Engineering Chemistry Research*, 63(18):8250–8260, 2024.

[125] R. Manosak, S. Limpattayanate, and M. Hunsom. Sequential-refining of crude glycerol derived from waste used-oil methyl ester plant via a combined process of chemical and adsorption. *Fuel Processing Technology*, 92(1):92–99, 2011.

[126] R. Ciriminna, C. Della Pina, M. Rossi, and M. Pagliaro. Understanding the glycerol market. *European Journal of Lipid Science and Technology*, 116(10):1432–1439, 2014.

[127] S. B. Glisic and A. M. Orlović. Review of biodiesel synthesis from waste oil under elevated pressure and temperature: Phase equilibrium, reaction kinetics, process design and techno-economic study. *Renewable and Sustainable Energy Reviews*, 31: 708–725, 2014.

[128] V. Hagenmeyer and M. Nohr. Flatness-Based Two-Degree-of-Freedom Control of Industrial Semi-Batch Reactors. In T. Meurer, K. Graichen, and E. D. Gilles, editors, *Control and Observer Design for Nonlinear Finite and Infinite Dimensional Systems*, pages 315–332. Springer Berlin Heidelberg, Berlin, Heidelberg, 2005.

[129] T. Meurer, K. Graichen, and E. D. Gilles, editors. *Control and Observer Design for Nonlinear Finite and Infinite Dimensional Systems*. Springer Berlin Heidelberg, Berlin, Heidelberg, 2005.

[130] A. U. Raghunathan, M. Soledad Diaz, and L. T. Biegler. An MPEC formulation for dynamic optimization of distillation operations. *Computers & Chemical Engineering*, 28(10):2037–2052, 2004.

[131] A. Caspari, C. Offermanns, P. Schäfer, A. Mhamdi, and A. Mitsos. A flexible air separation process: 1. Design and steady–state optimizations. *AIChE Journal*, 65 (11):467, 2019.

[132] H. G. Rackett. Equation of state for saturated liquids. *Journal of Chemical & Engineering Data*, 15(4):514–517, 1970.

[133] B. E. Poling, J. M. Prausnitz, and J. P. O'Connell. *The properties of gases and liquids*. McGraw-Hill, New York, 5th edition, 2001.

[134] Aspen Technology. Aspen Physical Property System: Physical property methods and models, 2013.

[135] Q. M. Yu-Wu, E. Weiss-Hortala, R. Barna, H. Boucard, and S. Bulza. Glycerol and bioglycerol conversion in supercritical water for hydrogen production. *Environmental Technology*, 33(19-21):2245–2255, 2012.

[136] N. R. Jaegers, W. Hu, T. J. Weber, and J. Z. Hu. Low-temperature ($<$ 200 °C) degradation of electronic nicotine delivery system liquids generates toxic aldehydes. *Scientific Reports*, 11(1):7800, 2021.

[137] W. Sakdasri, S. Ngamprasertsith, P. Saengsuk, and R. Sawangkeaw. Supercritical reaction between methanol and glycerol: The effects of reaction products on biodiesel properties. *Energy Conversion and Management: X*, 12(2):100145, 2021.

[138] H.-Y. Shin, S.-M. Lim, S.-Y. Bae, and S. C. Oh. Thermal decomposition and stability of fatty acid methyl esters in supercritical methanol. *Journal of Analytical and Applied Pyrolysis*, 92(2):332–338, 2011.

[139] Y. Zhu. *An Experimental Study on Thermal Stability of Biodiesel Fuel*. Master Thesis, Syracuse University, 2012.

[140] N. V. S. N. Murthy Konda, G. P. Rangaiah, and P. R. Krishnaswamy. A simple and effective procedure for control degrees of freedom. *Chemical Engineering Science*, 61 (4):1184–1194, 2006.

[141] W. L. Luyben, B. D. Tyreus, and M. Luyben. *Plantwide process control*. McGraw-Hill, New York, United States, 1999.

[142] Dassault Systèmes. Dymola Systems Engineering. `https://www.3ds.com/products-services/catia/products/dymola`, 2022. Accessed: March 22, 2023.

[143] University of California Santa Barbara. DASSL: Software | Computational Science and Engineering Research Group, 2022.

[144] S. Vasudevan and G. P. Rangaiah. Criteria for Performance Assessment of Plantwide Control Systems. *Industrial & Engineering Chemistry Research*, 49(19):9209–9221, 2010.

[145] N. V. S. N. Murthy Konda and G. P. Rangaiah. Performance Assessment of Plantwide Control Systems of Industrial Processes. *Industrial & Engineering Chemistry Research*, 46(4):1220–1231, 2007.

[146] Neste market data. Palm and rapeseed oil prices. `https://www.agora-energiewende.de`, 2023. Accessed: March 29, 2023.

[147] B. Bruns, F. Herrmann, M. Polyakova, M. Grünewald, and J. Riese. A systematic approach to define flexibility in chemical engineering. *Journal of Advanced Manufacturing and Processing*, 2(4):e10063, 2020.

[148] R. W. H. Sargent and G. R. Sullivan. The development of an efficient optimal control package. In J. Stoer, editor, *Optimization Techniques*, pages 158–168. Springer Berlin Heidelberg, Berlin, Heidelberg, 1978.

[149] C. Kirches, L. Wirsching, H. G. Bock, and J. P. Schlöder. Efficient direct multiple shooting for nonlinear model predictive control on long horizons. *Journal of Process Control*, 22(3):540–550, 2012.

[150] S. Kameswaran and L. T. Biegler. Simultaneous dynamic optimization strategies: Recent advances and challenges. *Computers & Chemical Engineering*, 30(10):1560–1575, 2006.

[151] C. Pablos, A. Merino, L. F. Acebes, J. L. Pitarch, and L. T. Biegler. Dynamic optimization approach to coordinate industrial production and cogeneration operation under electricity price fluctuations. *Computers & Chemical Engineering*, 149:107292, 2021.

[152] F. J. Baader, A. Bardow, and M. Dahmen. Simultaneous mixed-integer dynamic scheduling of processes and their energy systems. *AIChE Journal*, 68(8):e17741, 2022.

[153] C. Hank, S. Gelpke, A. Schnabl, R. J. White, J. Full, N. Wiebe, T. Smolinka, A. Schaadt, H.-M. Henning, and C. Hebling. Economics & carbon dioxide avoidance cost of methanol production based on renewable hydrogen and recycled carbon dioxide-power-to-methanol. *Sustainable Energy and Fuels*, 2(6):1244–1261, 2018.

[154] Y. H. Chew, A. L. Ling, and A. Jaya. Distillation Column Selection and Sizing, 2011.

[155] A. A. Kiss. *Advanced Distillation Technologies: Design, Control and Applications*. Wiley, 2013.

[156] R. W. Serth and T. Lestina. *Process Heat Transfer: Principles, Applications and Rules of Thumb*. Elsevier Science, 2014.

[157] D. W. Green and M. Z. Southard. *Perry's chemical engineers' handbook*. McGraw Hill Education, New York, ninth edition, 85th anniversary edition, 2019.

[158] R. Sánta. Investigations of the performance of a heat pump with internal heat exchanger. *Journal of Thermal Analysis and Calorimetry*, 147(15):8499–8508, 2022.

[159] S. S. Baakeem, J. Orfi, and A. Alabdulkarem. Optimization of a multistage vapor-compression refrigeration system for various refrigerants. *Applied Thermal Engineering*, 136:84–96, 2018.

[160] M. O. McLinden, C. J. Seeton, and A. Pearson. New refrigerants and system configurations for vapor-compression refrigeration. *Science (New York, N.Y.)*, 370(6518): 791–796, 2020.

[161] T. H. Karakoc and M. B. Ozerdem. *Sustainable Aviation: Energy and Environmental Issues*. Springer International Publishing and Imprint: Springer, Cham, 1st edition, 2016.

[162] B. Eppinger, L. Zigan, J. Karl, and S. Will. Pumped thermal energy storage with heat pump-ORC-systems: Comparison of latent and sensible thermal storages for various fluids. *Applied Energy*, 280:115940, 2020.

[163] G. F. Frate, L. Ferrari, and U. Desideri. Analysis of suitability ranges of high temperature heat pump working fluids. *Applied Thermal Engineering*, 150:628–640, 2019.

[164] K. A. Aikins, S.-H. Lee, and J. M. Choi. Technology Review of Two-Stage Vapor Compression Heat Pump System. *International Journal of Air-Conditioning and Refrigeration*, 21(03):1330002, 2013.

[165] A. Mota-Babiloni, C. Mateu-Royo, J. Navarro-Esbrí, F. Molés, M. Amat-Albuixech, and Á. Barragán-Cervera. Optimisation of high-temperature heat pump cascades with internal heat exchangers using refrigerants with low global warming potential. *Energy*, 165:1248–1258, 2018.

[166] C. Arpagaus, F. Bless, M. Uhlmann, J. Schiffmann, and S. S. Bertsch. High temperature heat pumps: Market overview, state of the art, research status, refrigerants, and application potentials. *Energy*, 152:985–1010, 2018.

[167] C. Mateu-Royo, C. Arpagaus, A. Mota-Babiloni, J. Navarro-Esbrí, and S. S. Bertsch. Advanced high temperature heat pump configurations using low GWP refrigerants for industrial waste heat recovery: A comprehensive study. *Energy Conversion and Management*, 229:113752, 2021.

[168] A. Cavallini, L. Cecchinato, M. Corradi, E. Fornasieri, and C. Zilio. Two-stage transcritical carbon dioxide cycle optimisation: A theoretical and experimental analysis. *International Journal of Refrigeration*, 28(8):1274–1283, 2005.

[169] L. J. Müller, A. Kätelhön, S. Bringezu, S. McCoy, S. Suh, R. Edwards, V. Sick, S. Kaiser, R. Cuéllar-Franca, A. El Khamlichi, J. H. Lee, N. von der Assen, and A. Bardow. The carbon footprint of the carbon feedstock CO 2. *Energy & Environmental Science*, 13(9):2979–2992, 2020.

[170] C. Schoeneberger, J. Zhang, C. McMillan, J. B. Dunn, and E. Masanet. Electrification potential of U.S. industrial boilers and assessment of the GHG emissions impact. *Advances in Applied Energy*, 5:100089, 2022.

[171] L. T. Biegler. *Nonlinear programming: concepts, algorithms, and applications to chemical processes*. SIAM, 2010.

[172] A. Caspari, L. Lüken, P. Schäfer, Y. Vaupel, A. Mhamdi, L. T. Biegler, and A. Mitsos. Dynamic optimization with complementarity constraints: Smoothing for direct shooting. *Computers & Chemical Engineering*, 139:106891, 2020.

[173] A. Fischer. A special newton-type optimization method. *Optimization*, 24(3-4): 269–284, 1992.

[174] M. Patrascu and P. I. Barton. Optimal campaigns in end-to-end continuous pharmaceuticals manufacturing. Part 2: Dynamic optimization. *Chemical Engineering and Processing - Process Intensification*, 125:124–132, 2018.

[175] D. Ralph and S. J. Wright. Some properties of regularization and penalization schemes for MPECs. *Optimization Methods and Software*, 19(5):527–556, 2004.

[176] R. C. Pattison and M. Baldea. Multistream heat exchangers: Equation-oriented modeling and flowsheet optimization. *AIChE Journal*, 61(6):1856–1866, 2015.

[177] SMARD. Market data visuals. `http://www.smard.de`, 2023. Accessed: March 22, 2023.

[178] R. Hannemann, W. Marquardt, U. Naumann, and B. Gendler. Discrete first- and second-order adjoints and automatic differentiation for the sensitivity analysis of dynamic models. *Procedia Computer Science*, 1(1):297–305, 2010.

[179] P. E. Gill, W. Murray, and M. A. Saunders. SNOPT: An SQP Algorithm for Large-Scale Constrained Optimization. *SIAM Review*, 47(1):99–131, 2005.

[180] Functional mock-up interface for model exchange and co-simulation. `https://fmi-standard.org`, 2023. Accessed: March 22, 2023.

[181] R. C. Pattison, C. R. Touretzky, T. Johansson, I. Harjunkoski, and M. Baldea. Optimal Process Operations in Fast-Changing Electricity Markets: Framework for Scheduling with Low-Order Dynamic Models and an Air Separation Application. *Industrial & Engineering Chemistry Research*, 55(16):4562–4584, 2016.

[182] R. Amrit, J. B. Rawlings, and D. Angeli. Economic optimization using model predictive control with a terminal cost. *Annual Reviews in Control*, 35(2):178–186, 2011.

[183] P. N. Köhler, M. A. Müller, and F. Allgöwer. Transient performance of economic model predictive control with average constraints. In *2017 IEEE 56th Annual Conference on Decision and Control (CDC)*, pages 5557–5562, 2017.

[184] M. Alamir and G. Pannocchia. A new formulation of Economic Model Predictive Control without terminal constraint. *Automatica*, 125:109420, 2021.

[185] K.-H. Lin and L. T. Biegler. Self-stabilizing economic model predictive control without pre-calculated steady-state optima: Stability and robustness. *Computers & Chemical Engineering*, 178:108349, 2023.

[186] J. Köhler, M. A. Müller, and F. Allgöwer. Analysis and design of model predictive control frameworks for dynamic operation—An overview. *Annual Reviews in Control*, 57:100929, 2024.

[187] J. Liu, X. Chen, Muñoz de la Peña, David, and P. D. Christofides. Sequential and iterative architectures for distributed model predictive control of nonlinear process systems. *AIChE Journal*, 56(8):2137–2149, 2010.

[188] R. Moliner-Heredia, I. Peñarrocha-Alós, and R. Sanchis-Llopis. Economic model predictive control of wastewater treatment plants based on BSM1 using linear prediction models. In *2019 IEEE 15th International Conference on Control and Automation (ICCA)*, pages 73–78, 2019.

[189] G. D. Patrón, K. Toffolo, and L. Ricardez-Sandoval. Economic model predictive control for packed bed chemical looping combustion. *Chemical Engineering and Processing - Process Intensification*, 198:109731, 2024.

[190] R. Huang, V. M. Zavala, and L. T. Biegler. Advanced step nonlinear model predictive control for air separation units. *Journal of Process Control*, 19(4):678–685, 2009.

[191] P. Schäfer, A. Caspari, K. Kleinhans, A. Mhamdi, and A. Mitsos. Reduced dynamic modeling approach for rectification columns based on compartmentalization and artificial neural networks. *AIChE Journal*, 65(5):e16568, 2019.

[192] P. Schäfer, A. Caspari, A. Mhamdi, and A. Mitsos. Economic nonlinear model predictive control using hybrid mechanistic data-driven models for optimal operation in real-time electricity markets: In-silico application to air separation processes. *Journal of Process Control*, 84:171–181, 2019.

[193] R. Nian, J. Liu, and B. Huang. A review On reinforcement learning: Introduction and applications in industrial process control. *Computers & Chemical Engineering*, 139:106886, 2020.

[194] J. C. Schulze, D. T. Doncevic, and A. Mitsos. Identification of MIMO Wiener-type Koopman models for data-driven model reduction using deep learning. *Computers & Chemical Engineering*, 161:107781, 2022.

[195] H. Scheu and W. Marquardt. Sensitivity-based coordination in distributed model predictive control. *Journal of Process Control*, 21(5):715–728, 2011.

[196] C. Conte, C. N. Jones, M. Morari, and M. N. Zeilinger. Distributed synthesis and stability of cooperative distributed model predictive control for linear systems. *Automatica*, 69:117–125, 2016.

[197] L. Grüne and J. Pannek. *Nonlinear Model Predictive Control: Theory and Algorithms*. Communications and Control Engineering. Springer Cham, Cham, 2017.

[198] J. B. Rawlings and B. T. Stewart. Coordinating multiple optimization-based controllers: New opportunities and challenges. *Journal of Process Control*, 18(9):839–845, 2008.

[199] A. N. Venkat, J. B. Rawlings, and S. J. Wright. Stability and optimality of distributed model predictive control. In *Proceedings of the 44th IEEE Conference on Decision and Control*, pages 6680–6685, 2005.

[200] A. Caspari, C. Offermanns, A.-M. Ecker, M. Pottmann, G. Zapp, A. Mhamdi, and A. Mitsos. A wave propagation approach for reduced dynamic modeling of distillation columns: Optimization and control. *Journal of Process Control*, 91:12–24, 2020.

[201] D. Angeli, R. Amrit, and J. B. Rawlings. On Average Performance and Stability of Economic Model Predictive Control. *IEEE Transactions on Automatic Control*, 57 (7):1615–1626, 2012.

[202] T. Faulwasser, L. Grüne, and M. A. Müller. Economic Nonlinear Model Predictive Control. *Foundations and Trends® in Systems and Control*, 5(1):1–98, 2018.

[203] D. W. Griffith, V. M. Zavala, and L. T. Biegler. Robustly stable economic NMPC for non-dissipative stage costs. *Journal of Process Control*, 57:116–126, 2017.

[204] V. M. Zavala and L. T. Biegler. The advanced-step NMPC controller: Optimality, stability and robustness. *Automatica*, 45(1):86–93, 2009.

[205] S. Chen, Z. Wu, D. Rincon, and P. D. Christofides. Machine learning-based distributed model predictive control of nonlinear processes. *AIChE Journal*, 66(11): e17013, 2020.

[206] T. Zhao, Y. Zheng, and Z. Wu. Feature selection-based machine learning modeling for distributed model predictive control of nonlinear processes. *Computers & Chemical Engineering*, 169:108074, 2023.

[207] P. O. M. Scokaert, D. Q. Mayne, and J. B. Rawlings. Suboptimal model predictive control (feasibility implies stability). *IEEE Transactions on Automatic Control*, 44 (3):648–654, 1999.

[208] M. Diehl, H. G. Bock, and J. P. Schlöder. A Real-Time Iteration Scheme for Nonlinear Optimization in Optimal Feedback Control. *SIAM Journal on Control and Optimization*, 43(5):1714–1736, 2005.

[209] L. Würth, R. Hannemann, and W. Marquardt. Neighboring-extremal updates for nonlinear model-predictive control and dynamic real-time optimization. *Journal of Process Control*, 19(8):1277–1288, 2009.

[210] I. J. Wolf, D. A. Muñoz, and W. Marquardt. Consistent hierarchical economic NMPC for a class of hybrid systems using neighboring-extremal updates. *Journal of Process Control*, 24(2):389–398, 2014.

[211] Z. Zhou, Z. Liu, H. Su, and L. Zhang. Model predictive control with fractional-order delay compensation for fast sampling systems. *Science China Information Sciences*, 64(7):172211, 2021.

[212] J. Jäschke, X. Yang, and L. T. Biegler. Fast economic model predictive control based on NLP-sensitivities. *Journal of Process Control*, 24(8):1260–1272, 2014.

[213] S. R. Logan. The origin and status of the Arrhenius equation. *Journal of Chemical Education*, 59(4):279, 1982.

[214] Aspen Technology. Biodiesel Production from Vegetable Oil: Aspen Plus Biodiesel Model, 2014.

[215] F. A. Aly and L. L. Lee. Self-consistent equations for calculating the ideal gas heat capacity, enthalpy, and entropy. *Fluid Phase Equilibria*, 6(3):169–179, 1981.

[216] V. Gopal and L. T. Biegler. Nonsmooth dynamic simulation with linear programming based methods. *Computers & Chemical Engineering*, 21(7):675–689, 1997.

[217] A. M. Sahlodin, H. A. J. Watson, and P. I. Barton. Nonsmooth model for dynamic simulation of phase changes. *AIChE Journal*, 62(9):3334–3351, 2016.

[218] T. Ploch, M. Glass, A. M. Bremen, R. Hannemann-Tamás, and A. Mitsos. Modeling of dynamic systems with a variable number of phases in liquid-liquid equilibria. *AIChE Journal*, 65(2):571–581, 2019.

[219] Neste market data. Palm and rapeseed oil prices. https://www.neste.com/investors/market-data/palm-and-rapeseed-oil-prices, 2023. Accessed: March 23, 2023.

[220] FRED economic data. Global price of Rapeseed Oil. https://fred.stlouisfed.org/series/PROILUSDM, 2023. Accessed: March 23, 2023.

[221] Chemanalyst. Methanol Price Trend and Forecast. https://www.chemanalyst.com, 2023. Accessed: March 23, 2023.

[222] Methanex. Methanex Methanol Price. https://www.methanex.com/about-methanol/pricing, 2023. Accessed: March 23, 2023.

[223] Chemanalyst. Caustic Soda Price Trend and Forecast. https://www.chemanalyst.com, 2023. Accessed: March 23, 2023.

[224] ChemNet. Phosphoric Acid Market. http://news.chemnet.com/Chemical-News/detail-2461845.html, 2023. Accessed: March 23, 2023.

[225] Statista. Wholesale biodiesel price in Germany from 2019 to 2022. https://www.statista.com/statistics/1295994/biodiesel-fuel-wholesale-price-in-germany, 2023. Accessed: March 23, 2023.

[226] C. A. Quispe, C. J. Coronado, and J. A. Carvalho Jr. Glycerol: Production, consumption, prices, characterization and new trends in combustion. *Renewable and Sustainable Energy Reviews*, 27:475–493, 2013.

[227] World Bank Blogs. Fertilizer prices expected to remain higher for longer. https://blogs.worldbank.org/opendata/fertilizer-prices-expected-remain-higher-longer, 2023. Accessed: March 23, 2023.

DOI: 10.18154/RWTH-2025-03483

Aachener
Verfahrenstechnik

RWTH AACHEN
UNIVERSITY